INTERNATIONAL DOCTORAL
SCHOOL OF THE USC

Daniel
Regueira Castro

PhD Thesis

Study of ^{16}O dissociation through α scattering in inverse kinematics with the Active Target Time Projection Chamber (AT-TPC)

Santiago de Compostela, 2025

Doctoral Programme in Nuclear and Particles Physics

ESCOLA DE DOUTORAMENTO
INTERNACIONAL DA USC

TESE DE DOUTORAMENTO

STUDY OF ^{16}O DISSOCIATION THROUGH α SCATTERING IN INVERSE KINEMATICS WITH THE ACTIVE TARGET TIME PROJECTION CHAMBER (AT-TPC)

Autor

Daniel Regueira Castro

Directora: Beatriz Fernández Domínguez

Co-Director: Francesc Yassid Ayyad Limonge

Titora: Beatriz Fernández Domínguez

PROGRAMA DE DOUTORAMENTO EN FÍSICA NUCLEAR E DE PARTÍCULAS

SANTIAGO DE COMPOSTELA

Acknowledgments

Let yourself be silently drawn by the strange pull of what you really love.
It will not lead you astray.

Yalāl ad-Dīn Muhammad Rūmī

A mamá y a papá, Angelina Castro Redondo y Juán José Regueira Vergara. Después de darle muchas vueltas, no se me ocurre nadie en el mundo que merezca más que vosotros los primeros agradecimientos de mi tesis. Gracias a los dos por apoyarme incondicionalmente. El camino ha sido duro y yo no lo puse fácil desde el principio, pero habeis sabido transmitirme unos valores y una forma de entender el mundo que es más importante que cualquier tesis o título: me habéis convertido en persona y por ello os estaré eternamente agradecido.

Mamá, contigo he aprendido muchos valores, como la compasión, el cariño, la tenacidad, la constancia y el perdón. Siempre he sentido que por mucho que la vida me pusiera trabas tenía una red de seguridad en ti y en papá. Siempre os he considerado un modelo a seguir y estoy muy orgulloso de ser vuestro hijo. Luchaste con uñas y dientes para sacar adelante a mis hermanos y a mí, para darnos una educación y un futuro. Nunca dejaste que nadie te pisara sin revolverte y abriste el camino a nuevas generaciones de feministas.

Recuerdo, aunque no os lo creáis, la caída del muro de Berlín y cómo ese día comprendí que mis padres eran especiales. Aprendí que en mi familia se celebraban las cosas importantes y que lo importante era la felicidad.

Papá, tus valores anticapitalistas, comunistas y antimaterialistas siempre los llevo con orgullo. Estoy orgulloso de tu lucha obrera en los astilleros allá por los ochenta, y de cómo nunca te dejaste pisar ni corromper por el poder establecido a lo largo de tu vida. Con vosotros aprendí que la historia presente se escribe con mentiras de los que ostentan el poder, ávidos de dinero y sangre, y que el tiempo pone a cada monstruo en su lugar, a que si vivimos una época de genocidio en la que, como dirían Los Suaves, "jóvenes pobres matan a jóvenes pobres mientras cuentan sus ganancias viejos ricos", en esa gran canción que es Ourense-Bosnia, era de valientes recordarlo en un papel como este. Que la censura del poder establecido se retorcería para su matización, pero que la verdad se impondría en algún momento. Como ves, mi papi, puedes tener la sensación de que tus recuerdos te fallan por una enfermedad maldita, pero mientras yo viva tu memoria quedará intacta.

Quisiera dedicarles unas palabras a mis hermanos y a sus compañeros de aventuras. Victor Regueira Castro y Alba Regueira Castro, para mí sois dos caras de una misma moneda. Vuestros valores se entrelazan y el cariño que siento por los dos es idéntico. Victor, eres la persona más bondadosa que conozco, nunca me has mentido y siempre me defendiste aunque supieras que no tenía razón, como buen hermano mayor. ¡Qué decir de mi hermanita! Heredaste la inteligencia de mamá y la mala leche de papá; no cambiaría nada en tí, eres y siempre serás perfecta tal y como eres. Encontrasteis en el camino a dos personas que me alegra poder llamar familia: Martín y María. Vosotros sacáis la mejor parte de mis hemanos como nadie podría hacerlo y haceis la vida de esta familia rarita un poco más feliz.

Continuando con la familia: un beso enorme a mis padrinos Chus y Fernando y a todos mis primos/as y tíos/as. Da gusto poder contar con vosotros y alegrarme por vuestros éxitos con una buena comilona (queda pendiente la de este papelajo, que estoy seguro que será para recordar).

Grazas ós meus directores de tese, Beatriz Fernández Domínguez e Yassid Ayyad Limonge, que contra todo prognóstico non acabamos tirándonos dos pelos. Fostes pacientes e comprensivos coas limitacións que me causaban as miñas enfermidades e espero devolvervos algo dese esforzo con esta tese. Ensinástesme e axudástesme moito. Yassid, has sigut un referent en tot el que concernia la diversió amb ATTPCROOT i el laboratori. Bea, gracias a ti aprendín unha morea de cousas sobre a física nuclear que antes de comezar este proxecto nin imaxinaba que podía chegar a comprender. Admírovos moitísimo ós dous, coas vosas virtudes e defectos. Teño claro que estes anos con vós mereceron moito a pena.

Dentro do grupo que formamos en FICA, ó que lle estou moi agradecido, quería facer unha mención especial a Manuel Caamaño e Hector García Pol (de FICA de corazón), dúas das personas máis admiradas por min nesta facultade e que, ademais de ser excelentes físicos, son excelentes persoas. Sempre me axudaron cando os necesitei e fixeron o meu periplo por isto da investigación moito máis divertido.

Esta tese non tería sentido sen lembrar o peor grupo de despacho e de experimentos que se pode ter: Juan Lois, co pelo máis odiosamente bonito do mundo; Cristina Cabo, sempre serás a m. e p. orixinal; e Daniel Fernández, co corazón máis grande que o peito. Fomos como unha reedición cativa das tartarugas ninja tentando non romper moitas cousas por aí, pero sempre deixando bo sabor de boca e un sorriso onde pasabamos. Alédome moito de tervos coñecido e espero que as nosas vidas sigan para mellor e sen perder o contacto.

In the international acknowledgements, I would like to thank the University of Michigan (MSU) and the FRIB laboratory for providing me with the experimental data for analysis, with a special mention to Saúl Beceiro, Daniel Bazin and Wolfgang Mittig, who made me feel at home during my stays in the experiments. Je voudrais remercier le laboratoire GANIL (Grand Accélérateur National d'Ions Lourds) dans lequel j'ai pu développer un grand nombre d'expériences dans lesquelles j'ai appris à faire mes premiers pas en physique expérimentale et dans lequel j'ai vécu l'expérience de la pandémie du COVID d'une manière unique, je crois. De ce laboratoire, je voudrais me souvenir avec toute mon affection de deux personnes qui m'ont traité comme un frère, Thomas Roger et Diego Ramos, merci beaucoup. Por último, mas não menos importante, a Jesús Lubián Ríos e Jonas Leonardo Ferreira, membros do Instituto Nacional de Ciência e Tecnologia - Física Nuclear e Aplicações (INCT-FNA), localizado no Instituto de Física da Universidade Federal Fluminense, que colaboraram sempre que lhes foi pedida ajuda no cálculo das secções efectivas diferenciais e sem os quais faltaria uma parte desta tese.

A tódoslos amigos que pasaron pola miña vida, que foron de gran axuda para que non acabase de perder o xuízo nos momentos máis complicados e para perdelo cando había que divertirse. Un abrazo especial a Alejandra Sayans que sé que estás pasando por un pequeño infierno personal como el mío y sé que acabarás consiguiendo grandes metas en esto o en lo que te propongas, sigues siendo la garrapata que más quiero.

A la Universidad de Salamanca (USAL), que después de mucho esfuerzo me enseñó el rigor y la paciencia necesarios para ser un buen físico, mencionando a dos docentes en particular: Alfredo Valcarce; gracias a sus clases nació mi interés por este área en concreto; y a Begoña Quintana, que me dió la primera oportunidad de investigar en un TFG que a la postre definió mi gusto por la física nuclear.

Quiero agradecer muy especialmente a Lucía Martín Blanco. Sabes que esta tesis nunca se hubiera producido sin tu ayuda durante años. Me diste todo tu apoyo en los momentos más difíciles de mi vida y no dejaste que tirara la toalla en la carrera. En cuanto me puse enfermo, siempre me animaste a seguir y, contra viento y marea, conseguimos acabarla. Creo sinceramente que tú te mereces una tesis más que nadie, pero por culpa de personajes innombrables e inmorales no se llegó a materializar. No obstante, eres la mejor física que conozco y no necesitas un papelucho para demostrarlo. Sabes que te quiero mucho y por eso te dedico esta canción en mi tesis. Por cierto, como aprendí de ti, esta tesis la he realizado siguiendo los preceptos del espiritu del 69. Espero que estés orgullosa de ella.

Picture yourself in a boat on a river
With tangerine trees and marmalade skies
Somebody calls you, you answer quite slowly
A girl with kaleidoscope eyes

Cellophane flowers of yellow and green
Towering over your head
Look for the girl with the Sun in her eyes
And she's gone

Lucy in the sky with diamonds

Follow her down to a bridge by a fountain
Where rocking horse people eat marshmallow pies
Everyone smiles as you drift past the flowers
That grow so incredibly high

Newspaper taxis appear on the shore
Waiting to take you away
Climb in the back with your head in the clouds
And you're gone

Lucy in the sky with diamonds

Picture yourself on a train in a station
With plasticine porters with looking glass ties
Suddenly, someone is there at the turnstile
The girl with kaleidoscope eyes

Lucy in the sky with diamonds

Lucy in the Sky With Diamonds, canción de The Beatles

Esta tesis también quiero dedicarla al único ser vivo que me tatuaría y tatué en el cuerpo: mi gatito (Figura censurada por imperativo da Universidade de Santiago de Compostela, a explicación da censura e que a figura dun gato con garabata non é pertinente para unha tese científica que será publicada nun repositorio internacional, todo o mundo que me quere sabe que non estou de acordo coa decisión). Simba, gracias por ser mi compañero también todos

estos años. Estudiaste toda la carrera conmigo, aguantaste mis alegrías y mis decepciones como solo un gato sabe hacer, ronroneando. Te quiero mucho también, mi pequeño león. Gracias por darme tu amor incondicional.

Quero finalizar agradecendo á miña compañeira de vida, Cristina Veiga Novoa, que me regalou a primeira cita que aparece nos agradecementos como resumo da miña forma de entender o mundo. Gracias por aparecer na miña vida no momento adecuado. Igual nunca pensabas que o teu nome aparecería nunha tese de física nuclear, pero mira, cando menos o esperas, a física nuclear estóupache na cara. Aprendín contigo que o mundo che dá o que proxectas e que existen persoas cunha sensibilidade especial que fan del un lugar menos tormentoso. Ó teu lado vou deixando pouco a pouco de estar en guerra co mundo e tento ver o bonito de cada momento. Estou seguro de que temos un longo futuro xuntos, sempre que queiramos seguir sendo amiguitos e, se non, sabes que te seguirei querendo moitísimo da única maneira que sei quererte, ben. Admirote moito como persoa e como profesional da tradución e a interpretación (para eso si fai falla talento e non estas cousiñas que garabateo eu). Como non, unha parte importante destes agradecementos son para ti, que estes últimos dous anos tamén me aturaches, e inda que digas o contrario, fácil, fácil non son. Regáloche esta canción dun dos teus grupos favoritos, que tamén di moito se se presta atención.

Free fall through our midnight
This epilogue of our own fable
Heedless in our slumber
Floating nescient, we

Free fall through this boundlessness
This madness of our own making
Falling isn't flying
Floating isn't infinite

Come, our end, suddenly
All hail our lethargy
Concede suddenly

To the quickened dissolution
Pray we mitigate the ruin
Calling all to arms and order

Drifting through this boundlessness
This madness of our own making

Sound our dire reveille
Rouse all from our apathy
Lest we
Cease to be

Stir us from our
Wanton slumber
Mitigate our ruin
Call us all to arms and order

Sound the dread alarm
Through the primal body
Sound the reveille
To be or not to be
Rise
Stay the grand finale
Stay the reading of our swan song and epilogue

One drive to stay alive
Elementary
Muster every fiber
Mobilize
Stay alive

Stir us from our
Wanton slumber
Mitigate our ruin
Call us all to arms and order

Descending canción de Tool

Para as persoas con discapacidade coma min, acadar a máxima titulación académica, a de doutor(a), en España non tería de ser, como inda o é, unha fazaña hercúlea, froito non apenas do talento e o esforzo, senón tamén, e moito, da loita contra un sistema sanitario e educativo que pon numerosas pedras no camiño. Os que chegan ó cumio fano sobre todo grazas á súa familia, amigos e compañeiros de traballo e estudos, e malia un sistema non equitativo e non garante da igualdade de oportunidades. Desexo que o meu sufrimento para chegar ata aquí sexa cada vez menor para as futuras xeracións de persoas con algún tipo de limitación, e apelo as institucións públicas competentes para que sigan traballando na integración efectiva e eficaz das persoas con discapacidade á vida académica e profesional. Gustaríame falar do meu caso particular, pero fareino en futuras publicacións ou congresos onde este tema interese de verdade.

Moitas gracias a todos os que dediquen un tempiño a ler esta tese.

Contents

List of Figures

List of Tables

Chapter 1

Abstract

The E20020 experiment uses an ^{16}O beam over an active target of ^{4}He from NSCL's ReAccelerator facility ReA6 linear accelerator (linac) at 10 MeV/u. The experiment was carried out in the Facility for Rare Isotope Beams (FRIB) at Michigan State University with the Active Target Time Projection Chamber (AT-TPC) [1] placed at the centre of the SOLARIS solenoid magnet.

The experimenters used an ^{16}O beam from the linear accelerator facility at 10 MeV/u. The AT-TPC was placed in the centre of the SOLARIS magnet, which was then ramped up to a field of 3 teslas (T). This magnetic field has field lines parallel to the beam propagation, causing the charged particles to bend and facilitating their containment in the detector for further analysis. The AT-TPC was filled with 700 Torr of pure helium gas, which was used as the reaction target and the detector media.

This experiment (E20020) aims to search for resonance in ^{16}O just above the four alpha separation energy of 14.4 MeV. The experiment will observe the decay of this resonance into four alpha particles. The fifth alpha is the alpha "recoil" from the target.

Another reaction of interest is the $^{12}C^{*}$ dissociation in three alpha particles, appearing from the excited oxygen at 7.17 MeV decay; this resonance is the equivalent of the Hoyle state, an excited state of ^{12}C very close to the alpha-particle separation energy. This resonance would correspond to the Hoyle state, an excited state of ^{12}C very close to the alpha-particle separation energy, the threshold above which the nucleus can emit an alpha particle (^{4}He). This state was first proposed in 1954 by Fred Hoyle to explain the production of carbon in stars.

The analysis results of several excited states of this reaction, paying particular attention to responses that give me back events with multiplicity 4 and 5, trying to differentiate events from the condensate state or Hoyle states [2].

This thesis details the differential cross-section for the ground state and the excited states $E_x = 6.049$, 6.129, 6.917, 7.117, and 9.845 MeV and a multi-decomposition analysis of the states between 6 and 7.2 MeV.

The detector's energy resolution for this experiment does not allow the complete separation of these nearby states, as they are separated by less than 1 MeV, with some states being affected

by neighbouring states. A multi-decomposition analysis is carried out to determine at which levels these effects occur, making various adjustments with multiple combinatorics of states. The conclusion is that considering the statistics for this experiment, the best option is to perform an MDA between 5.5 and 7.5 MeV, covering all four excited states.

In a first approximation, each excited state is adjusted to 300 KeV, and an individual study is conducted at the exact width of the combination of the closest states. Considering the states' closeness and the detector's resolution in excitation energy, a multi-decomposition analysis of the four closest excited states is carried out, obtaining satisfactory results when these states are combined. These studies help with the reliability of calculating the excitation energy of the direct Hoyle effect and its subsequently calculated branching ratio (BR).

The results obtained for the direct Hoyle BR, which is at an oxygen excitation energy of 14.765 $\pm$ 2.443 MeV, sufficient energy for the α decay of ^{16}O and the subsequent decay of ^{12}C directly into three alphas or sequentially through ^{8}Be, is an upper bound $\Gamma_{DirectHoyle} < 0.044^{+0.034}_{-0.026}$, consistent with previous results such as those of D. Dell'Aquila et al.[3]. It is compatible with the results of earlier experiments, always bearing in mind that this is the first experiment to measure direct Hoyle decays without going through the sequential one.

Chapter 2

Introdution

The abundance of heavy elements in the Universe is determined by the production of carbon in stars, which is fundamental to life on Earth. Carbon and oxygen did not originate in the Big Bang but formed later in the cores of stars. The nuclear fusion reactions in stars are responsible for every gram of carbon and oxygen found in all living things. In the initial stages, large, short-lived stars use hydrogen, helium and lithium reserves to synthesize heavier elements such as carbon and oxygen. These essential elements - carbon and oxygen - are then scattered across space as these massive stars near the end of their lives and explode spectacularly. This dispersal clears the way for new stars and planets to form from the rich cosmic material, creating the conditions necessary for life to emerge. Studying the precise timing and intricate processes behind these events reveals a new perspective on the evolution of life throughout the Universe.

The proposed research will validate a detection system based on active target technology to improve the measurement of the triple-alpha process, which is crucial to stellar evolution.

When nuclides are grouped in nuclear physics, the astrophysical relevance of light nuclei and their structural similarities to classical systems are immediately apparent.

The alpha particle (^4He) is the most abundant nucleus in the Universe. It is highly stable in mass and has a first excited state above 20 MeV. These characteristics make it essential both in astrophysics and nuclear structure. Most of the energy produced by stellar hydrogen fusion, whether stable or explosive, is accounted for by converting hydrogen into helium.

In more complex atomic nuclei, the alpha particles arrange themselves in a continuum, resulting in excited rotation bands, entangled ringlike fundamental states and linear arrangements. For nuclei with equal numbers of protons and neutrons, called "conjugated alpha nuclei" [4], these properties are more pronounced and more accessible to observe.

Alpha clustering is still evident and can be enhanced when a single nucleon or pair of nucleons is added to the system. Excited states with significant alpha partial widths are a sign of clustering behaviour, and these states can have a profound effect on the reaction rates of astrophysical systems if the excitation energy is tuned to the so-called Gamow energy, the preferred thermal energy for statistically breaking the Coulomb barrier.

Stable ^{12}C (six protons and six neutrons) is produced exclusively by what is known as the triple-alpha event, in which two alpha particles (two protons and two neutrons) combine to

make ^{8}Be (four protons and four neutrons) and capture a third α particle, producing ^{12}C in a transient resonance state which decays electromagnetically to the ^{12}C ground state [2]. This process occurs only a tiny percentage of the time (0.04%), and although fundamental to the origin of life, it is highly inefficient.

This exotic resonance is named after Sir Fred Hoyle, who predicted its existence in the 1950s at a given energy of 7.654 MeV and with a determined spin and parity of 0+ [5]. Shortly after having been predicted theoretically, this state became experimentally observable [6]. Fusing three alpha particles is virtually the only possible way to synthesize stable carbon in the Universe and perhaps one of the most important processes occurring in Nature.

Recently, results published in Nature [7] suggest that this process has a much stronger influence on the production of heavy elements (Gd-Sn) in proton-rich supernovae than had been expected.

Although Hoyle-state properties are crucial to carbon nucleosynthesis in stars, our understanding of them is still minimal. More precise measurements are needed to reduce uncertainties in stellar evolution models. Accurately determining the reaction rate of the triple-alpha process is currently a significant challenge in nuclear astrophysics.

A 10 MeV/u ^{16}O beam from NSCL's ReA6 linear accelerator (linac) was used for the experiment. The Active Target Time Projection Chamber (AT-TPC) [1] was positioned in the SOLARIS magnet's centre and adjusted to a 3 Tesla field. This experiment (E20020) will look for ^{16}O just above 14.4 MeV by studying its decay into four (^{4}He) particles.

Another reaction of interest studied with this experiment is the Hoyle state, which would appear very close to this 4-alpha oxygen splitting resonance, making its study a little more complicated. Physical tools such as the Dalitz plot will be used to differentiate these and other reactions.

Conducted at Michigan State University's Facility for Rare Isotope Beams (FRIB), the experiment used the AT-TPC positioned at the centre of the SOLARIS magnet and subjected to a 3 Tesla (T) magnetic field. The E20020 experiment uses a ^{16}O beam directed at an active ^{4}He target from the NSCL's Re-Accelerator facility, specifically the 10 MeV/n ReA6 linear accelerator (linac).

The experiment aims to obtain data on the kinematics of the reactions produced, both elastic and inelastic, by obtaining adjusted values of the effective cross-sections within the theoretical values for different excitation energies. This study also aimed to get new values for measuring the branching ratio of the Hoyle state, which was calculated for the first time directly with the AT-TPC.

Chapter 3

Objetives

The main objective of this thesis is the study of the E20020 experiment carried out at the Facility for Rare Isotopes (FRIB) belonging to Michigan State University (MSU).

The goal of the E20020 experiment is to investigate α-clustering states in ^{16}O through inelastic α-scattering above the α-separation energy, with direct measurements of α-decay.

The primary focus is on the region just above the 4-α separation energy, particularly the excited 0_6^+ state at 15.097 MeV, whose spin still needs to be confirmed, and a potential new excited state found around 15 MeV, which aligns with theories of possible 4-α cluster states similar to the direct and sequential Hoyle state observed in ^{12}C.

Direct measurements of the 4-α decay products, along with their angular and energy distributions, would provide an initial determination of the decay nature of these states through particle analysis in a Dalitz plot.

The experiment is carried out with a pure ^{16}O beam, purified by the different linear accelerators and fragments and re-accelerated by ReA6 until it reaches sufficient energy.

This is the first experiment carried out with SOLARIS within the FRIB facilities. The Active Target-Time Projection Chamber (AT-TPC) is located within SOLARIS and surrounded by a magnetron that reaches a magnetic field of 3T parallel to the axis.

The detector is filled with pure helium at a density of 0.151 $\frac{mg}{cm^3}$ to reach a pressure of 700 Torr.

The applied magnetic field causes the particles to curve and thus be able to achieve greater ranges of direct detection of the reaction products.

A beam of pure ^{16}O is made to collide against the pure helium in the chamber and the reaction products are studied in their different channels.

In particular, this thesis studies the elastic collision of ^{16}O against ^4He and the first excited states, trying to give a good result for the excitation energies and their differential cross sections.

On the other hand, as ^{16}O is an element whose first four excited states are separated by only 1 MeV, a study of the mixture of states will also be carried out through a multi-decomposition analysis (MDA).

In the second part of the objectives, an attempt will be made to give a good approximation of the Branching Ratio of the decomposition of ^{16}O into ^{12}C and its subsequent fission into a particular state called the direct Hoyle state. This part is especially complicated because the decay of Carbon into 3 alpha particles occurs in a proportion of 0.04% of the time compared to 99.96% which decays into $^{8}Be + \alpha$, which decays very quickly into 3 alphas.

To carry out this second study, the Dalitz plot will be used, which is a mathematical-physical tool with which the conservation of energy and momentum of three-body reactions can be studied, provided that they meet a series of special conditions such as equal mass.

As an extra, the objectives include a total understanding of the ATTPCROOTv2 program with which the AT-TPC chamber is analyzed from the raw data obtained in the experiment thanks to the padplane and the complex data dump system.

Once the complex structure of the program has been understood, the aim is to improve the method of data unpacking to obtain the direct variables using direct mathematical tools such as convolution through the Fourier transform for greater cleaning of the initial signal.

New tools such as GENFIT will also be adapted to the ATTPCROOTv2 program in order to make better adjustments to the data and obtain new indirect variables.

Chapter 4

Theory

4.1 Some remarks in Nuclear Astrophysics

Nuclear astrophysics is a branch of astrophysics concerned with studying nuclear reactions, nuclear structure and properties of atomic nuclei in the context of astrophysical environments. It aims to understand how nuclear processes and reactions are critical for stars' evolution and behaviour, energy production, and the dynamics of the Universe.

This branch of physics plays a crucial role in explaining the abundance of chemical elements observed in the Universe. Nuclear astrophysics provides insights into stellar life cycles, the explosive events that form galaxies, and the fundamental processes that underlie cosmic phenomena. Nuclear physics, astrophysical modelling, and observational data are combined to gain an in-depth understanding of nuclear processes in the Universe.

Topics range from stellar nucleosynthesis (element formation in stars) to nuclear reactions in extreme environments (e.g., supernovae and neutron stars) and the behaviour of matter at high temperatures and pressures in astrophysical environments.

4.1.1 Stellar nucleosynthesis

Stellar nucleosynthesis is the process of synthesising atomic nuclei from preexisting nuclei or nucleons using various nuclear reactions. All the forces—strong, gravitational, electromagnetic, and weak—are known to be involved in this creation process.

An atomic nucleus comprises a precise number of protons and neutrons called nucleons. The number of protons identifies the element of the nucleus and is known as the atomic number, symbolised by Z. The number of neutrons, called N, determines the isotopic composition of the component. The total number of nucleons is represented by A, and the relationship between them is expressed as Z + N = A. This relationship is conventionally defined as ${}^{A}\mathrm{S}$, where S is the chemical symbol for the element with the atomic number Z.

Nucleosynthesis of heavy elements occurs through thermonuclear reactions in the core of stars up to the Fe-peak, neutron captures in stellar interiors and explosions (building nuclei

above the Fe-peak), and spallation reactions in the interstellar medium, whereby light nuclei (Li, Be, and B) are produced by fragmentation of heavier ones (C, N, and O).

In particular, this work will focus on the study of the formation of two stable elements in Figure 4.1, ^{16}O, studying in more detail some excited states and ^{12}C, from which we will try to extract information about the decay width, both for ^{16}O in 4 alphas and the well-known Hoyle state of ^{12}C in three alphas.

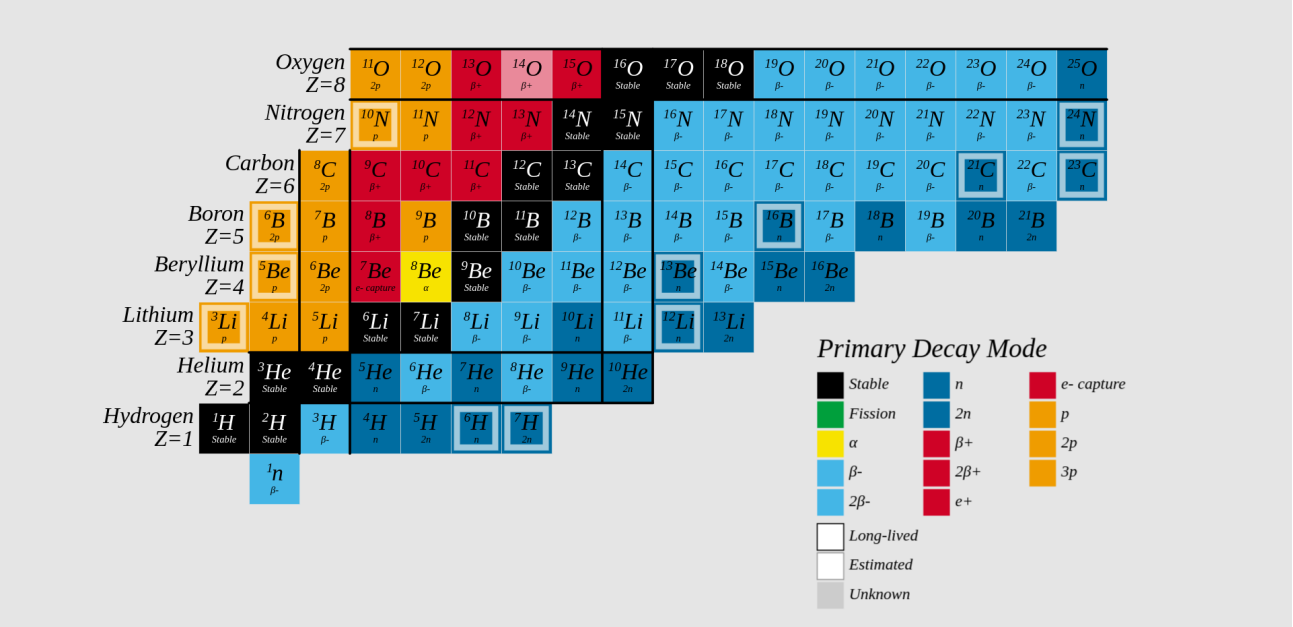

Figure 4.1: Nuclear chart of light elements from Z=1 to 8. Adapted from [8], open source. The figure shows how the two elements under study (^{12}C and ^{16}O) occupy the stable element zone of the drip lane, while ^{8}Be, another aspect of interest in the clustering of states, has a primary decay mode of alpha decay.

4.1.2 Processes involved in nucleosynthesis

The formation of different nuclei can be differentiated into two big groups: the appearance of light hearts in the first stage of life of a star and the earlier Universe where the nucleotides down to A=70 were created, and the second stage where the high nucleotides appear after different extreme processes that often lead to the death of the star itself, like violent neutron-rich environments such as the merger of two neutron stars, supernovae or dark holes formation. Under these conditions, nuclei take up neutrons faster than they can decay.

The first process in forming new elements inside starts, called primordial nucleosynthesis, is the production of H, He and ^{7}Li. Nucleosynthesis first occurred within a few minutes of the Big Bang; a few minutes after the Big Bang, a quark-gluon plasma condensed into protons and neutrons. About 1 second to 3 minutes after the Big Bang, the temperature is enough to allow the neutrons to fuse with protons to make deuterium nuclei. Deuterium nuclei are combined in adequate pressure and temperature conditions to make helium. After that, reactions between isotopes of He, H, protons and neutrons produced lithium and the first massive stars in this phase of the Universe. This process of fusion of elements occurs from the shell to the core and

ends at ^{56}Fe, where the binding energy per nucleon attaches to a maximum and starts to decay for the more massive elements. Iron nucleus ^{56}Fe is close to the peak with a binding energy per nucleon value of approximately 8.8 MeV/n, as seen in figure 4.2. It's one of the most stable nuclei that exist. At this point, the start has a core of Iron, and we can talk about the beginning of the star's death.

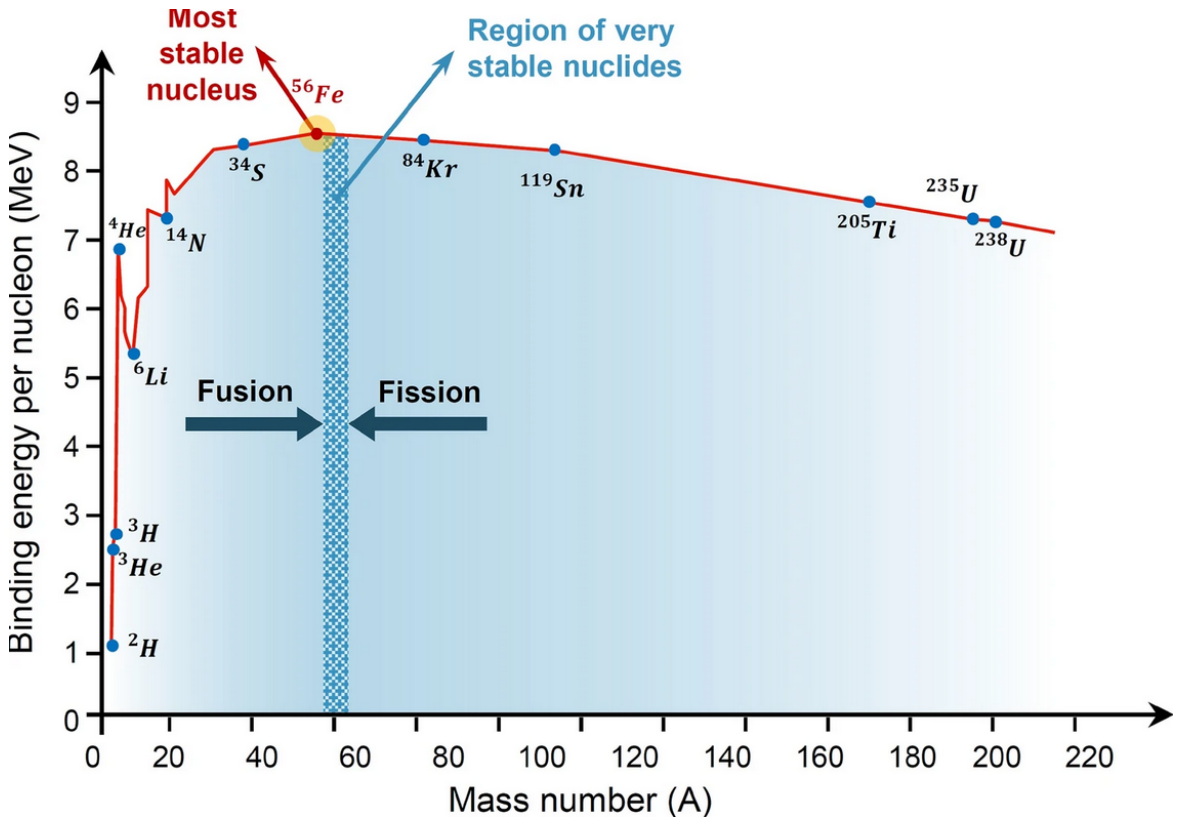

Figure 4.2: Representation of Binding energy per nucleon versus atomic number A. Except for the lighter nuclei, the average binding energy per nucleon is about 8 MeV. The maximum binding energy per nucleon occurs around mass number A = 50 and corresponds to the most stable nuclei. The iron nucleus Fe56 is close to the peak. Its binding energy per nucleon is about 8.8 MeV. It's one of the most stable of all existing nuclei. Figure taken from [9] with License CC BY 4.0. Original content from this work may be used under the terms of the Creative Commons Attribution 4.0 licence. Any further distribution of this work must maintain attribution to the author(s) and the title of the work, journal citation and DOI.

Exciting processes occur in the formation range of the light nucleus. One of them is the CNO cycle, which this thesis treats by studying the importance of the 26Si in the rupture of the cycle.

There are three basic processes in which heavy nuclei can be built by continuously adding protons or neutrons: p-process, s-process and r-process.

Burbidge et al. [10] and Cameron [11] (1957) opened the way to understanding the formation of heavy nuclei ($A \geq 70$). They studied the solar system abundance distribution; they determined that the heavy nuclei were formed in the three processes (r, s and p), which we still use today.

The slow neutron capture process, S-process, is a nucleosynthesis process at relatively low neutron density and intermediate temperature conditions in stars. The s-process and the r-process may be responsible for generating many of the heavy elements in the Universe. Under these conditions, the rate of neutron capture by atomic nuclei is slow relative to the rate of radioactive beta-minus decay. A stable isotope captures a neutron in this process, but a radioactive isotope decays to its stable daughter before the next neutron is captured. This process produces stable isotopes by moving along the valley of beta stability in the chart of isotopes. The S-process has approximately half of the isotopes of the elements heavier than Iron and, therefore, plays a vital role in the galactic chemical evolution. The S-process differs from the more rapid R-process of neutron capture by its slow rate of neutron capture.

4.1.3 CNO-cycle

The carbon-nitrogen-oxygen (CNO) cycle is a sequence of thermonuclear reactions that provides most of the energy the massive stars radiate. It occurs typically in hot stars, so for the Sun, a Star with a medium size represents a small part of the emitted energy.

The German American physicist Hans Bethe, in 1938, first described the process. He postulated ^{12}C as the most stable element in the mass range. He proposed a reaction cycle of four proton capture reactions and two betta plus decays that would facilitate a catalytic fusion of four hydrogen nuclei to a helium nucleus. The reactions involving the CNO-cycle are as follows:

$$\mathbf{^{12}C} +^{1} H \rightarrow^{13} N + \gamma$$

$$^{13}N \rightarrow^{13} C + e^{+}$$

$$^{13}C +^{1} H \rightarrow^{14} N + \gamma$$

$$^{14}N +^{1} H \rightarrow^{15} O + \gamma$$

$$^{15}O \rightarrow^{15} N + e^{+}$$

$$^{15}N +^{1} H \rightarrow \mathbf{^{12}C} +^{4} He + \gamma$$

The production of carbon and heavier elements during helium burning [12], as well as the overall evolution of stars [13], is profoundly affected by the characteristics of the decay of the Hoyle state. This process exclusively follows a sequential pattern at typical stellar temperatures around T $\approx 10^8$ - 10^9 k. This leads to the ground state of ^{8}Be, followed by the s-radiative capture of a third alpha to reach the Hoyle state.

The importance of studying the ^{12}C structure for a correct understanding of nucleosynthesis processes can be seen in heavier nuclei formation processes such as the CNO cycle, as it can play a significant role in the break-up times of the CNO cycle. However, in astrophysical scenarios where helium is burning at lower temperatures - such as in helium-accreting white dwarfs or neutron stars with a low accretion rate - a different mode of decay of the Hoyle state takes precedence. This is the non-resonant or direct α decay [14].

The two α particles bypass the formation of ^{B}Be through the 92 keV resonance. Recent theoretical calculations suggest that at temperatures below 0.07 GK, the reaction rate of the direct process is significantly enhanced compared to the rate calculated under the sequential scenario only [15].

Stellar hydrogen burning is characterised by two typical reaction sequences: the proton-proton chains and the carbon-nitrogen-oxygen (CNO) cycles. Although the p-p chain is most important in stars of the mass of the Sun or less, theoretical models show that the CNO cycle is the dominant energy source in the most massive stars.

Nuclear reactions on possible breakout processes off the Hot-CNO cycle are of great interest in nuclear astrophysics and the nuclei's structure that occur at very high temperatures enough to allow $\boldsymbol{\alpha}$ capture reaction on these isotopes.

4.1.4 Hot-CNO cycle

The CNO and hot-CNO cycles differ mainly in the context and conditions under which they occur in the nuclear reactions that fuel stars. In hot-CNO, the temperature is sufficiently high to make nuclear reactions faster and more efficient, allowing massive stars with more extreme core temperatures to use this cycle more efficiently. Massive stars with more extreme core temperatures can use this cycle more efficiently.

The CNO cycle occurs in stars of medium to high mass at temperatures between 15 and 20 million degrees, while the hot CNO cycle is a more efficient version of the CNO cycle that occurs at temperatures above 30 million degrees, typically in hotter and more massive stars.

Type I X-ray stellar bursts are intense X-rays induced by a thermonuclear reaction produced in the atmosphere of neutron stars belonging to a stellar binary system. For rates close to stable burning, the burst ignition depends critically on the hot CNO breakout reaction ^{15}O ($\boldsymbol{\alpha}$,$\boldsymbol{\gamma}$) ^{19}Ne that regulates the flow between the hot CNO cycle and the rapid proton capture process.

The neutron star accretes material from its partner surface layers rich in H and He. The high densities and gravity achieved in the accretion disk may trigger the burning of the H at enough temperature, leading to the hot CNO cycle that feeds the rp-process. The break out of the CNO cycle is done through the ^{15}O ($\boldsymbol{\alpha}$,$\boldsymbol{\gamma}$) ^{19}Ne reaction and also through the chain [16]:

$$^{12}C(^{1}H,\gamma)^{13}N(^{1}H,\gamma)^{14}O(\alpha,^{1}H)^{17}F(^{1}H,\gamma)^{18}Ne(\alpha,^{1}H)^{21}Na$$

This last reaction supplies the $\boldsymbol{\alpha}$p-process [17] via the reaction chain:

$$^{21}Na(^{1}H,\gamma)^{22}Mg(\alpha,^{1}H)^{25}Al(^{1}H,\gamma)^{26}Si$$

With this chain, the process can escape from the CNO cycle and synthesise neutron-deficient isotopes up to the Ca/Ti region.

The typical energy range for the $\boldsymbol{\alpha}$p-process is T $\sim$ 1-2 GK with Gamow windows in the E $\sim$ 1.3 $\sim$ 2.0 MeV range. This rapid isotope production leads to a fast increase of the released energy ($\sim 10^{38}$ ergs/s) that is visible in the luminosity curve of the X-ray burster (XRB).

In some cases, the luminosity curve shows a double-peak or double-humped structure caused by a sudden decrease of the reaction flow in the so-called "waiting points".

4.1.5 Role of Oxygen resonance at 14.4 MeV in CNO cycles

The 14.44 MeV resonance in ^{16}O is a very relevant phenomenon in the CNO cycles of stars, particularly in the nuclear fusion process in which oxygen (in the form of ^{16}O) plays a key role. It corresponds to a specific energy level in ^{16}O. When protons (hydrogen) collide with ^{16}O at energies of about 14.44 MeV, there is a high probability of an efficient nuclear reaction.

The main reaction that is affected by this resonance is:

$$^{16}O + p \rightarrow^{17} F + \gamma$$

In this reaction, a proton (p) fuses with a nucleus of ^{16}O, producing a nucleus of ^{17}F and releasing a photon (a γ ray). In the CNO cycle, this type of resonance directly affects the efficiency of nuclear fusion in the most massive stars. At several million degrees, the protons in the stars' cores have enough energy to reach the 14.44 MeVs resonance.

This resonance increases the rate of hydrogen fusion by allowing reactions with ^{16}O to occur with greater probability. The 14.44 MeV resonance makes the CNO cycle more efficient, as the energy released by the fusion reaction is increased, speeding up the hydrogen-to-helium conversion process and improving the energy production in the star's core.

This phenomenon also has an essential effect on the luminosity of the stars that carry out the CNO cycle. The presence of this resonance facilitates an increase in energy production, which contributes to massive stars where the CNO cycle is much more luminous than smaller stars where the proton-proton cycle predominates.

The efficiency of the CNO cycle due to this resonance can influence the evolution of massive stars. Stars that use this cycle as their primary energy source tend to have a hotter core, which affects the rate at which they consume their hydrogen fuel and determines their future evolution and eventual transformation into supernovae or other stellar events.

4.2 Nuclear structure

Nucleons have an approximate mass of the order of GeV and are bound together with a binding energy of about 8 MeV/nucleon. The nucleus can exist in an excited state, which leads to an increase in its total energy. This energy is quantised in a way reminiscent of the electron

shells in atoms, resulting in nuclear energy levels characterised by quantised spin and parity values. In atoms, electrons are influenced by the Coulomb force that binds them to the nucleus. Meanwhile, individual nucleons are attracted to one another by the strong nuclear force, a phenomenon for which scientists struggle to find a precise and universal description.

There are several theoretical approaches to understanding the behaviour of the nuclear system. The first attempt was the liquid-drop model, which postulates that the nucleus behaves like an incompressible fluid composed of nucleons. First proposed by Gamow and later formulated by Weizsäcker, this model originated in the 1930s. In particular, Weizsäcker's formulation achieved accurate predictions of binding energies for nuclei within the stability region. It also successfully explained other nuclear properties, such as size scaling proportional to $A^{1/3}$. This model was later used to describe the phenomenon of nuclear fission by N. Bohr and J. Archibald [18].

The semi-empirical mass formula, also known as the Bethe-Weizsäcker formula, is a mathematical equation used in nuclear physics to estimate the binding energy of atomic nuclei and predict an atom's nuclear mass. The formula combines theoretical principles with empirical data. The basic form of the semi-empirical formula for nuclear mass is shown in the following procedure.

$$B = a_v A - a_s A^{2/3} - a_c \frac{Z(Z-1)}{A^{1/3}} - a_A \frac{(A-2Z)^2}{A} + \delta(A,Z) \tag{4.1}$$

- B represents the binding energy of the nucleus.
- a_v, a_c, a_s, and a_A are empirical constants of volume, coulomb, surface and symmetry, respectively, determined by fitting the formula to experimental data.
- A is the number of nucleons (protons plus neutrons).
- δ represents corrections for odd-even nucleon effects and other minor corrections.

Semi-empirical mass formulae help predict nuclear binding energies and stability. They tell us the energy associated with the strong nuclear force binds the protons and neutrons in an atomic nucleus. Calculating the binding energy makes it possible to estimate the nuclear mass, which is crucial in understanding nuclear structure, nuclear reactions, and nuclei's stability.

The coefficients have been adjusted to reproduce the experimental binding energies as accurately as possible. However, some peaks are not accurately reproduced. These deviations are due to effects arising from the internal structure of the nuclei, which are not considered in this model. These deviations are related to so-called "magic numbers". Magic numbers correspond to specific configurations of protons and neutrons that exhibit exceptional stability. The experimental observation of these magic numbers motivated scientists to develop a new model strongly influenced by atomic physics. This led to the nuclear shell model proposed by M. Goeppert-Mayer [19].

4.2.1 Independent particle model (IPM)

The Independent Particle Model (IPM) is a theoretical framework used in nuclear physics to describe the behaviour of the nucleons (protons and neutrons) within the nucleus of an atom. It assumes nucleons move independently within nuclei, similar to electrons in atomic orbitals in shell models. It treats nucleons as if they were moving independently within the nucleus. There are no significant interactions between them except for the strong nuclear force that keeps them together. Nucleons are assigned to single-particle states, each characterised by specific quantum numbers such as energy, angular momentum and spin. These states are analogous to atomic orbitals in the atomic shell model. The Pauli exclusion principle prevents more than one nucleon from being in the same single-particle state. It takes into account their spin and isospin properties.

By solving Schrödinger's equation, $\mathrm{H}\Phi = \mathrm{E}\Phi$, the properties of a nucleus can be determined. Equation 4.2 represents the realistic Hamiltonian by excluding second-order terms such as three-body interactions. In this equation, T_i represents the nucleon kinetic energy, while V_{ij} represents the nucleon-nucleon interaction potential. Solutions to this equation correspond to states characterised by singular, well-defined configurations. These states are called single-particle states, and their associated eigenvalues are called single-particle energies (SPE).

$$H = \sum_{i=1}^{A} T_i + \sum_{i=1}^{A} \sum_{j \neq i}^{A} V_{ij} \tag{4.2}$$

In IPM, the nucleus is characterised by non-interacting nucleons affected by a spherically symmetric central potential calling effective potential U^{eff}. The fact that the nucleons move freely in a central potential contradicts the presence of a strong nuclear interaction in a dense medium. However, this potential is relatively weak compared to the kinetic energy of the particles involved. The above equation can be rewritten as the sum of a Hamiltonian of the independent particle model part and a Hamiltonian of residual interactions (equation 4.3).

$$H = \sum_{i=1}^{A} T_i + \sum_{i=1}^{A} \sum_{j \neq i}^{A} V_{ij} = \sum_{i=1}^{A} \left(T_i + U_i^{eff}(r) \right) + \sum_{i=1}^{A} \left(\sum_{j \neq i}^{A} V_{ij} - U_i^{eff}(r) \right) = H_0 + H_{res} \tag{4.3}$$

The effective potential U^{eff} can be broken down into different terms to solve the Hamiltonian:

- The easiest way to describe initial effective potential is the central potential was the harmonic oscillator (HO), as shown in Eq. 4.4. HO has been chosen because it is easy to handle and can exactly reproduce observed patterns of low magic numbers.

$$V_N = \frac{1}{2} m(\omega r)^2 \tag{4.4}$$

- The second term to consider is related to the centrifugal barrier (Eq. 4.5 that emerges with the solution of the Schrödinger equation.

$$V_{cf} = \frac{l(l+1)\hbar}{2\mu r^2} \tag{4.5}$$

  Where l is the relative angular momentum between nucleon and nucleus, μ is the smallest mass of the system, and r is the radius.

- To reproduce the higher magic numbers, a radial shape of the spin-orbit potential is introduced (Formula 4.6).

$$V_{SO} = -\frac{1}{\hbar^2} V_{so} \langle \vec{\ell}\vec{s} \rangle \left(\frac{1}{r} \frac{\partial V_N(r)}{\partial r} \right) \tag{4.6}$$

  where:

$$-\frac{1}{\hbar^2} V_{so} \langle \vec{\ell}\vec{s} \rangle = -V_{so} \left(j(j+1) - \ell(\ell+1) - s(s+1) \right) = \begin{cases} -V_{so} \frac{\ell}{2} & \text{for } j = l + 1/2 \\ +V_{so} \frac{\ell+1}{2} & \text{for } j = l - 1/2 \end{cases} \tag{4.7}$$

  In the equation, V_{so} is the spin-orbit strength, $\vec{\ell}$ and $\vec{s}$ the angular momentum and spin operators for a single nucleon, and $\langle \vec{\ell}\vec{s} \rangle$ their expectation value. The spin-orbit potential depends on the orientations of the angular momentum and spin operators ($\vec{\ell}\vec{s}$). This factor divides the planes with ℓ >zero into two sets, as shown in Equation 4.7, where j denotes the total angular momentum.

The Harmonic Oscillator potential is only an approximation, as it does not reproduce the short-range properties of the nuclear force. A more realistic approximation for the last component is the Woods-Saxon (WS) potential [20]. This spherically symmetric potential reflects the distribution of the density of the matter in the nucleus. As the nucleus radius increases, this potential gradually decreases to zero. R is the nuclear radius $r_0 A^{1/3}$, the surface diffusivity and V_0 is the depth of the potential well, typically about 50 MeV. The expression of the Woods-Saxon potential is as follows:

$$V_N^{WS} = -\frac{V_0}{1 + exp(\frac{(r-R)}{a})} \tag{4.8}$$

This potential is discussed more in detail in the Appendix B.

After the introduction of all these elements to the potential, it is possible to describe the complete central potential with the sum of the different contributions described above and the addition of the Coulomb term is shown in equation 4.9, described by M. Goeppert-Mayer and Haxel, Jensen, J. Hans and Suess between 1948 and 1949 [21], to correctly describe the appearance of stable structures (magic numbers) in some nuclei.

$$U^{eff}(r) = V_N + V_{cf} + V_{SO} + V_C \tag{4.9}$$

4.2.2 Nuclear Shell model

The nuclear shell model is a theoretical framework in nuclear physics describing the structure of atomic nuclei in terms of energy levels and proton/neutron arrangement within the nucleus. It is analogous to the electron shell model used in nuclear physics to describe the structure of electrons in atoms. It has been instrumental in advancing our knowledge of nuclear physics, providing a fundamental framework for understanding the behaviour of atomic nuclei. The shell model distributes nucleons (protons and neutrons) into different energy levels or shells within the nucleus. These energy levels are similar to the energy levels of electrons within atoms but are specific to the atomic core.

In the shell model, specific numbers of protons or neutrons are called "magic numbers". Nuclei with a magic number of nucleons tend to have a greater degree of stability and to have lower energy states. Some known magic numbers for protons and neutrons are 2, 8, 20, 28, 50, 82... Nuclei with these numbers of nucleons often exhibit increased stability. Like electrons in atomic shells, nucleons fill these energy levels or shells. Each shell may contain a certain number of nucleons.

The energy levels of the nucleons in the nucleus determine the order of nuclear shells. Like electron shells, nuclear shells are labelled with quantum numbers such as 'n', 'l', and 'j'. In the nuclear shell model, nucleons have orbital angular momentum associated with their motion in the nucleus; this contributes to the overall characteristics of the nucleus, including the nuclear spin and magnetic moment.

In the case of a spherically symmetric potential, the wave function (momentarily disregarding its spin) for any nucleon located in polar coordinates (r, θ, ϕ) concerning the centre of the nucleus has the form that is seen in the Formula 4.10, which can be decomposed into a radial part (R_{nl}) and an angular part corresponding to the spherical harmonics Y_l^m

$$\Psi_{nlm} = R_{nl}(r)Y_l^m(\theta, \phi) \tag{4.10}$$

The energy eigenvalues depend on the principal quantum number, n, and the orbital angular momentum, l. However, they exhibit degeneration concerning the magnetic quantum number m. These energy levels are organised into discrete groups known as "shells", each separated by a substantial energy gap immediately above it.

In their lowest energy state, nucleons occupy energy levels in ascending order, with two protons (or neutrons) occupying each accessible proton (or neutron) energy level. If we dealt with a simple harmonic potential (i.e. V(r)αr^2), uniformly spaced energy levels would be produced. This would confuse the characteristic shell structure and the presence of magic numbers. Consequently, the Saxon-Woods model (Eq. 4.8)again proves to be a reasonable approximation.

For such a potential, the lowest energy level corresponds to 1s (i.e. with quantum numbers n = 1 and l = 0). This level can accommodate up to 2 protons or neutrons. This is followed by the 1p level, which can accommodate 6 protons or neutrons. This explains the first two magic numbers: 2 and 8. Then, it comes to the 1d level, which is very close in energy to the 2s level, forming the same shell. This combination allows 2 protons (neutrons) in 2s and 10 protons (neutrons) in 1d, resulting in the following magic number: 20.

The following two energy levels, 1f and 2p, are also close together, allowing for an additional 6 protons (neutrons) in the 1f level and 14 protons (neutrons) in the 2p level. This would imply that the following magic numbers are 28 and 40. However, experimentally, it is found to be 50. To explain this discrepancy, an essential feature of the nuclear shell model is spin-orbit coupling, which arises from the interaction between the intrinsic spin of nucleons and their motion within the nuclear potential. This interaction is responsible for splitting energy levels within a shell and gives rise to the observed nuclear energy spectra. The nuclear shell model has successfully explained and predicted the properties of many stable and unstable nuclei, including their energy levels, nuclear spins and magnetic moments. It has played a crucial role in understanding the structure and behaviour of nuclear fuels.

The solution to this inconsistency comes from a term in the nuclear potential itself, which is proportional to the orbit angular momentum of the electron L and S from the spin S.

$$V(r) \rightarrow V(r) + W(r)\mathbf{L} \cdot \mathbf{S} \tag{4.11}$$

The combination of the orbital angular momentum and the spin angular momentum of the nucleons results in a total angular momentum, denoted as "j", which is characterised by the possible values j = l + 1/2 or j = l - 1/2. This angular momentum is directly proportional to the energy shift due to the spin-orbit coupling term.

$$j(j+1) - l(l+1) - s(s+1), with \rightarrow s = 1/2 \tag{4.12}$$

Figure 4.3 shows how these different components affect the ordering of the single-particle energies (SPE). The brackets indicate the results of the Harmonic Oscillator (HO) method, which successfully reproduces the lower magic numbers but fails to reproduce the higher ones. With the blue lines, the change in SPE when a Woods-Saxon (WS) potential is used as the central element, together with the addition of the centrifugal term. In the green lines, the figure shows the total effective nuclear force, which includes the spin-orbit term and, remarkably, reproduces all the magic numbers simultaneously.

While the shell model works well for many nuclei, it doesn't account for all nuclear properties, especially for nuclei with significant deviations from spherical symmetry. More complex models, such as the collective and deformed shell models, are needed to provide a more accurate description.

4.2.3 Clustering in the nuclei

Following George Gamow's proposal of the theory of alpha decay [22], it was natural to explore a model in which the nuclei of atoms were made up of alpha particles. Gamow presented a detailed theory of the structure of atomic nuclei in his 1931 book 'Constitution of Nuclei'. [23], which preceded the discovery of the neutron in 1932. He postulated that nuclei with several protons and neutrons that were multiples of four (4n), such as ^{8}Be, ^{12}C and ^{16}O, were composed mainly of *alpha* particles. Meanwhile, other nuclei were thought to contain protons and electrons in addition to α particles.

As the neutron had not yet been identified, this model was developed using available knowledge. The subsequent discovery of the neutron and other advances in nuclear physics led to a

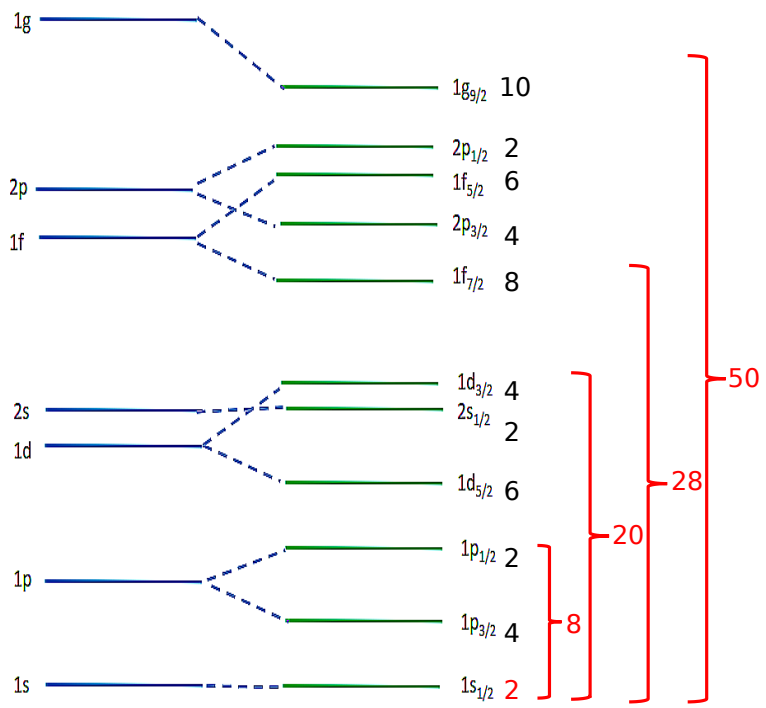

Figure 4.3: Representation of the single-particle energies of the spherical harmonic oscillator potential (entire black numbers), the Woods-Saxon potential + the centrifugal term (blue), and a full shell model potential with the inclusion of the central, centrifugal, and spin-orbit terms (green). The red brackets indicate the nuclear magic numbers.

better understanding of the structure of the nucleus, including the development of the nuclear shell model, which explained the arrangement of nucleons in the nucleus in quantum mechanical terms. Overall, Gamow's pioneering work has laid the foundation for future research in nuclear physics and improved our understanding of the internal structure and properties of atomic nuclei.

The paper by Hafstadt and Teller cited in [24], had a significant impact because it integrated both alpha particle and single particle aspects. Several other alpha models are considered in the section devoted to alpha particles, and in his work cited in [25], Wheeler introduced the resonant group method (RGM), a microscopic approach that includes aspects of groups. The RGM uses antisymmetric wave functions and strictly observes the Pauli exclusion principle, which allows for the coexistence of different cluster structures within the same atomic nucleus. Another important work by Margenau cited as [26] helped lay the foundation for microscopic approaches such as antisymmetric molecular dynamics, especially related to the Hartree-Fock method.

Ikeda's diagram, introduced in 1968 and documented in [27], has proved an effective tool for identifying situations where clustering may occur. This diagram provides a visual representation of the different cluster structures that could be present in the excited states of light nuclei and proposes that specific cluster configurations will emerge for excitation energies close to the corresponding decay threshold. In addition, the review article by von Oertzen, Freer and

Kanada-En'yo, published in [28], provides a comprehensive discussion of the Ikeda diagram, along with a historical overview and recent developments in the field.

Clustering is a fundamental aspect of the dynamics of many nuclear particles. It coexists with the establishment of a mean field. Assuming spherical symmetry, this leads to the appearance of a nuclear shell structure. It's worth noting that clustering leads to states in light nuclei that cannot be explained when creating the shell model alone. Nevertheless, the nuclear shell model plays an essential role in the development of nuclear clusters and in the description of unique deformed shapes of nuclei, which are stabilised by quantum effects arising from the many-body system, in particular the deformed shell gaps, as opposed to the spherical shell gaps.

Cluster theory suggests that the nucleus consists of clusters of alpha particles instead of individual protons and neutrons. The alpha particle is firmly bound to retain some properties even inside a larger nucleus. This approach has existed since the early days of nuclear physics and has recently become prominent with the Hoyle state of ^{12}C.

Once Gamow's theory of alpha decay had been developed, the next natural step was to develop an approach in which atomic nuclei are composed of alpha particles. These alpha clustering phenomena in atomic nuclei have long been an exciting area of research in nuclear physics.

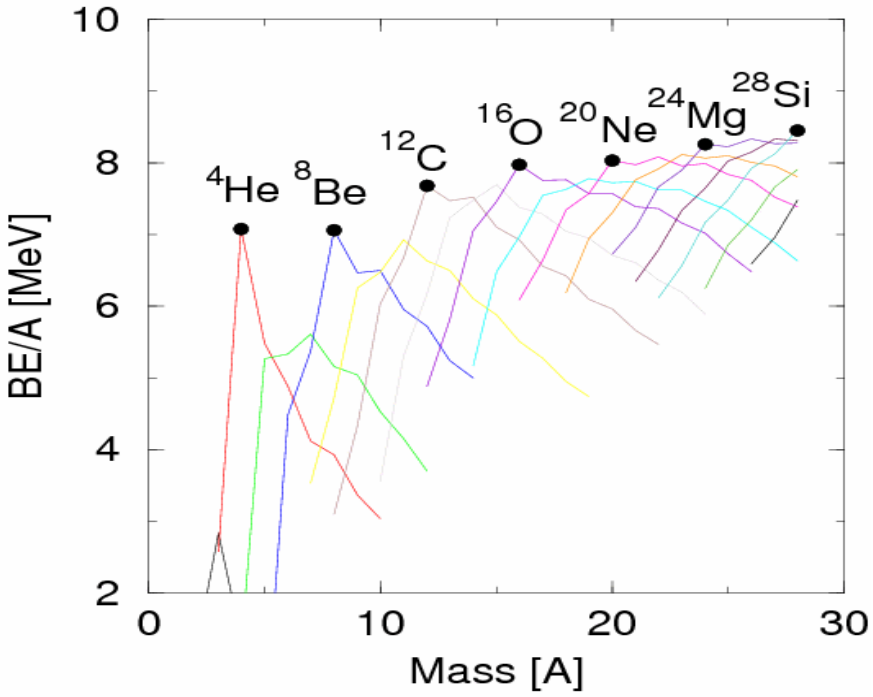

Figure 4.4: The binding energy per nucleon of the light nuclear systems (up to A = 28) is shown by the lines connecting the isotopes of each element. Black circles mark the nuclei of the α particles. Figure taken from [29] with permission ID 600204589 from IOPscience.

Researchers recognised the potential for α particles to arrange themselves in a geometric pattern early in studying the subject. When the binding energy per nucleon in light nuclei

is examined (Fig. 4.4), it is clear that nuclei with an even and equal number of protons and neutrons, known as α-conjugate nuclei (such as 8 Be, 12 C, 16 O, 20 Ne, etc.), exhibit remarkable stability. This stability is related to the correlations discussed above. Hafstad and Teller [24] studied these systems and plotted the evolution of the binding energy against the number of "bonds" or connections among the α particles (Fig. 4.5). The relatively linear relationship they observed suggested a seemingly constant α-α interaction and the resilience of the α-particle in the ground states of these nuclei. It's important to note that this perspective is not widely accepted, as the clustered structure is now thought to be less pronounced in most ground states. Nevertheless, these early ideas laid the groundwork for later developments. Indeed, Brink used the geometric model for the excited states of these nuclei. Earlier, Morinaga had even suggested, in what was a rather radical prediction for the time, that it might be possible for α-particles to arrange themselves linearly [30].

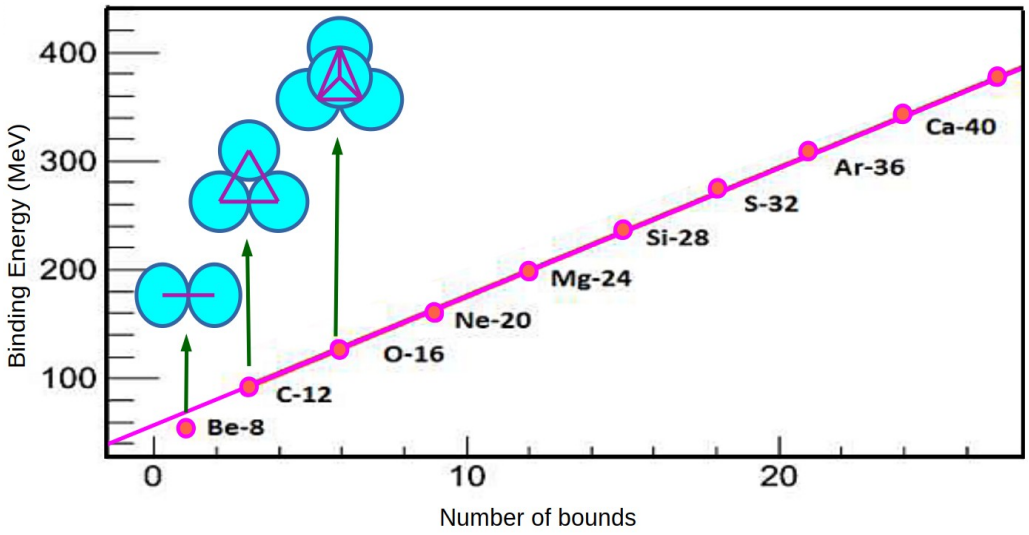

Figure 4.5: Evolution of the binding energy against the number of "bonds" or connections among the α particles. The figure shows three examples of clustering in ^{8}Be, ^{12}C and ^{16}O alpha particles and their spatial arrangement.

The concept that the cluster structure may not be apparent in the ground state but may emerge as the internal energy of the nucleus increases became crucial in the 1960s [31]. For a nucleus to develop a cluster structure, it must be energetically feasible. When the nucleus is split into its cluster components, an amount of energy equal to the mass difference between the host nucleus and the individual clusters must be provided. Therefore, a similar amount of energy is required near the point of contact of the clusters within the host nucleus, with adjustments for the interaction energy between the clusters. In essence, the cluster structure is expected to become apparent close to, and possibly just below, the cluster decay threshold.

The Bloch-Brink model, developed in the 1950s and 1960s, is one of the most famous microscopic theories describing cluster structures [32]. This model originated for the 2-alpha cluster system [33] and has been generalised to multi-system.

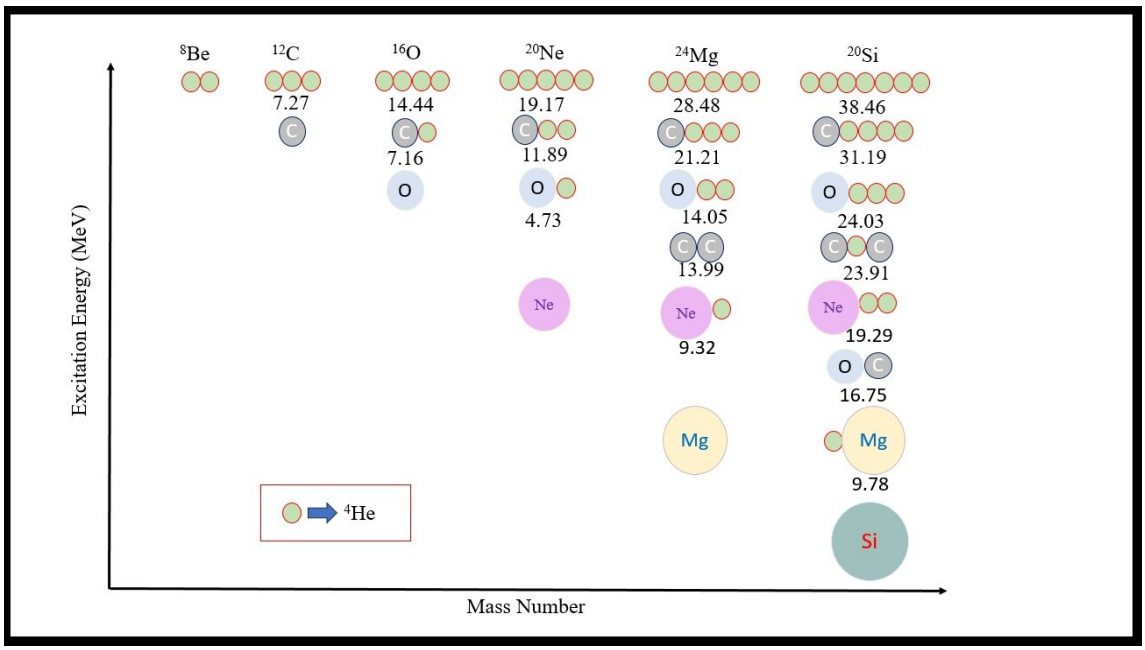

Figure 4.6: Ikeda diagram [27] representing Energy threshold for individual decaying modes. The diagram gives the threshold energies in MeV for each decay. The systematics indicate the possible molecular nature around each energy.

The competition between the mean field of the nuclear interaction, which leads to more spherical forms, and the tendency of nuclei to cluster is illustrated by the following: In the mean-field description, the particles move independently. In the clustering scenario, alpha clusters inherently reduce certain degrees of freedom [34].

The Ikeda diagram shows the manifestation of this rivalry. This diagram shows that cluster states are present at elevated excitation energies, typically at or above the threshold of alpha decay. An updated Ikeda diagram can be seen in Figure 4.6. It's important to note that many non-cluster states coexist within this energy range. The precise prediction, confirmed experimentally, is that Cluster structures are mainly found close to cluster decay thresholds.

The diagram shows that each step taken to approach or cross the cluster decay threshold introduces a new degree of freedom related to clustering. As a result, there is a gradual transition from the tightly bound compact ground state to the complete liberation of the N α (number of α particles) structure. In diagrammatic form, the diagram suggests a linear arrangement of α-particles as the N α limit is approached. However, it's important to note that this linear configuration is not necessarily the most stable. Some argue that the linear structure has an inherent instability [28], although many interpretations associate this limit with a linear arrangement.

Symmetries play an essential role in shaping the collective excitations of the nucleus. However, their influence goes further, affecting clustering in light systems primarily through their impact on the mean field. Interestingly, a somewhat complicated interplay exists between the mean field and the degrees of freedom associated with clustering. To illustrate this concept, let's begin with an analysis of a relatively simple and simplified approach to the nuclear mean field, which nevertheless proves quite powerful.

In applying the harmonic oscillator (HO) to the nuclear problem, it is assumed that each nucleon moves within a parabolic potential characterised by a linear restoring force. This potential results from the collective interaction of all the other constituents of the nucleus.

$$E = \hbar\omega \left(n + \frac{3}{2} \right) \tag{4.13}$$

The solution of the Schrödinger equation leads to the well-known energy levels for a three-dimensional atom. Oscillations can occur along any of the three Cartesian coordinate axes. The quantum number n represents the number of oscillator quanta.

Deformation of the nucleus or its potential, such as stretching along the z-axis, requires a reduction of the potential along the x and y-axes to maintain the total nuclear volume. This stretching of the potential along the z-direction decreases the vibrational frequency along this axis. In contrast, in the case of an axially symmetric potential, an increase in the vibrational frequency occurs in the perpendicular directions. The equation 4.13 can then be rewritten as follows:

$$E = \hbar\omega_{\perp} n_{\perp} + \hbar\omega_z n_z + \frac{3}{2}\hbar\omega_0 \tag{4.14}$$

Where E represents the system's energy, $\omega_{\perp}$, ω_z, and ω_0 are angular frequencies associated with different directions or modes, and $n_{\perp}$ and n_z are quantum numbers corresponding to the respective angular frequencies. The characteristic oscillator frequencies for oscillations perpendicular ($\perp$) and parallel (z) to the deformation axis are now required. These frequencies are constrained in such a way that $\omega_0 = 2\omega_{\perp} + \omega_z$. Additionally, the quadrupole deformation is given by:

$$\epsilon = \epsilon_2 = \frac{\omega_{\perp} - \omega_z}{\omega_0} \tag{4.15}$$

With deformations of the axial lengths, $def_{\perp}$:def_z, 2:1 and 3:1 corresponding to $\omega_{\perp}$:ω_z = 2:1 and 3:1 and ϵ_2 = 0.6 and 0.86. The distorted harmonic oscillator has provided valuable insights into nuclear behaviour since Schrödinger's solutions offer a reasonable approximation to the more realistic flattened nuclear potentials governing the mean-field motion of nucleons.

The resulting shell structure leads to a series of unique numbers as the potential deforms. We can see that the shell structure reappears when the axial strain increases to integer values. This gives rise to new sequences of numbers at each level of deformation. Group theory methods have typically characterised these unique numbers and their degeneracies. However, a comprehensive group theory framework covering flattened and elongated deformations has not been established.

Such degeneracies occur whenever the angular frequency ratios ω_x: ω_y: ω_z, where ω_x, ω_y and ω_z are simple integers. This leads to the formation of a shell structure, which gives rise to corresponding deformed magic numbers.

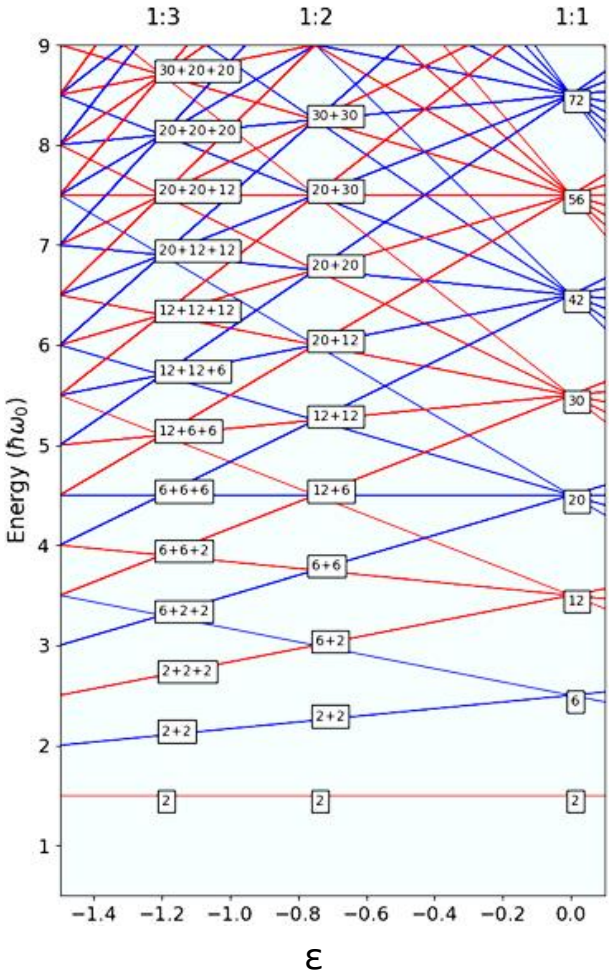

Figure 4.7: On the flattened side of the distorted harmonic oscillator (HO), the degeneracies corresponding to the flattened shapes are expressed by expanding them concerning the spherical degeneracies. The axial deformations are shown at the top of the figure. Figure taken from [35] with License CC BY 4.0.

Suppose we focus on the sequence of degeneracies rather than on the magic numbers themselves. In that case, we observe that the spherical degeneracies (2, 6, 12, 20, ...) are repeated twice when deformed by 2:1 and three times when deformed by 3:1. This pattern indicates the presence of two interacting spherical harmonic oscillator potentials at a 2:1 deformation and three at a 3:1 deformation, and so on. This symmetry becomes apparent in the context of magic numbers. The characteristic energy levels of the deformed harmonic oscillator are shown in Figure 4.7.

In an extension of earlier work by Bengtsson [36], [37] delved deeper into the intricacies of deformed magic numbers to investigate cluster decompositions explicitly. Rae demonstrated that the deformed magic numbers could be represented as sums of spherical numbers. At each level of deformation, this representation revealed the associated cluster structure. For example,

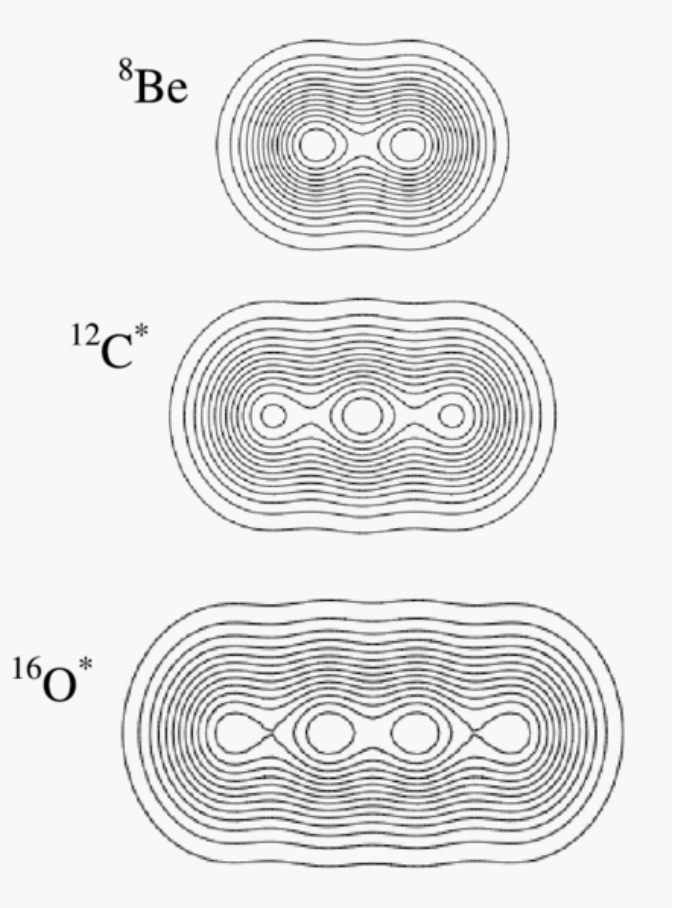

Figure 4.8: Densities are associated with the linear configurations found in the 2α, 3α, and 4α systems, which represent ^{8}Be, ^{12}C, and ^{16}O, respectively. [29] with permission ID 600204578 from IOPscience.

at a deformation of 2:1, superdeformed cluster states should be identified in nuclei such as ^{8}Be $(\alpha + \alpha)$, ^{20}Ne ($^{16}O + \alpha$), ^{32}S ($^{16}O + {}^{16}O$) and so on. Meanwhile, at 3:1 deformation, which corresponds to hyperdeformation, cluster states such as ^{12}C $(\alpha + \alpha + \alpha)$, ^{24}Mg $(\alpha + {}^{16}O + \alpha)$ and others should be present, as can be seen in the table 4.1. Consequently, combining Rae's ideas and the Ikeda picture determines cluster states excitation energy, deformation and single-particle configuration. While more sophisticated models allow for a more realistic description of the nuclei, the concepts developed here are still the fundamental principles that guide our understanding of these nuclear states.

The calculated densities further support this interpretation. Figure 4.8 shows the densities associated with the 2:1, 3:1 and 4:1 structures. These are associated with the 2+2, 2+2+2 and 2+2+2+2 symmetries, respectively. These density patterns are reflections of the same symmetries that are evident in the magic numbers. The exciting aspect of this correspondence is that it can be explained by an underlying SU(3) symmetry. Nazarewicz and Dobaczewski [38] showed that for 2:1 deformation, the plane scheme can be effectively described by two coupled SU(3) groups, for 3:1 by three groups, etc. The cluster-like structures observed in this case are due to the SU(3) symmetry.

The concept that correlations and clustering play a dominant role in light nuclear systems is

Magic numbers $\omega_\perp$:ω_z = 2:1	Spherical Magic Numbers	Cluster Configuration
4	2+2	$\alpha + \alpha$
10	8+2	$\alpha + {}^{16}O + \alpha$
16	8+8	${}^{16}O + {}^{16}O$
28	20+8	${}^{40}Ca + {}^{16}O$
40	20+20	${}^{40}Ca + {}^{16}O$
Magic numbers $\omega_\perp$:ω_z = 3:1	**Spherical Magic Numbers**	**Cluster Configuration**
6	2+2+2	$\alpha + \alpha + \alpha$
12	2+8+2	$\alpha + {}^{16}O + \alpha$
18	8+2+8	${}^{16}O + \alpha + {}^{16}O$
24	8+8+8	${}^{16}O + {}^{16}O + {}^{16}O$
36	8+20+8	${}^{16}O + {}^{40}Ca + {}^{16}O$
48	20+8+20	${}^{40}Ca + {}^{16}O + {}^{40}Ca$

Table 4.1: Correlation between deformed magic numbers for 2:1 and 3:1 deformations and spherical cluster decompositions [37].

strongly supported by the appearance of cluster-like structures in ab initio-type calculations [39]. The properties of these structures are related to the boundary conditions that give rise to the characteristic standing wave patterns. These symmetries, evident in both deformed harmonic oscillators, magic numbers and densities, emphasise the formation of cluster structures from alpha particles due to the stability of the ${}^{4}He$ nucleus.

4.3 Cluster structures at the experimet

In the present work, studying a ${}^{16}O$ beam colliding with a 4He gas allows the study of different cluster states. On the one hand, the formation of ${}^{16}O$ from 4 alpha particles and, on the other hand, the ${}^{12}C$ from the secondary reaction ${}^{16}O(\alpha,2\alpha){}^{12}C*$ will lead to the study of the Hoyle state. At an energy of **7.16 MeV**, the ${}^{12}C* + \alpha$ cluster structure should be seen, and at **14.44 MeV**, a 4α structure.

The study of the composition of ${}^{16}O$ and consequently of ${}^{12}C*$ is of great interest because of its significant association with the presence of α stars in nuclei and its implications for the dynamic relationship between nuclear structure and astrophysics. ${}^{12}C$ is also an essential component in the structure of living organisms, including humans. According to current understanding, the origin of ${}^{12}C$ is attributed to the 3α process in stellar nucleosynthesis environments.

4.3.1 Quadruple alpha decay in 16O

The ^{16}O was represented as a tetrahedral configuration of alpha particles according to the Hafstad and Teller model [24]. From the Ikeda perspective, this would be associated with a densely packed, energetically favourable ground state.

Diverse theoretical methods have been used to analyse the structure of 16O, including Hartree–Fock (HF) [40], Alpha decay widths of excited states of ^{16}O [41], Nilson–Strutinksy (NS) [42], Alpha cluster model (ACM) [43] and a basic core+α potential model [44]. Significantly, certain universal features and themes appear.

The first excited state in ^{16}O, located at 6.049 MeV, has a spin and parity of $J^{\pi} = 0^{+}$. This state is very close to the α decay threshold. In both NS and HF calculations, this state is associated with a 4p-4h structure, implying an excitation of an α particle to the sd shell. In NS calculations, this 4p-4h structure is related to a shell gap, manifested for oblate deformations. Similarly, HF studies identify a structure closely associated with trial harmonic oscillator wave functions, where all oscillator quanta are concentrated along only two axes. The α-cluster model also correlates the 6.049 MeV state with a quasi-planar structure.

The rotational properties of this state, together with the quadrupole moment corresponding to the gamma width of the 2^{+}(6.917 MeV) transition to the 0^{+} excited state [43], are in good agreement with most calculations. Notably, this state corresponds to a 4p-4h excitation, and considering the characteristic intrinsic density, it is inferred that this state has a $^{12}C + \alpha$ cluster structure. The core + α potential model developed from this perspective reasonably reproduces the experimental properties of this band, including the α decay widths [44].

The subsequent cluster configuration predicted by the Ikeda diagram relates to the 4α state, represented as a linear alignment of α particles. In NS calculations, this structure is associated with an 8p-8h arrangement, where two α-particles are extracted from the 16O core and placed in Nilsson orbitals from the sd and fp-shells most strongly aligned with the prolate deformation. The result is a linear 4α configuration. The experimental point of view on this matter is a little less clear. Support for the linear structure comes from measurements of the $^{12}C(\alpha, {}^{8}Be)$ reaction [45]. It's plausible that a linear chain could fragment into two smaller chains associated with the ^{8}Be ground state.

4.3.2 Hoyle State

The 3α process occurs during the helium-burning phase of stellar nucleosynthesis. It involves initially merging two α particles, followed by their fusion with a third [5]. The resulting excited carbon-12 nucleus, called $^{12}C*$, undergoes radiative deexcitation. The transient nature of the unbound $^{8}Be*$ nucleus (with a lifetime of 10^{-16} seconds), formed in the intermediate stage, acts as a bottleneck for the whole process. Consequently, the observed abundance of carbon in the Universe cannot be explained by considering a non-resonant two-step process.

Fred Hoyle predicted the Hoyle state [46], an excited spin-0 state of $12C$ in 1954. Its existence is crucial for understanding the presence of carbon in red giant stars and determining the carbon content of the solar system, which has implications for life as we know it.

Named after the British astrophysicist Fred Hoyle, the Hoyle state is a highly excited and unique energy state in the nucleus of (^{12}C). In the 1950s, Hoyle proposed the existence of this state to account for the stellar abundance of carbon [46].

While first-principles calculations suggest a bent arm structure for Hoyle's state, this has yet to be experimentally confirmed [47]. Many experiments have attempted to probe this structure by investigating the decay properties of the state [48]. Sequential decay is much more likely than democratic decay. This is due to the formidable challenge of connecting multiple alpha particles through the Coulomb barrier. The highest observed fraction of democratic decay for this state is 0.043% of all decays [3]. The theoretical assessment of the democratic contribution lags behind the experiment by a factor of at least 10 [49]. These results have important implications for our understanding of the abundance of carbon in the solar system.

The Hoyle state is an excited energy state in the (^{12}C) nucleus, consisting of six protons and neutrons. It has a specific energy level called E_{Hoyle}. The Hoyle state is closely associated with the triple-alpha process, a nuclear reaction in which (^{12}C) is produced by the fusion of three alpha particles. The reaction can be represented as:

$$3(^4He) \rightarrow ^{12}C + E_{Hoyle} \tag{4.16}$$

In this equation, three alpha particles combine to form a ^{12}C nucleus, releasing energy. The energy released in this reaction is crucial to powering stars and is responsible for creating carbon, which is essential for life as we know it. The energy level of the Hoyle state is finely tuned to the energy required for three alpha particles to come together to form a stable carbon-12 nucleus. This fine-tuning is critical because if the energy level of the Hoyle state were even slightly different, the formation of carbon by the triple-alpha process would be much less efficient. This, in turn, would significantly affect the chemical composition of the Universe.

The second stage of the 3α process, where $\alpha + {}^8Be \rightarrow {}^{12}C + \gamma$, must occur via a resonant state in ^{12}C with angular momentum and parity $J^\pi = 0^+$, situated in proximity to the $\alpha + {}^8Be$ emission threshold. The presence of this state was quickly validated through experimental confirmation [50] at an excitation energy of 7.654 MeV.

Ab initio calculations show that the Hoyle state at ^{12}C is gaseous and thinly populated, with weak interactions between the constituent alpha molecules [51]. In addition, there have been proposals for the possible existence of Bose-Einstein condensates with α-particles [52], as well as molecular-like structures where three α-particles form linear chains, obtuse triangles or bent arm configurations [53, 54, 55] (Fig. 4.9).

Among the different observables, some of these models can predict the branching ratio (B.R.) between the sequential and the direct decay pathways of the Hoyle state [56]. Therefore, obtaining accurate experimental data on this branching ratio is paramount, as it serves as a benchmark for evaluating theoretical models that attempt to explain the α-clustering at ^{12}C.

The prevailing approach has been to study the decay of the Hoyle state through the emission of 3α, mainly to check the rate of direct decay relative to the rate of sequential decay. Freer et al. in 1994 [57] provided an upper limit for the direct decay branch, suggesting that the branching ratio (B.R.) of the Hoyle state decay bypassing the ^8Be ground state is less than 4%, expressed as:

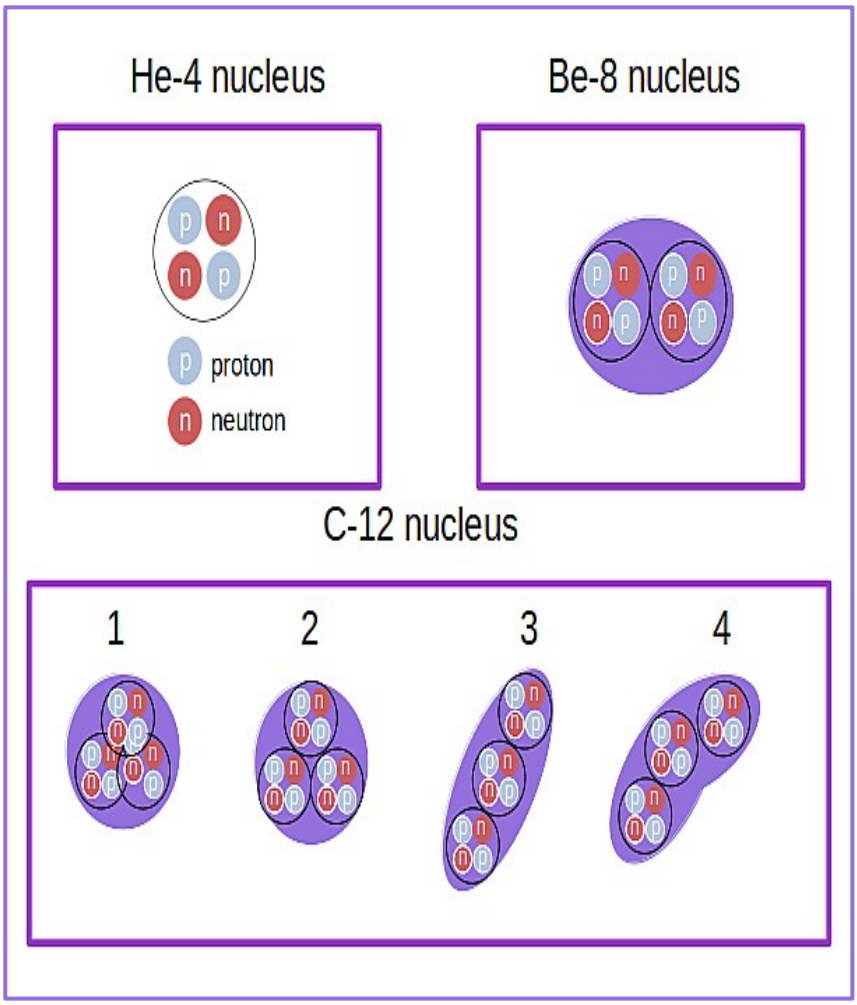

Figure 4.9: Schematic illustrations of α clustering in atomic nuclei in α particle, ^{8}Be, and ^{12}C (four possible cases, one corresponding to condensate state, two the triangle disposition, three lines and four bent lines). The purple areas represent atomic nuclei allowing some movements of α clusters.

$$\frac{\Gamma_\alpha - \Gamma_{\alpha_0}}{\Gamma_\alpha} < 0.04 \tag{4.17}$$

Here, Γ_α represents the total width of the α decay, and Γ_{α_0} illustrates the partial width of the α emission leading to the ground state of ^{8}Be.

Raduta et al. [58] reported results strongly contradicting the previous results, indicating a relatively high value of the direct B.R. at 17% ± 5%. A series of new experiments aimed at determining the true value of the direct decay B.R. of the Hoyle state were carried out in response to these divergent results. Kirsebom et al. obtained a new upper limit of 0.5% (95% confidence) using the kinematic fitting method [59]. Two recent experiments by Rana et al. [60] and Morelli et al. [61] suggested non-zero values for the direct decay B.R., namely $\frac{\Gamma_\alpha - \Gamma_{\alpha_0}}{\Gamma_\alpha} < 0.91\% \pm 0.14\%$ and $1.1\% \pm 0.4$

An improved upper limit for the direct B.R. of 0.2% (95% confidence level) was obtained by Itoh et al. [62] in a highly statistical experiment. It should be noted that, as discussed in [62], strip detection introduces a non-negligible background that reduces the sensitivity to the signal of the direct BCR. Given the importance of understanding alpha cluster effects in the nuclear structure of 12C, it is essential to improve our knowledge of the direct BCR of the Hoyle state. This is particularly important because theoretical estimates of this quantity are on the order of 0.1%.

Chapter 5

Active Target Time Projection Chamber

Active-Target Time Projection Chamber (AT-TPC) was constructed and commissioned at the NSCL (National Superconducting Cyclotron Laboratory, Michigan State University). It is an active target detector custom-made for low-energy nuclear reactions in inverse kinematics with radioactive ion beams [63]. The detector is usually sited at the National Superconducting Cyclotron Laboratory (NSCL) at Michigan State University, but experiments are performed at other facilities as well: Notre Dame, TRIUMF, Argonne...

5.1 Operation mode

The Active target time projection chamber is a cylindrical detector with two modes of operation: active target and time projection chamber. Active targets filled with gas act simultaneously as targets in the experiments. It is the tracking medium to recognize the path left by the particles when interacting after the reactions.

5.1.1 Active targets

The active targets are oriented to the study of short-lived radioactive nuclei, for which high efficiency and thick targets are necessary to boost the luminosity of the experiments due to the weak intensity of the available beams. Using active targets is exciting, especially when doing experiments where the particle's recoil energy after the reaction is minimal and loses a lot of energy or does not have enough energy to emerge from a solid target, no matter how fine.

The problems with solid targets at low energy are solved with active targets. Also, solid angles close to 4π were covered without the limitations in the energy of the thick target. The reaction in the active volume can occur in any place along the detector. In the case of AT-TPC, it is a cylinder of 1 m in length; the beam loses energy through the chamber due to the nuclear and electromagnetic interaction with the particles, and depending on the nominal energy at the entrance, the beam stops entirely like in the case of the ^{16}O describe in this thesis. Thanks to this kind of target, even if the energy of the beam is deficient, by reconstructing the traces derived from the reaction, it is possible to obtain the information on the vertex and the

angles that give us access to all the derived kinematics and beam slowing in gas gives excitation function.

In the AT-TPC, we need to consider the pressure and temperature of the gas and the number of electrons present in the target at those conditions. Target gas has to provide sound electron amplification (mixtures). Considering that usually, the targets are light elements such as hydrogen or helium, the number of free electrons is deficient. To solve this problem, a quencher is typically used to increase the number of electrons; for example, in previous experiments in AT-TPC, such as the e15250 experiment, a mixture of 95% helium and 5% isobutane was used.

5.1.2 Time projection chamber

The time projection chamber (TPC) is a three-dimensional cylinder extension of the drift chamber principle. It comprises a sizeable gas-filled volume with readout structures at one of the cylinder's bases.

A strong electric field is applied between the anode and cathode planes at the cylinder bases. Charged particles traverse the chamber and ionize the gas. The electric field forces the electrons to drift to the pad plane, where the position in the XY coordinates and arrival time are measured. From these measurements, the entire particle trajectory can be reconstructed.

To avoid transversal divergence of the drifting electrons and to curve the trajectory of the charged particles, the TPC is operated inside a strong magnetic field in parallel to the electric field with a solenoid magnet; thanks to that, it is possible to work with other observable the magnetic rigidity of the particles.

5.2 AT-TPC

5.2.1 Description of detector

AT-TPC consists of a cylindrical detector of 1 m length and 29.5 cm of radius in the bases. The detector's inner part is filled with a gas that acts as a scattering target for the reaction and a tracking medium for the charged particles (Figure 5.1).

AT-TPC structure is formed by a cylinder of epoxy-coated fibreglass with a length of 1 m and a diameter of 56 cm. The upstream end of the volume is sealed with a stainless steel cathode. In the centre of this cathode is a thin foil window through which the beam enters the detection system. The downstream end is closed by an aluminium flange, which supports the sensor plane that acts as an anode. This inner volume is filled with the gas that serves as a target.

As we said previously, the main idea of this detector is to use the gas as an active target; the inner part of the cylinder is a concentric shielding volume contained by a cylindrical aluminium

vessel. The shielding volume isolates the cathode's high electric potential from the environment, preventing possible sparking in the cathode. It is filled several times with nitrogen to clean the active volume, which acts as an inert gas with a high dielectric constant, preventing other environmental gases like oxygen.

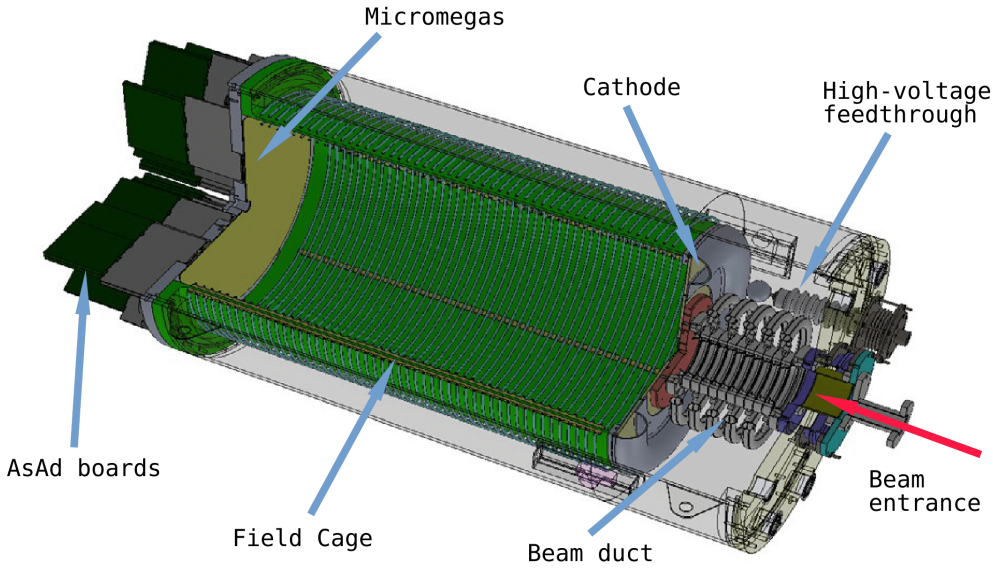

Figure 5.1: Schematic view of the main elements of the AT-TPC detector on which the experiment proposed in this thesis is performed. Figure taken from [64] with ELSEVIER LICENSE with License Number 5999311016660.

The cylinder is positioned in the centre of a solenoid magnet, capable of providing fields near 3T at the centre of rotation. The solenoid curve trajectory of the charged particles is used to obtain their energies and angles to identify them in the analysis fully. Another significant improvement of this magnetic field is that it is possible to measure the total range of particles with long tracks because they are trapped in the magnetic field, describing a paraboloid.

The total variation of the field inside the volume was measured, and fluctuations less than 2% were encountered between the centre and the border of the detector, as we can see in Figure 5.2.

A high uniform electric field, to the order of 10^4V between the cathode and the anode, is produced parallel to the axis of the TPC and the magnetic field to ionize the gas and stimulate the drift electrons to derivate to the pad plane. The wall of the cylinder is surrounded by 50 inside and outside rings to guarantee the uniformity of the electric field. Those rings form a structure called a field cage; the inner rings have a radius of 28.1 cm, while the outer 31.1 cm. The rings are connected to the anode by a chain of 20 M Ω resistors that gradually decrease the voltage between each ring to stabilize the electric field.

The entrance of the beam in the chamber is an aluminized para-aramid window of 25.4 mm in diameter and 3.6 μm. The beam travels through the gas, ionizing it. The ionized electrons are pulled along the active volume to the end of the detector, composed of a sensor plane equipped with a bulk-fabricated Micromegas device [65].

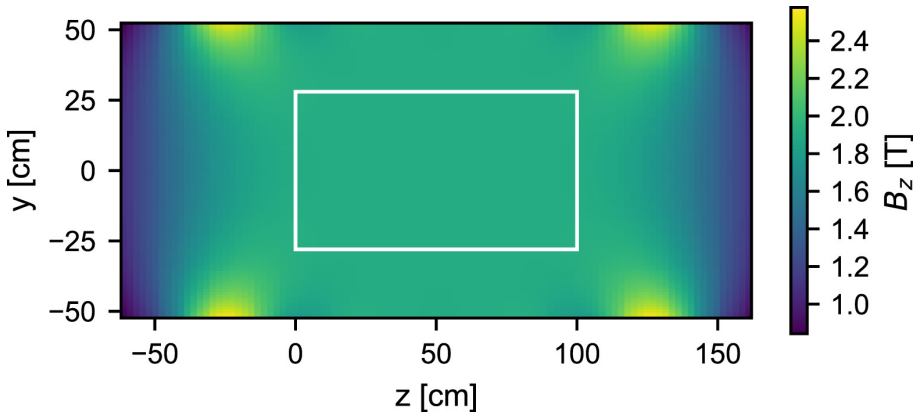

Figure 5.2: Simulation to ensure uniformity of the magnetic field throughout the AT-TPC chamber volume. Since the chamber is 29.7 cm in radius, it can be ensured that the magnetic field is uniform throughout the volume. Figure taken from [64] with ELSEVIER LICENSE with License Number 5999311016660.

After micromegas, a sensor plane (pad plane) recovers the signals. With a digital electronic system connected via feed-through boards that isolate them from the gas volume, it is possible to read the electronic signal that well from the reactions pad by pad. To ensure the electrons' appropriate drift in each experiment, the active volume contains a uniform electric field that can attach thousands of KV/m between the anode and the cathode. This electric field is uniform, and to ensure that a resistor chain surrounds the inner walls, this resistor gradually decreases the voltage between 50 rings surrounding the inner part and with a central distance between them.

The AT-TPC is sited in the centre of a large-bore solenoidal magnet to curve the charged particles. The magnet was initially designed for medical resonance imaging (MRI), and it can attach fields up to 3T. There is a simple rail mechanism to insert the cylinders into this solenoidal.

Depending on the energy, the nuclide's Z, and the magnetic field's intensity, the particle's trajectory bends more or less to determine its energies. In the first approximation of the online analysis, this property helps distinguish light particles such as 4He from protons. One of the principal motivations of this longitudinal magnetic field parallel to the electric field is to encapsulate the very light particles, forcing them to describe a helicoidal trajectory and be capable of measuring their total range. Another benefit is the addition of the curvature radio of each track, which makes it possible to obtain the total energy of each particle involved in the reaction.

5.2.2 Micromegas and Pad plane

The Micromegas (short for Micro-Mesh Gaseous Structure) [65] is a structure integrated into the AT-TPC ideated to the multiplication of the drift electrons recoiled for the pad plane and recover the XY position of the reactions. The system consists of a steel mesh of 18-micron thickness at approximately 100 microns from the pad plane. With this GAP and the negative polarization of the mesh, we can obtain approx. A gain of up to 10000 per electron is enough to maximize the necessary process of electronic readout with the pads.

The Micromegas device consists of a micromesh installed between the active target and the pad plane on the sensor plane. The mesh is separated by insulating pillars at 122 microns above the pads. A 100 V to 1000 V potential is applied between the mesh and the pad plane to create a high electric field region just above the pads.

When ionization electrons from a reaction drift into this separate region through the holes of the mesh, they are multiplied via an avalanche process and produce a detectable signal on the nearest pad to the avalanche. The distance between the pad plane and the mesh is relatively tiny in comparison to the size of a pad, so the signal induced by a given ionization electron is usually confined to one pad only [63].

The pad plane is optimized for detector inclinations from 0º to 7º, relative to the beam axis; the size of the central triangles is the fourth part of the external ones to maximize the resolution in the beam near zone to reconstruct the shorter traces. It provides a finer resolution near the reaction vertex. The sensor plane consists of a printed circuit board of diameter 56 cm with 10240 triangular gold electrodes, which allows the system to act as an instantaneous recorder of reactions in the XY plane. The triangular pad shape was chosen to maximize the detector's spatial resolution. The distribution of these pads in the circular area is 6144 small pads arranged in a hexagon with a height of 0.5 cm surrounded by an outer region of 4096 large pads with a height of 1.0 cm, as shown in Figure 5.4. The main idea is to have a reasonable number of pads depending on the part of a study of the track; if we are outside of the boundary region, it is not necessary to have a resolution so fine. The 10240 pads of the sensor plane allow a realistic three-dimensional event reconstruction for arbitrary reactions.

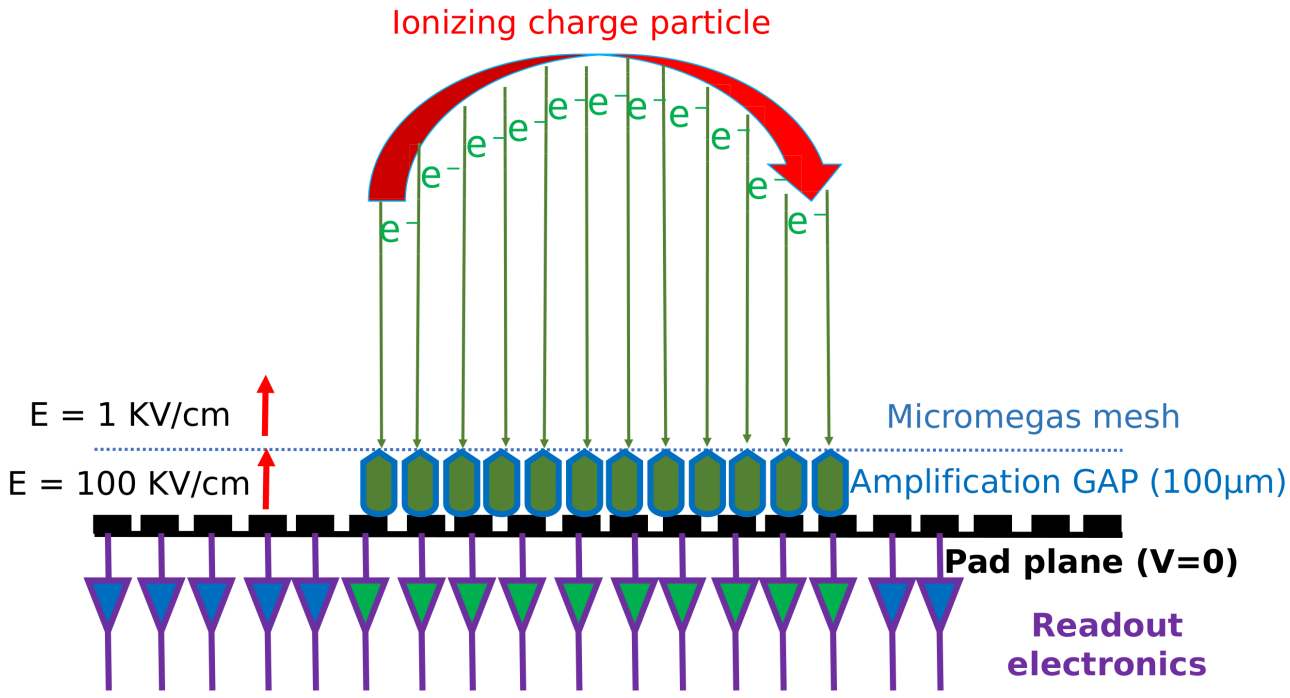

Figure 5.3: Schematic diagram explaining the amplification produced in the AT-TPC mesh and the subsequent data readout with the readout electronics system.

This very robust structure, resistant to sparking, can operate in different conditions (gases,

pressures). The gain of the Micromegas system depends strongly on the good parallel separation between the mesh and the pads. This separation or GAP is very uniform thanks to the bulk fabrication process of installing the mesh to the pad plane [66].

The signal amplitude depends strongly on the preamplifier gain for each channel, and the preamplifier was polarized at 120 fC. The signal amplitudes were normally distributed with a mean of 457 bins for the small pads and the fourfold bins for the large pads. Taking into account that the size of the central pads is the third part of the external ones, the signal amplitude, which is proportional to the area of the individual detectors, was renormalized to one dividing the amplitudes from each group of pads, large and small, by the mean amplitude of each group [63].

Across the sensor plane, the signal amplitude remains uniform, with variations generally distributed at random. Due to this random distribution, an asterisk-like pattern appears on the readout signal. However, that coincides with boundary conditions of different readout electronic cards, so interference is ideally identified. This indicates that the variations in amplitude are not due to variations in the mesh gap.

To summarise, the main idea of the pad-plane operation is that when a charged particle goes through a series of adjacent pads, the charge accumulated in each place is recorded gradually for the acquisition system. With that charge accumulation and the disposition of each pad, we can obtain a great sensitivity and an excellent angular resolution, even for small tracks. Another advantage of this design is the possibility of quitting some pads on the centre of the plane; with that hole, the recoil nuclei could pass through the chamber without interaction with the pad plane. With the hole, the AT-TPC can be used with other secondary detectors after the chamber to identify the recoil nuclei or beam events, possibly increasing the beam's intensity without modifying the gain in the zone.

5.2.3 Electronics and Data Adquisition

To obtain a better solution to extract the information of the pads, a system accommodates the electronics for the 10240 pads without cable connections. Forty front-end cards fit in the pentagonal pattern, and shielding covers the electronic cards in pairs.

For digitizing and recording the entire trace for each of the 10240 channels, AT-TPC is instrumented with digital electronics developed by the Generic Electronics for TPCs (GET) collaboration [67].

The electronics hardware is divided into several modules Figure 5.6. At the lowest level is the ASIC for GET (AGET) chip, a custom application-specific integrated circuit (ASIC) that controls the sampling and the shaping of signals and makes a test comparing the threshold and signal to generate a channel-level trigger.

Each AGET can read out sixty-eight channels from the detector, four of which are used to correct the electronic noise. This chip amplifies the signal with a variable gain preamplifier. The AGETs are mounted in groups of four on AsAd (ASIC Support and Analog to Digital conversion) boards.

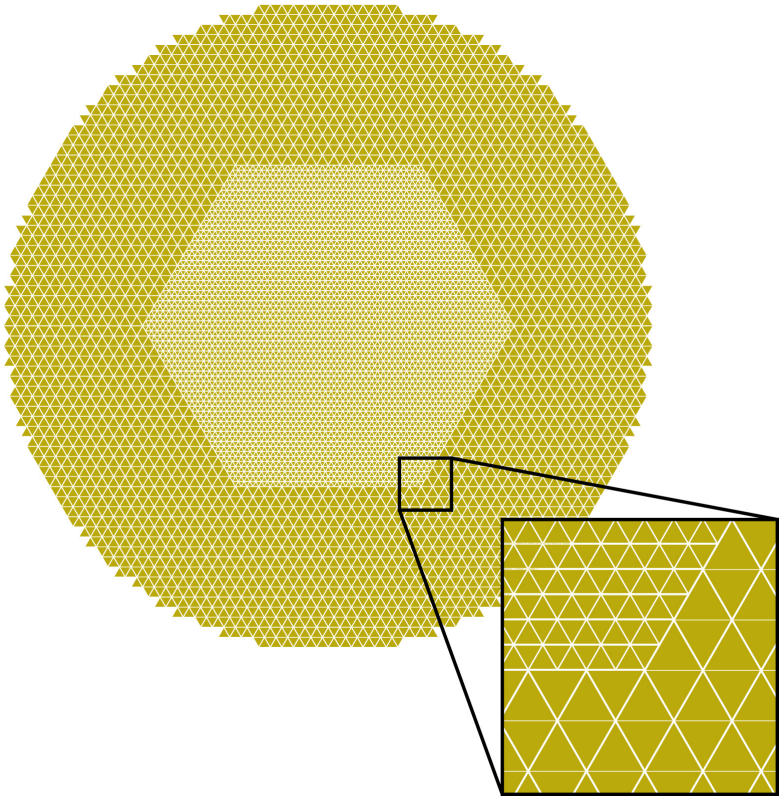

Figure 5.4: Representation of the padplane. In the figure, you can see how the central pads are smaller than the outer pads. This system is set up to improve the resolution in the areas close to the beam and obtain a better measurement of the reaction vertex. Figure taken from [64] with ELSEVIER LICENSE with License Number 5999311016660.

Each AsAd hosts a four-channel Analogical Digital Converter, 12-bit ADC. When the trigger is released, the ADC digitizes the signal from each AGET and transmits it. Between triggers, the ADC sends the multiplicity signal. The input end of each AsAd board is attached to an isolation circuit that prevents sparks in the detector from damaging the electronics and is connected directly to the sensor plane. The AsAd assemblies operate inside the high magnetic field of the solenoid during experiments, so the tests have shown that the performance of the electronic system is the same with and without the magnetic field.

The top level of GET electronics is the CoBo (Concentration Board). Each of the AT-TPC's 10 CoBos is connected to four AsAd boards. When a trigger is issued, the CoBo collects the board data, applies an event time stamp, and builds the event. It then sends the event over a 10 Gb/s fibre-optic link to a network switch to be distributed to a cluster of computers.

To maintain the CoBos synchronized, another board called the Multiplicity, Trigger, And Time (MuTAnT) distributes a global time stamp and manages clock synchronization across the system. This board collect all of the running multiplicities and hit patterns from the CoBos and combines that information to obtain a global trigger for the system. In level 1 of the trigger, the assortments are summing to generate a trigger when a global threshold is reached. In a second level, an attempt is made to match a pre-defined pattern of hit channels.

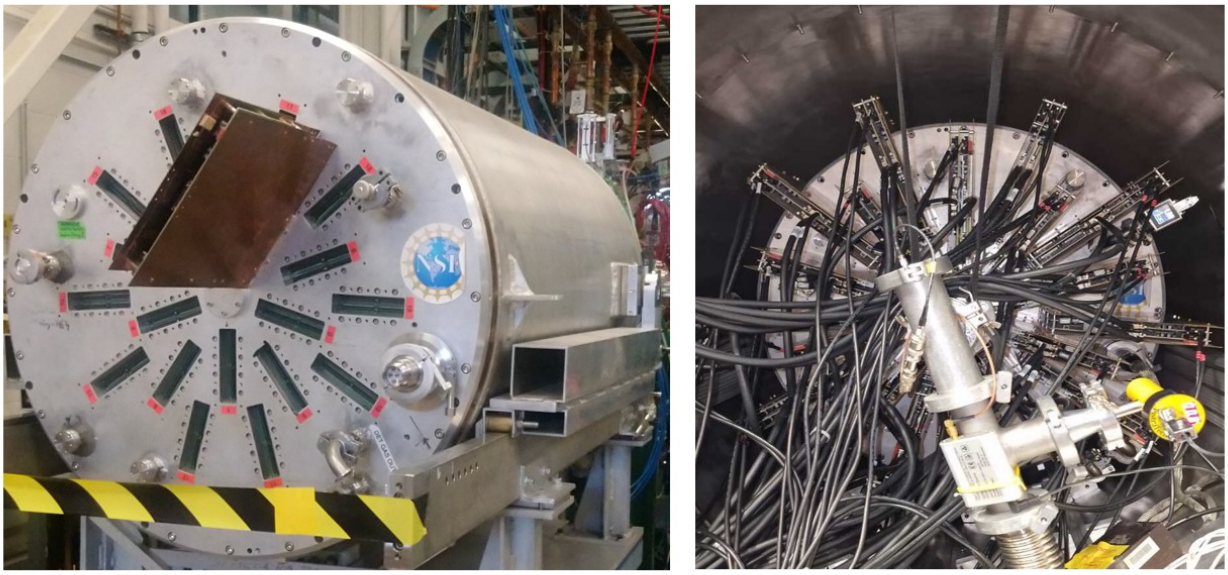

Figure 5.5: Photograph of the connections to the AT-TPC padplane. The figure shows a series of cards connected to the back of the padplane. Each card (AsAd) obtains information from a group of pads.

A digital custom distributed data acquisition system reads out the AT-TPC detector. The ten CoBos are connected via a high-speed network to a cluster of the same number of computers. The data of each CoBo was recorded by that computer running a data router program developed by GET collaboration. The usage of several computers in parallel can produce up to 11 MB of raw data per event in full-readout mode. GET cooperation also developed the Electronics Control Core (ECC) server, which controls all the systems. The ECC reads configuration parameters for the CoBos and MuTAnT and uses this information to set the appropriate registers on the boards and establish communications between the boards and the data routers; for another size, it is responsible for starting and stopping data acquisition on the CoBos.

In summary, the trigger configuration can be programmed and needs to filter out unreacted beam events. The GET electronics provide discriminators on each pad. The running multiplicities of each AsAd are routed to the MuTanT through the CoBos. AGET front-end chips provide various gains and shaping times.

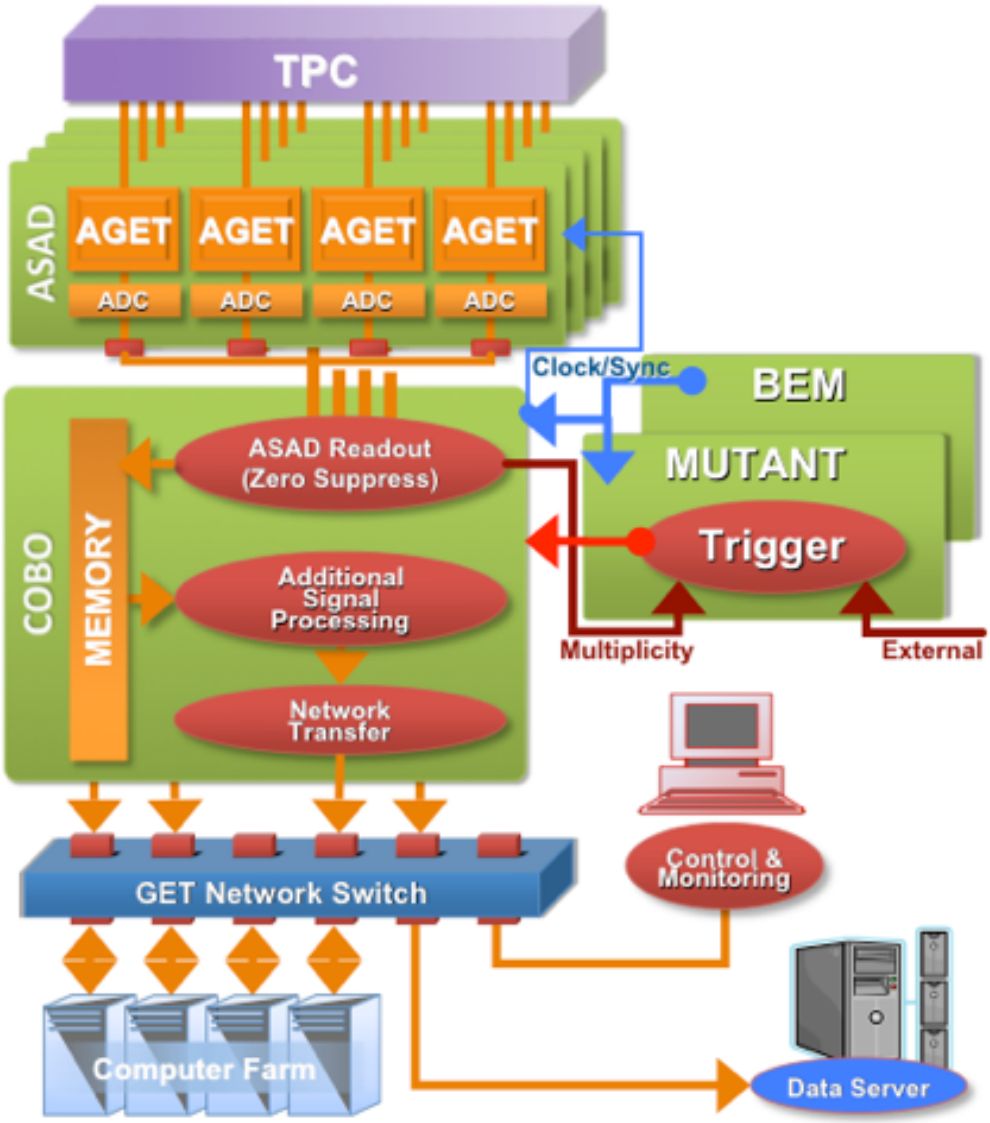

Figure 5.6: Schematic of the electronics used in AT-TPC to recognize and decode the data obtained in the experiments. Figure taken from [64] with ELSEVIER LICENSE with License Number 5999311016660.

5.3 ATTPCROOT

ATTPCROOTv2 is a series of algorithms, classes, routines..., for the most part, written in C++ language, based in FairSoft and FairRoot, that build up a robust framework for simulation and analysis of active target detectors, in particular, the AT-TPC (Active Target Time Projection Chamber), as well as the Prototype AT-TPC detectors. The FairSoft distribution provides the software packages needed to compile and run the FairRoot framework and experiment packages based on FairRoot. FairSoft is a source distribution company that produces recurring releases for macOS and Linux. FairRoot and FairSoft are not developed directly by the AT-TPC group but used by ATTPCROOTv2 to be compiled and executed. Other secondary programs that ATTPCROOT uses are, for example, Eigen, FLANN, or for the unpacking and visualizing raw data HDF5 library.

The framework allows investigators to unpack the raw data of experiments, complete analysis, and compare the results with realistic simulations based on the Virtual Monte Carlo package given by Geant4, which is wholly integrated into the main program. In the case of simulations, the user can create an event-by-event reaction into a realistic detector environment based on the same idea of Geant4.

After unpacking raw data or creating simulated data, pulse shape analysis can process the readout from the AT-TPC pad planes. Collecting points extracted from the padplane from each event can be analyzed using pattern recognition algorithms. The trajectories of particles in the detector can then be tracked, extracting information about the angles or track length, among other details.

5.3.1 Unpack and track reconstruction

Data unpacking and reconstruction or digitalization of the simulated tracks require a multi-step process involving many classes and algorithms. This section will summarise the critical steps in constructing and analyzing traces for accurate data and simulation.

The raw data obtained by the DAQ system was compressed and saved in HDF5 format. The direct observables we work with are the charge deposited in the pad plane and the position XY of the tracks for each pad, which reconstruct the 2D events. To perform a three-dimensional reconstruction of the reactions, relying on the drift velocity created by the electric field on the free electrons in the medium is necessary.

Once the positively charged nuclei pass through the medium, they separate and drag the free electrons of the gases inserted in it as sources of loosely bound electrons; for example, in some experiments, the chamber could be filled with 95% helium acting as a target and 5% CO2 acting as a source of free electrons. These electrons are dragged due to the intense electric field towards the cathode, where they are amplified and detected by the pad plane, both in position and charge. In the case of this thesis's experiment, the chamber was filled with pure helium. This will simplify the detection of events of interest.

Each trace's mark on the XY plane gives access to another direct variable: the phi angle due to the particle's curvature induced by the magnetic field parallel to the magnetic field.

Calibration of the Z variable is relatively straightforward when the detector is not tilted around the z-axis. In the case of the experiments described in this thesis, the detector axis is parallel to the electric and magnetic field so that the z component can be obtained directly from the formula:

$$z = \frac{v_d z_0}{\nu} \tag{5.1}$$

Where v_d is the drift velocity of the free electrons in the gas, z_0 the vertex and $\boldsymbol{\nu}$ the ADC clock frequency.

Each event consists of 512 synchronized time buckets for all 10240 pads. Depending on the experiments and the energy, you can select a writing ratio of 6.25 MHz for low-energy

experiments. In higher-energy experiments, they were written at 3.125 MHz, i.e., each time packet in the time bucket was 160 ns and 33 ns of time.

A pulse shape analysis was performed to determine if a signal was recorded in a given pad. In the first step, for the calibration of the z component, the baseline of the pad is subtracted, and an amplitude threshold is applied; with that previous step, we ensure that any electronic noise peaks will not be identified as the actual peak, then several beam measurements are selected without interaction into the camera, this will give several measurements of a peak in the TimeBucket corresponding to the start of the camera. The cathode can be easily fixed with accumulation events. By having both ends of the chamber fixed, the drift velocity can be easily determined, and with it, the z-distance of any trace traversing the chamber.

With the three-dimensional information, it is now possible to reconstruct the theta angle and, above all, the radius of curvature of the traces to obtain the energy from the magnetic field using the magnetic rigidity defined as the following:

$$B\rho = \frac{p}{e} \tag{5.2}$$

Where B is a magnetic field, p is the particle momentum, e is the particle's charge, and $\boldsymbol{\rho}$ is the radius of curvature of a particle immersed in a magnetic field B.

Chapter 6

Data Analysis

6.1 Observables

In active target experiments, especially those related to ATTPC that incorporate a magnetic field, it is necessary to consider clarity when obtaining direct observables. In the e20020 experiment, two observable are available: the particle energy in the form of charge deposited in the gas volume and the XY positions of the particles detected by the pad plane. Together with the drift time, these give us a three-dimensional reconstruction that provides access to the reaction angles.

With this information about the direct observables, and considering that the magnetic field bends the trajectory of the charged particles, we can access the indirect observables, such as the radius of curvature of the reaction's outgoing particles or the length of the trace. Reconstruction algorithms such as Random SAmple Consensus (RANSAC) or Kalman filter will determine these. With all this information, we have access to the complete kinematics of the reaction.

Since the direct observables inevitably depend on the pad plane, a study of the pad plane is carried out, making a heat map, dividing the experiment into two stages, and trying to see possible electronic problems in the experimental connections that could affect our final results Figure 6.1.

As seen in the fourth quadrant of the pad plane ($x > 0$; $y < 0$), there is a disconnected region during the whole experiment, which can affect the calculation of the reaction angle when reconstructing traces, energies or beam reaction vertices.

As mentioned above, to obtain the z-component of the traces, use is made of the time determined by the time bucket. The time bucket is divided into 512-time slots, and as there is a sampling frequency of 3MHz, a simple count will give a time step of 0.3 microseconds per time step. The camera's length determines the dependence between the sampling frequency and the distance. This dependence can be defined perfectly well by taking Beam events at the end of the detector and window events Figure 6.2.

With these time bucket data and the length of the chamber, the electron drift velocity can be calculated, taking into account that the size of the chamber is 1m and the sampling rate is 3 MHz:

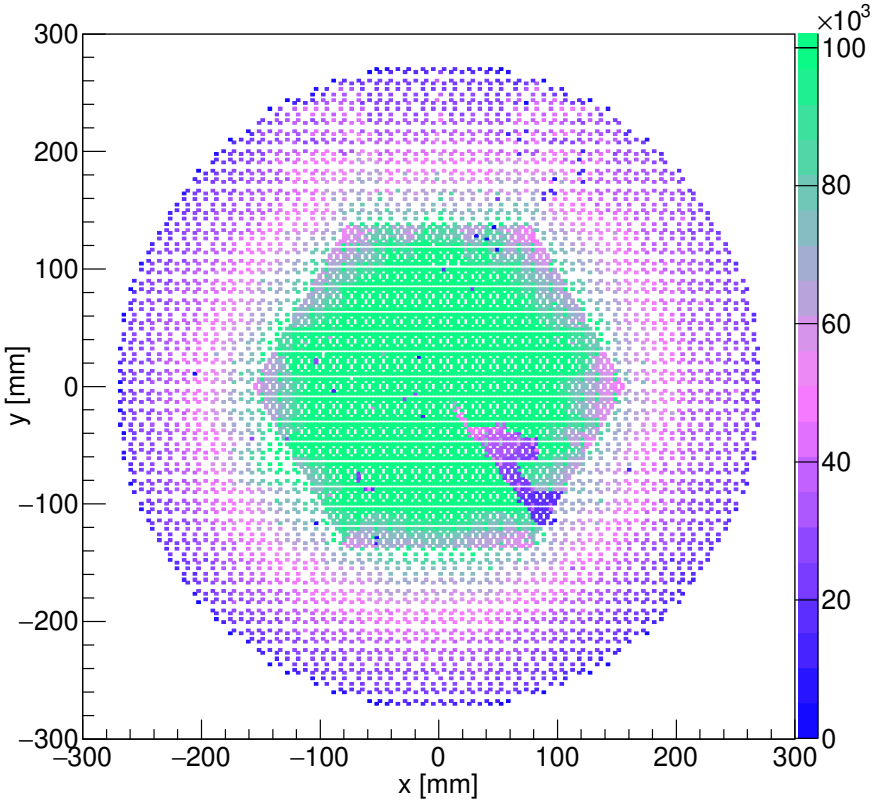

Figure 6.1: Accumulation of points of the traces obtained in the pad plane after pattern recognition analysis without filtering. The figure shows that during the experiment in the fourth quadrant, a set of pads remained disabled, affecting the quality of the data and the statistics when fitting, as it will increase the number of broken traces that will not be correctly identified.

$$v_d = 0.896 \frac{cm}{\mu s} \tag{6.1}$$

One of the most critical points when reconstructing traces in experiments with active targets in a time projection chamber type detectors is to clean up the time signal. Initially, a threshold value is imposed for which, if the signal is smaller than this value, it is disregarded for each time bucket of each ADC. All time buckets above or below the previously calculated time window are set to zero, thus avoiding electronic noise in and out of the signal. The highest peak in the ADC signal of each enabled pad is selected by performing a pulse interpolation to calculate the average value of that peak. Once I have the average value, the pulse is corrected by summing the neighbouring TBs ($\pm$ 5) and dividing by the total integrated pulse load to smooth it.

In addition to the signal cleaning, a Fourier space convolution filtering process is performed on each of the individual ADC signals in the pads, affecting the signal cleaning and all indirect observables in the experiment.

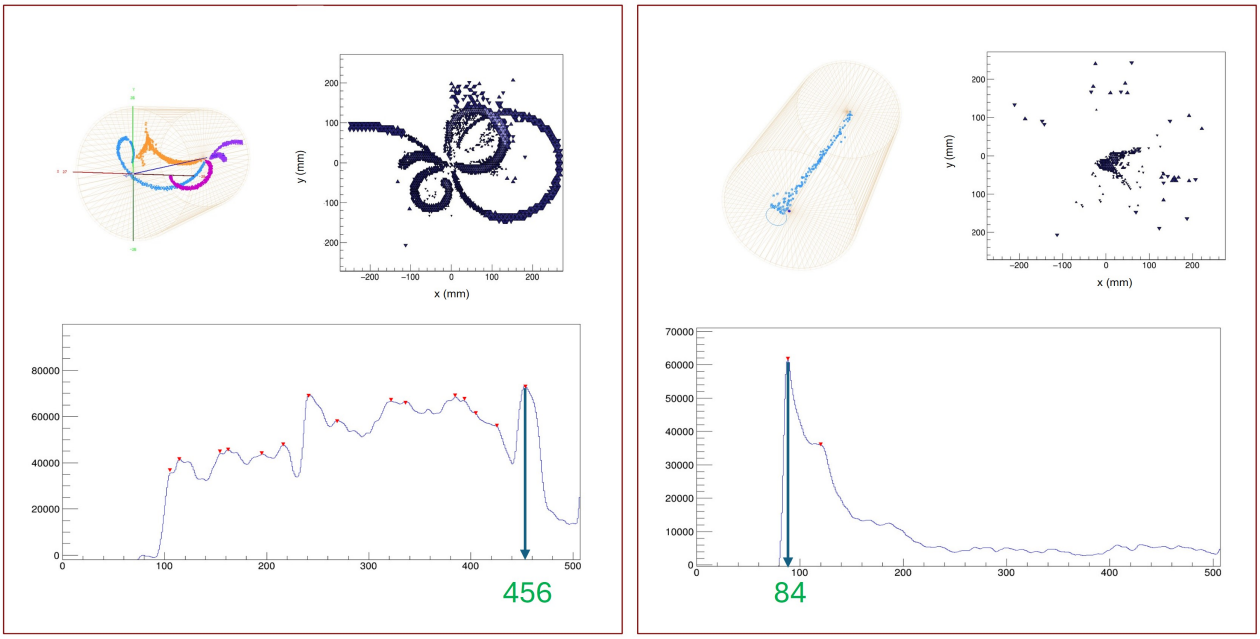

Figure 6.2: Calculation of the temporal width of the TB. In the figure on the left above, you can see a window event; with its temporal representation of the TB, the temporal entry point of the camera can be obtained (figure on the left, below). The figure on the right shows a beam event, where the oxygen travels through the whole chamber without reacting. Thanks to this type of event, the endpoint of the chamber can be obtained (bottom right). With these two points, the time width for calculating the drift velocity is obtained.

6.2 Inverse kinematics

Nuclear inverse kinematics has many applications in nuclear physics research. It can be used to probe the structure of exotic nuclei, study nuclear reactions relevant to astrophysical processes (e.g., nucleosynthesis in stars), and understand the properties of nuclear matter under extreme conditions.

An advantage of nuclear inverse kinematics is that it allows researchers to access excited states of nuclei that are difficult to populate using other techniques. It also provides a way to study the properties of short-lived and rare nuclei, which are of interest in nuclear astrophysics and fundamental nuclear physics research.

In nuclear physics, two main approaches, direct and inverse kinematics, are used to study nuclear reactions. In direct kinematics, a beam of particles (such as protons or electrons) is aimed at a target atomic nuclei, and the scattered particles are detected at different angles. In inverse kinematics, the roles of the target and the particles in the beam are reversed.

In inverse kinematics experiments, a beam of particles (often heavy ions) of known energy and momentum is directed at a detector system. The target nucleus is placed in the path of the scattered particles, typically at a well-defined position within the detector.

As the beam particles scatter off the target nucleus, they change direction and energy. The scattered particles are detected, and their trajectories are measured using sophisticated detector

systems such as particle tracking detectors, silicon detectors or time-of-flight detectors.

By analysing the scattered particle data, researchers can reconstruct various properties of the target nucleus. This includes determining the momentum distribution of the target nucleus, the excitation energy and the angular distribution of the scattered particles.

For example, inverse elastic resonance scattering kinematics principles are used to determine the compound nucleus's excitation energy and momentum conservation is applied to adjustable resonance scattering. In particular, in the scenario where a heavy incoming particle X with energy E interacts with a stationary target (Eq. 6.2).

$$m_X v = (m_X + m_a)\vec{v}_{\text{cm}} \iff \vec{v}_{\text{cm}} = \frac{m_X \vec{v}}{m_X + m_a} \tag{6.2}$$

In this context, $\vec{v}_c m$ represents the velocity of the centre of the mass frame and the compound nucleus. At the same time, $\vec{v}$ corresponds to the velocity of the incoming particle X in the laboratory. It's important to note that the magnitude of $\vec{v}_c m$ is equal to "v", which gives the following relationship:

$$E_{\text{cm}} = \frac{m_X + m_a}{2}(v_{\text{cm}})^2 = \frac{m_X}{m_X + m_a}E \tag{6.3}$$

Using equation 6.2, it is possible to obtain the centre-of-mass energy of the scattered and incident particles as follows.

$$E^{sca}_{\text{cm}} = \frac{m_a}{2}(v_{\text{cm}})^2 = \frac{(m_a \cdot m_X)E}{2(m_X + m_a)^2} \tag{6.4}$$

$$E^{X}_{\text{cm}} = \frac{m_X}{2}(v - v_{\text{cm}})^2 = \frac{(m_X)}{2}\left(\frac{(m_a)v}{(m_X + m_a)}\right)^2 = \left(\frac{(m_a)}{(m_X + m_a)}\right)^2 E \tag{6.5}$$

A sketch of the geometry of the decay of the compound system in the laboratory and centre of mass frames can be seen in Figure 6.3. Again, using $v_c m^a = v_c m$ and the law of cosines on the triangle (ABC), it is obtained:

$$(v^a)^2 = 2(v_{\text{cm}})^2(1 + \cos(\phi_{\text{cm}})) = 2\left(\frac{m_X v}{(m_X + m_a)^2}\right)^2 (1 + \cos(\phi_{\text{cm}})) \tag{6.6}$$

Furthermore, $\phi_{cm} = 2\theta_{lab} \rightarrow 1 + cos(\phi_{cm}) = 2cos^2(\theta_{lab})$, so that the energy of the light scattered particle, a, in the lab frame is given by:

$$E = \frac{E^a(m_X + m_a)^2}{4m_a \cdot m_X cos^2(\theta_{lab})} \tag{6.7}$$

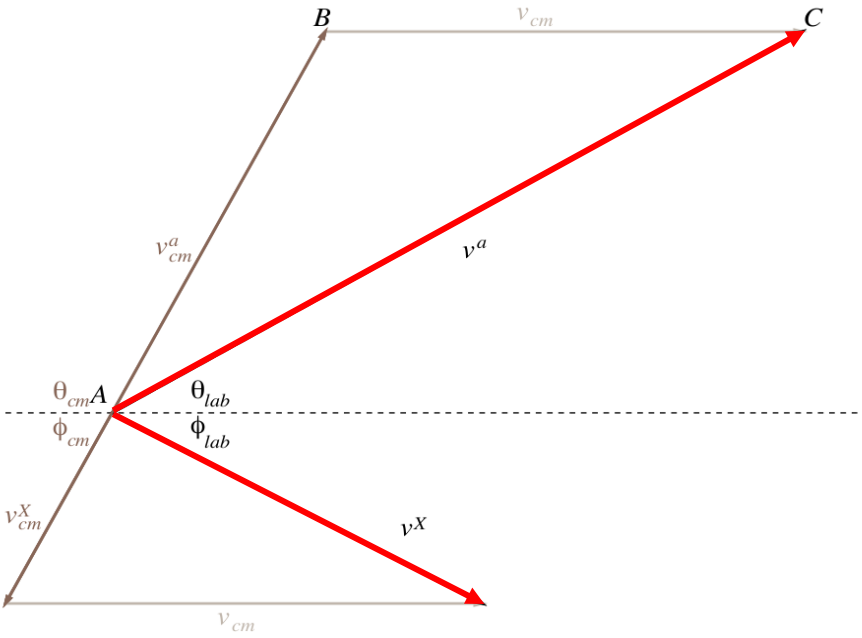

Figure 6.3: Schematic of the decay of the compound nucleus in the laboratory and centre-of-mass frame. Small scattering angles in the laboratory frame correspond to large angles in the centre of mass via $\theta_{cm} = \pi - 2\theta_{lab}$. All angles are concerning the dashed line.

The excitation energies of the decay can be determined simply by knowing the mass, energy, and angle of the light scattering. Compared to conventional direct kinematics scattering, where the light particle acts as a bullet, the reverse kinematics approach offers a significant advantage. In particular, it provides an approximately four times higher energy for the light ejectile in the laboratory when the scattering angle θ_{lab} is close to 0 degrees.

Overall, nuclear inverse kinematics is a valuable tool for probing the internal structure of atomic nuclei and gaining insight into the fundamental forces and particles that govern matter's behaviour at the nuclear level.

6.3 Algorithms for trace reconstruction

6.3.1 Fourier Convolution

The signals collected on the ATTPC pad plane show baseline fluctuations corresponding to the time the beam travels through the chamber, a parasitic load present throughout the experiment. On the other hand, each ADC can pick up noise due to different inconveniences that may occur during the experiment, resulting in a noisier signal that hinders the trace reconstruction process6.4.

The Fourier transform is a powerful mathematical tool for signal filtering. Using the convolution theorem, which states that the Fourier transform of a convolution is the scalar dot-to-dot

product of the transforms, i.e., a convolution in one domain (the time domain) is equivalent to the dot-to-dot product in the other domain (the spectral domain) a noisy signal f can be filtered by applying a convolution with a function of convenience g.

$$\sqrt{2\pi} \cdot \mathscr{F}(f) \cdot \mathscr{F}(g) = \mathscr{F}[f \otimes g] = \frac{\mathscr{F}(f) \otimes \mathscr{F}(g)}{\sqrt{2\pi}} \tag{6.8}$$

This would result in the **convolution theorem**:

$$f \otimes g = \sqrt{2\pi} \cdot \mathscr{F}^{-1}[\mathscr{F}(f) \cdot \mathscr{F}(g)] \tag{6.9}$$

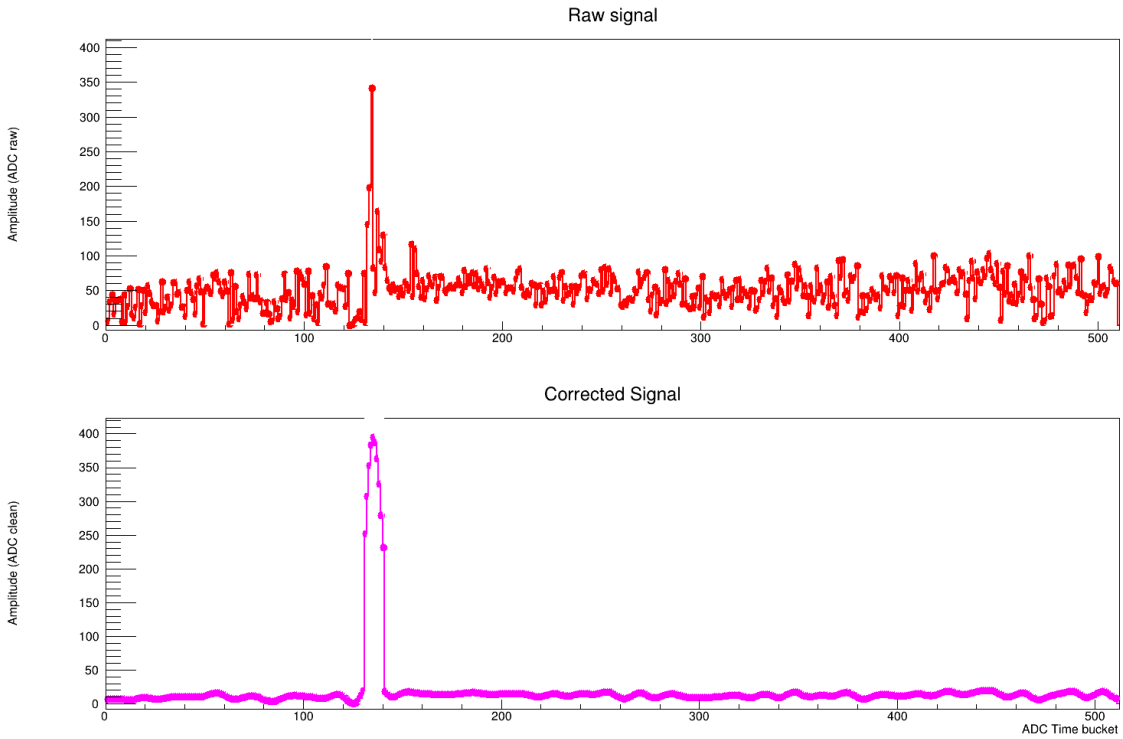

Figure 6.4: Individual representation of a signal from a pad of the pad plane. The figure above shows the signal, which is not very sharp in temporal width, with fluctuating background noise. After applying the Fourier filter (figure below), the signal is much sharper, and the high-frequency noise is flattened, making reconstructing the trace points easier.

To incorporate as a filter function to be convoluted with our ADC time response, the sinc = sin(x)/x function is selected for two reasons. On the one hand, in digital signal processing, the sync filter is an idealised filter that removes all frequencies above a given bandwidth and leaves only the lower frequencies where electronic noise is found in the dual signal space. On the other hand, the ease of use in Fourier space, since the idea is to multiply point to point in that space and the Fourier transform of the sinc function is nothing more than the rectangle function, which is defined as 1 for a given width (trying to remove only the high frequencies of the signal so as not to affect the shape of the pulse) and zero for the rest.

$$sinc(t) = \frac{sin(\pi t)}{\pi t} \rightarrow \mathscr{F}^{-1}(sinc(t)) = rect[\nu] \tag{6.10}$$

Once the temporal signal has been cleaned, the next step in the analysis is to reconstruct the three-dimensional tracks.

As explained above, the components related to the individual activation of the pads in each event are obtained. These tracks pull weakly bound or free electrons out of the target and make them drift to the pad plane, returning each of the positions (x_i, y_i, z_i) used to reconstruct the final trajectory.

The non-activation of pads, zones that are disconnected during the experiment (broken traces), the pileup or reactions close to the edges of the camera, and a meagre threshold selection are some of the reasons that can incorporate noise to the correct identification of the segments belonging to the same trace, which can lead to erroneous identifications, overestimated multiplicities or the impossibility of calculating the range of the particles. All this added to the fact that a magnetic field is incorporated, and the charged particles describe helicoids of revolution, making it necessary to apply identification and adjustment techniques such as those described below.

Three processes are carried out using three big blocks of reconstruction algorithms to identify individual traces on an event-by-event basis and adjust their parameters.

The first is a curve detection algorithm developed by the Institute for Pattern Recognition (iPattern) at the Niederrhein University of Applied Sciences, Krefeld, Germany [68]. Using a series of parameters, the aim is to identify which points in a set of points are part of the same structure. These parameters will account for the level of sensitivity or number of points selected to be part of the same cluster and their subsequent treatment with the consequent algorithms.

On the other hand, the Random Sample Consensus (RANSAC) [69] method is used to clean the noise and first identify the traces, working in parallel to the TripClus algorithm, which allows us to obtain a first approximation of the direct and indirect variables used in the study. Once these variables have been received, an adjustment programme adapted to the needs of ATTPCROOTv2 based on Kalman filtering methods is used to improve the results obtained with RANSAC and to try to join broken traces found on the relative distances between them, radii of curvature and angles.

Finally, GenFit's fitting algorithms are used, particularly a filtering method based on Kalman algorithms.

6.3.2 Algorithm for curve detection in 3D Clouds: Pattern Recognition Analysis

The TriplClust algorithm [68] groups the points into clusters representing curves or noise, where clusters representing curves may overlap at vertices. It consists of the following four steps.

1. Smoothing by position averaging of neighbouring points.
2. Find triplets of points that are approximately collinear.
3. Hierarchical clustering of triplets of points.

4. Pruning by removing small clusters and (optionally) splitting clusters with large gaps between them.

Triplet clusters are then transformed into point clusters by labelling each point with the cluster label of the triplet to which they were assigned. This divides the points of the curve into sets that represent different curves. Points that do not belong to any triplet or are assigned to triplets not belonging to any cluster are labelled as noise. Since a dot can belong to several triplets, the resulting clusters can be superimposed, and some dots can be labelled simultaneously. This means that the final clusters are a combination of the original points.

Parametric curve detection strategies in noisy point clouds typically start by describing curves parametrically. This involves assuming a specific parametric model to define the shape of the curve, often starting with elementary shapes such as straight lines and then identifying parameter values that encapsulate significant point data. This method assumes a priori knowledge of the curve shapes. It requires the implementation of a mechanism for voting on parameter values, which may involve an exhaustive examination of all data points or random sampling.

This method takes a non-parametric approach, eliminating the need for prior assumptions about curve shapes. The problem is reformulated as a clustering task, focusing solely on the objectives of discrimination between points representing noise and those belonging to curves and partitioning the curve points into sets representing different curves outlined above. Consequently, the goal is to divide the point set into an unknown number of potentially overlapping clusters, each representing curves and a separate cluster representing noise.

The algorithm utilised in this study is based on the initial construction of point triplets, which are subsequently grouped into clusters, each representing a track. The notion of triplet aggregation was recently introduced by Lezama et al. for identifying continuations within 2D dot patterns [70].

In this algorithm, several parameters must be carefully selected depending on the type of experiment to be analysed. As presented below, the parameters are interrelated, and a variation in one can cause essential information losses in physics to be analysed.

The parameters and selections made for this experiment are as follows:

Smoothing radius (rsmooth):

To understand the choice of the smoothing radius, we must first introduce the concept of the characteristic distance d_{NN}. The distance between adjacent points within a given curve can be considered a characteristic data length. It measures the points' dispersion around the curve's central axis. The distance to the nearest neighbours is calculated for each point to estimate this point distance.

To avoid information loss in the clusters and to consider that ATTPC has a resolution of 0.2 mm in the centre pads, this parameter shall be chosen to be one so that the algorithm does not leave any loading points unselected. Once this distance is selected, the smooth radius is

defined for this algorithm as twice that distance, so the logical choice to minimise load losses is 2, in this case, as the default value.

Collinear points ($K_{triplet}$):

The second step in the algorithm consists of building groups of three approximately collinear points, i.e. triplets. Let the indices of the points A, B, and C in the point cloud be i, j, and k, that is, $A = \vec{q}_i$, $B = \vec{q}_j$, and $C = \vec{q}_k$. The cosine of the angle α between the triplet branches is given by:

$$\cos(\alpha) = \frac{\langle AB, BC \rangle}{\|AB\| \cdot \|BC\|} = \frac{\langle \vec{q}_j - \vec{q}_i, \vec{q}_k - \vec{q}_j \rangle}{\|\vec{q}_j - \vec{q}_i\| \cdot \|\vec{q}_k - \vec{q}_j\|} \tag{6.11}$$

Each triplet is represented by two vectors, the midpoint $\vec{m}$ and the direction $\vec{e}$ between the outer points (Fig. 6.5).

$$\vec{m} = \frac{1}{3}(\vec{q}_i + \vec{q}_j + \vec{q}_k) \quad \text{and} \quad \vec{e} = \frac{\vec{q}_k - \vec{q}_i}{\|\vec{q}_k - \vec{q}_i\|} \tag{6.12}$$

In this case, a sufficiently high number (24) is selected to form the triplets tested as part of the same cluster within the previously imposed distance. Special care must be taken at this point because as the number of points to be tested increases, the possibility of deviation towards electronic noise areas of a trace increases, which is an essential part of the trace's direction.

Triplet angle threshold ($a_{triplet}$):

The triplet is discarded if the triplet angle α is more significant than a threshold value or if $\cos(\alpha)$ is less than a threshold value.

$$\cos(\alpha) = \frac{\langle AB, BC \rangle}{\|AB\| \cdot \|BC\|} < 1 - a_{triplet} \tag{6.13}$$

A parameter of 0.01 corresponds to an angle of $\alpha = \cos^{-1}(1 - 0.01) \approx 8.11°$. This choice of a slight angle between triplets is made to be able to distinguish as far as possible reactions such as the Hoyle effect or the splitting of a ^8Be into two alphas that are practically parallel and separated by a relatively small distance.

Triplets per point ($n_{triplet}$):

Only the triplets with the smallest angle α or with the highest $\cos(\alpha)$ are retained from the remaining triplets of each centre. Therefore, for n points, the total number of triplets does not exceed $n \cdot n_{triplets}$.

The idea is to choose a low number for this parameter related to $k_{triplet}$. If $n_{triplet} = 2$ is imposed, the shortest trace identified by our method is 48 points. This imposes the minimum

number of points to be considered a trace and avoids the analysis of loose point clouds detected by the pad plane in the form of deposited charge.

Minimum triplets per cluster ($m_{cluster}$):

If the data is almost noise-free, it is possible to set $m_{cluster}$ to two. However, such circumstances are rare. Setting $m_{cluster}$ higher is advisable to manage the noise level effectively.

In this experiment, very long traces are expected, occupying practically the entire chamber. Therefore, considering the previous choices, a tiny selection of this parameter would result in the traces not being entirely detected. In this case, the parameter is set to at least five triplets.

Distance scale factor ($s_{cluster}$):

As in the case of the $k_{triplet}$ parameter, a set of triplets is defined, in this case, 3 A, B and C, each of which will have an angle and a direction associated with it (depending on the weight of each triplet) as shown in the figure 6.5.

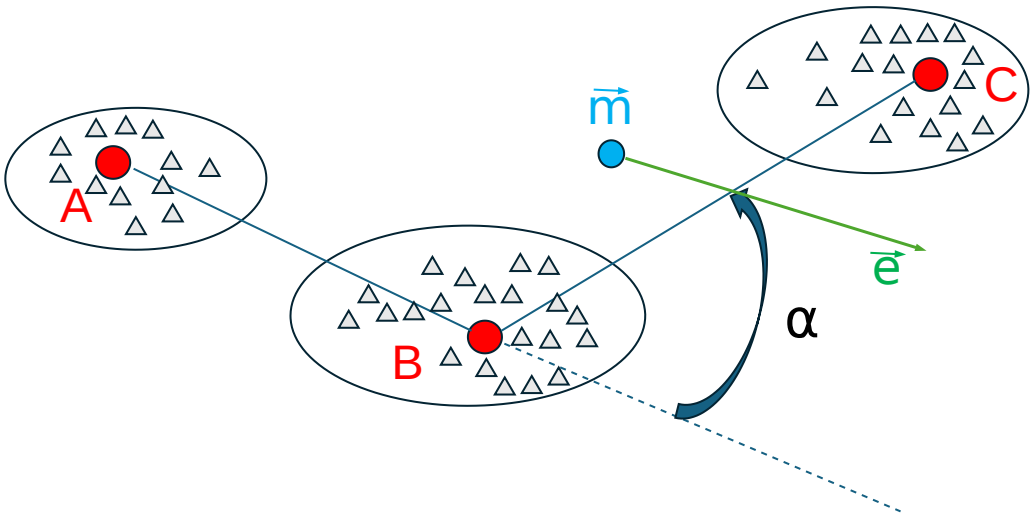

Figure 6.5: Triplet of point clouds. The red dots represent the charge accumulation nodes in triplets A, B, C and alpha, the angle described in equation 6.12. m is the midpoint, and e is the direction of the clusters considering the triplet weights.

If two triplets of point clouds are assumed, the conditions that are imposed for them to be similar are:

In the first instance, the perpendicular distances between the midpoints $\vec{m}_{i,j}$ and the extrapolated lines formed with the directional vectors $\vec{m}_{j,i} + \vec{e_{j,i}}$ must be small 6.14.

$$d_{i,j}^{\perp} = \|\vec{m}_{j,i} - \vec{m}_{i,j} + \langle \vec{m}_{i,j} - \vec{m}_{j,i}, e_{j,i} \rangle \cdot e_{j,i}\| \tag{6.14}$$

Conversely, the angular Φ, which comprises their directional vectors, must also be small (Eq. 6.15).

$$\Phi = \cos^{-1}(|\langle \vec{e}_i, \vec{e}_j \rangle|) \tag{6.15}$$

The combination of equations 1 and 2 gives the total distance that is required for two subsets of points to be on the same track (Eq. 6.16):

$$d((A_i, B_i, C_i), (A_j, B_j, C_j)) = \frac{\max\{d_1^{\perp}, d_2^{\perp}\}}{\mathbf{s_{cluster}}} + |\tan(\phi)|. \tag{6.16}$$

The relative effect of angle and perpendicular distance can be controlled using the scale factor $s_cluster$, which is 0.3 for this clustering.

Clustering threshold ($t_{cluster}$):

The specific values of the triplet distances given in equation 6.16 determine the choice of the cut-off threshold ($t_{cluster}$) for the clustering process. Consequently, $t_{cluster}$ may need to be adjusted when adjusting $s_{cluster}$. The implementation includes an option to display the resulting threshold. Starting from the value determined by the automatic stopping criterion, alternative values for $t_{cluster}$ can be experimented with if this results in too many or too few clusters. In the experimental investigation, it was found that a value of $s_{cluster} = \frac{d_{NN}}{3}$ roughly corresponds to values of $t_{cluster}$ between 2 and 3.5. For this clustering, a value of 2.8 is set for this factor.

An essential aspect of hierarchical clustering is determining when to stop the agglomeration process. The algorithm of Pattern Recognition Analysis uses a simple stopping criterion: a constant threshold ($t_{cluster}$) on the distance (c_{dist}) for merging two clusters. This method is effective when the range of acceptable distances remains constant, such as when choosing the scale factor ($s_{cluster}$) to make the distance measure approximately scale invariant.

6.3.3 RANSAC

The algorithm RANSAC, first published by Fischler and Bolles in 1981 [69], is the first step in identifying traces belonging to the same particle and separating them from the noise.

The Random Sample Consensus algorithm consists of an iterative method in which the aim is to obtain a parametric mathematical model that describes a given function, in our case, a two-dimensional circumference, which is the projection of the traces on the pad plane, and to separate them from other particles that do not belong to the same particle and from the noise.

The algorithm is considered to converge when it reaches a minimum number of points to be considered a trace, and the error is less than an acceptable threshold.

The general idea is to select a random subset of data within the data sample where our curved trace consisting of points called "inliers" surrounded by noise called "outliers" is located. This subset will be analysed to see if it fits the proposed model within a predetermined uncertainty, and each point is considered to fall within the inliers or an outlier. This process is repeated iteratively until a previously imposed minimum tolerance is reached to assume that a trace has been found. The event is discarded as empty if this tolerance is not achieved (Fig. 6.6).

To represent the information flow of the RANSAC method, a pseudo-code program is presented in Appendix C.

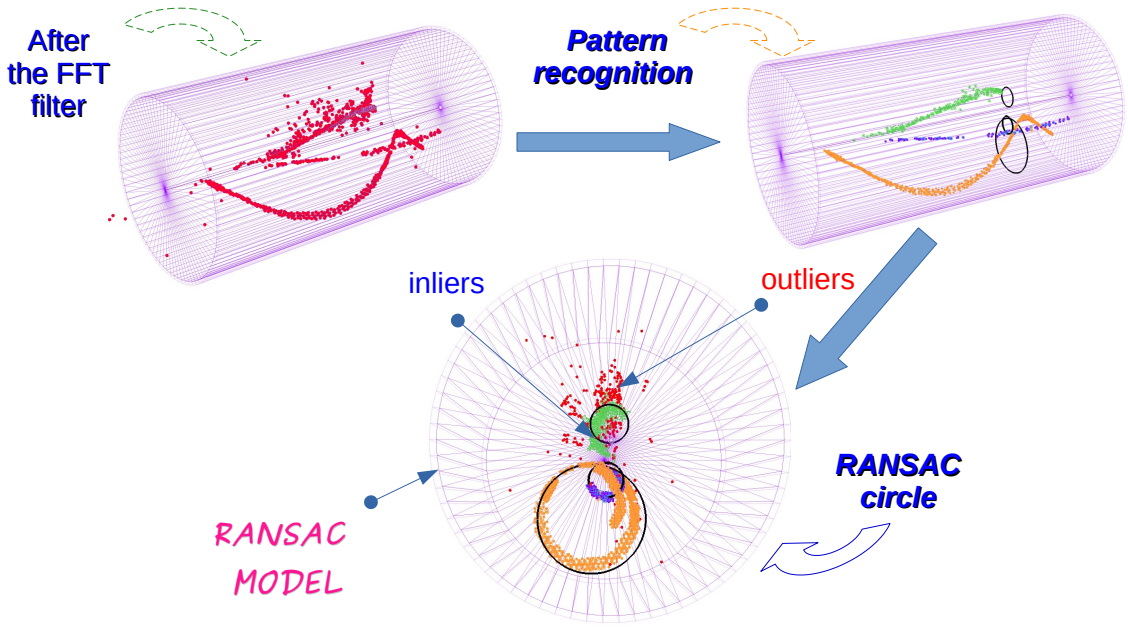

Figure 6.6: Information flow diagram for obtaining the radii of curvature and angles of each event. The figure shows an inelastic event of $^{16}O + \alpha \rightarrow^{12} C + 2\alpha$. In the first part, a first filtering of the raw data is performed with a convolution using FFT. Then, the pattern recognition analysis is performed to obtain the variables of interest. In the last step, you can see a representation of the 2D circumference obtained with RANSAC and then adjusted with the Kalman filter.

In the experiment, for each event identified, an analysis is performed to determine the traces, all the enabled pads are taken from each one, and the iterative algorithm shown below is applied. Three random pads are selected and checked to see if they fit a proposed model, in my case, a two-dimensional circle. Once these 3 points are found to fit a circle, the rest are checked individually to see if they fit within a certain tolerance to that model. Those that fit are considered valid or "inliers", and the others are discarded as "outliers". Using the points selected as good, the circumference model is reformulated to start the process again iteratively up to a previously fixed number of times.

Once the correct traces for pattern recognition have been determined for each event, two

specific two-dimensional RANSAC models are used to calculate each trace's radius of curvature (RANSAC kCircle2D) and the angles theta and phi (RANSAC kline).

In both cases, only the initial part of the trace (10%) is used, which is more than enough to determine the radius of curvature and the reaction vertex. For these two, the initial points are adjusted to a circumference by imposing a threshold in the method that is not too high (7 mm for the radius) so as not to lose the low energy helios that come out close to 90^{o} in the laboratory system. The reference system is transformed in the case of the angles as input for the linear RANSAC.

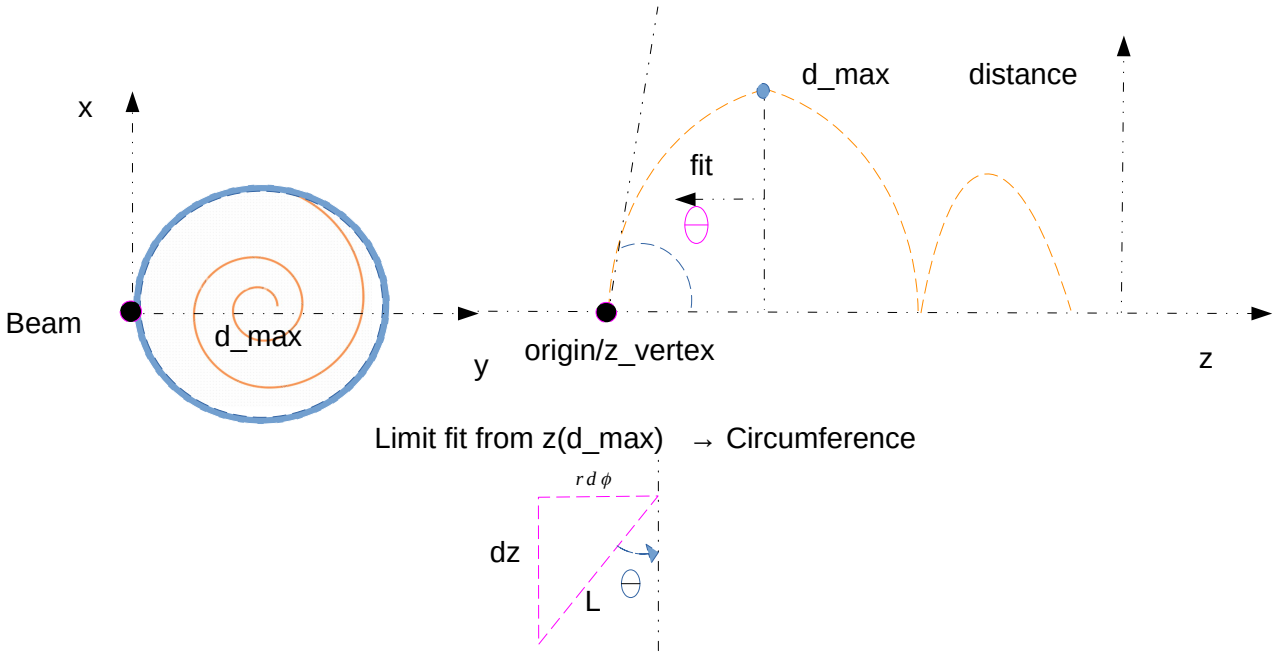

Figure 6.7: Obtaining the scattering angle of a particle describing a downward spiral path. From the maximum arc length, the maximum distance it will travel in the XY plane perpendicular to the trajectory can be obtained. Once this distance has been obtained and a coordinate transformation has been carried out to represent the distance travelled Z versus the arc length, the angle *theta* can be obtained from the trigonometric relations shown in the figure below.

To separate the traces, they are clustered into groups by imposing a minimum number of points to be considered a cluster and a minimum distance between clusters to be considered part of the same trace. Once the paths have been identified, the angles, reaction radii, and vertices for pattern recognition are calculated using the RANSAC algorithms for circles and lines.

As shown in the figure 6.7, the start of the two-dimensional spiral in XY can be set to a circle of diameter d=$\sqrt{x^2+y^2}$=2r if the arc length of the spiral is plotted against the z-coordinate, in the limit where z tends to the point of maximum arc length, we have:

$$dz = lcos\theta \quad \text{and} \quad rd\varphi = lsin\theta \tag{6.17}$$

By dividing the two equations, we can obtain the azimuthal angle, dependent on theta:

$$\varphi = \frac{z}{r}\frac{sin(\theta)}{cos(\theta)} \tag{6.18}$$

The angle theta of the outgoing reaction particle is obtained directly by plotting the z-component versus the arc length.

$$\theta_{lab} = acos(\frac{z}{arclength}) \tag{6.19}$$

A RANSAC-based algorithm calculates the radius of curvature and the vertex to recognise circles from the pads previously determined as valid. All these variables are used in the subsequent adjustment to determine the kinematics best.

6.4 Diffusion and Covariance matrix

As will be shown in the following sections, one of the most critical points in the trace reconstruction is the calculation of the covariance matrix, both in the pattern recognition analysis and in its subsequent implementation in the fitting step with GenFit, since a rebuilding of the reaction vertex is performed by chi^2, which will be critical in the reconstruction of the physics by inverse kinematics.

One of the algorithms currently used for tracking is the RANSAC transform. A bivariate normal distribution based on the covariance matrix computed from the diffusion effect improves inlier collection directly in the RANSAC model.

The Lorentz forces act on particles with charge q and velocity $\vec{v}$ in the presence of external electric $vecE$ and magnetic fields $\vec{B}$ (Eq. 6.20).

$$\vec{F} = q(\vec{E} + \vec{v} \times \vec{B}) - \gamma\vec{v} \tag{6.20}$$

The extended version with the term -$\gamma\vec{v}$ is called the friction force [71]. Collisions between the drifting electrons and the gas molecules cause this effective friction. The friction constant γ is related to the mass m and τ, the average time between the collisions, by $\gamma = m/\tau$. For long periods, it is possible to assume that F$\simeq$0. The velocity can now be the result of the equation:

$$\vec{v} = |\vec{E}|\mu\left(\hat{E} + (\hat{E} \times \hat{B})\omega\tau + (\hat{E} \cdot \hat{B})\hat{B}\omega^2\tau^2\right)\frac{1}{1+\omega^2\tau^2} \tag{6.21}$$

Where $\mu = \frac{q\tau}{m}$ is the mobility and $\omega = \frac{qB}{m}$ is the cyclotron frequency. Assuming that $\vec{E}$ is parallel to $\vec{B}$, equation 6.21 can be rewritten more simply as:

$$\vec{v} = \mu \cdot \vec{E} \tag{6.22}$$

The cross-sectional area determines the mobility via the relationship $\mu \propto \frac{1}{\sigma}$. For electrons, the cross-section is influenced by the electric field, so it is difficult to establish a simple relationship between velocity and electric field. In contrast, the ion velocity is directly proportional to the electric field because its cross-section remains relatively constant over a wide energy range. In both cases, this velocity is referred to as the drift velocity and is denoted as v_{drift}.

The electrons resulting from ionisation diffuse due to random collisions with gas molecules, which means that the electron's microscopic speed isn't constant. The spread of an electron cloud after a time t_0 can be characterised by a Gaussian distribution [72], assuming that the electron cloud starts at a single point at the origin of the coordinate system and that the random diffusion effect is uniform in all three spatial directions.

$$n = \frac{1}{\sqrt{4\pi\vec{D_L}t}} \cdot (\frac{1}{\sqrt{4\pi\vec{D_T}t}})^2 \cdot \exp\left(-\frac{x^2+y^2}{4\vec{D_T}t} - \frac{(z-v_dt)^2}{4\vec{D_L}t}\right) \tag{6.23}$$

This expression represents the spatial distribution of a quantity n, where D_L and D_T are diffusion coefficients, v_d is a velocity, and t is time. When an electric field is applied to induce drift, the diffusion behaviour along the direction of the electric field (the Z direction) is different from the diffusion behaviour in the perpendicular directions (the X and Y directions). There are, therefore, two different diffusion factors: one for the X and Y directions (D_T) and another for the Z direction (D_L). The following equations, therefore, give the width of the electron cloud at the time t:

For the transverse direction:

$$\sigma_T = \sqrt{2D_Tt} \tag{6.24}$$

For the longitudinal direction:

$$\sigma_L = \sqrt{2D_Lt} \tag{6.25}$$

Where σ_T and σ_L are the transverse and longitudinal resolution respectively, to eliminate the dependence on time, the diffusion constants are defined as $D_T = \sqrt{\frac{2\vec{D_T}}{v_d}}$ and $D_L = \sqrt{\frac{2\vec{D_L}}{v_d}}$ for both diffusion coefficients. The diffusion constants will also depend on the gas mixture used in the TPC.

6.4.1 Transverse spatial resolution as a function of drifting distance

It is possible that a charged deposit may not be fully detected on the pad and may extend beyond its boundaries. Consequently, the centre of a detected cluster may not precisely coincide with the xy coordinates of the primary ionisation event. It is, therefore, imperative to ensure that only fully enclosed clusters are considered for data analysis.

Charge deposits where the centre of gravity is closer to the chip edge than the most likely cluster radius are excluded from further analysis. This criterion ensures that only accurately reconstructed primary electrons are included in the reconstruction of the primary particle tracks. The pattern of the top GEM also reveals a periodic structure.

Suppose the xy projection of a particle track aligns closely with one of the chip edges. In that case, there's a chance that some of the primary electrons associated with that track won't be detected on the chip due to transverse diffusion. As a result, not only will the wrong number of charge depositions be associated with that track, but the entire track will be reconstructed with inaccurate parameters.

The recorded tracks are predominantly parallel to the x-axis of the readout chip. To ensure that virtually all primary electrons of a track are detected and the track is accurately reconstructed, tracks closer than 4σ of the maximally expected transverse diffusion to the top or bottom edge of the readout chip are discarded.

The sum of two components, one due to the detector's geometry and the other due to the diffusion constants, provides a good approximation of the transverse resolution.

$$\sigma_T = \sqrt{\sigma_{xy,0}^2 + D_T^2 z_{drift}} \tag{6.26}$$

The standard deviation of a uniform distribution depends on the range of the distribution. For a continuous uniform distribution on the interval [a, b], the standard deviation (σ) can be calculated using the formula

$$\sigma_{xy,0} = \frac{b-a}{\sqrt{12}} \tag{6.27}$$

Where a is the lower limit of the interval and b is the upper limit of the interval. The detector has 0.2 mm of position resolution, which imposes a geometrical resolution of $\sigma_{xy,0} = \frac{0.02}{\sqrt{12}}\ cm$.

6.4.2 Longitudinal spatial resolution as a function of drifting distance

The longitudinal single-point resolution of the pixel TPC is determined both by its intrinsic resolution and by the contribution of the diffusion of electrons during drift, which serves as the transverse single-point resolution.

$$\sigma_L = \sqrt{\sigma_{z,0}^2 + D_L^2 z_{drift}} \tag{6.28}$$

The intrinsic resolution of the detector in the longitudinal direction is limited by the precision of the Time of Arrival (ToA) measured. The ToA mode allows determining the time of detection of a hit. The ToA is calculated with the activation of the pad:

$$ToA = t_{shuter} - \frac{n}{f_{clock}} \tag{6.29}$$

Where $t_{shutter}$ is the length of the trigger signal, n is the number of clock cycles counted, and f_{clock} is the clock frequency.

The precision of the ToA measured, neglecting secondary effects, can be expressed as follows:

$$\delta(ToA) = \sqrt{\delta(t_{shutter})^2 + \delta(\frac{n}{f_{clock}})^2} = \sqrt{\frac{2T_{clock}^2}{12}} \tag{6.30}$$

with the clock period $T_{clock} = \frac{1}{f_{clock}} = 0.320\ \mu s$. Taking into account the drifting velocity ($v_{Drift} = 0.86\frac{cm}{\mu s}$), the intrinsic detector resolution in the drifting direction is thus:

$$\sigma_{z,0} = \frac{T_{clock} v_{Drift}}{\sqrt{6}} \simeq\ 0,112\ cm \tag{6.31}$$

The frequency of the readout system is a contribution to the longitudinal resolution. Here $f_{clock} = 3.125$MHz. In that case, the transverse and longitudinal resolutions have the final form:

$$\sigma_L = \sqrt{\frac{1}{6}(\frac{v_d}{f_{clock}})^2 + z_{Drift} D_L^2} \tag{6.32}$$

6.4.3 Covariance matrix

Standard TPC readout systems combine a micro-pattern gas detector with a pixellated readout. Due to the small size of the pixels, only a single electron is detected in a readout channel.

Consequently, there is no correlation between X and Y coordinates. In this base, the non-diagonal elements of the shade are zero. As a result, the covariance matrix is a 3 x 3 diagonal matrix based on transverse and longitudinal diffusion [73].

$$cov = \begin{pmatrix} \sigma_T^2 & 0 & 0 \\ 0 & \sigma_T^2 & 0 \\ 0 & 0 & \sigma_L^2 \end{pmatrix} \tag{6.33}$$

In the ideal case, when a fixed size of binning is used for dual space, and the charge cloud's width is small, all hits' lines pass through one bin.

For this thesis, as long as the X and Y coordinates and the time, i.e., the Z coordinate, are calculated for three degrees of freedom, this criterion will be applied to estimate the diffusions and consequently for the covariance matrix.

In the experiment, we only have 3 degrees of freedom. Still, in the case of the Genfit adjustment, as will be explained below, 6 degrees of freedom are requested (adding the moments). This means that this way of calculating the errors and covariance matrix, which is valid for the PRA, is not valid for the final adjustment since, with this method, a change of base is being made that cannot be extrapolated to the calculation of the GenFit covariance matrix with a 6x6 matrix.

6.5 Kalman Filter

The Kalman filter is implemented inside GENFIT, an open-source, extensible toolkit for trace fitting that combines appropriate algorithms, trace representations, and impact geometries in a modular framework. It is suitable for various experiments, as it works independently of the specific event topology, the detector configuration or the magnetic field arrangement.

It is written entirely in C++ and makes extensive use of object-oriented design. It uses the standard C++ template library and the ROOT data analysis framework. GENFIT has been developed in the framework of the PANDA experiment at FAIR - Facility for Antiproton and Ion Research (Darmstadt, Germany), by J. Rauch and T. Schluter, is now distributed as a stand-alone package. Several experiments have adopted it.

This software package also handles track models with different propagation mechanisms and track parameterisations. This flexibility is advantageous in the early stages of an experiment when other track reconstruction methods can be compared and the best method selected.

Kalman filtering is an efficient recursive method for finding the best estimate of a dynamic system's state from noisy measurements.

The physical model must be able to take the state vectors and generate an estimate of the new state vectors at the next instant. For AT-TPC, a suitable model might include the Lorentz force and a contribution to account for gas-stopping power. The state vector represents the system's state at a given time, consisting of components such as a particle's position and momentum. A Kalman filter models a system using state vectors and a physical model.

The Kalman filter fits each point individually. It only iterates through the data set once. Every iteration uses the model to predict the new state vector based on the previous iteration's state. The measured data point is then averaged with this predicted state vector to adjust it.

The algorithm works in two steps: the prediction step and the update step. A five-dimensional column vector describes a charged particle's state vector (or track parameter) in a

magnetic field bound to a surface (detector layer), thus wholly specifying five parameters. A step in the algorithm is defined as incorporating the measurement information of a further hit k into a state vector that already contains the knowledge of all the matches up to k-1. The state vector at the measurement location of hit k-1 is given before the filtering step.

In the predicting step, the Kalman filter produces estimates of the current state variables, along with their uncertainties (covariance matrix) [74]. In the prediction step, the estimated track parameter $x_{k-1|k-1}$ vector is propagated from the detector layer x_{k-1} to the next layer containing a measurement.

$$x_{k|k-1} = f_{k-1|k-1}(x_{k-1|k-1}) \tag{6.34}$$

Where $f_{k|k-1}$ is the trace propagation from surface (k-1) to surface k and the corresponding covariance matrix

$$C_{k|k-1} = F_{k|k-1} C_{k-1|k-1} F^T_{k|k-1} + Q_k \quad \text{with} \quad F_{k|k-1} = \frac{\partial x_k}{\partial x_{k-1}} \tag{6.35}$$

Being F_{k-1} is the Jacobian matrix of propagation from (k-1) to k, and Q_k is a noise matrix that accounts for effects such as multiple scattering and energy leakage energy loss.

In the update step, these estimates are updated using a weighted average between prediction and measurement via χ^2 minimisation, with higher certainty estimates given more weight. The main difference from the simple χ^2 fitting is that the track parameters are updated when new measurement points are included. Because of this, we can take into account the evolution of the track parameters step-by-step while still accounting for the multiple Coulomb scattering and the energy loss through the matter. The algorithm updates the state vector and the covariance matrix so that the track is closer to the actual hit than the predicted track.

The Kalman filter fits n $\geqslant$ 2 tracks to a common vertex geometrically. The virtual measurements are the fitted track parameters, n, which are conveniently extrapolated inwards and assumed to be uncorrelated; hence, the global covariance matrix is (6×6) block diagonal. The goal is to estimate a "state vector" consisting of the vertex position and the moments of all tracks at the vertex.

6.5.1 Helix Track Parameters

Due to the magnetic field, the charged particles are bent into a helical trajectory. An initial estimation of the parameters defining the circle resulting from the projection of the helix onto the transverse plane begins the process of linearised helix fitting. The path lengths to the intersections between the fitted circle and the detector elements can be derived from the circle parameters in configurations using a barrel-type detector system with extremely accurate radial position measurements. In Riemann fitting, these path lengths can be derived directly from the parameters characterising the fitted plane.

The tracking detector layout is assumed to be approximately rotationally symmetric about the z-axis, although not necessarily mirror symmetric about the origin at z = 0. The coordinate

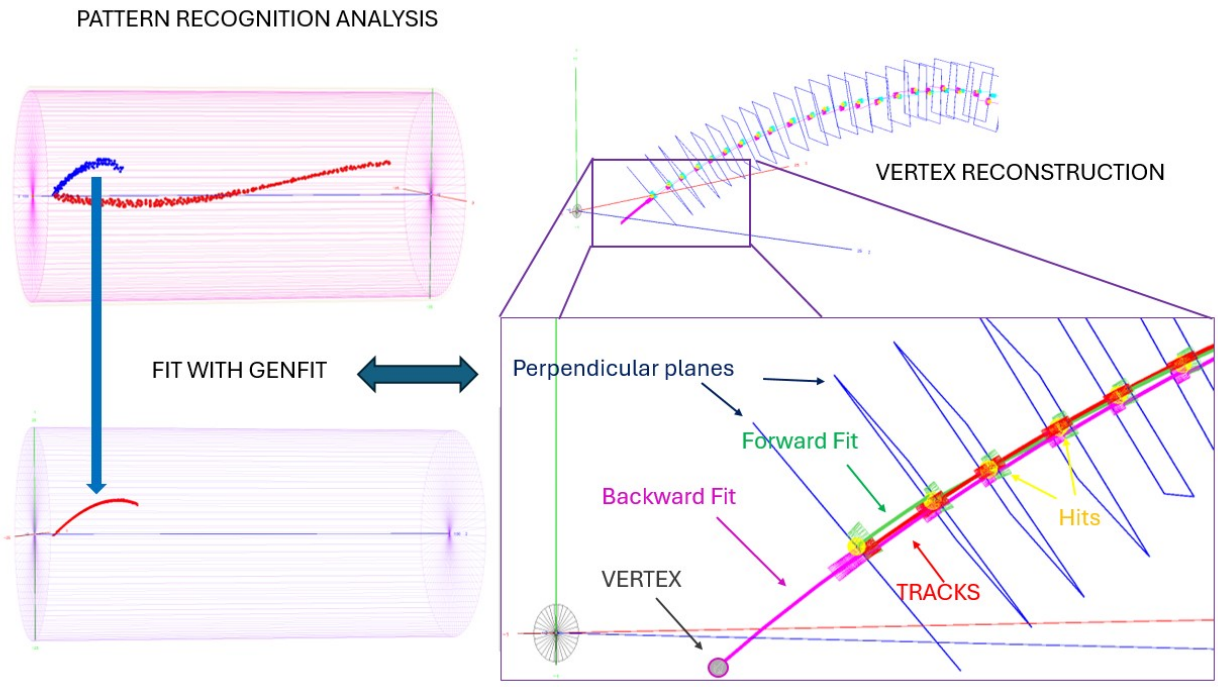

Figure 6.8: Helical trace fitted through the Kalman filter provided by Genfit. It can be seen in the figure how the collection of hits that form a trace are fitted through planes perpendicular to the direction of motion of the particle. After the pattern recognition, an adjustment is made with the help of the Genfit programme. This takes into account the individual adjustments of each hit (spatial reconstructed point) forwards and backwards in each step to build the traces that will form the curve that the particle makes from the end of the path to the vertex, which will be calculated with a certain tolerance around the z-axis.

axes (x, y, z) form a right-handed orthogonal base, with the x-axis conventionally referred to as horizontal and the y-axis oriented to point upwards.

Surfaces in this scenario are classified as cylinders with a radius denoted by R or planes that can be normal to the z-axis, parallel to the z-axis, or tilted to the z-axis. These planes can appear as tangible structures or as conceptual entities. Cartesian, cylindrical, and spherical polar coordinates are defined for spatial points and moments within the space under consideration.

The method works in Cartesian coordinates that have a well-known change of base to cylindrical coordinates (eq. 6.36); $[x, y, z]_{cartesian} = [R, \phi, z]_{cylindrical}$.

$$x = R \cdot \cos(\phi); \quad y = R \cdot \sin(\phi) \quad and \quad z = z \tag{6.36}$$

With a radius R and an azimuth angle ϕ:

$$\begin{aligned} R &= \sqrt{x^2 + y^2} \\ \Phi &= \arctan\left(\frac{y}{x}\right), \quad 0 \leq \Phi < 2\pi \end{aligned} \tag{6.37}$$

For the Momenta, the Cartesian coordinates are also selected in the model, taking into account that: $[p_x, p_y, p_z]_{cart} = [P, \theta, \phi]_{sph} = [p_T, \phi, p_z]_{cyl}$, with:

$$\begin{aligned} p_x &= |\vec{P}| \cdot sin\theta \cdot cos\phi \\ p_y &= |\vec{P}| \cdot sin\theta \cdot sin\phi \\ p_z &= |\vec{P}| \cdot cos\phi \end{aligned} \tag{6.38}$$

The internal track parameters of a fitter are often defined as follows:

$$[x, y, z, p_x, p_y, p_z] \tag{6.39}$$

With the corresponding 6 × 6 covariance matrix according to the method developed for Waltenberger (RAVE = "Reconstruction (of vertices) in Abstract, Versatile Environments") [75] and used in this thesis.

6.5.2 Track Fitting Algorithm

Clustering techniques can be used to combine the responses of individual electronic channels to improve the accuracy of the position measurements in this detector. The positional measurements are called hits, whether from a single detector channel or combining several. Pattern recognition algorithms determine which hits contribute to each particle track. Each hit identified at this stage as belonging to a track is then used as input to a fitting procedure that determines the best estimates of a particle's position and momentum at each point along its path.

The extended Kalman filter is a recursive algorithm that effectively determines the optimal estimator $\hat{\vec{x}_k}$ for the unknown actual state vector $\hat{\vec{x}_k}$ of a system based on a sequence of noisy measurements. It also computes the covariance matrix C_k of $\vec{x_k}$. The state vector includes the track parameters, while the index k indicates that the state vector and its covariance matrix are provided at the k hit detector plane.

The state vector $\vec{x_{k-1}}$ and the covariance matrix C_{k-1} contain information about all hits up to index k - 1 before proceeding to a recursion step. These are extrapolated to the detector plane of hit k using the track following code during the prediction step [74]. The predicted state vector is denoted by $\tilde{\vec{x_k}}$, and C_k denotes the predicted covariance matrix. This covariance matrix is obtained by combining the propagated track covariance matrix C_{k-1} (resulting from Gaussian error propagation via transformation with the Jacobian of the propagation operation $\tilde{\vec{x_k}} = f(\vec{x_{k-1}})$ with a noise matrix that accounts for effects such as multiple scattering and energy loss straggling. The algorithm calculates the update for both the state vector and the covariance matrix, taking into account the measurement $\vec{m_k}$:

$$\begin{aligned} \tilde{x}_k &= \tilde{x}_k + K_k \tilde{r}_k \\ C_k &= (I - K_k H_k)\widetilde{C}_k \end{aligned} \tag{6.40}$$

With the residual $\tilde{r}_k$ and the weight of the residual K_k (or Kalman gain):

$$\begin{aligned} \tilde{\vec{r}}_k &= m_k - H_k \tilde{\vec{x}}_k, \\ K_k &= \widetilde{C}_k H_k^T (H_k \widetilde{C}_k H_k^T + V_k)^{-1} \end{aligned} \tag{6.41}$$

and the covariance matrix V_k of the quantity m_k. I is the unit matrix of the respective dimensionality. The projection matrix H_k is a linear transformation from the coordinate system of the state vector $\vec{x}_k$ to the coordinate system of the position measure m_k of hit k, that is the detector plane of the hit.

The elements of the covariance matrix C_k decrease as more hits are included, reducing the impact of a single hit on the value of the state vector. The χ^2 contribution of hit k is $\chi_k^2 = \vec{r}_k^T (V_k - H_k C_k H_k^T)^{-1} \vec{r}_k$ with filtered $\vec{r}_k = m_k - H_k \vec{x}_k$. It adds $dim(\vec{m}_k)$ degrees of freedom to the whole χ^2.

6.5.3 Vertex Reconstruction with χ^2 Fit

A reconstruction hit is an object that represents a position measurement from a detector used in a track fit. It contains the vector of the measurement's raw coordinates and the corresponding covariance matrix. To understand the method of vertex reconstruction, the iterative adjustment using the Kalman filter method will be explained step by step in the following.

AT-TPC outputs its measurements in 3D Cartesian coordinates, x,y, and z. These measurements are represented as a three-by-one-column vector, z. AT-TPC also provides the associated variance-covariance matrix for these measurements, cov. The subscript m denotes the measurement parameters.

$$\begin{pmatrix} x_{m_k} \\ y_{m_k} \\ z_{m_k} \end{pmatrix}; \quad cov = \begin{pmatrix} \sigma_{x_m}^2 & \sigma_{x_m}\sigma_{y_m} & \sigma_{x_m}\sigma_{z_m} \\ \sigma_{y_m}\sigma_{x_m} & \sigma_{y_m}^2 & \sigma_{y_m}\sigma_{z_m} \\ \sigma_{z_m}\sigma_{x_m} & \sigma_{z_m}\sigma_{y_m} & \sigma_{z_m}^2 \end{pmatrix} = \begin{pmatrix} \sigma_T^2 & 0 & 0 \\ 0 & \sigma_T^2 & 0 \\ 0 & 0 & \sigma_L^2 \end{pmatrix} \tag{6.42}$$

The Kalman Filter estimates the object's position and velocity based on the ATTPC measurements. The estimate is represented by a six-by-one-column vector, and its associated variance-covariance matrix is represented by a six-by-6 matrix.

$$\begin{pmatrix} x_{m_k} \\ y_{m_k} \\ z_{m_k} \\ px_{m_k} \\ py_{m_k} \\ pz_{m_k} \end{pmatrix}; \quad COV = \begin{pmatrix} \sigma^2_{x_m} & \sigma_{x_m}\sigma_{y_m} & \sigma_{x_m}\sigma_{z_m} & \sigma_{x_m}\sigma_{px_m} & \sigma_{py_m}\sigma_{y_m} & \sigma_{x_m}\sigma_{pz_m} \\ \sigma_{y_m}\sigma_{x_m} & \sigma^2_{y_m} & \sigma_{y_m}\sigma_{z_m} & \sigma_{y_m}\sigma_{px_m} & \sigma_{y_m}\sigma_{py_m} & \sigma_{y_m}\sigma_{pz_m} \\ \sigma_{z_m}\sigma_{x_m} & \sigma_{z_m}\sigma_{y_m} & \sigma^2_{z_m} & \sigma_{z_m}\sigma_{px_m} & \sigma_{z_m}\sigma_{py_m} & \sigma_{z_m}\sigma_{pz_m} \\ \sigma_{px_m}\sigma_{x_m} & \sigma_{px_m}\sigma_{y_m} & \sigma_{px_m}\sigma_{z_m} & \sigma^2_{px_m} & \sigma_{px_m}\sigma_{py_m} & \sigma_{px_m}\sigma_{pz_m} \\ \sigma_{py_m}\sigma_{x_m} & \sigma_{py_m}\sigma_{y_m} & \sigma_{py_m}\sigma_{z_m} & \sigma_{py_m}\sigma_{px_m} & \sigma^2_{py_m} & \sigma_{py_m}\sigma_{pz_m} \\ \sigma_{pz_m}\sigma_{x_m} & \sigma_{pz_m}\sigma_{y_m} & \sigma_{pz_m}\sigma_{z_m} & \sigma_{pz_m}\sigma_{px_m} & \sigma_{pz_m}\sigma_{py_m} & \sigma^2_{pz_m} \end{pmatrix} \tag{6.43}$$

Where x_i, y_i, and z_i are the spatial coordinates, px_i, py_i, and pz_i are the moments associated with the coordinates, and $sigma_i$ are the covariance matrix elements related to this metric.

The properties of the covariance matrix are used to calculate the matrix elements associated with the moments. It must be symmetric so that the upper elements of the triangle are equal to the lower elements of the triangle. The sample variance (Eq. 6.44) can be used for the diagonal elements, and the sample covariance (Eq. 6.45) can be used for the non-diagonal elements:

$$var(x) = \frac{\Sigma_1^m (x_i - \bar{x})^2}{m-1} = \sigma^2_{x_m} \tag{6.44}$$

$$cov(x,y) = \frac{\Sigma_1^m (x_i - \bar{x})(y_i - \bar{y})}{m-1} = \sigma_x \cdot \sigma_y \tag{6.45}$$

At this point, a problem arises because the only direct observables are the spatial coordinates. The programme needs to obtain a covariance matrix for the moments that are not too far away from the final, post-iterative solutions.

To solve this problem, the results of the moments, radii, and angles obtained from the pattern recognition analysis are used to approximate the means of these indirect observables. Once these averages have been established, an attempt is made to find a range of variation for the moments by relying on the positions' variation.

$$\begin{aligned} \sigma_{px} &= (B \cdot \sqrt{x_i^2 + \bar{y}^2} \cdot Z \cdot (2.99792458/10.0) \cdot cos(\phi)) - \bar{p}_x \\ \sigma_{py} &= (B \cdot \sqrt{y_i^2 + \bar{x}^2} \cdot Z \cdot (2.99792458/10.0) \cdot sen(\phi)) - \bar{p}_y \\ \sigma_{pz} &= (B \cdot \rho \cdot Z \cdot (2.99792458/10.0) \cdot \frac{cos(\theta)}{sin(\theta)}) - \bar{p}_z \end{aligned} \tag{6.46}$$

Where B is the magnetic field, and Z is the particle's charge. An important issue here is the agreement of the units. GenFit is set up to work in cm for the coordinates and in Tm for the moments, so the units for the first three members of the main diagonal of the covariance matrix will be cm^2 and for the second three $(Tm)^2$; the cross terms will have units of $Tm \cdot cm$. Any error at this point would lead to undesirable vertex results.

By working out the system of equations giving the momentum-dependent diagonal elements, one can come to:

$$\begin{aligned} \sigma_{px} &= (\mathcal{C} \cdot \rho \cdot cos(\phi)) - \bar{p}_x \\ \sigma_{py} &= (\mathcal{C} \cdot \rho \cdot sen(\phi)) - \bar{p}_y \\ \sigma_{pz} &= (\mathcal{C} \cdot \rho \cdot \frac{cos(\theta)}{sin(\theta)}) - \bar{p}_z \end{aligned} \tag{6.47}$$

With $\mathcal{C} = B \cdot Z \cdot (2.998/10.0)$. Applying the following trigonometric ratios and the tangent ratio ($tan\theta = \frac{\varrho}{z}$) can be used to remove the dependencies on the angles and have only a simple dependency on the Cartesian coordinates.

$$\begin{aligned} sen(\phi) &= \frac{y}{r \cdot sen(\theta)} = \frac{y}{\rho} \; with \; r = \frac{\rho}{sen(\theta)} \\ cos(\phi) &= \frac{x}{r \cdot sen(\theta)} = \frac{x}{\rho} \; with \; r = \frac{\rho}{sen(\theta)} \end{aligned} \tag{6.48}$$

Obtaining the following relationship between position and moment variances

$$\begin{aligned} \sigma_{px_m} &= \frac{\mathcal{C} \cdot (x_i - \bar{x})^2}{m-1} = \mathcal{C} \cdot \sigma_{x_m} \\ \sigma_{py_m} &= \frac{\mathcal{C} \cdot (y_i - \bar{y})^2}{m-1} = \mathcal{C} \cdot \sigma_{y_m} \\ \sigma_{pz_m} &= \frac{\mathcal{C} \cdot (z_i - \bar{z})^2}{m-1} = \mathcal{C} \cdot \sigma_{z_m} \end{aligned} \tag{6.49}$$

Using the fundamental changes seen at the beginning of the section and keeping in mind the units, which are cm for positions and Tm for moments, it is possible to obtain the new covariance matrix, keeping the correlations in the zero cross terms.

$$COV = \begin{pmatrix} \sigma_T^2 & 0 & 0 & 0 & 0 & 0 \\ 0 & \sigma_T^2 & 0 & 0 & 0 & 0 \\ 0 & 0 & \sigma_L^2 & 0 & 0 & 0 \\ 0 & 0 & 0 & \mathcal{C} \cdot \sigma_T^2 & 0 & 0 \\ 0 & 0 & 0 & 0 & \mathcal{C} \cdot \sigma_T^2 & 0 \\ 0 & 0 & 0 & 0 & 0 & \mathcal{C} \cdot \sigma_L^2 \end{pmatrix} \tag{6.50}$$

The new matrix maintains unit consistency and avoids possible angular deviations in the covariance matrix calculations by relying only on the reaction vertex.

Once it has been clarified how to calculate the covariance matrix that is inserted as a seed in the Kalman Fitter, a step-by-step study of the information flow is ready:

1. **Initialize System State**

   Hits collection: Different applications require different initialisations of a Kalman filter's system state. In this work, the Kalman Filter initialises the state using the first measurement.

   In the case of ATTPC, only position information is included in the input measurements. The output system state will contain the object's position and velocity. When the first measurement is taken (Figure 6.9), the only information known about the object is where it started moving. The system state estimate is set to the input position. The error covariance of the system state will be set to the position accuracy of the first measurement. All the information collected during pattern recognition is directly or indirectly reused in this first step. For example, the coordinates of each hit or the total angles of the traces are used to calculate the errors.

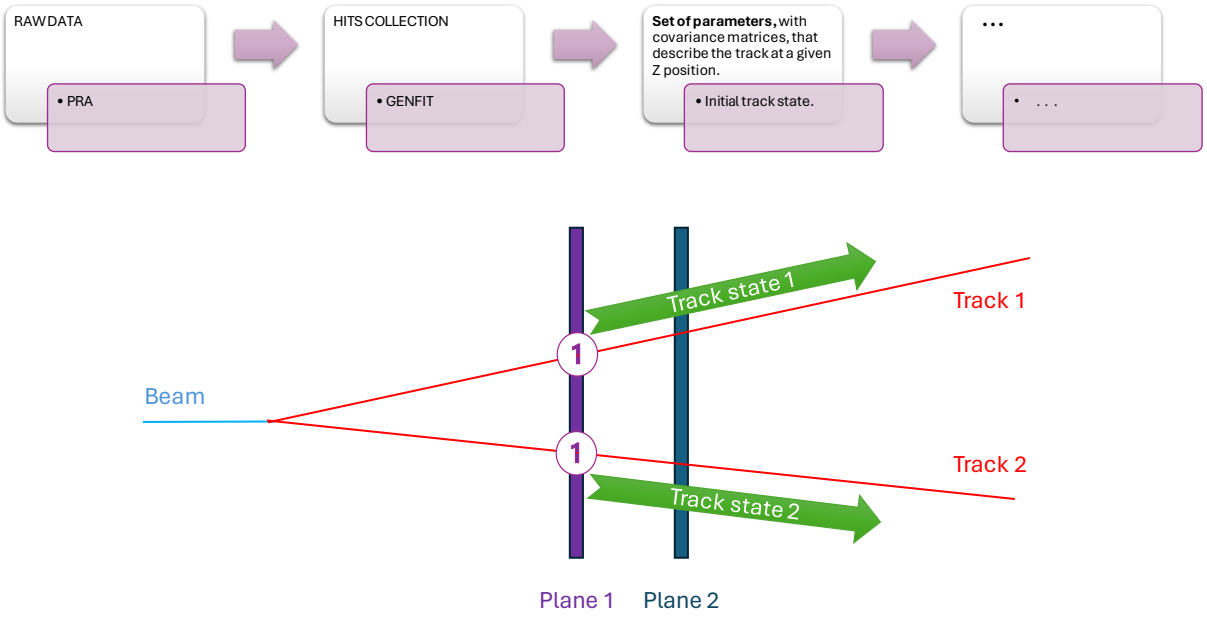

Figure 6.9: Flux diagram of the data for the first state of Kalman fitter

2. **Reinitialize System State**

   The system state estimate is reinitialised because a velocity estimate needs a second position measurement for computation.

   The updated system state estimate will be the second measured position and the calculated velocity. The position accuracy of the second measurement and an approximate velocity

accuracy will be the updated system state error covariance. This approximate velocity accuracy can be tuned and adjusted after the data has passed through the filter.

In steps one and two, the system estimate is initialised and re-initialised using the initial measurements. The approach to this initialisation may vary between different implementations of the Kalman filter. Still, the aim is consistent: creating a system state estimate that can be continuously refined using the Kalman filter equations with future measurements(Figure 6.10). Steps three to six detail the procedure for filtering in measurements and updating the state estimate.

3. **Predict System State Estimate**

The system state estimate is reinitialised because a second position measurement is required to calculate velocity accurately using linear approximation. The current position estimation includes the position of the second measurement and the inferred speed. The updated system state covariance also includes the position precision of the second measurement plus an estimated velocity precision. It should be noted that this approximation of the velocity accuracy can be adjusted and fine-tuned after the data has been filtered.

These first steps involve using the initial measurements to initialise and reinitialise the system estimation. Although the specific implementation of the Kalman filter may vary, the overall objective remains the same: to produce an estimate of the system's state that can be updated for future measurements by applying the equations of the Kalman filter.

4. **Compute the Kalman Gain**

The Kalman filter calculates a Kalman gain for each incoming measurement, determining how much the measurement affects the state estimate. Essentially, the Kalman gain, when confronted with a very noisy measurement, prioritises the existing state estimate over the potentially inaccurate new data.

This basic concept is at the core of the Kalman filter's effectiveness. It allows the filter to intelligently balance its current estimate against the incoming readings, producing an optimal estimate that strikes the right balance between the two sources of information.

5. **Estimate System State and System State Error Covariance Matrix**

When the inputs are measured, the Kalman gain is critical for estimating the system's state and the error covariance matrices. Once calculated, it is used for two crucial calculations.

First, it contributes to determining the new state estimate. By appropriately weighting the measure, the Kalman gain helps improve the estimate to reflect the most accurate representation of the system's current state.

Secondly, the Kalman gain impacts the calculation of the system state's error covariance. This calculation incorporates the uncertainty associated with the measurement into the overall error covariance matrix, refining the model's understanding of the system state.

These two computations, guided by the Kalman Gain, are fundamental steps in the Kalman Filter algorithm. Given the measurement uncertainty, they allow it to update and refine its estimates iteratively.

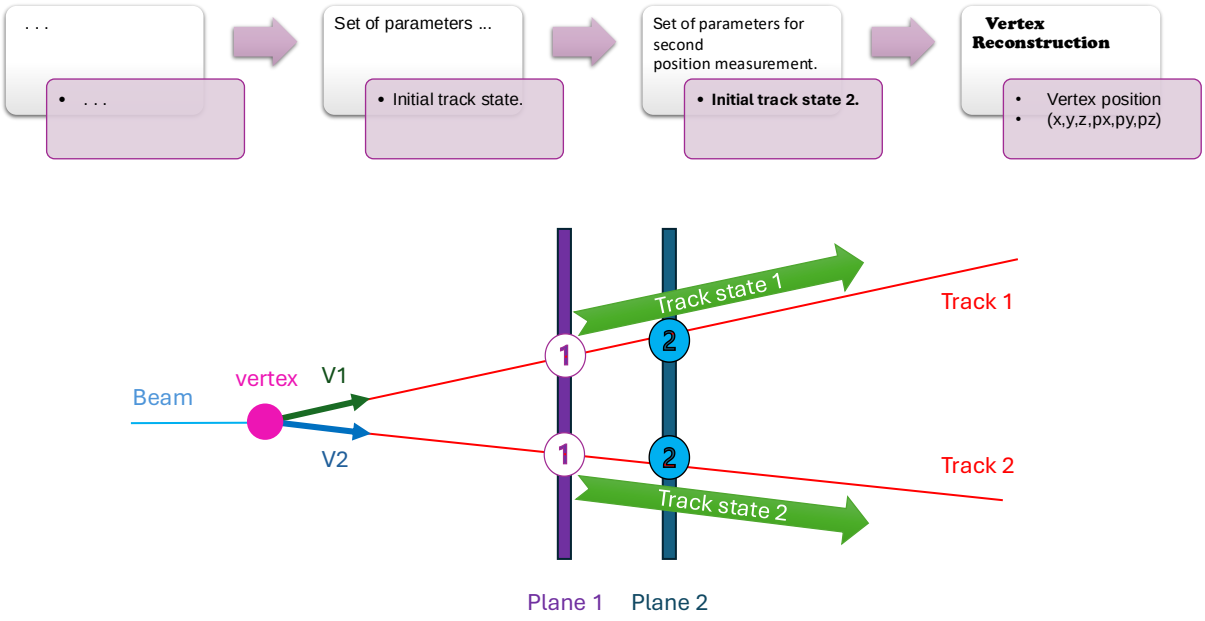

Figure 6.10: Second flux diagram of the data for the reconstruction of the vertex with Kalman fitter

Once the methodology used in the Kalman method is known, the technique for vertex selection is studied. To obtain the eigenparameters of the vertex by minimising the χ^2, described below.

A full chi2 fit was used to reconstruct the initial vertex from two charged tracks. As input to the method, we have the positions (x, y, z), the moments (p_x, p_y, p_z) obtained previously by PRA and their respective covariance matrices (explained at the beginning of this section), and the deposited charge for each trace. The initial vertex is the first point of the trace reconstructed with PRA and the closest to the (0,0,z) axis.

To calculate the vertex, the base is changed from the base positions and moments used so far to the base M(q/p, u', v', u, z) at some position of the vertex z. where q/p is the load on the momentum of each of the tracks, u' and v' are the tracks' directions concerning the X and Y axes, respectively, and u,v are the tracks' X and Y positions.

With these data, a matrix $M_{1,2}$ 6.51 can be constructed for each pair of traces with 10 measurements for this base, with subscript one referring to trace one and subscript 2 to the second trace.

$$M_{1,2} = (q/p_1, u'_1, v'_1, u_1, v_1, q/p_2, u'_2, v'_2, u_2, v_2) \tag{6.51}$$

Initially, the two curves are extrapolated as two stratified lines. The idea of the method is to find a function F(a) (eq. 6.52) that minimises χ^2 where a is a matrix that contains the information of the reaction vertex between two moment traces with $\vec{P}_1$ and $\vec{P}_2$ moments.

$$F(a) = C_1 \cdot a + C_2 \cdot a \cdot a^T \cdot k \tag{6.52}$$

C_1 and C_2 are constant matrices, and k is a constant vector.

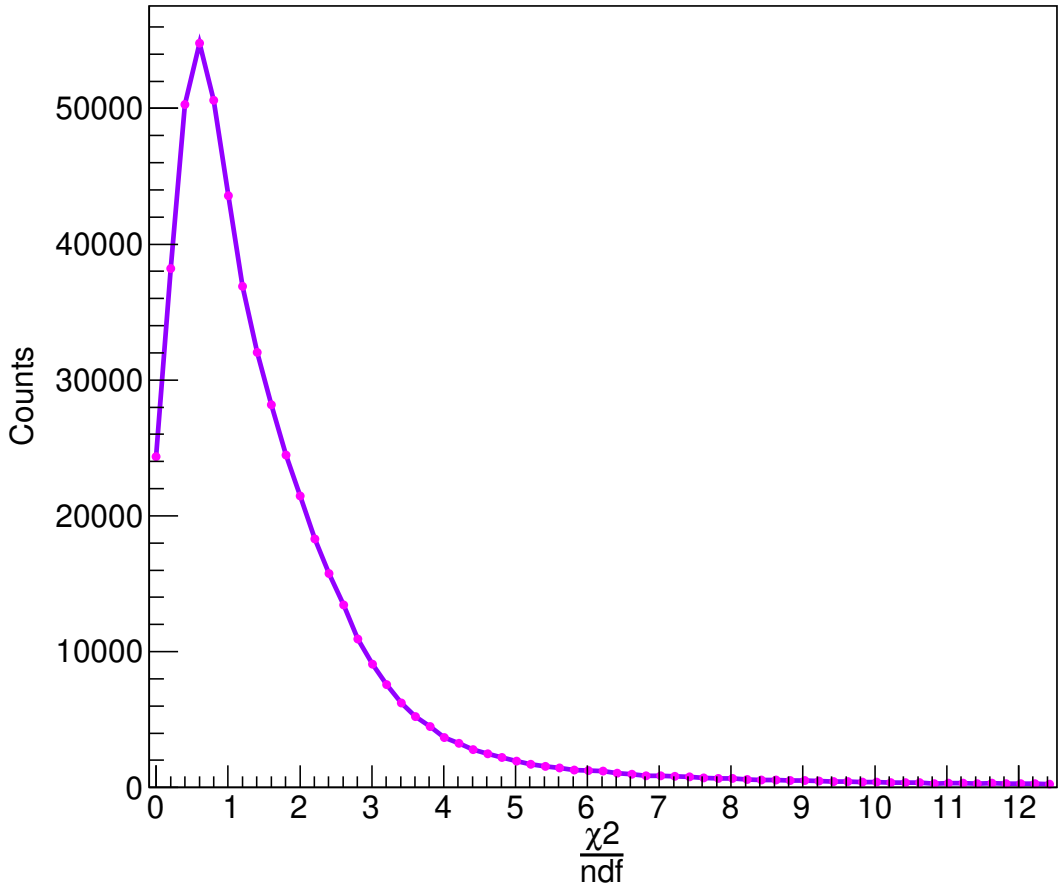

Figure 6.11: χ^2/ndf obtained by fitting all the experiment data after all the filters and the particle identification of the alpha scattering particles of each event with the highest angle are applied.

The final expression for minimising χ^2 iteratively within the Genfit fitting programme with Minuit [76] is:

$$\chi^2 = (F(a) - M_{1,2})^T \cdot COV^{-1}_{M_{1,2}} \cdot (F(a) - M_{1,2}) \tag{6.53}$$

With initial values parameters, χ^2 fit gives a better estimate of the errors and better positions of the initial vertex, which will be used to reconstruct all the reaction kinematics using the inverse kinematics method.

The $\frac{\chi^2}{ndf}$ (with ndf the number of degrees of freedom) is calculated by dividing the squared differences between the observed data and the expected data by the number of degrees of freedom in the model. The lower the value, the higher the goodness of the fit. It represents the magnitude of the deviation between the observed and expected data.

The statistic is of the form:

$$\chi^2 = \sum_{i=1}^{n} \frac{(X_i - \mu_i)^2}{\sigma_i^2} \tag{6.54}$$

It is a sum of squares of standardised normal random variables. If the fit is good, i.e. μ_i and σ_i^2 are well estimated, then each fraction is assumed to be close to one. Therefore, the sum gives n, and $\frac{\chi^2}{n}$ provides a number close to 1.

Figure 6.11 represents precisely this chi-square between the degrees of freedom for the fit of the experiment data discussed in the thesis, once treated with Genfit and calculating their covariances as indicated in this section. It can be seen that there is an accumulation around 1, which suggests that a priori correct fit is being made after pattern recognition. The computation of the chi-square plotted is performed for the data treated as indicated in topic 6, selecting in the particle identification only the alpha particles and with the beam corrections to be treated in that unit.

Chapter 7

Vertex-Energy and Efficiency Reconstruction

7.1 Energy Reconstruction

In the experiment, an ^{16}O beam from the ReA6 linear accelerator (linac) at NSCL's ReAccelerator facility at 10 million electron volts per nucleon (MeV/u). The AT-TPC was placed in the centre of the SOLARIS magnet, which was subsequently ramped up to a field of 3 Tesla (T) parallel to the axis of the chamber. The experiment (E20020) aims to search for the resonance in ^{16}O just above the four-alpha separation energy of 14.4 MeV. The decay of this resonance to four alpha particles will be observed in the experiment. This resonance would correspond to the Hoyle state, an excited state of ^{12}C that is very close to the alpha particle separation energy, the threshold energy above which the nucleus can emit an alpha particle (^{4}He). Fred Hoyle proposed it in 1954 [30] to explain how carbon is produced in stars. Another analysis to be presented in this thesis is the study of the resonances of the bound states and GS for the reaction ^{16}O(^{4}He, ^{4}He)^{16}O.

The AT-TPC was filled with 700 Torr of pure helium gas as a reaction target and detector medium. The fifth alpha is the target's alpha recoil. The initial energy of the oxygen-collimated beam is 160 MeV, 10 MeV/n a priori, more than enough to cover the states of interest. The beam has a circular width of about 2 cm. Therefore, it is necessary to create an exclusion zone on the pad plane for this area and the surrounding pads, reducing the gain or directly limiting the pads that may be affected. The ^{16}O beam range at this energy, experimental pressure, and temperature conditions is about 2 m. It travels throughout the chamber, losing energy through electromagnetic and nuclear collisions. This fact will affect the determination of the reaction peak since it loses about one-third of its energy at the end of the path, and the calculations of the kinematics and effective cross-sections would be affected if the corresponding corrections were not made.

The added difficulty in incorporating a magnetic field parallel to the beam direction is that the charged traces are bent into helical paths with complicated parametrisation. On the positive side, ATTPC and SOLARIS provide the experiment with new variables for reconstructing the kinematics, such as the radius of curvature.

7.1.1 Brho determination

As mentioned in the section 6.3, different iterative methods are used to obtain the radius of curvature. Firstly, RANSAC is used to simulate a circumference whose radius of curvature will be that of our charged particle. Secondly, a Kalman filter-based algorithm is used to refine it.

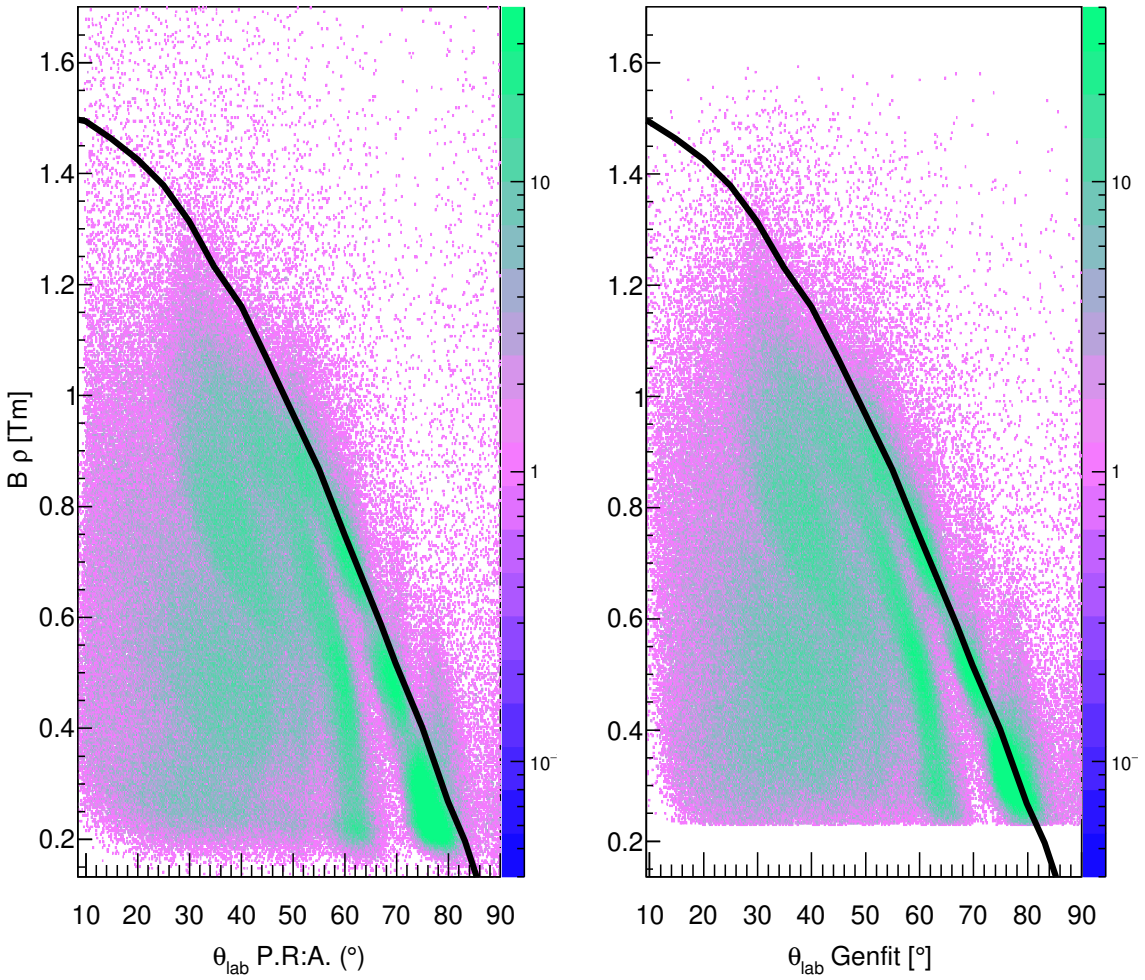

Figure 7.1: Final results for the magnetic rigidity versus scattering angle in the laboratory reference system for all the experiment statistics. On the left can be seen the results obtained after the trace identification with the PRA and the cuts in the particle identification, and on the right are the results for the magnetic stiffness correction coming from the Genfit fitting results and its subsequent correction, taking into account the reaction vertex and the ^{16}O excitation energies.

Rigidity is a measure of the momentum of the particle. It refers to the fact that a particle with a higher momentum is more resistant to being deflected by a magnetic field. It is defined as R = B ρ = pc/q, where B is the magnetic field, ρ is the particle's radius due to that field, p is the particle's momentum, c is the speed of light, and q is its charge. It is often written as "Bρ ".

The action of a static magnetic field defines rigidity. The direction of the field is perpendicular to the particle's velocity vector. Thus, a force is exerted perpendicular to the velocity vector and the field, defining a plane through which the particle travels. The definition of the Lorentz force implies that the particle will move circularly in a uniform field, giving a constant curvature radius.

7.1.2 Energy Beam correction

In the ^{16}O experiment at alpha, the density of the active target is enough to give a beam energy loss across the chamber of about 1/4 of the initial energy, which means that corrections must be made carefully. The range of the oxygen particles in ATTPC at different energies of our beam along the chamber (Table 7.1) is calculated using The Stopping and Range of Ions in Matter (SRIM) [77], a collection of software packages developed by Professor James F. Ziegler that estimates many features of ion transport in matter.

Ion Energy [MeV]	$\frac{dE}{dx}$ Elec. $[\frac{MeV}{mm}]$	$\frac{dE}{dx}$ Nuclear $[\frac{MeV}{mm}]$	Projected Range [m]
0.01	$6.050\ 10^{-1}$	1.676	$263.81\ 10^{-6}$
0.1	1.718	$5.465\ 10^{-1}$	$2.82\ 10^{-3}$
...	...	...	...
1	6.343	$1.010\ 10^{-1}$	$18.79\ 10^{-3}$
...	...	...	...
65	6.139	$2.860\ 10^{-3}$	0.484
...	...	...	...
100	4.515	$1.946\ 10^{-3}$	0.923
...	...	...	...
130	$3.687\ 10^{2}$	$1.438\ 10^{-3}$	1.59
150	3.284	$1.352\ 10^{-3}$	1.78
160	3.113	$1.203\ 10^{-3}$	1.98

Table 7.1: Table energy loss SRIM for the ^{16}O. It shows the different factors considered when calculating the energy loss, such as energy loss due to electric collisions or nuclear interactions. With the energy provided in the experiment and with a pure oxygen beam passing through the pure helium target, two metres would be reached before the beam comes to a complete stop.

Using the SRIM programme and knowing that the beam has an initial energy of 160 MeV and is travelling through helium gas at a pressure of 700 Torr, we can obtain information about the initial distance the beam could travel before stopping, which in this case is about 2 m.

The energy losses due to electromagnetic and nuclear collisions are enough for the beam to have an energy of about 110 MeV at the end of the chamber. For each distance L, the final range it would have at each point in the chamber is calculated, and a simple extrapolation using the SRIM tables gives the beam's energy at each end.

$$E_i \rightarrow R_i$$

$$R_f = R_i - L$$

$$R_f \rightarrow E_f$$

The straggling between the end and start points must be known to perform the simulations correctly. If the straggling in the initial and final parts of the range is known, then the value in the amount of interest can be obtained. Once the straggling has been determined to a certain length, the effective distance travelled by the particle can be obtained by randomising the actual size of the track (L) according to a Gaussian distribution.

7.1.3 Particle Identification (PID)

In the experiment, the fact that there is a magnetic field and that the radius of curvature of the particles has been obtained is used directly to identify the particles. Since the radius of curvature depends directly on the electric charge of each nucleus, which is more prominent in the heavier ones, and since the energy loss is smaller than the number of protons in the nucleus, the plot of Bρ versus energy loss provides the necessary graphs to study the kinematics of ^{16}O in inverse kinematics.

In the identification of the particles, three zones can be distinguished. A zone of low energy loss and low Bρ, which corresponds to low charged particles; the location of higher central statistic, which corresponds to ^{4}He from elastic and inelastic collisions; and a third zone of high energy, which corresponds to heavy particles such as ^{16}O itself or ^{12}C. A two-step identification is done to identify and correct traces wrongly identified as noise.

In the first step, the total energy loss of the particles is calculated from the number of points of the trace (7.1) for outgoing particles with angles less than 90° since the width of the trace is also proportional to the charge. After the corresponding cut in the helium region, the differential energy loss per unit length (7.2) is plotted against Bρ to make a second cut in the traces to minimise noise.

$$E_{loss} = \frac{Q_i}{P} = \frac{\sum q_i}{n^o of hits} \tag{7.1}$$

$$\frac{de}{dx} = \frac{Q_i}{X_i} = \frac{\sum q_i}{\sum (x_{i-1} - x_i)} \tag{7.2}$$

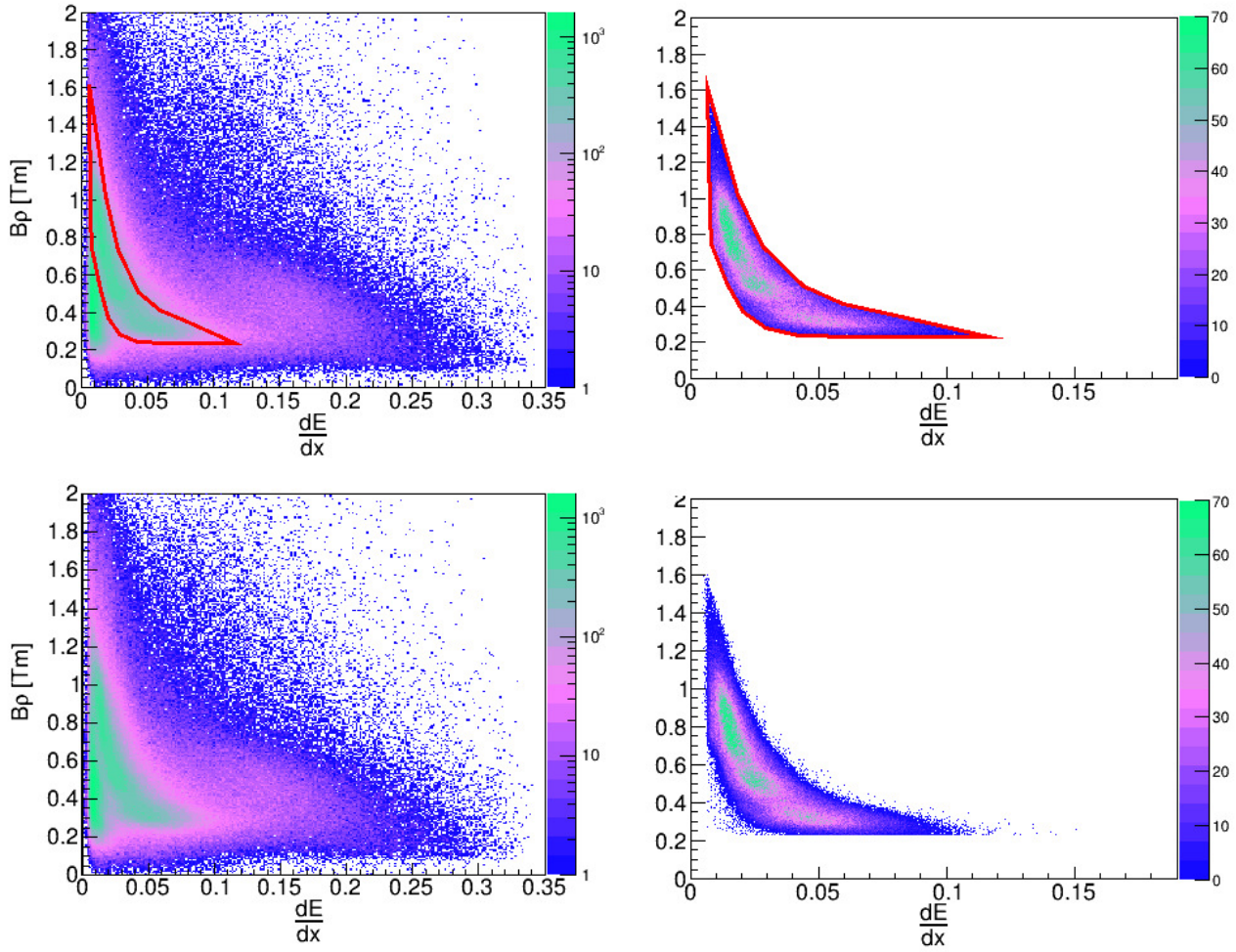

Figure 7.2: Particle Identification (PID). The figure shows particle identification by calculating the charge deposited on the detector per unit length of the traces. In the figure on the top left, the energy loss is calculated taking into account 60 % of each trace measured from the vertex, and in the analogous figure below, 40 %. In them, three regions can be seen: the one selected with the red cut, corresponding to the α particles; on the right, the heavy particles; and below it, an accumulation corresponding to light particles. The figure on the top right corresponds to the cut made, and the figure on the bottom right corresponds to how the top cut affects different length selections.

7.2 kinematic reconstruction

Once the magnetic stiffness has been determined using the fitting program, the energy can be calculated from the equations that join the magnetic field and the energy in the laboratory frame.

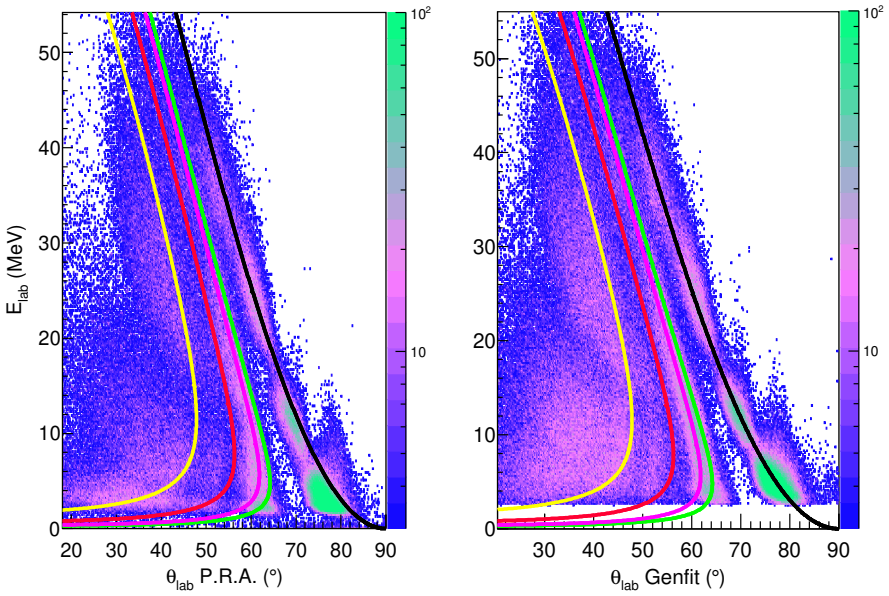

Figure 7.3: Comparison between the results obtained for pattern recognition and their subsequent adjustment for energies versus angles in the laboratory frame in inverse kinematics. The figure on the left shows the results for the PRA, and the figure on the right shows the final adjustment. All the filters presented in the thesis, vertex corrections, PID cuts, etc., are considered in both figures. The lines are the LISE++ calculations where the black line represents the ground stare, the green line the first excited state of $^{1}6O$, the higher angle red line the state corresponding to 7.117 MeV, the inner red line the state corresponding to 9 MeV and the yellow line the Q(α) of oxygen corresponding to 14.44 MeV.

A two-step reconstruction is performed to calculate the kinematics. First, GenFit is used to fit the pattern recognition data, then the theta angles and energy in the laboratory frame are corrected. The first step of the theta angle reconstruction in the laboratory is obtained as explained in section 6.3.3 from the arc length traced by the particles in the chamber and the z-position of the particle at one-tenth of the distance identified by GENFIT as a valid trace. In the case of laboratory energy, it can be obtained using magnetic rigidity.

The Lorentz force is equal to the centrifugal force on a circular path of radius ρ in a magnetic field B:

$$qvB = \frac{mv^2}{\rho} \tag{7.3}$$

Where q, m, v are the particle's charge, mass and velocity. With a dimensional analysis (eq. 7.4), a simple relation between the moment and radius of curvature can be obtained, where the charge is a multiple of the elementary charge, so q = ne.

$$B\rho[Tm] = \frac{p[kgm/s]}{ne[As]} = \frac{e}{c}\frac{p[eV/c]}{ne} = \frac{p[eV/c]}{nc} \tag{7.4}$$

$$B\rho \approx \frac{10}{3}\frac{p[GeV/c]}{n} \rightarrow p \approx \frac{3}{10}ZB\rho \tag{7.5}$$

$$E = \sqrt{p^2 + M_\alpha^2} - M_\alpha \tag{7.6}$$

Once the adjusted energy and angle for the angle correction are obtained, the corrected excitation energy is calculated as described in the next section. The recalculated excitation energy is added to the mass of the recoil particle, and the adjustment correction is made to give the final variables to be used in the calculation of the cross sections(Figure 7.3). For the energy, it is considered that the dependence of B *rho* on the angle is $1/\sin(\theta)$, and they are proportional. Therefore, multiplying the obtained energy by the factor $\sin(\theta_{old})/\sin(\theta_{new})$ gives the new energy.

7.3 Excitation Energy

The Missing Mass Technique measures the momentum of all the particles involved; the latter relies on conserving momentum. It depends on momentum conservation and knowing the beam energy only needs to detect one of the outgoing particles to recover E_x.

This technique is used to study transfer reactions involving the exchange of a nucleon or cluster of nucleons between a target and a projectile. It has been widely used in nuclear structure studies to determine the energy position and orbital occupation of the excited states of many nuclei and in nuclear astrophysics to determine the partial decay widths of nuclear states involved in resonance reactions and the cross-section. In this case, elastic and inelastic collisions of two bodies are studied 7.7.

$$A + B \rightarrow C + D \tag{7.7}$$

A acts as a beam (^{16}O), and B acts as a particle at rest (^4He) in the laboratory frame. Following the conservation of energy and momentum, two particles with different kinetic energies and directions are produced in the outgoing channel after the collision. The equation 7.8 shows the momentum-energy vector four associated with each of the particles involved in the collision.

$$\begin{cases} P_A = (E_A, \vec{p_A}) \\ P_B = \left(m_B, \vec{0}\right) \\ P_C = (E_C, \vec{p_C}) \\ P_D = (E_C, \vec{p_D}) \end{cases} \tag{7.8}$$

The energy-momentum is conserved, and as seen in equation 7.9, the particle that is not measured is isolated to obtain its excitation energy from the energy and angle of particle c.

$$P_A + P_B = P_C + P_D \tag{7.9}$$

$$P_D = \sqrt{P_A^2 + P_{\mathbf{B}}^2 + P_C^2 + 2P_AP_B - 2P_AP_C - 2P_BP_C} \tag{7.10}$$

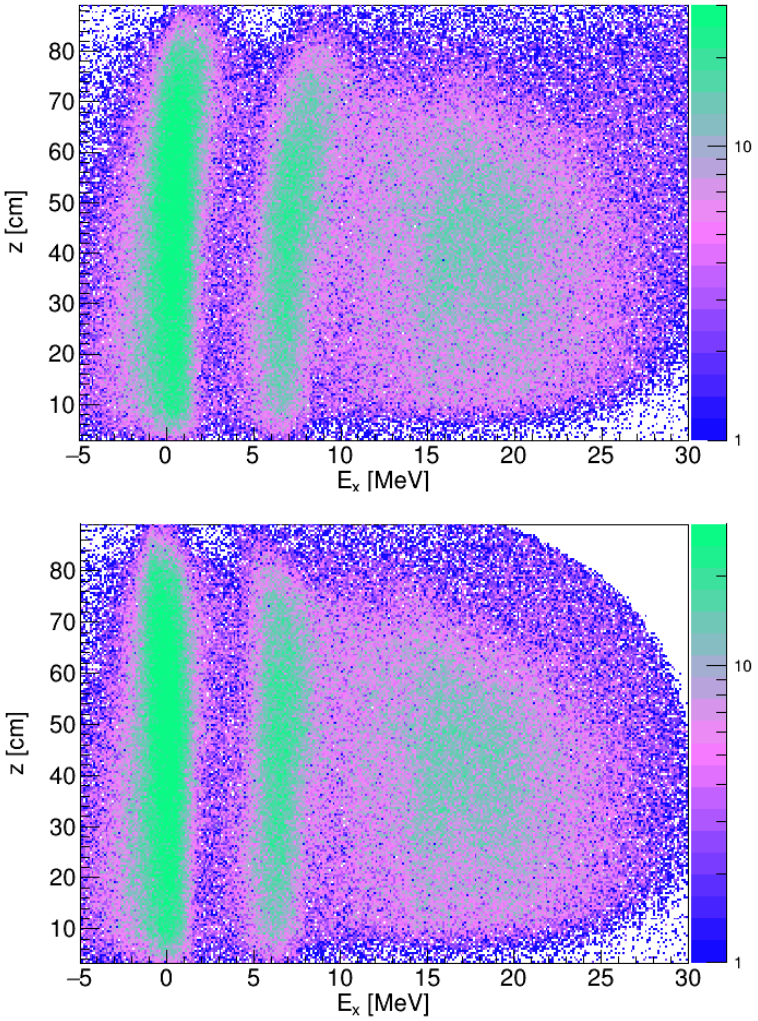

Figure 7.4: The two figures show the reaction vertex for each filtered event after PID. The figure above shows a curvature due to different effects, such as electric field scattering and evolution with the excitation energy along the chamber. This may be because the vertex corrections for Genfit are made for a fixed beam energy of 10 MeV/n. The figure below already applies different corrections to the ground state and excitation energy evolution along ATTPC.

Using 4-vectors simplifies the calculation since their square is invariant with the reference frame. It depends only on their mass and E_x, according to the equation 7.11. The solution of the equation 7.9 allows the calculation of E_x as it can be seen in the equation 7.12.

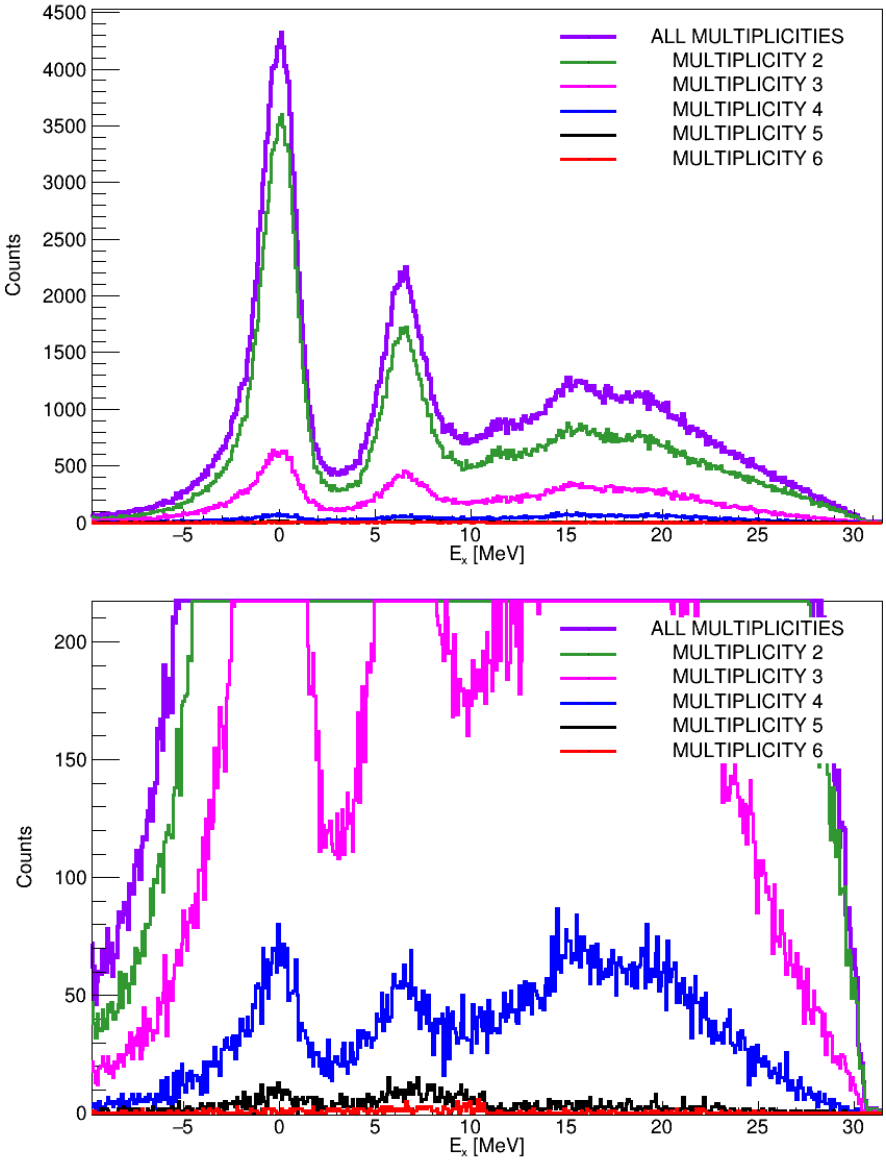

Figure 7.5: To perform all the calculations, a separation of the accumulation of the types of events in different multiplicities is made; in the figures, you can see this separation by different colours for the total excitation energy (violet). The events corresponding to multiplicity 2 are shown in green, multiplicity 3 in pink and multiplicities 4, 5 and 6 in blue, black and red, respectively.

The excitation energy is obtained from the known masses (m_A,m_B,m_C, and m_D) of the particles involved, the kinetic energy and angle of one of the particles in the outgoing channel ($T_{C,lab}$ and $\theta_{A,C}$) and the kinetic energy of the beam (T_A). The value of the constant C can be found in the equation 7.13. The momentum of A and B is given by $p = \sqrt{2mT + T^2}$.

For a more exhaustive analysis of the experiment, the events are differentiated according to the number of traces detected in each of them. This is called **multiplicity**, associating a number to the different multiplicities, which will be the number of traces detected after fitting (Figure 7.5).

The method used to separate the traces is as follows: Once each trace has been adjusted with GenFit, each event's number of traces per exit angle is selected, setting a limit of 1 degree for traces that may belong to the same particle (broken traces). The PID also discards traces that are too short or do not have enough charge.

For the study of cross sections, only events with multiplicity 2 or 3 are selected, i.e. events with two traces corresponding to elastic or inelastic scatterings of a ^{16}O and an α particle or events misidentified as multiplicity 3 when an extra trace is added to the count from any physical or mathematical artefact.

The multiplicities corresponding to fragmentation of oxygen into different particles correspond to multiplicities equal to or higher than 3. As shown in the figure 7.5, they are significantly less than the scattering events.

$$P^2 = (m + E_x) \tag{7.11}$$

$$E_x = \sqrt{C - 2\left(m_B + m_A + T_A\right)\left(m_C + T_C\right) + 2p_A p_C cos(\theta_{A,C})} - m_D \tag{7.12}$$

$$C = m_A^2 + m_B^2 + m_C^2 + 2m_A E_A \tag{7.13}$$

Using these formulae and plotting the excitation energy against the beam path in the chamber, as shown in 7.4, one can see the excitation energy dependence on the beam energy loss, corrected as explained in section 7.1.2 and inserting the corrected beam energy into the formula. In this case, only the trace with the highest angle of the outflow reaction is shown since, in all cases, it is the one corresponding to the scattering alpha, and it is the trace that is of interest for studying oxygen in inverse kinematics.

To represent the excitation energy of the scattering particle, corrections are made for the multiplicity of the different events and the results are shown in Figure 7.5. The corrections are because the PRA and the subsequent fitting consider each piece of the broken traces as an individual trace, which overestimates the multiplicity. To correct for this effect, each path is selected individually. When its departure angle is calculated, if two atoms have the same angle and do not have the same vertex, they are considered parts of the same trace. They are, therefore, combined for the multiplicity calculation.

Multiplicity is also used to check excitation energy calculations. The reaction behaviour can be seen by separating the excitation energy into different contributions. For multiplicity two, the dominant terms must be the ground state and excited states below the threshold decay energy in alphas for ^{16}O (Q(α) = 7.162 MeV).

Once the particles have been filtered by multiplicity, discard the events with a multiplicity greater than 5. Another enjoyable task is to make sections every 10 cm of the chamber, from 5 cm to 95 cm, in excitation energy (Figure 7.6). This is to see which part of the detector is more interesting for studying the collisions. The chamber's beginning and end are removed to

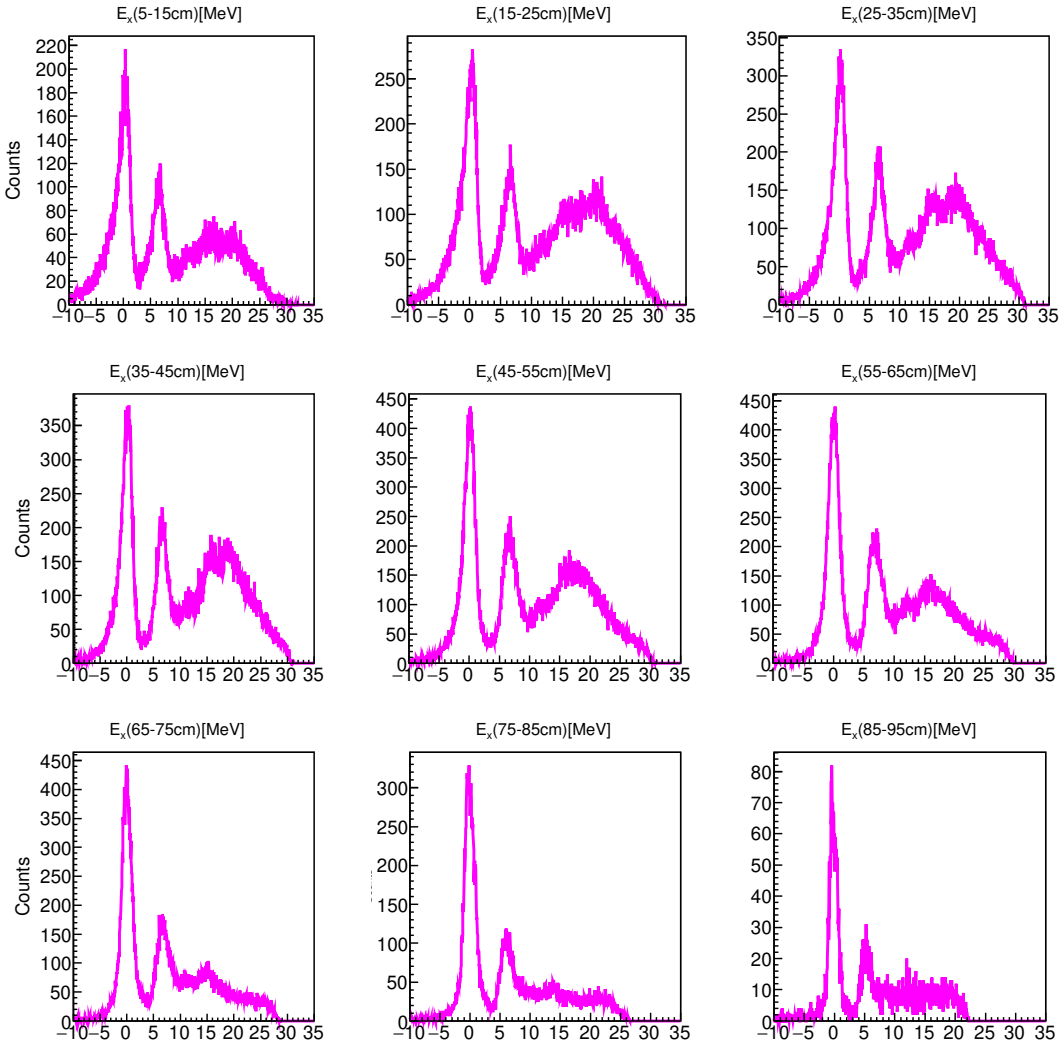

Figure 7.6: Evolution of the excitation energy along the chamber. The cuts are made every 10 cm, starting at 5 cm from the chamber and ending at 95 cm to avoid effects at the entrance of the chamber window and edge effects in the vicinity of the padplane.

avoid effects in the window (e.g. fragmenting of the window materials) or near the pad plane (deformation effects with the electric field).

These corrections not only affect the selection of the excitation energy but, as will be seen in the next section, in an experiment such as the one discussed in this thesis, where there is a sizeable relative loss of beam energy in the active target, they are of great importance in the subsequent calculation of the maxima and minima of the angles at the centre of mass. Figure (7.7) shows the effect on the ground state for the same selected sections along the length of ATTPC. The shift for each part affects the global calculation of the cross-section by shifting the minima and maxima to larger angles concerning the theoretical calculations.

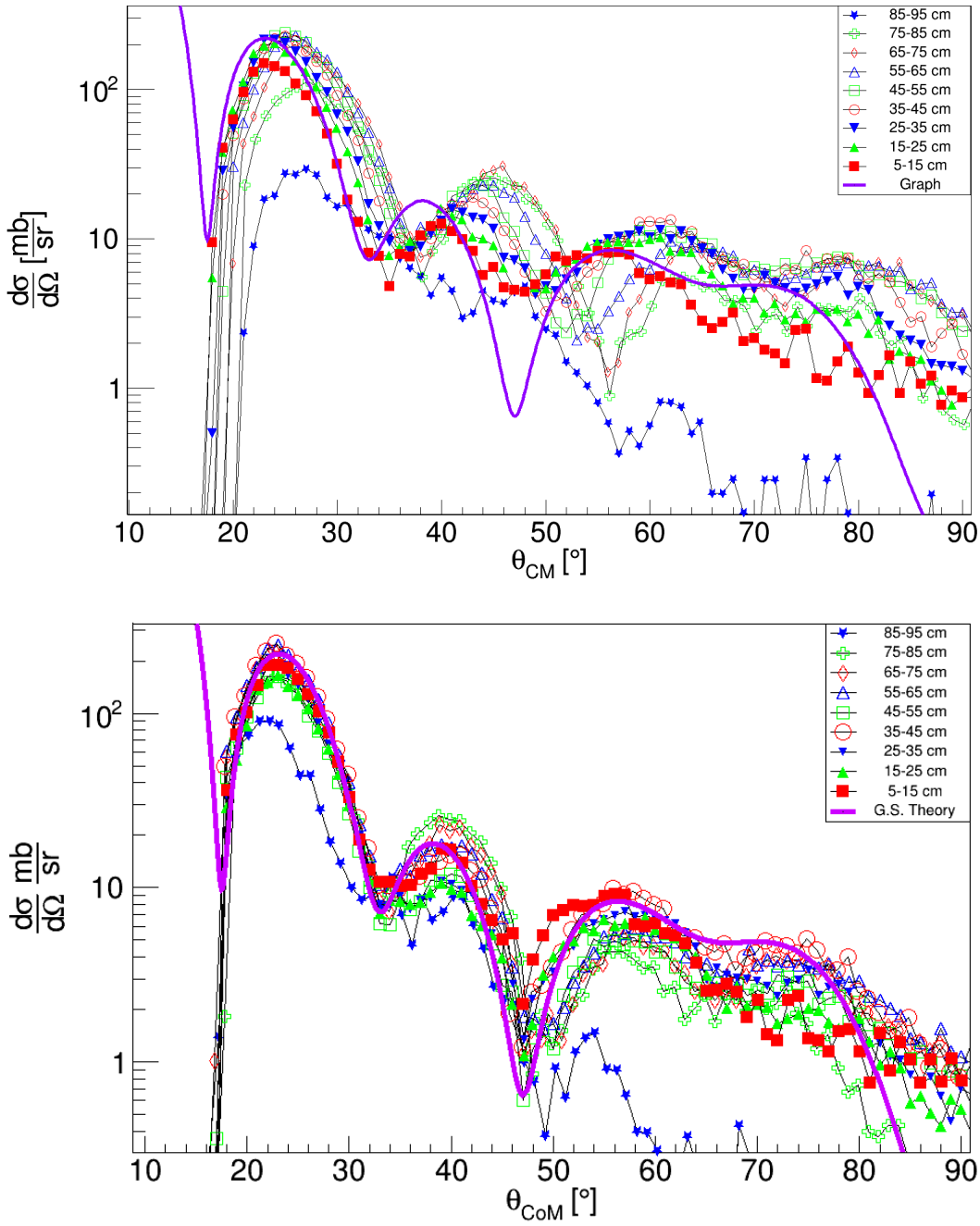

Figure 7.7: Comparison of the effect of vertex corrections for the ground state. A calculation is made for the fundamental state every 10 cm to see the evolution. As can be seen in the comparison, the curved evolution of the excited states with the reaction vertex causes the effective sections to deform at a greater angle at the centre of mass.

7.4 Efficiency

A GEANT4 Monte-Carlo simulation was performed to evaluate the efficiency of the detection system. This simulation used a kinematic model of elastic scattering to generate events in the case of the ground state. It covered all physically achievable angles and energy levels. An

individual study is carried out for the ground state and each of the excited states since the calculation of the angle at the centre of mass depends directly on the excitation energy, and the efficiency will be different depending on the state of the nucleus.

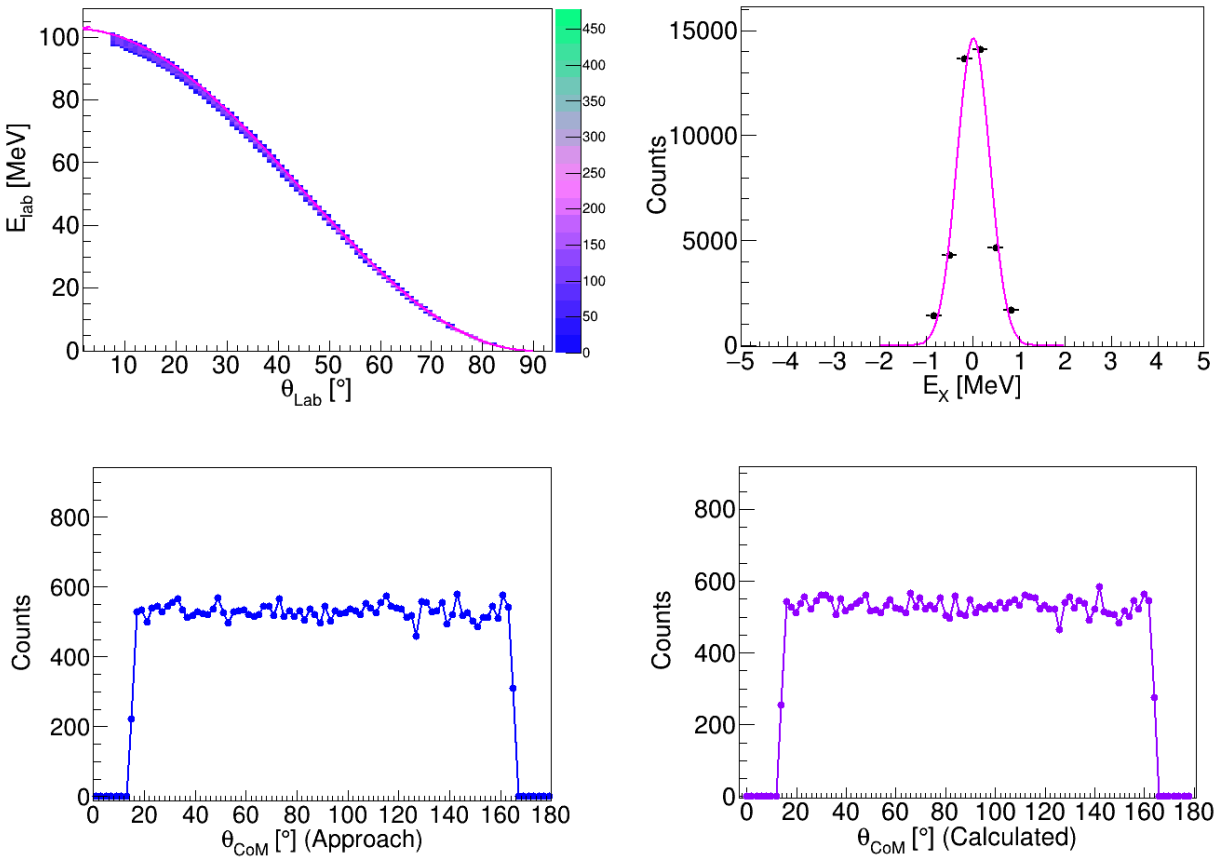

Figure 7.8: The figure shows an MC simulation with 50000 elastic events and 25000 alphas. The energy versus angle in the laboratory system is plotted on the top left. The figure on the top right is the excitation energy of that reaction. The two figures below are the accumulation of events for different centre-of-mass angles between 15º and 165º for the approximation $\theta_{CM} \simeq 90 - (2 \cdot \theta_{lab})$ approximation and calculated from the formula 7.12 presented in Section 7.3 respectively.

For AT-TPC experiments, a simulated version of the detector implemented with Geant4 has been realised, keeping the absolute chamber volumes and implementing the accurate experimental helium densities and the electric and magnetic fields used. The remaining reaction variables are then determined, starting with the laboratory energy and angle. A simulated representation of the detector, complete with trigger simulation, was then used to process these simulated events.

The output data of this simulated detector reflects the format of the data generated by the real detector. This allows the events to be analysed using the identical analysis program. To calculate the overall efficiency of the detection system, the number of events giving valid angle and energy values during the analysis process was counted, and this number was divided by the total number of simulated events using the same input parameters.

In a previous step of the efficiency calculation, a study is made of the behaviour of the Monte Carlo simulations when they are first treated by the algorithm, including the RANSAC method explained above, and, as a final step, adjusted using the Kalman Filter method and the possible deviations at different angles.

In this study the ground state of 50000 elastic events between 15º and 165º CoM is simulated (Figure 7.8), ensuring the excitation energy is perfectly centred at zero. A particular deviation of 2 MeV from the initial 160 MeV of the beam is included in the simulation. This is done to make the possible experimental energy fluctuations more realistic.

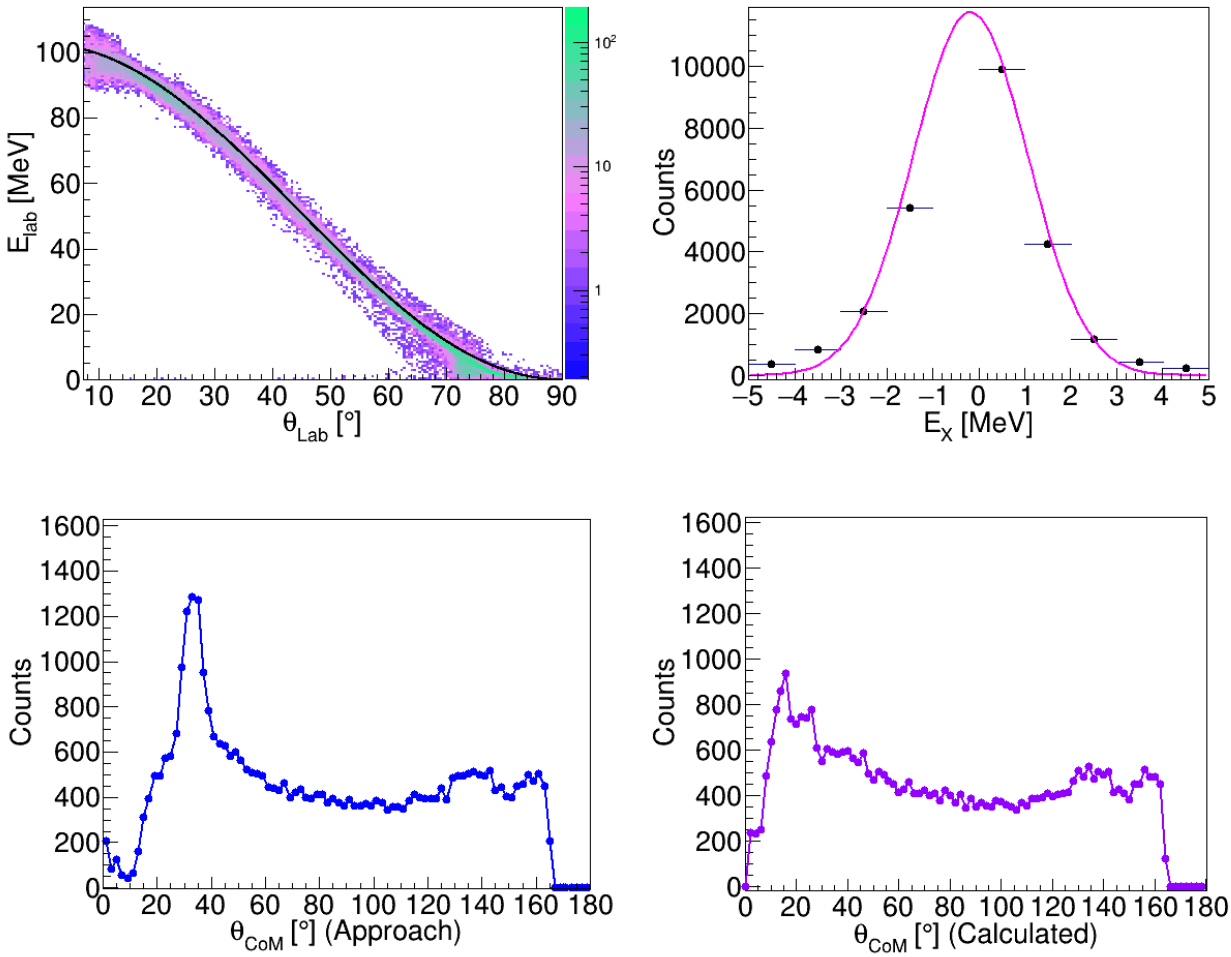

Figure 7.9: The figure shows the P.R.A. of the previous MC simulation. The energy versus angle in the laboratory system is plotted on the top left. The green line represents the theoretical curve calculated with LISE ++. The figure on the top right is the excitation energy of that reaction. The two figures below are the accumulation of events for different centre-of-mass angles between 15º and 165º for the approximation $\theta_{CM} \simeq 90 - (2 \cdot \theta_{lab})$ approximation and calculated from the formula 7.12 presented in Section 7.3 respectively.

The study also takes into account the approximation $\theta_{CM} \simeq 90-(2\cdot\theta_{lab})$ for the ground state as an acceptable solution when the laboratory energies and angles do not have large dispersions compared to that calculated using the formula 7.12.

The simulation calculates the initial parameters to be adjusted with Genfit. The exact process is carried out using the same parameters for the real data. The previous step is to obtain the energies and angles using the Ransac method.

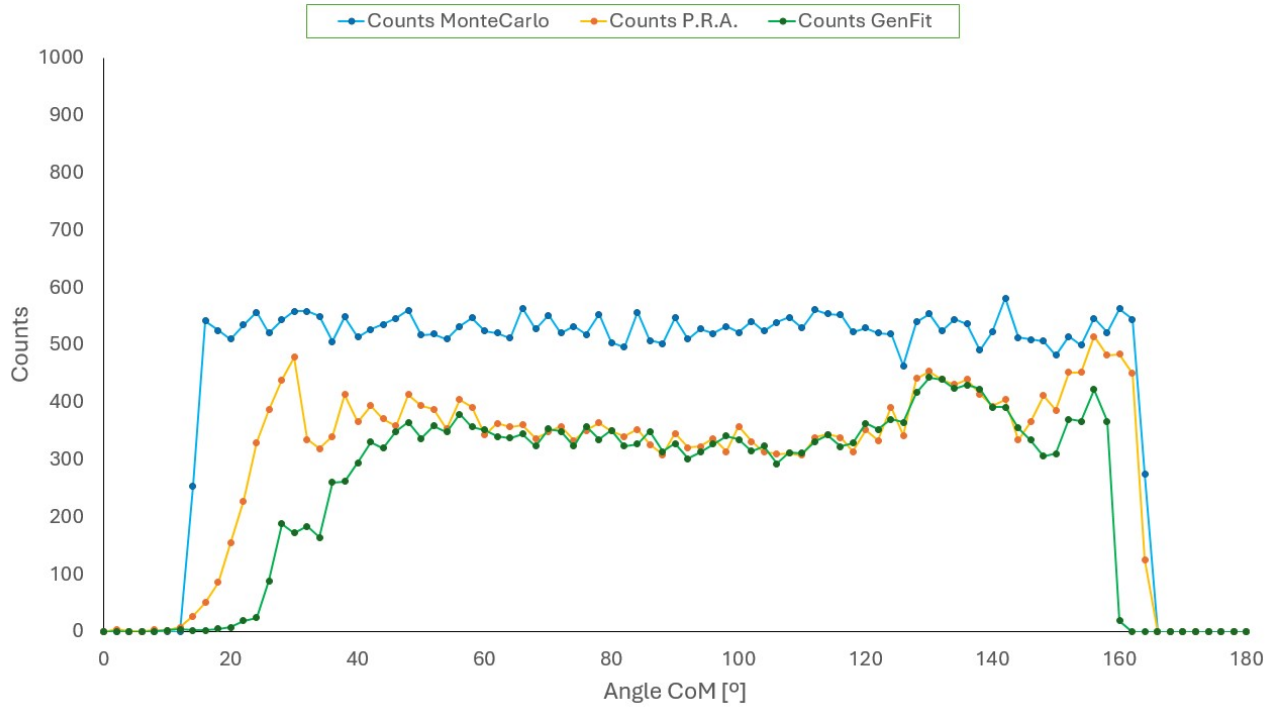

Figure 7.10: This figure shows the accumulation of counts per degree in CoM for the 50000 event MC simulation (blue), the P.R.A. (orange) and the Genfit fit (green) superimposed for comparison.

As shown in figure 7.9 there is a significant discrepancy between the CoM calculation of the proposed approximation and the other one calculated with the formula 7.12 prior to adjustment with GenFit (in P.R.A. step). This is because the angle at the centre of mass depends on the angle in the laboratory and the energies at this angle. This approximation is no longer valid since dispersion increases as one approaches larger angles in the laboratory (small angles in CoM).

Once the P.R.A. data are obtained, the Genfit adjustment uses the same parameters and corresponding covariances as the accurate data.

This effect is due to a lousy reconstruction for small angles in the laboratory of the curvature radius with the RANSAC method; this may also be due to a misidentification of segmented traces, which leads to a higher accumulation for angles close to 90^{o} misidentified as alphas in the excitation energy.

To avoid this effect in the reconstruction, once through the fit, only alpha particles are selected from among the particles with the highest angle in each event using the same PID method used in the real data.

Genfit provides a reasonable reconstruction of the data supplied by the P.R.A. of the angle in CoM and serves as one of the fitting method's validations (Figure 7.10). The fitting method does not go outside the limits the detector imposes, adapting well to the simulated MC data.

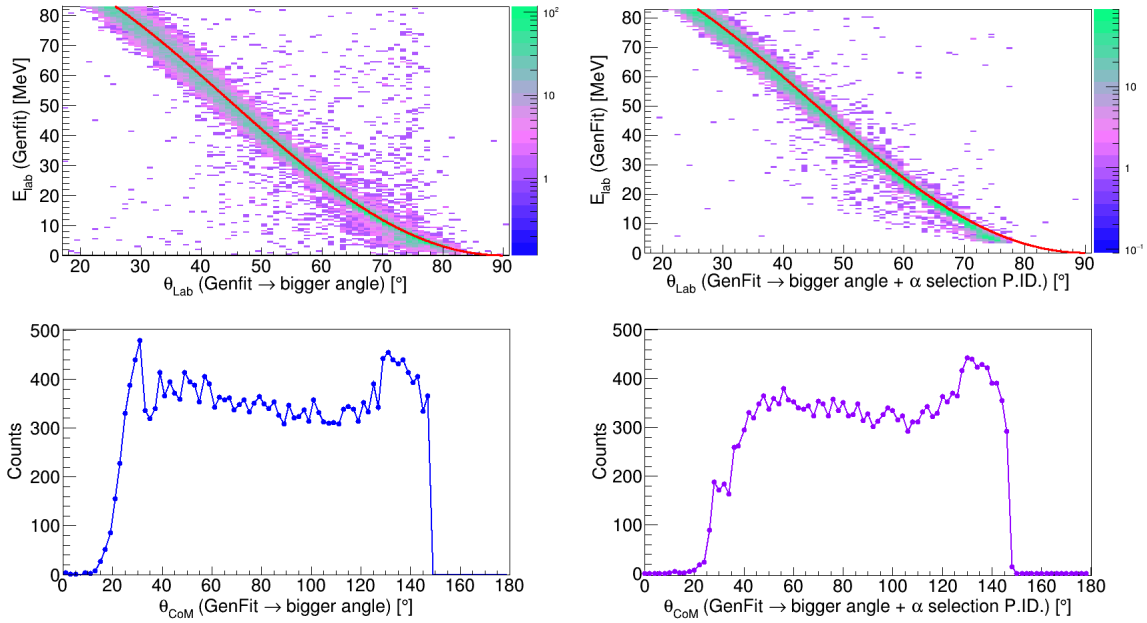

Figure 7.11: The figure shows the fit of MC simulation. The fit's energy versus angle in the laboratory system is plotted on the top left. The red line represents the theoretical curve calculated with LISE ++. The figure on the top right is the energy versus angle in the laboratory system for the GenFit. The two figures below are the fit events accumulation for different centre-of-mass angles between 15º and 165º for the approximation $\theta_{CM} \simeq 90 - (2 \cdot \theta_{lab})$ approximation and calculated from the formula 7.12 presented in Section 7.3 respectively.

Correcting for these effects at lower angles can be done homogeneously without creating artefacts that affect only one angle of the detector if one selects not only the excitation energy but, from each event, the trace with the highest angle, as is done for actual data.

As shown in figure 7.11 the GenFit adjustment corrects an underestimation of the energy for large angles inherited from obtaining the $B\rho$ with the RANSAC method. Also, and not less important, the validation of the process of obtaining the angles in the center of mass compared to the ground state approximation of $\theta_{CM} \simeq 90 - (2 \cdot \theta_{lab})$, which is a good test when calculating the efficiencies for the different excited states.

Figure 7.10 shows 50000 events of calculating the centre of mass angles for the Monte Carlo simulation in blue after going through the same analysis as the real data. Dividing the Genfit-adjusted simulation, in green, by the raw Monte Carlo data gives the geometric efficiency for the GS.

This methodology for calculating geometrical efficiency is implemented for each excited state and will be used to calculate their effective cross-section.

The small peak that can be seen between 15° and 30° with an angle at the center of mass (Figure 7.12) corresponds to angles greater than 70° in the laboratory.

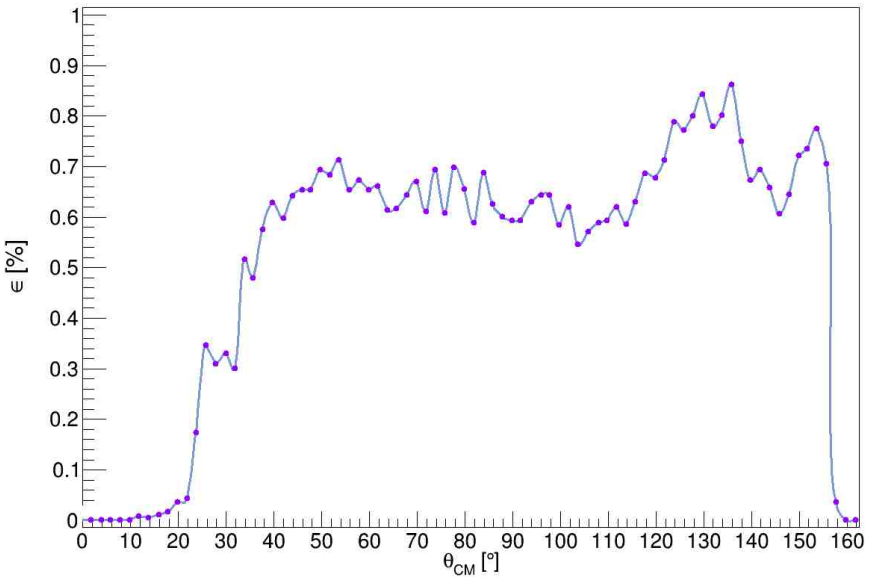

Figure 7.12: Fit geometric efficiency of the ground state for 50000 simulation events and a separation of 2° in the centre of the mass reference system. Fits a cubic function $(-0.544 + 0.048x - 0.0006x^2 + 2.352 \cdot 10^{-6}x^3)$ with a $\chi^2 = 0.119$ for the angles of interest and number of degrees of freedom 85, covering all the interest zone.

Fluctuations at small angles in CoM are easily explained by the intense magnetic field, which causes particles with low energy to be more affected. Although this curve should not occur in the fundamental state, the effect at low energies can be seen perfectly in the Pattern Recognition.

To solve this problem and to apply as realistic an efficiency as possible, a function is established that does not fit as well as possible at the CoM angles of interest and has a smooth decay towards the lower angles.

Experimental data will be used to check if this function correctly fits the GS efficiency and, if so, the same procedure will be applied to the excited states.

Once the efficiency for the ground state has been calculated, the same calculations are performed for the excited state efficiencies studied in this thesis.

As can be seen in figure 7.13, the efficiencies for the lowest (6.049 MeV) and highest (7.117 MeV) excited states within the nearest ^{16}O excited states, as well as for the ground state, do not vary much. It seems reasonable to use the same function as obtained for the ground state for the efficiency in the calculation of the cross sections of the excited states without much variation in the final results.

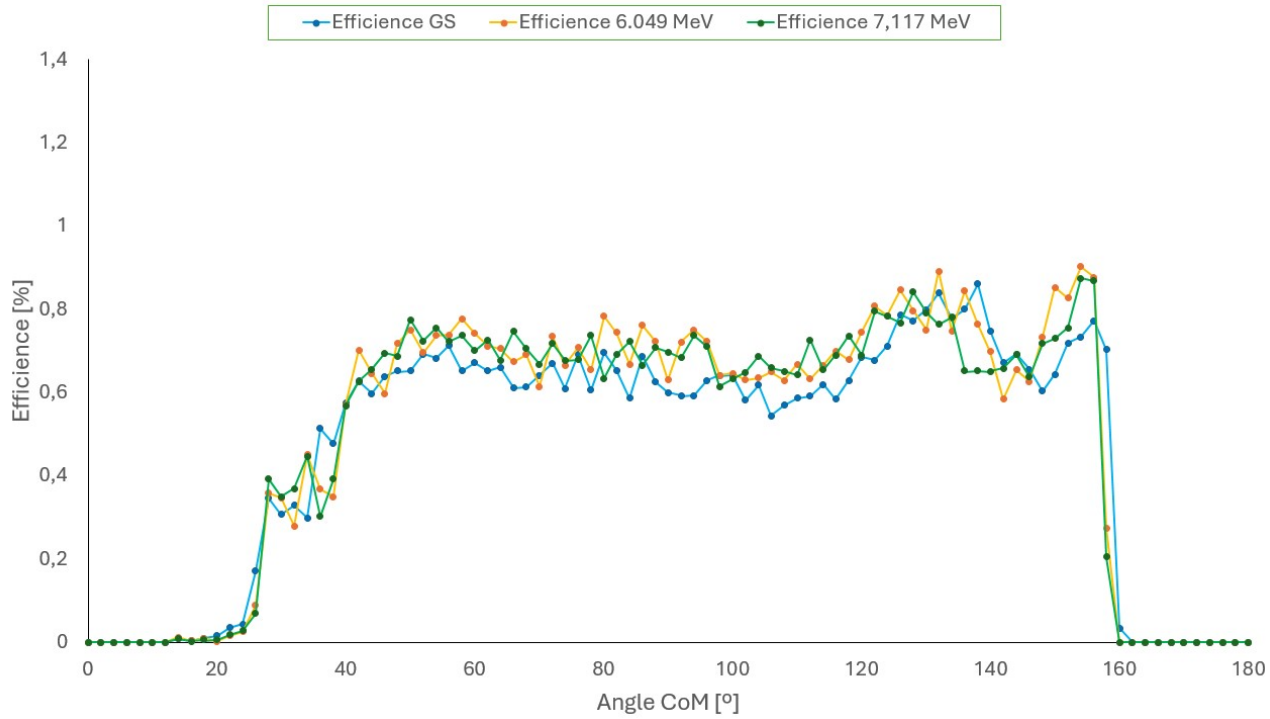

Figure 7.13: Comparison between GS efficiencies and excited states. In blue is the geometrical efficiency of the detector for the GS. Orange and green show the same calculation for the excited states of oxygen at 6.049 and 7.117 MeV respectively.

Chapter 8

Results

8.1 Differential cross sections

The calculation of the differential cross-section is based on the equation 8.1.

$$\frac{d\sigma}{d\Omega} = \frac{N^{mesure}}{N_{beam} N_{target} \mathcal{E} \Delta\Omega} \tag{8.1}$$

Where N^{mesure} is the number of particles obtained for a given angular range at the centre of mass, N_{beam} is the number of beam particles hitting the target, N_{target} is the number of target centres per cm^2, $\Delta\Omega$ is the solid angle maintained by the θ_{CM} disk, and ϵ is the geometric efficiency.

In practice, simulations are performed for each excited and ground state to obtain the geometric efficiency. These simulations are fitted with the same reconstruction algorithms used for the data. The ratio between the number of counts simulated by Monte Carlo for a given energy and the number of counts after fitting gives the geometric efficiency per angle, which is used to obtain the cross-section.

Except for the number of particles hitting the target and the number of targets, all cross-sectional factors can be obtained experimentally. Considering that the solid core can be approximated as follows:

$$d\Omega = d\phi d\theta sin(\theta) \tag{8.2}$$

Inserting equation 8.2 into equation 8.1 allows the differential cross-section to be calculated experimentally, as shown in equation 8.3.

$$\frac{d\sigma}{d\Omega} = \mathcal{F} \frac{N^{mesure}}{d\phi d\theta sin(\theta) \mathcal{E}} \tag{8.3}$$

$\mathcal{F} = \frac{1}{N_{target} \cdot N_{beam}}$ is obtained from the fit of the cross-section to the theoretical data. When applied to the excited states, this factor will allow us to get the different cross sections without knowing the number of incident particles or targets. Given that the solid angle under which a spherical cap whose radius is seen under an angle theta from the centre of the sphere and the entire azimuthal angle is covered in the detector, the experimental results for the cross-section can be obtained from the indirect observations as follows in the equation:

$$\frac{d\sigma}{d\Omega} = \mathcal{F} \frac{N^{mesure}}{2\pi \Delta\theta_{CM} sin(\theta_{CM}) \mathcal{E}} \tag{8.4}$$

8.1.1 Theoretical Cross-Sections

The theoretical calculations of the cross sections were provided by Jesús Lubián Ríos and Jonas Leonardo Ferreira, members of the Instituto Nacional de Ciência e Tecnologia - Física Nuclear e Aplicações (INCT-FNA), based at the Instituto de Física da Universidade Federal Fluminense.

In the 16O+4He collision, it was known that the coefficient strength of the imaginary part of the optical potential should be small compared to that used in standard procedures when considering medium and heavy mass targets.

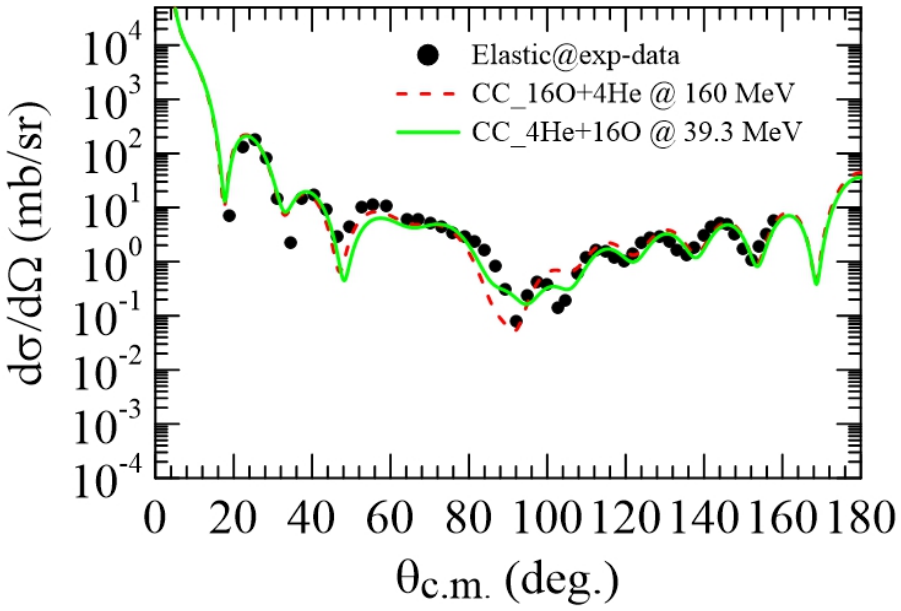

Figure 8.1: The dots in the figure represent the experimental results [78] (permission American Physical Society ("APS") with license number RNP/25/MAR/089607), the green curve represents the theoretical fit to these data and the red dotted curve the theoretical fit taking into account the 10 MeV/n energy of the thesis experiment.

They reached this conclusion in their recent work on $^{6}Li +^{12} C$, $^{6}Li +^{19} F$ and $^{16}O +^{12} C$ alpha transfer [79]. In particular, the elastic scattering of the $^{4}He +^{16} O$ in inverse kinematics is

well described when the coefficient strength $N_i = 0.2$ is assumed in a single-channel approach. Where N_i is the normalisation coefficient for the imaginary part of the optical potential.

In this type of calculation, the São Paulo potential is usually used in the real and imaginary parts as $U(R) = (N_r + iN_i)Vspp$, where the N_r and N_i coefficients are the normalisation coefficients for the real and imaginary parts of the optical potential. The normalisation for the real part is $N_r = 1.0$. Experimental data to approximate the theory were obtained from [78], receiving the result for the ground state that can be seen in figure 8.1.

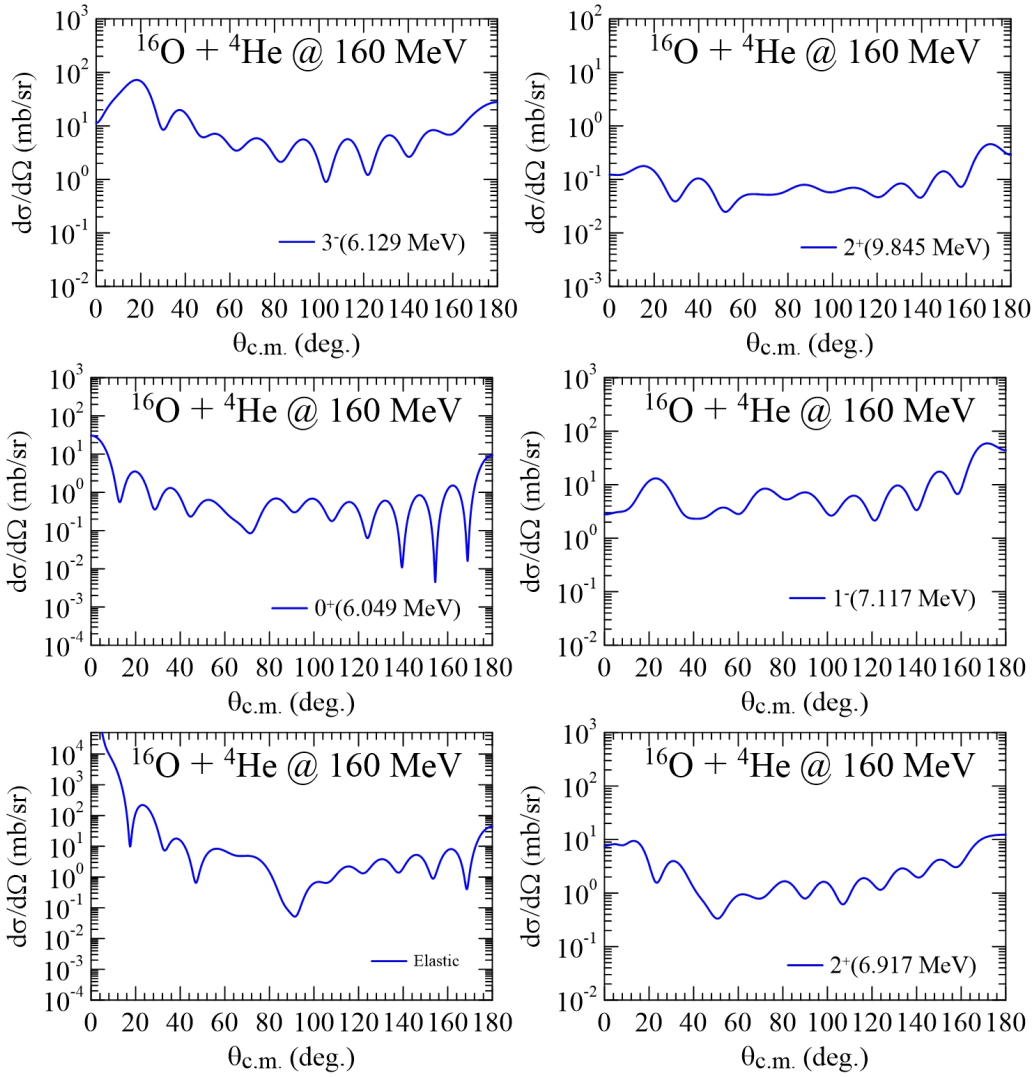

Figure 8.2: The optical model parameters for the São Paulo potential were calculated by Jesús Lubián Ríos and Jonas Leonardo Ferreira for the ground and excited states for this thesis. These cross-sections are calculated for a pure ^{16}O beam with an energy of 10 MeV/n.

The normalisation for the imaginary part in a one-channel calculation (i.e. only the ground states of the projectile and target are considered) is $N_i = 0.2$. If the S.P. potential is replaced by a Woods-Saxon potential with geometric parameters W = - 25.0 MeV, rw = 0.86 fm, and

aw = 0.65 fm, the theoretical angular distribution is very similar to that obtained with the S.P. potential in the imaginary part of the optical potential.

Next (Figure 8.2), the inelastic channels were explicitly included in the Schrödinger equation. In this case, the absorption for the imaginary part of the optical potential should be renormalised to adequately describe the elastic scattering after including the inelastic channels. Therefore, the new parameters of the W.S. in the imaginary part were W = - 12.0 MeV, rw = 0.94 fm and aw = 0.80 fm. The results sent previously were obtained considering the S.P. potential in the real part and the W.S. with the geometric parameters W = - 12.0 MeV, rw = 0.94 fm.

The coupled channel calculation approach was used to obtain the angular distributions, considering the FRESCO code, a program developed by Ian Thompson from 1983 to 2006 to perform coupled reaction channel calculations in nuclear physics [80]. It uses Fortran 90 or Fortran 95 on Unix, Linux, Vax, and Windows machines.

8.1.2 Elastic scattering cross sections and conversion to the centre of mass angles

In nuclear physics, the term "ground state" refers to the lowest energy state of the atomic nucleus. It is the configuration in which the nucleons (protons and neutrons) occupy their lowest energy levels within the nucleus. Understanding this ground state is crucial to understanding the structure and properties of atomic nuclei, as it serves as the basis for describing nuclear excitations and properties in higher energy states.

The ground state of a nucleus plays a central role in determining its stability and various properties, including its spin, parity and magnetic moment. The energy associated with the ground state is directly related to the nuclear binding energy, which quantifies the energy required to hold the nucleons together within the nucleus.

Before calculating the ground state or an excited state, it is checked that the initially estimated drift velocity matches the chamber width, i.e. that the GenFit fit has not introduced vertex deviations that could affect the cross-section calculation. To do this, an accumulation of all events with all vertex traces is plotted against the excitation energy to locate the pad plane and input window walls (Fig. 8.3) and correct the drift velocity before the fit if it is needed.

To obtain the final cross-sections, we proceed as indicated in the flowchart 8.4, starting with the variables obtained in the pattern recognition and making the adjustments based on the Kalman filter and the appropriate corrections.

Once the drift velocity has been set for all events, we work with the highest angled trace that falls within the identification as alpha. This higher angle trace is the scattering alpha that will provide the necessary information to reconstruct the variables in inverse kinematics. With this selection, comparing the pattern recognition and the fit of other essential variables in the calculations, such as the theta and phi angles (Fig. 8.5), is also convenient.

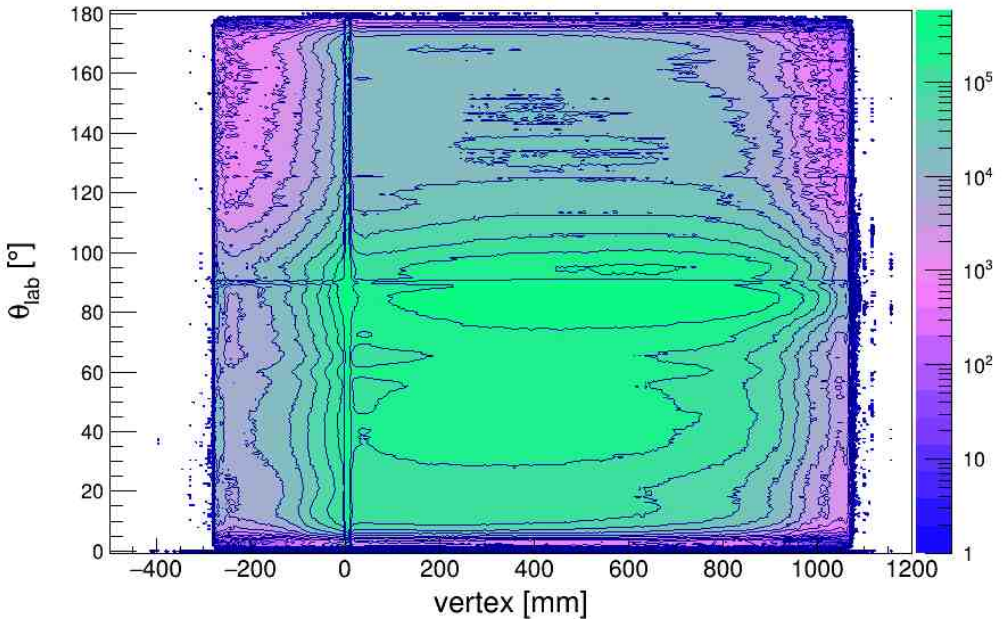

Figure 8.3: The y-axis shows the accumulation of the angles in the laboratory identified with the RANSAC method of all the traces of the experiment, and the x-axis represents the width of the chamber in cm before fitting the data with GenFit and making the vertex corrections. At zero cm, an accumulation belonging to the ATTPC chamber window appears and from 1000 mm onwards, it can be seen that there are hardly any traces identified; what is identified after that is electronic noise, indicating that the choice of drift velocity is optimal for this experiment.

To correct the angles and energies obtained in the adjustment with GenFit, the excitation energy of each scattering alphas is calculated, as shown in section 7.3, from the beam energy, whose calculation can be seen in section 7.1.2, from the masses of the particles involved in the reaction and from the angles and energies obtained from the fit. Once the initial excitation energy has been received, it is corrected by the ground state, which centres it at zero, and it is from this new excitation energy that the correction is carried out. This correction is necessary because, without access to the modifications due to the effects of the electric field, the energies are deformed in the regions close to the edges, and it is a way of minimising these effects.

Working with the missing mass equations (Eq. 7.12), one can arrive at an excitation energy-dependent expression to recalculate the angle with the above corrections.

$$cos(\theta_{sca}) = \frac{\sqrt{\frac{Z_2 T_{beam}^2 + Z_1 C_1^2}{T_{beam}^2 + 2T_{beam} m_{beam}}}}{p_{sca}} \leftarrow p_{sca} = \sqrt{2m_{sca}E_{lab} + E_{lab}^2} \tag{8.5}$$

$$C_1 = dm - m_{tar}E_{eje} + m_{beam}(m_{tar} - E_{eje}) \leftarrow dm = \frac{m_{beam}^2 + m_{tar}^2 + m_{sca}^2 + m_{recoil}^2}{2} \tag{8.6}$$

$$Z_1 = 2C_1(m_{tar} - E_{sca}) \tag{8.7}$$

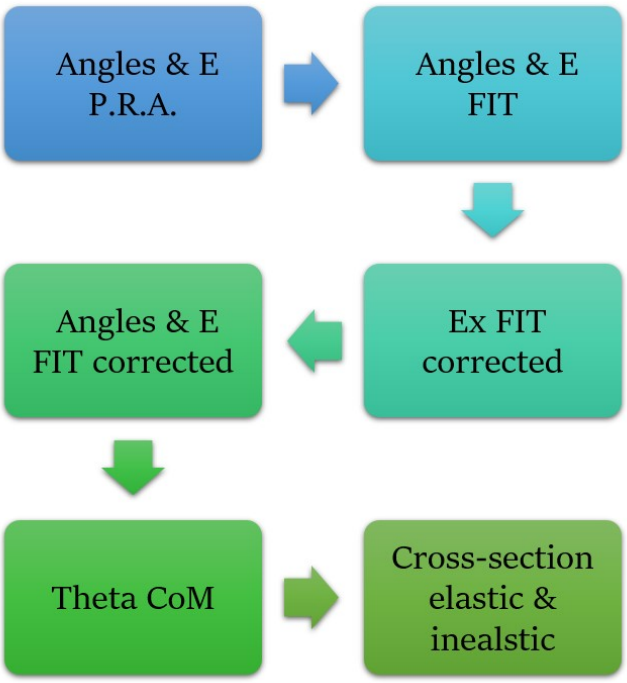

Figure 8.4: Flow chart for calculating the angle at the centre of mass and its subsequent application to the cross-section.

$$Z_2 = (m_{tar} - E_{sca})^2 \tag{8.8}$$

In this experiment, beam and recoil refer to ^{16}O, target (tar), and scattering (sca) refer to alpha particles.

Once the angle for calculating the cross-section has been obtained in the laboratory, the centre of mass is changed. The Mandelstam variables are used to make the change. Mandelstam variables are four commonly used in high-energy particle physics to describe the kinematics of particle collisions. They are defined in terms of the four moments of the particles in the collision. The Mandelstam variables are defined for a scattering process involving two particles, labelled 1 and 2, with four-momentums p1 and p2, respectively.

A definition of the angle at the centre of mass invariant under Lorentz transformations can be obtained using the Mandelstam variables in Appendix A.

From these definitions of inverse kinematics, it is possible to derive the angle at the centre of mass as:

$$\theta_{cm} = \pi - acos(s^2 + s(2t - m_1^2 - m_2^2 - m_3^2 - m_4^2) + \frac{m_1^2 - m_2^2 * m_3^2 - m_4^2(ex)}{\omega(s, m_1^2, m_2^2) \cdot \omega(s, m_3^2, m_4^2(ex))}) \tag{8.9}$$

With $\rightarrow \omega(x, y, z) = x^2 + y^2 + z^2 - 2xy - 2yz - 2xz$

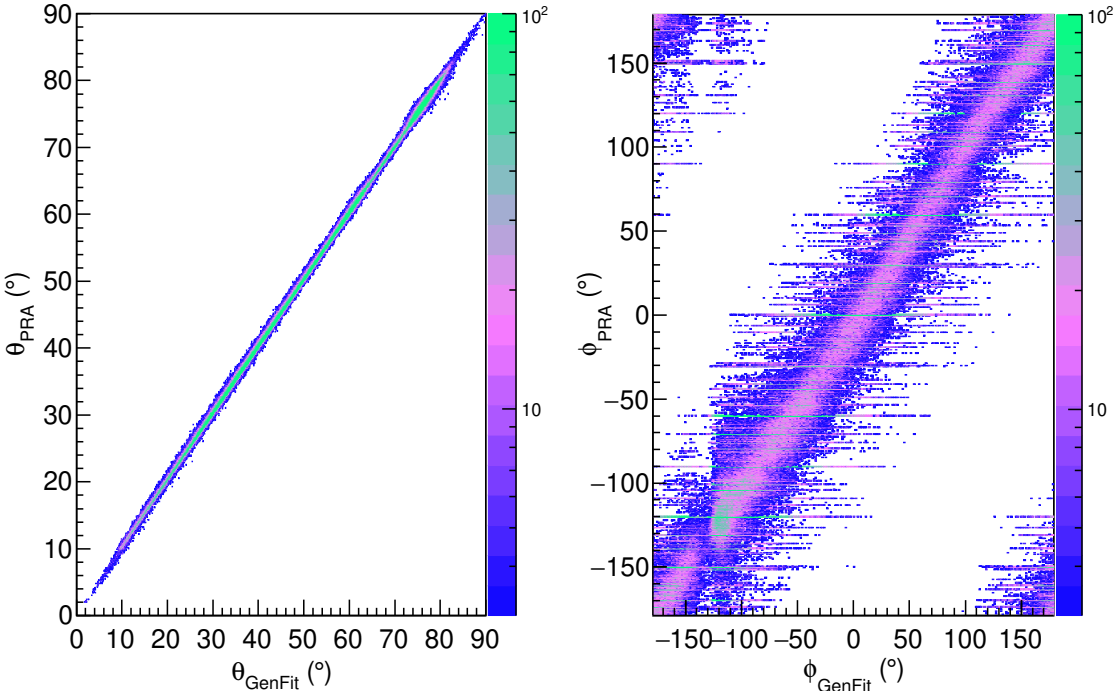

Figure 8.5: The figure on the right plots the theta scattering angle calculated with the RANSAC algorithm against the one fitted with the Kalman filter corresponding to GenFit. The figure on the right shows the same cases with the azimuthal angle. The right-hand figure shows a gap close to 130^0, corresponding to the non-functioning pad plane in this region.

To check for significant deviations in the angle calculations, the angle at the centre of mass is plotted against the angle in the laboratory (Fig. 8.6) and compared with the theoretical results. To compare with the theory, we use the data provided by LISE for an elastic collision with the same experimental conditions and take as inelastic reference two excited states studied in this thesis, the one with higher and the one with lower energies.

In this experiment, the beam comprises pure ^{16}O, with a certain percentage of negligible impurities. To continue the analysis, the events corresponding to elastic collisions are selected. In this case, a selection is made between ± 2 MeV around 0 in excitation energy by the corrections to it that can be seen in figure 7.4. These events are put into a so-called excitation function. This function gives the cross-section for different reaction states. This has three elements to calculate: the centre of mass angle, the centre of mass energy, and the cross-section.

The centre-of-mass angle is the simplest of the three quantities for an elastic reaction at non-relativistic energies. The following equation simplifies the calculation of the angle in the centre of mass.

$$\theta_{cm} = 2(90^o - \theta_{lab}) \tag{8.10}$$

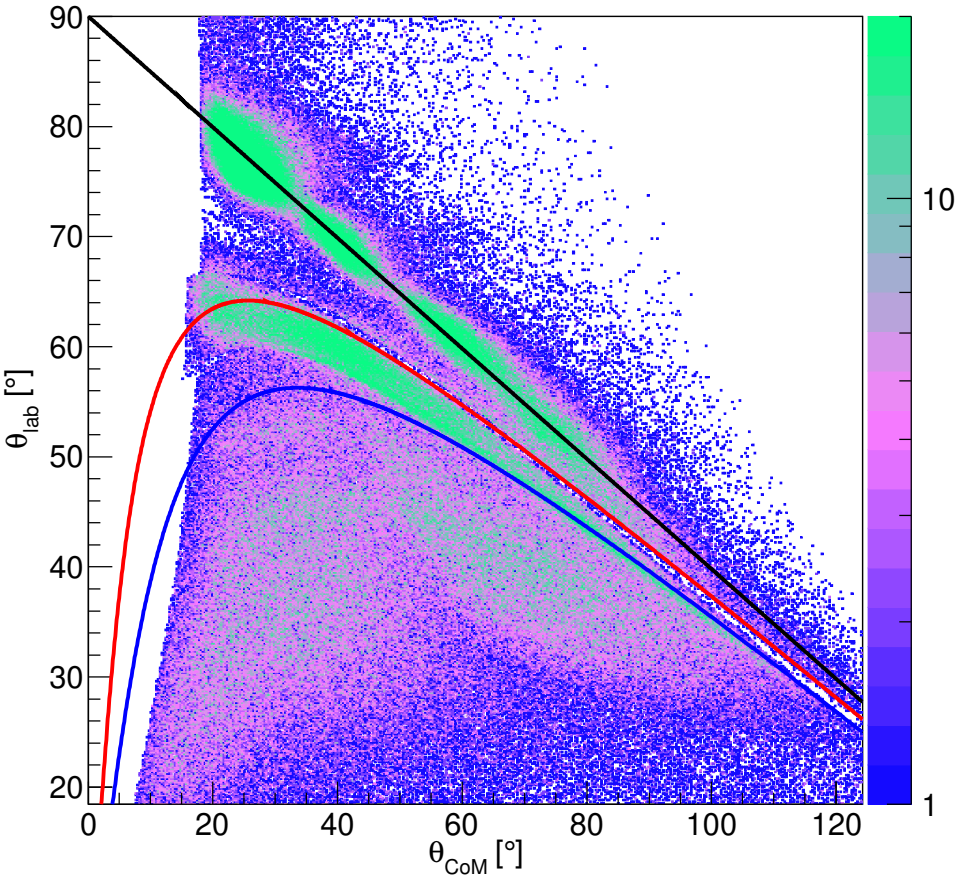

Figure 8.6: Plot of the angle at the centre of mass versus the angle in the laboratory of the scattering particle. The theoretical lines were obtained using LISE++. The ground state is black, the state corresponding to 6.049 MeV is red, and the state corresponding to 9.845 MeV is blue.

8.1.3 Inelastic scattering cross sections

Excited states of a nucleus refer to the energy levels or states of a nucleus that have a higher energy than the ground state. A nucleus can become excited and enter a higher energy state when it absorbs energy, typically in the form of gamma rays or through collisions with other particles.

The excited state of the nucleus can be transient. The nucleus will eventually return to its ground state by emitting the excess energy through gamma rays. These excited states can be observed and studied in nuclear physics experiments and are essential for understanding nuclear structure and how nuclei interact.

Studying the excited states of nuclei is crucial in nuclear astrophysics, nuclear reactors, and nuclear weapons. In some cases, specific excited states play an essential role in nuclear reactions and can significantly influence the behaviour of atomic nuclei in different environments.

Previous experiments, such as Systematic analysis of inelastic α scattering off self-conjugate A=4n nuclease by S. Adachi et al. [81] have measured the yields of the excited states under

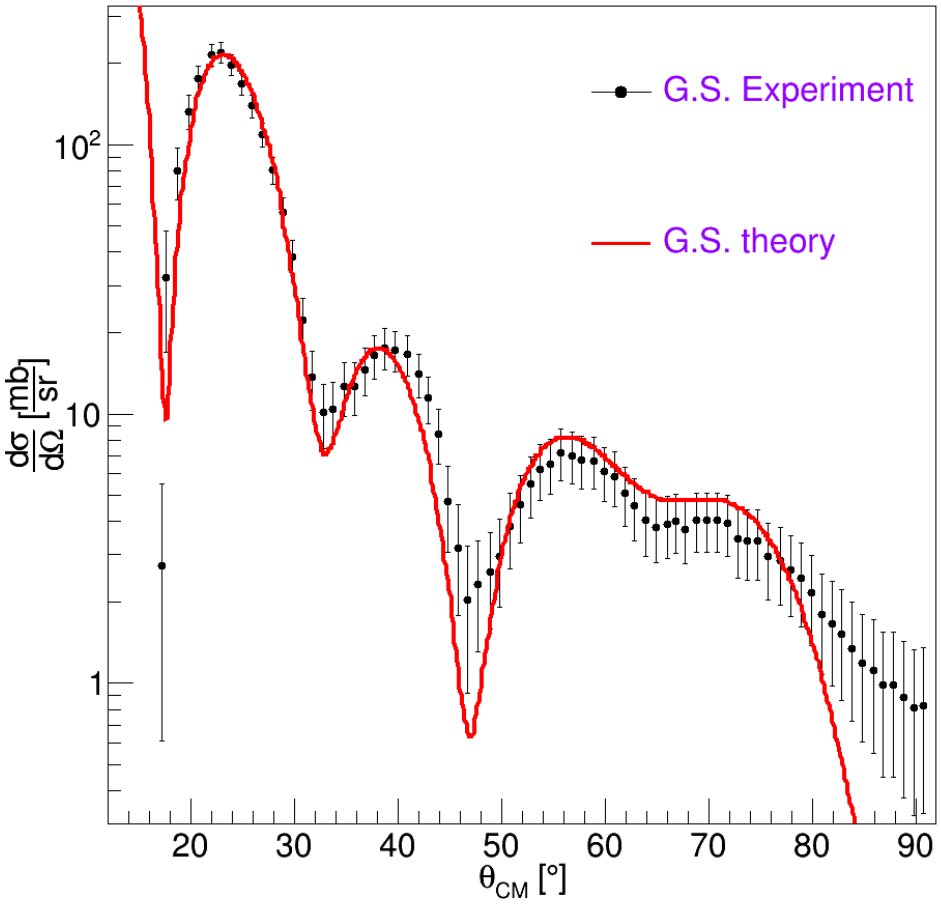

Figure 8.7: Differential cross section for the ground state calculated over the excited energy cutoff between -2 MeV and 2 MeV. The errors are calculated by scaling the number of counts error as $\sqrt{N}$, with N the number of counts for each degree in the CoM.

study, which serve as a starting point for what can be expected when discretising overlapping events.

As shown in figure 8.8, the first two excited states corresponding to L=0 and L=3 strongly overlap. The same applies to the third and fourth excited states, L=2 and L=1. Regarding the yields' intensity, the state corresponding to L=3 stands out from all the others. This and the camera's resolution can make finding the cross-section values for each excited state under study challenging.

In Figure 8.6, it can be noted that the fundamental state agrees with what is expected; for the excited states, it can be seen that there is not enough resolution in the detector to resolve them. Therefore, a multi-decomposition analysis study will be carried out later to find out what percentage of contamination from other states is introduced by the selection of the excitation energy.

For recalculating the energy, it is taken into account that according to equation 7.5, p $\simeq$ B,

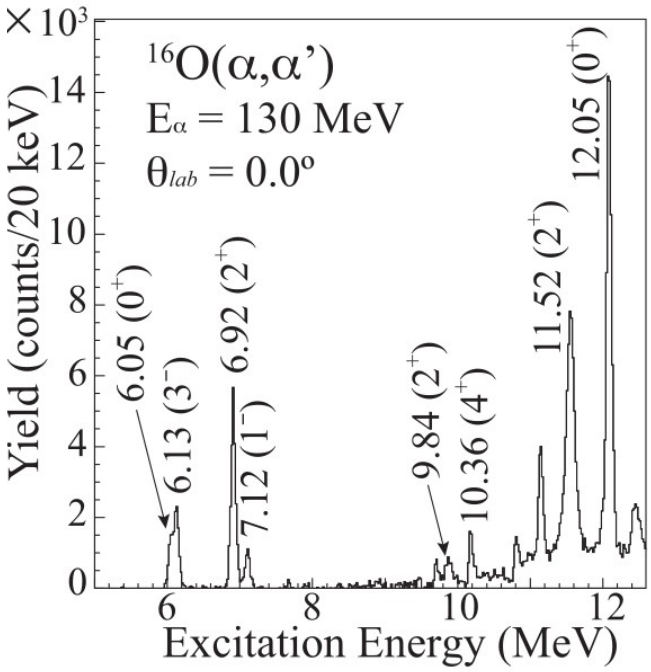

Figure 8.8: Excitation-energy spectra for the (α,α') reactions at E_α = 130 MeV measured at θ lab = 0.0^o Figure taken from [81] (American Physical Society ("APS") license number RNP/25/MAR/089471)

and combining it with the equation 8.11. The energy can be corrected from the new angle as is presented in the equation 8.13.

$$B\rho = \frac{B \cdot r}{sen(\theta_{lab})} \tag{8.11}$$

$$p_{new} \simeq p_{old} \cdot \frac{sen(\theta_{old})}{sen(\theta_{new})} \tag{8.12}$$

$$E_{new} \simeq \sqrt{p_{new}^2 + m_{sca}^2} - m_{sca} \tag{8.13}$$

With this correction for the energy of the scattering particle and its insertion into equation 8.5, we can obtain its angle at the centre of mass for each of the excited states as given in equation 8.9.

Once all the necessary variables have been obtained, the formula 8.4 calculates the differential cross-section. An angular spacing of 1 degree is used for calculating the cross-section since this is allowed by the statistics and the angular resolution for the ground state.

To obtain the cross sections for the excited states, we work the same way as the ground state, taking into account that the efficiencies have to be recalculated individually for each excited

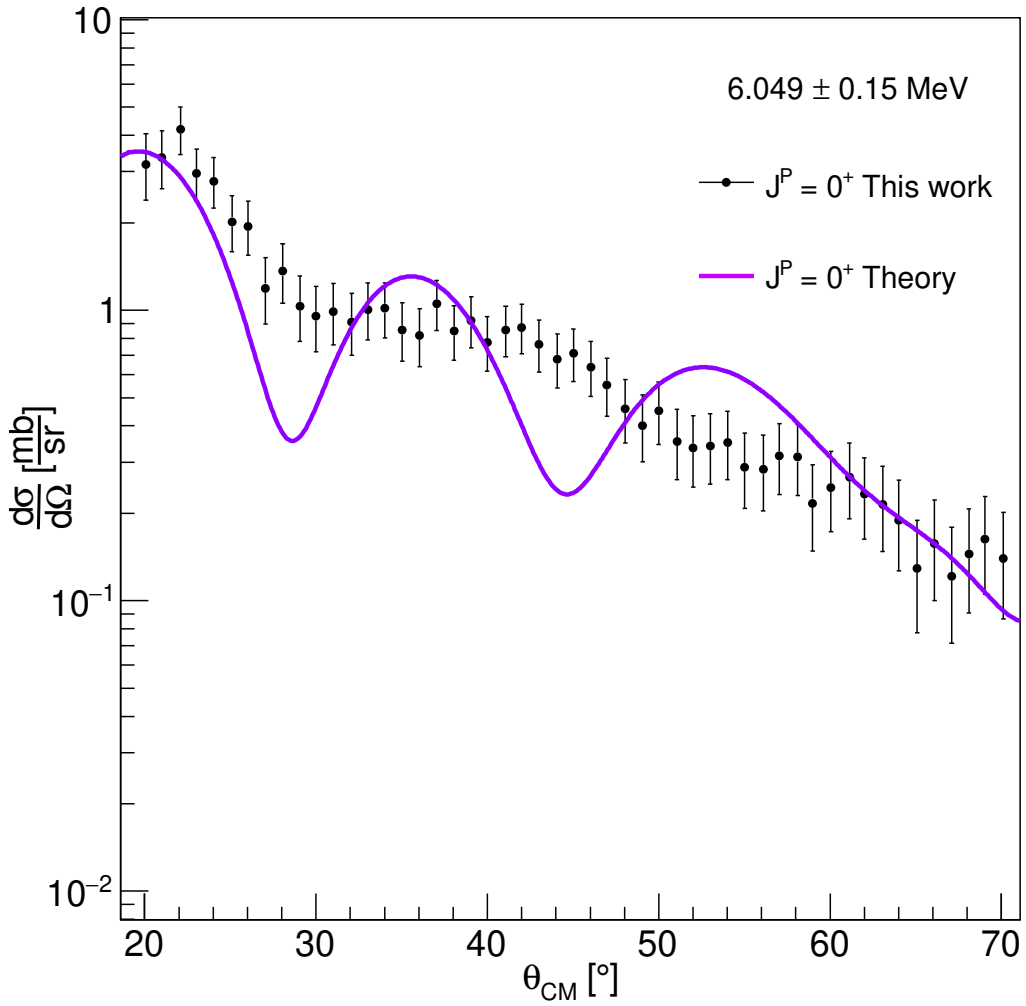

Figure 8.9: Differential cross section for the first excited state corresponding to the theoretical excitation energy 6.049 MeV of oxygen l=0. The calculation is performed for an excitation energy cutoff of 300 KeV around this value. The purple line corresponds to the theoretical X.S. value.

state and that the angle at the centre of mass is calculated from the equation 8.4, making 300 keV cuts in the excitation energy around the energies tabulated in theory (Fig. D.1).

E_x [MeV]	J^P	Factor	χ^2/ndf	$\theta_{CM}low[\circ]$	$\theta_{CM}high[\circ]$
0	0^+	0.295 10^{-3}	0.872	20	80
6.049	0^+	x 1.912	1.074	20	70
6.129	3^-	x 1.886	0.955	20	65
6.917	2^+	x 1.5067	2.121	20	50
7.117	1^-	x 2.499	2.114	20	50
9.845	2^+	x 0.406	0.765	20	60

Table 8.1: Experimental results of the cross-sections calculated according to the formula 8.4 between the angles at the centre of mass indicated in the table. These values are calculated at 300 KeV around the theoretical excited state for all excited states. In the case of GS they are ± 2 MeV around 0 MeV.

8.2 Multi-Decomposition-Analysis (MDA)

Multipole decomposition analysis (MDA), applied to inelastic alpha scattering, is invaluable in delineating the strength distribution in excitation energy regions where multiple states overlap. It has been widely used in the study of nuclear incompressibility and clustering structures within nuclei. Therefore, investigating and resolving this puzzle in the context of inelastic alpha scattering is crucial. Surprisingly, no systematic measurement of inelastic alpha scattering has been carried out to assess the reliability of the theoretical calculations used in the MDA.

Individual portions around excitation energies between 6 and 10 MeV are taken to perform MDA, making 300 KeV cuts centred on each theoretical energy. Once the cuts have been selected, MDA is applied to each of them to obtain the new theoretical curves of the angular distributions and fit them to them.

$$\left.\frac{d\sigma}{d\Omega}\right|_{exp} = \mathcal{F}\frac{N^{mesure}}{2\pi\Delta\theta_{CM}sin(\theta_{CM})\mathcal{E}} \tag{8.14}$$

A single cross-section predicted by multiplicity is used, assuming that the shape of the differential cross-section remains constant for a given multiplicity regardless of the excitation energy. Furthermore, it was verified that our conclusions remain consistent even when we fail to make this approximation. Centroids and amplitudes of observed resonances coincided, regardless of assuming that theoretical angular distributions are dependent on excitation energy. Each predicted cross-section had been normalised to correspond to 100% of the energy-weighted summation rule.

The normalisation factors obtained with the MDA method for each state studied in this work are in table 8.2.

Figure 8.10 shows the multi-decomposition analysis of the four excited states between 5.5 and 7.5 MeV that are the subject of this thesis. It can be seen how the states corresponding to L=0, L=2 and L=3 are dominant in the decomposition for angles between 20º and 50º CoM, which is in agreement with S. Adachi et al. in 8.8.

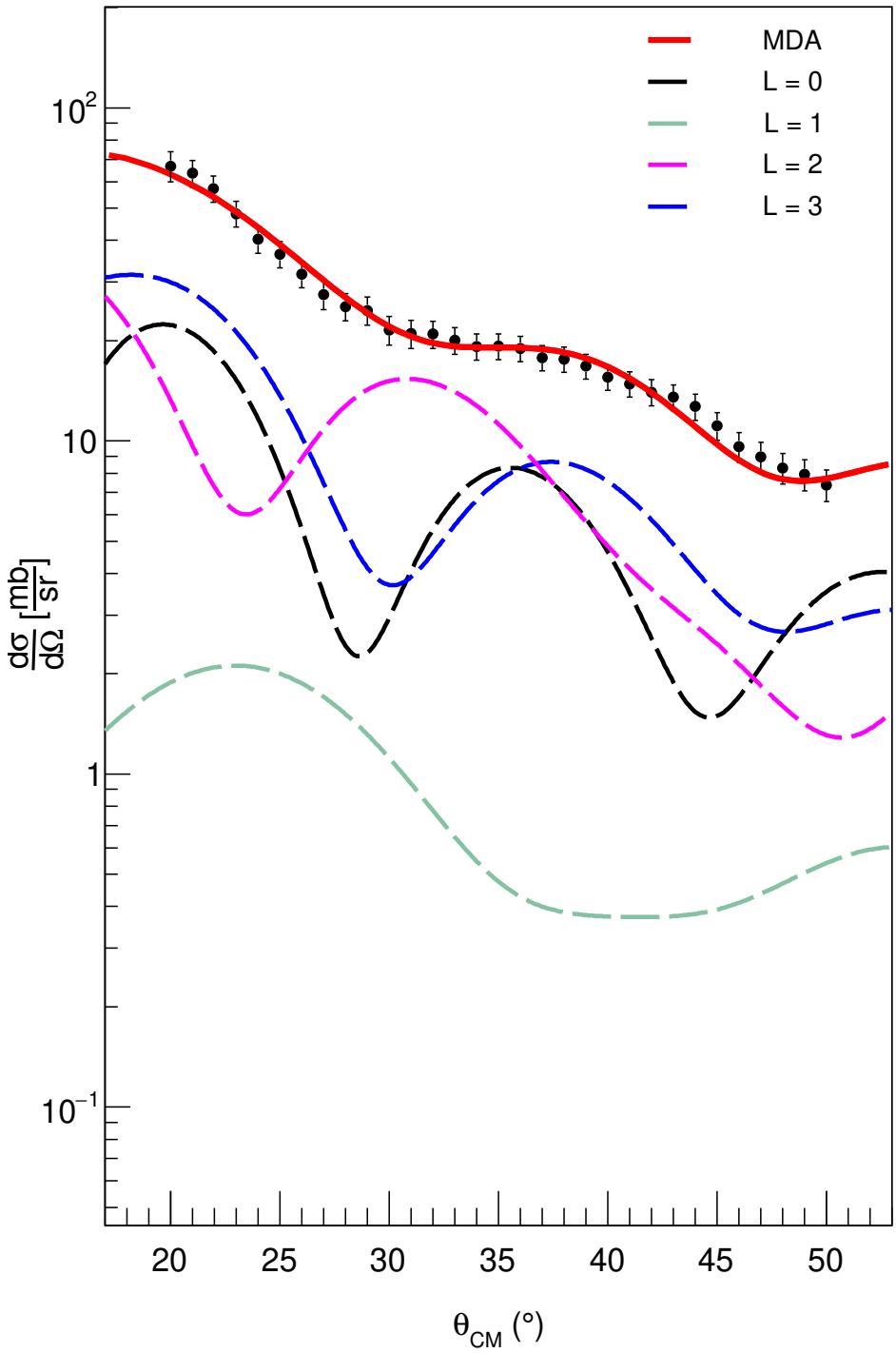

Figure 8.10: Multi-decomposition analysis for excited states around 6 and 7 MeV. In particular, a range of energies between 5.5 MeV and 7.5 MeV is selected for the fit. The state corresponding to 6.049 MeV is shown in black, 7.117 MeV in green, 6.917 MeV in pink and 6.129 MeV in blue. The red line represents the MDA taking these four states with the selection in excitation energy mentioned above.

E_x [MeV]	MDA	Normalization factor	$\Delta\theta_{CoM}$
Between	l = 0	6.357 (± 2.239)	
5.5 MeV	l = 1	0.161 (± 0.129)	20^o - 50^o
-	l = 2	3.864 (± 0.346)	
7.5 MeV	l = 3	0.436 (± 0.241)	

Table 8.2: Table MDA ^{16}O. This thesis studies the relative normalisation factors for the convolutions of Multi-decomposition analysis of the different excited states around 5.5 and 7.5 MeV.

With multi-decomposition analysis, an individual study of each state is performed, taking as reference the same values taken for the individual fit of excited states, i.e., it is fitted for values of 300 KeV around each of the excited states and using the same angular limits.

The states L=0, L=3 and L=2, L=1 are too close (less than 200 KeV), making the decomposition of states in the area between 6 and 7 MeV very difficult, considering the spatial resolution of AT-TPC.

Multiple adjustments are made, and each excited state's normalisation factor is calculated, trying to take a limit of integration appropriate to the detector's resolution, obtaining MDA results that do not agree with the experiment's physics. Due to the low statistics and resolution of the AT-TPC detector the best option to obtain a consistent result is the one presented in Figure 8.10, where an MDA is performed between 5.5 and 7.5 MeV covering all four excited states.

Fluctuations in the fits may be due to effects not accounted for in the theoretical model or minor deviations in the range calculation from the energy deposited by the projectile. It may also be due to the uncertainty associated with the optical potential parameters, which can sometimes be as high as 20 % to 30 % [82].

8.3 Hoyle state Branching Ratio

Multiplicity, or the number of traces detected per event, is used for calculations related to the Hoyle effect and branching ratio. The experiment is divided into different multiplicities, and depending on the type of event to be treated, one or the other is chosen. For example, the elastic collisions must have a multiplicity of 2 or 1 if the pad plane does not identify the weighing trace.

To find the events corresponding to the Hoyle effect, the reactions $^{16}O^* + \alpha \rightarrow {}^{12}C + \alpha$; $^{16}O^* + \alpha \rightarrow {}^{12}C^* + \alpha \rightarrow {}^{8}Be + 2\alpha$ and $^{16}O^* + \alpha \rightarrow {}^{12}C^* + \alpha \rightarrow 3\alpha + \alpha$ are studied by separating them into different multiplicities. These reactions are studied precisely to find an indirect value of the B.R. in the first two equations following the steps of article [3] and to obtain a direct value of the Hoyle state from the decay of the excited Carbon with enough energy to decay alpha again.

Recent experimental results give an upper limit on the direct decay of the Hoyle state into 3 α compared to the sequential decay into $^{8}Be + \alpha$ of less than **0.043**% (95% C.L.).

The full kinematics of the reaction is reconstructed by simultaneously detecting the four alpha particles emitted in the final state, namely the alpha ejected used to mark the excitation of the ^{12}C residue in the Hoyle state ($E^* = 7.654$ MeV), and the three alpha particles fed by the Hoyle state decay.

Once the events are separated by several traces per event or multiplicity, a second, finer selection is made to identify the different reactions. As it has been done so far, to work with the excitation energy, we work with the trace with the highest angle, which is statistically assumed to be the scattering alpha of the primary reaction.

The conditions imposed on the intra-event trace identification algorithm for different multiplicities are as follows:

- **Multiplicity 3**
  - $\boxed{^{12}C + \alpha}$
    - For the scattering alpha from $^{16}O + \alpha$, a minimum excitation energy of 7.162 MeV is required for ^{16}O to decay to alpha.
    - The second highest angle particle must be an alpha particle identified in the PID.
    - The particle with the lowest angle will necessarily be a heavy particle corresponding to the ^{12}C
  - $\boxed{^{8}Be + 2\alpha}$
    - As in the previous case, the $Q(\alpha_{sca}) \geq 7.162$ MeV threshold for oxygen must be exceeded.
    - In this case, as there are only three particles, the aim is to recover events where a trace has not been identified for whatever reason. This requires that the two remaining particles or one of them is alpha as a first step.
    - In the case of finding more alpha particles, the traces are checked two by two, and it is imposed that the angle between them is sufficiently small (e.g. $5^{\underline{o}}$) since the beryllium decay alphas are correlated and will practically go together.
  - $\boxed{3\alpha + \alpha : \textbf{Hoyle}}$
    - This possibility is ruled out since, in the thesis experiment, having 16O versus alpha in the output channel would give five alphas, and it is doubtful that the scattering alphas and the second larger angle alpha would not be identified and at the same time recover the three alphas of the Hoyle effect.

- **Multiplicity 4**

  - $\boxed{^{12}C + \alpha}$

    * The reaction in the outflow channel has three elements: alpha from scattering with oxygen and Carbon and Helium from decomposition. As in previous events, we check that the excitation energy is sufficient to reach this state and check if there has been any misidentification of traces, such as electronic noise identified as traces or broken traces identified as two independent ones.

  - $\boxed{^{8}Be + 2\alpha}$

    * As in the case of multiplicity three, it is necessary to achieve $Q(\alpha_{sca}) \geq 7.162$ MeV threshold for oxygen.

    * Here, it is interesting that all the particles are alphas, or all but one, which would correspond to ^{8}Be.

    * As in the previous case, we check two by two if the alphas are correlated and very little separated; in case we find four separated two by two, we would be facing a case of double decay of two 8Be and the loss of the identification of the scattering particle.

  - $\boxed{3\alpha + \alpha : \textbf{Hoyle}}$

    * In the case of the Hoyle state, it has to exceed the 7,162 MeV excitation energy of the oxygen experiment and 7,765 MeV needed for the remaining Carbon to decay to three alpha of the Hoyle state.

    * The excitation energy of the scattering particle is set between 14 and 15 MeV.

    * For this experiment, it is expected to find five alphas for the Hoyle effect, so it is assumed that if it meets the above conditions, it is taken as a valid event, and it is checked in the visual form if these are events in which the scattering alpha has not been identified as it is the lowest energy.

- **Multiplicity 5**

  - $\boxed{^{12}C + \alpha}$

    * This channel is treated in the same way as the analysis for multiplicity 4.

  - $\boxed{^{8}Be + 2\alpha}$

* As in the case of multiplicities 3 and 4, the first of the filters is the oxygen $Q(\alpha_{sca})$.

* In the same way as for multiplicity 4, the right combination of ^8Be and alpha is sought that makes angular sense.

* In this case, searching for and even differentiating double decays from a single decay, thanks to the detector's resolution, which can separate traces very close to the scattering angle, is possible.

– $3\alpha + \alpha$: **Hoyle**

* In the case of the Hoyle state, it has to exceed the 14,765 MeV excitation energy, which is the theoretical value to date of the Hoyle state.

* The excitation energy of the scattering particle is also set between 14 and 15 MeV, so is left half a MeV around the theoretical value.

* Again, it is assumed for first filtering that if it is within the excitation energy range and considering that all the particles in the output channel are alphas, the Hoyle event can be considered. In this case, one has to be very careful as it may be the case that it is a space phase coming from the direct decay of oxygen into four alphas.

In cases where multiplicity six or higher is found, the same approach is used for multiplicity 5, considering events identified erroneously with broken traces or with a low number of specified points on the pad plane (possibly electronic or identification algorithm noise).

8.3.1 Dalitz plot

In a second filtering step, the Dalitz plot will be used. A Dalitz plot is a graphical representation of the distribution of squared invariant masses in a three-body decay. In particle physics, it is often used to analyse the distribution of a particle decaying into three daughter particles. The Dalitz plot can be constructed based on the squared invariant masses of the daughter particles.

The Dalitz plot, named after its inventor Richard Dalitz (1925-2006), was first applied to the "$\tau - \kappa$ puzzle". This puzzle involved strange particles that decayed to 2 or 3 pions, now understood as different decay modes of kaons [83].

Dalitz describes the decay of a particle with spin zero into three other particles of spin zero and the invariant mass and quantum states of resonances associated with the decay.

The Dalitz plot variables are usually defined as:

- $s_{12} \rightarrow$ The squared invariant mass of particles one and 2.
- $s_{13} \rightarrow$ The squared invariant mass of particle one and particle 3.
- $s_{23} \rightarrow$ The squared invariant mass of particle two and particle 3.

These variables can be represented in the form of:

$$s_{12} = (p_1 + p_2)^2 = (E_1 + E_2)^2 - (\mathbf{p}_1 + \mathbf{p}_2)^2 \tag{8.15}$$

$$s_{23} = (p_2 + p_3)^2 = (E_2 + E_3)^2 - (\mathbf{p}_2 + \mathbf{p}_3)^2 \tag{8.16}$$

$$s_{13} = (p_1 + p_3)^2 = (E_1 + E_3)^2 - (\mathbf{p}_1 + \mathbf{p}_3)^2 \tag{8.17}$$

Here, p_i represents the four-momentum of particle i, and E_i and $\mathbf{p}_i$ are its energy and three-momentum, respectively.

In a Dalitz plot, it is usually plot s_{12} on one axis and s_{13} on the other axis or s_{12} on one axis and s_{23} on the other, depending on the specific analysis you are conducting.

The distribution of events in the Dalitz plot can provide information about the dynamics of the particle decay process. Different regions of the Dalitz plot correspond to other physical processes or amplitudes, and their analysis can contribute to an understanding of the underlying physics.

The Dalitz plot is a visual representation of the phase space of triple decay involving only spin-zero particles, as is the case when looking for the Hoyle space in the decay of Carbon in three alphas. For a three-body decay of spin-0 particles, the Dalitz plot will exhibit a characteristic triangular shape arising from the kinematic constraints imposed by energy and momentum conservation.

We must consider the number of degrees of freedom in a final state with three particles of spin 0.

There are 12 initial degrees of freedom corresponding to the Lorentz quadrivectors where the masses of the three particles are known, the laws of conservation of energy and momentum give us another four unknowns, and finally, the system can rotate in the three directions of the XYZ plane. So, as shown in table 8.3, the problem can be reduced to two independent variables.

CONSTRAINTS	Degree of Freedom
3 four-vectors	12
4 momentum conservation	-4
3 masses	-3
3 Euler angles	-3
TOTAL	2

Table 8.3: Table of degrees of freedom (d.o.f.) for a 3-body decay. The total number of independent degrees of freedom is 2.

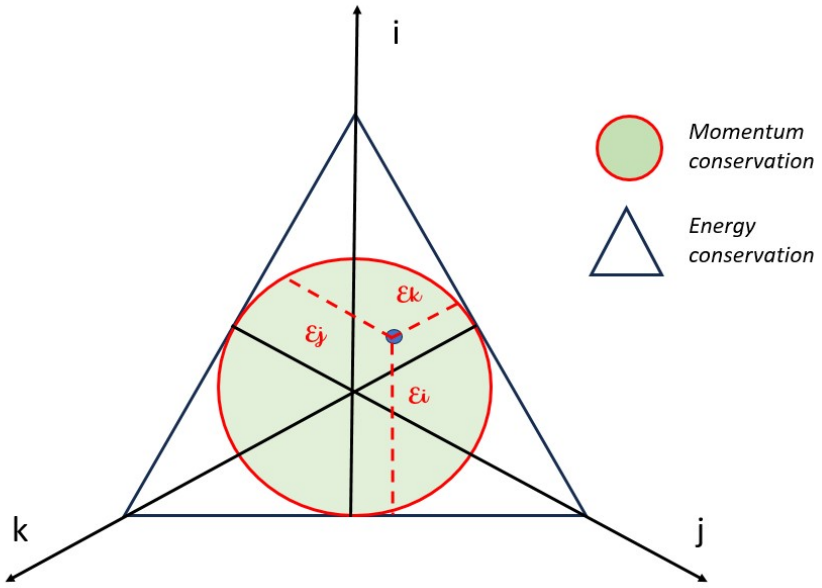

Figure 8.11: The figure represents the conservation of momentum and energy in a three-dimensional representation of three particles leaving the same reaction.

Viviani's Theorem is a geometric result that relates a point inside an equilateral triangle to the distances to the sides of the triangle. The Theorem is named after its discoverer, the Italian mathematician Vincenzo Viviani, and states the following:

In an equilateral triangle, if a point is chosen in the triangle's interior, line segments are drawn from that point to the triangle's three vertices. The sum of the lengths of these line segments equals the size of one side of the triangle (Figure 8.11).

The following equations are used to calculate the Dalitz figure:

$$x = \frac{\sqrt{3}(\epsilon_2 - \epsilon_1)}{2Q} \tag{8.18}$$

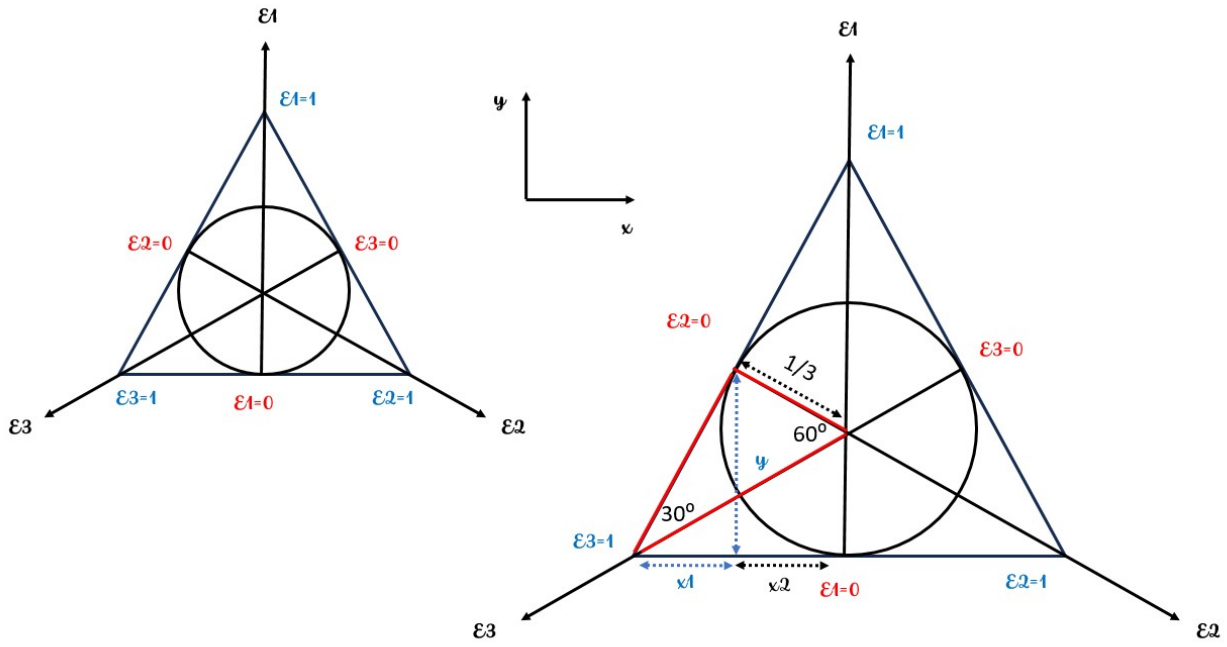

Figure 8.12: Trigonometric representation of the energies of the three particles involved in the decay, leading to the equations 8.18 and 8.19 to be represented to differentiate between direct and sequential decay processes.

$$y = \frac{(2\epsilon_3 - \epsilon_1 - \epsilon_2)}{2Q} \tag{8.19}$$

Where $Q = (\epsilon_1 + \epsilon_2 + \epsilon_3)$ and ϵ_i is the kinetic energy of each particle involved in the process, and the numbering of the particles is arbitrary. The result is an equilateral triangle with three axes of symmetry that go from each point of the triangle to the centre of the opposite side.

The square of the invariant amplitude gives the three-body decay, M $\rightarrow$ 1 + 2 + 3. If the invariant amplitude is constant, the Dalitz diagram is uniformly populated (Figure 8.13) a. A three-body disintegration is determined by the invariant square of the length.

Fermi's golden rule eq gives the differential decay width for the decay of a particle of mass M and quadri-momentum P, which decays into n particles with momentum p_i. 8.20 .

$$d\Gamma_n = \frac{S\,|\mathcal{M}|^2}{2M} dN_n(P; p_1, p_2, \ldots, p_n) \tag{8.20}$$

Where:

- $d\Gamma_n \rightarrow$ Decay rate or dispersion rate for a physical process involving n final particles. It represents the probability of a specific event occurring with n final particles.
- $S \rightarrow$ symmetry term or a coupling constant.

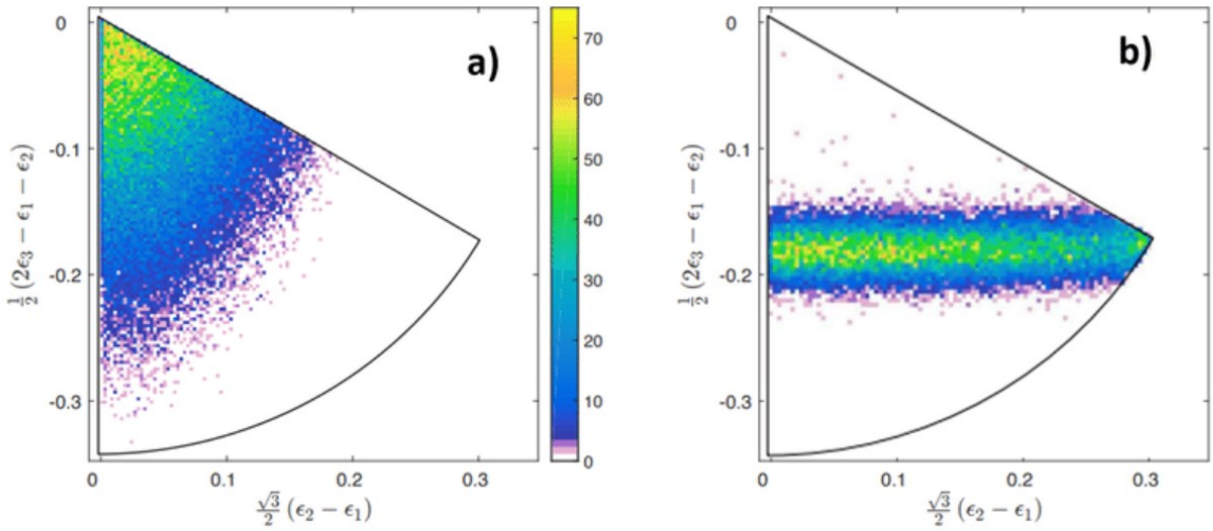

Figure 8.13: a) Dalitz plot showing the energy distribution in a 3-body decay, with the centre of the Dalitz plot dominating, consistent with an equal energy distribution. b) The Dalitz plot shows the sequence of Hoyle's decay, with a few points outside the sequence. Figure taken from [84]

- $|\mathcal{M}|^2 \rightarrow$ The square of the matrix element, which is a quantity related to the probability amplitude of the physical process. It is a measure of the probability of the process occurring.

- $dN_n(P; p_1, p_2, \ldots, p_n) \rightarrow$ Differential element of the phase space for the physical process. It describes how the final particles are distributed in phase space, where P is the total quadri-momentum of the system and p1,p2,...,pn is the quadri-momentum of the final particles.

In a three-body collision for the Lorentz invariant phase space volume, the differential element is written as follows:

$$dN \propto \int p_1\, dp_1\, p_2\, dp_2\, p_3\, dp_3 \frac{1}{E_1 E_2 E_3} \delta(E_1 + E_2 + E_3 - M) \tag{8.21}$$

If it is taken into account that:

$$E_1^2 = p_1^2 + m_1^2 \rightarrow 2E_1\, dE_1 = 2p_1\, dp_1 \tag{8.22}$$

Lorentz invariant phase space volume can be rewritten as:

$$dN \propto dE_1\, dE_2 \int dE_3\, \delta(E_1 + E_2 + E_3 - M) = \int dE_1\, dE_2 \tag{8.23}$$

or any other two variables, therefore:

$$dN \propto dm_{12}^2 \cdot dm_{23}^2 \tag{8.24}$$

Inserting the result obtained in equation 8.24 into equation 8.20 and substituting the symmetry constant for its value gives the decay rate.

$$d\Gamma = \frac{1}{(2\pi)^3} \frac{1}{32M^3} |\mathcal{M}|^2\, dm_{12}^2 \cdot dm_{23}^2 \tag{8.25}$$

The non-uniformity in the population of the Dalitz diagram gives information about the final state interactions in the decay. If interactions occur between the different final states, the Dalitz plot has a shape that depends on the resonance formed; two-body resonances emerge in such diagrams. In particular, the 2-body resonances will appear in the Dalitz diagram visibly (Figure 8.13 b).

The kinetic energy functions given in equations 8.18 and 8.19 are plotted to select the events, only selecting energies around the possible Hoyle state with a width of 1 MeV. As shown in Figure 8.18, the characteristic triangle of the Dalitz type is obtained in the simulation. Once this is received, the centre of the resulting equilateral triangle is found, and the circle inscribed in its interior is traced. The events belonging to the interior of the circumference are those susceptible to Hoyle events. The points are located within the circle's boundary with the unit radius, or point of minimum energy for the three particles which satisfy that $\epsilon_1/Q + \epsilon_2/Q + \epsilon_3/Q = 1/2$ in the present case.

8.3.2 Simulations

To verify the data obtained in the Dalitz plot, two simulations are carried out, one for the decay of Carbon through a previous decay through ^8Be, which decays in 2 alphas with an approximate width of 0.1 MeV, and another one for the decay of ^{12}C in three alphas as we can see in figure 8.14.

This type of simulation aims to test the capacity of the method used to solve events such as those dealt with in this thesis. It aims to test the selection of traces made by pattern recognition and the subsequent use of these variables in the adjustment made with Genfit. In all cases, the same constraints are used for the real data.

The simulation uses the Geant4 toolset implemented in ATTPCROOTv2 and adapts it to the experiment analysed in this thesis.

Initially, the geometry of the system to be simulated is defined. This involves describing the location and shape of objects and detectors in a three-dimensional environment. Geant4

provides tools to create detailed geometries, such as geometric solids and volumes, which, as an active target experiment, the entire cylinder interior will act as an active detector or volume for the whole of the cylinder interior.

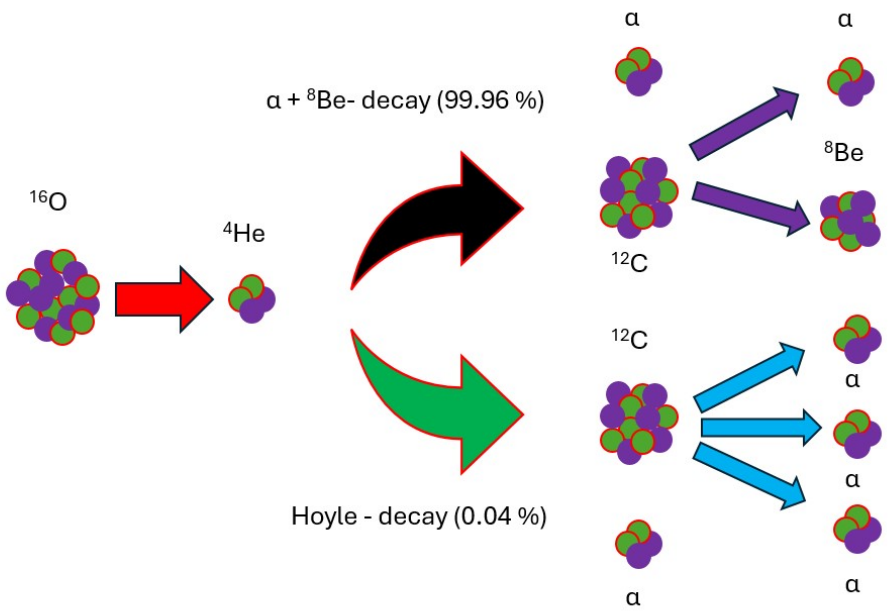

Figure 8.14: Ideographic scheme for the two decay channels contributing to the Hoyle state. On the one hand, we have the sequential decay of Carbon into Beryllium and Helium, and on the other, the appearance of the triple-alpha characteristic of the direct Hoyle effect.

The dimensions to be simulated will be 1 m in length and a 29 cm base radius for the cylinder containing the gas. The gas will consist of pure Helium at 700 Torr pressure or a 0.00015 g/cm^2 density. On the other hand, a magnetic field of 3T parallel to the electric field of 50 V/cm will be implemented, which will have the same direction as the beam. The beam is simulated as a collimated beam of 2 cm thickness and an initial energy of 10 MeV/n of pure ^{16}O.

The two simulations are carried out in two stages as described below:

- **Sequential decay**: For the consecutive decay of ^8Be, a first simulation is performed with the inelastic collision of ^{16}O with 14.528 MeV excitation energy against an alpha particle, which will produce three alphas and an 8Be particle. The excitation energy is imposed to have enough energy to alpha-decay oxygen and subsequently ^{12}O. In the second step, this nuclide is decayed into two alphas (Figure 8.15).

  One of the main problems in identifying this type of event, as seen in Figure 8.15, is the overlapping of the traces tested to avoid broken traces in pattern recognition and the subsequent adjustment with GenFit. In calculating simulations, we tried to analyse real data coherently and carried them out using the same parameters to filter it.

Like Beryllium in two alphas, it shares the same vertex and has practically the same angle. Part of the beginning of the trace is identical at the time of identification. Many of them can be identified by multiplicity in the experimental data as a non-decaying ^{8}Be particle or even a three-body reaction if one of the traces is lost. Identification in the Dalitz plot may be impaired for this reason.

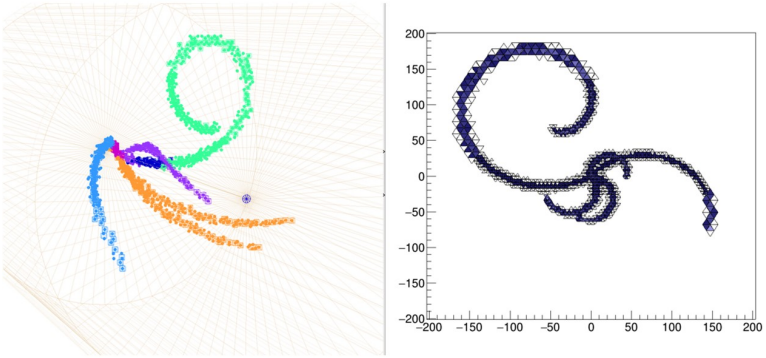

Figure 8.15: Simulation sequential decay. The figure on the right shows a three-dimensional representation of a sequential decay of ^{16}O into four alphas. Orange shows the ^{8}Be decaying to 2 alphas, and purple shows the third alpha of the intermediate ^{12}C. The scattering alpha is shown in green. The figure on the right represents the image formed on the padplane.

- **Direct decay**: In the case of the Hoyle state, a first step in the simulation is performed in which ^{16}O decays inelastically with excitation energy 7.336 MeV (minimum energy for Q(α)) at ^{12}C plus one alpha and in a second step the decay of ^{12}C into three alpha particles is simulated (Figure 8.16).

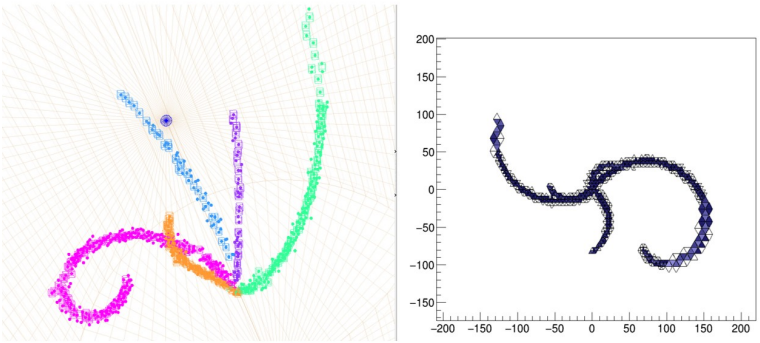

Figure 8.16: Simulation direct decay. The figure on the right shows a three-dimensional representation of a direct decay of ^{16}O into four alphas. Orange, blue and purple traces represent the triple-alpha decay (Clearly separated) of the intermediate ^{12}C. The scattering alpha is shown in pink. The figure on the right represents the image formed on the padplane.

Direct decay does not have trace identification problems like $8Be$, and it is easier to simulate and check the Dalitz plot. The excitation energy imposed in the simulation is 14.44 MeV, obtained in previous experiments.

Once Monte Carlo performs the simulation, it is checked if the fitting methods give logical results, i.e. if the simulated excitation energies and angles are recovered once the data have been passed through the Kalman Filter fitting program. The data obtained in the two simulations are merged and fitted to see if the algorithm used on the data can discretise events with the same multiplicity but coming from different types of decay at similar energies. The Dalitz plots for each case should resemble those described above.

To check the response of the methods used, several simulations are carried out around the area of interest, i.e. between 14.5 and 15.5 MeV, so there is sufficient energy for the alpha decay of oxygen and the subsequent decay of Carbon.

The simulations involve collisions of oxygen with Helium, leading to Carbon's direct or indirect decay into three alpha or Beryllium plus alpha, respectively.

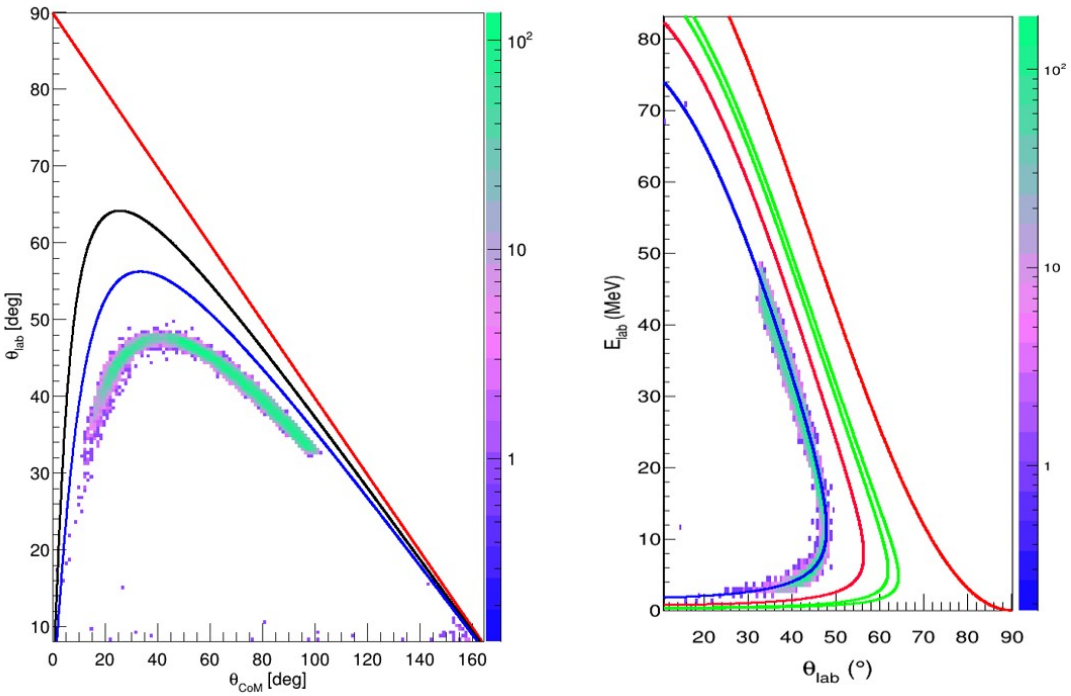

Figure 8.17: In the two figures, we can see the representations of the energies and centre of masses angles for 20000 simulations (10000 direct and 10000 sequential) of oxygen decaying in the two channels under study. The left figure shows the angle in the laboratory versus CoM, and the right figure shows the energy versus angle in the laboratory reference system. The outer red lines represent the G.S. of Oxygen colliding in Helium, and different lines of inelastic collisions between two particles are represented towards the inside. The figure on the right shows how the black line corresponding to the scattering of Carbon coincides with the simulated energies and angles after fitting with the same methodology as for the experimental data.

Several simulations covering the most sensitive area regarding identification are performed to test the fitting method used in the thesis to the experiment data. The simulations are performed at 160 MeV beam energy and with an energy width of 5 MeV to make the possible fluctuations in energy more realistic.

Different simulations run at energies from 14.5 to 15.5 MeV to ensure coverage within the alpha decay zone of Carbon. The simulations are performed in 2 steps. In the first step, we simulate the inelastic collision of ^{16}O on ^{4}He, giving rise to 2 α and a carbon; in the second step, we simulate the decay of the Carbon in the two possible channels, sequential or direct.

As shown in figure 8.17, the simulations and subsequent adjustments maintain good behaviour in terms of the angles in the laboratory and the CoM, as well as in the energies obtained since they are arranged around the kinematic line of the Carbon for this initial Oxygen energy.

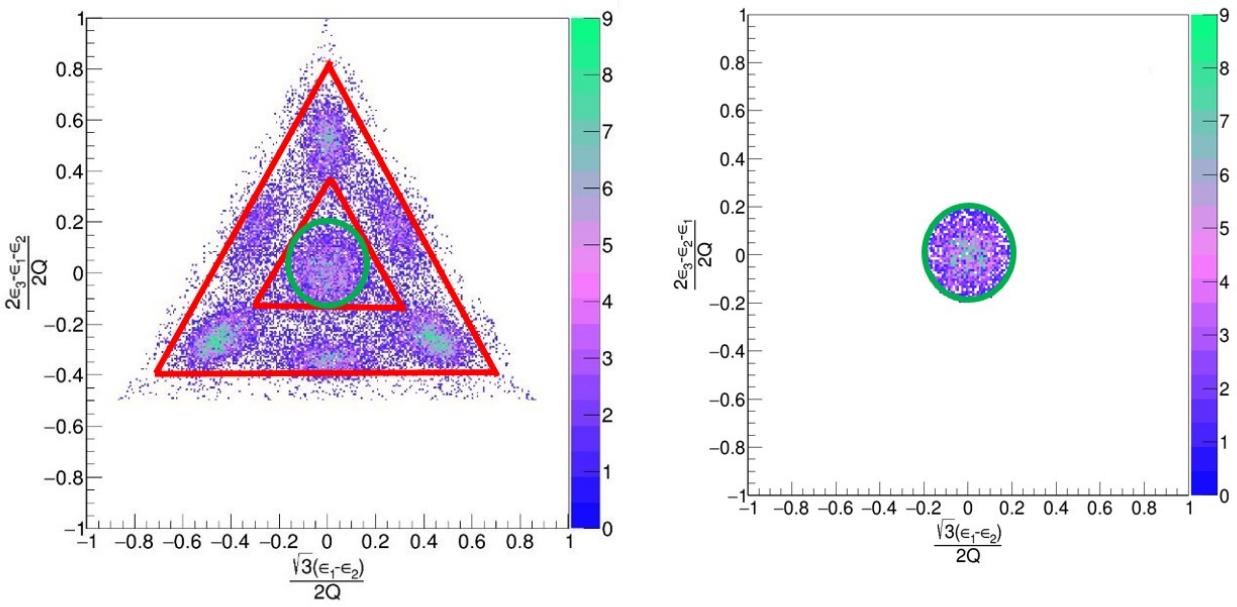

Figure 8.18: Dalitz plot representation for the 20000 simulated events. The figure on the left represents all the data extracted after applying the same adjustment as the experimental data. The figure on the right represents the circular selection for the uncorrelated events to be performed in the experiment.

All simulations are mixed in the same fit for a reasonable test of the fit. As seen in the left figure of the plot 8.18, the events corresponding to uncorrelated and correlated traces are perfectly separated.

In the case of the experiment data, special care will be taken when making this selection since broken traces, incomplete traces that collide with the edges of the camera, or individual identification of two traces that are too close together (as examples of wrong identifications) require a second manual filtering (event by event) to prevent unwanted events from slipping

into the central area of the Dalitz plot and to identify the events susceptible of being a direct Hoyle.

After performing 10,000 simulations of direct and sequential decays, it is obtained that by passing it through the same adjustment as the real data, 73% of sequential decay is recovered, and 79% of direct Hoyle. This makes sense as it is easier to miss events whose traces can be misidentified in the fit as they are very close in angle.

This thesis will consider these data when calculating the branching ratio of the direct Hoyle events of interest.

From the simulation I also obtain a reference for the detector resolution for direct and sequential Hoyle events, which I will use in the data to directly avoid data that falls outside the edges of the triangle and the circumference, thus avoiding incorporating noise into the identification.

8.3.3 Branching Ratio and Excitation energy results for Hoyle state

All the trace filters explained at the beginning of this chapter are implemented to obtain the most reliable results in the Hoyle state branching ratio. The events of interest in this case are those around the Hoyle state, so a sufficiently large excitation energy is imposed to avoid possible errors in the beam correction. The selected excitation energy is between 14 and 15 MeV, i.e. half a MeV around the theoretical results.

Several criteria are used to calculate the Dalitz figure based on the data. First, a multipolarity criterion is used for only events with three or more particles.

In all cases, events in which all particles are α particles and those identified as carbons in the PID are identified and separated. Only events corresponding to possible α carbon decays are represented in the Dalitz plot.

Once all processes have been identified, the events in the Dalitz plot can be separated geometrically, corresponding to correlated and uncorrelated events as seen in the figure 8.20.

A series of finer filters are applied to select the geometric events in such a way as to minimise the chances of finding erroneous events on the geometric surfaces. On the one hand, it is imposed that the scattering particle coming from the alpha decay of oxygen has to have an excitation energy of at least 7.162 MeV, enough to decay into Carbon. In the second step, a minimum excitation energy of 7.33 MeV is imposed for the second higher-angle particle for the alpha decay of Carbon. Finally, a maximum angle of 60° is imposed on this particle since it will be affected by the maximum angle that Carbon can reach as a scattering particle of the secondary reaction.

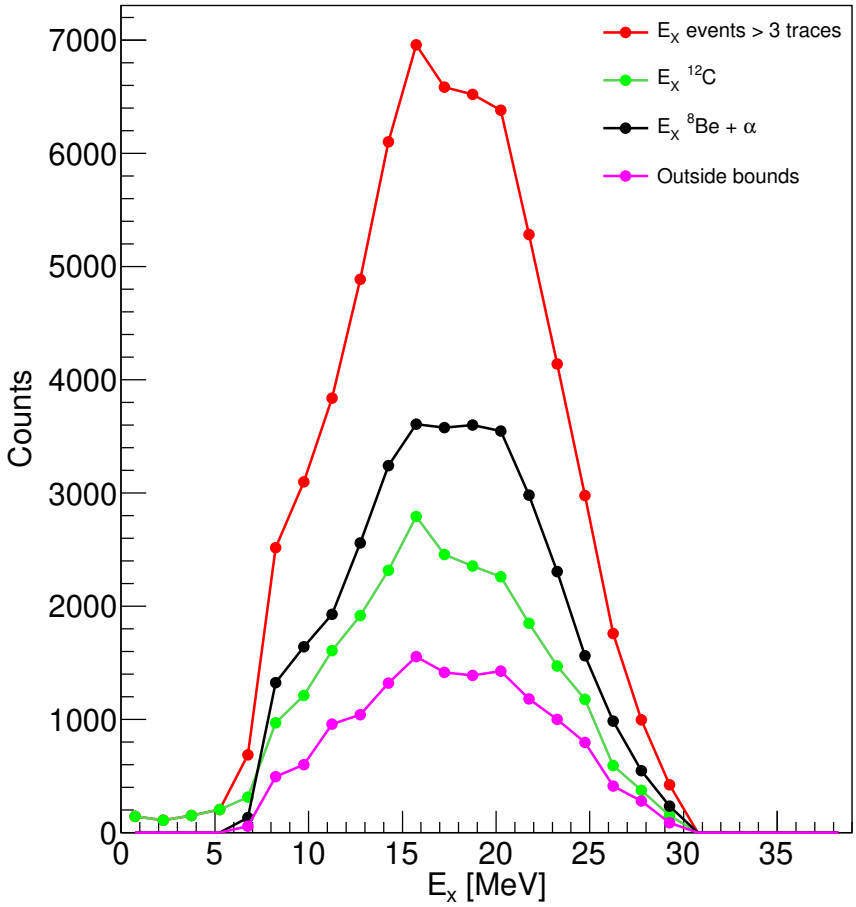

Figure 8.19: The figure shows the excitation energy for events with more than three particles. In red are events with three particles or more, in green are identified as Carbon, in black are events in which all particles are alpha, and in pink, the outside bounds does not belong to any of the events of interest, seen in the simulation.

As can be seen in figure 8.20, recoverable Hoyle events meeting all the strict selection criteria are scarce, which is not surprising since approximately 1 Hoyle event is expected for every 2500 decays of Carbon in 2 correlated alpha particles and taking into account that this Carbon comes from an earlier reaction, the collision of oxygen with Helium with its probability of decay in this channel.

Appendix F shows eight examples of Hoyle events that meet these criteria and other reactions that must be filtered out and may appear as false Hoyle events. The difficulty lies in applying the filtering method and visually verifying that the responses obtained correspond to what is expected and not to misidentification, broken traces, or electronic noise randomly taken as valid traces.

By plotting the accumulated excitation energies for the Dalitz plot events and the events filtered by geometry, excitation energies and angles, the following histograms are obtained, which will be used for the calculation of the branching ratio in the next step and the excitation energy at which the simultaneous Hoyle events at three α are found directly (Figure 8.21).

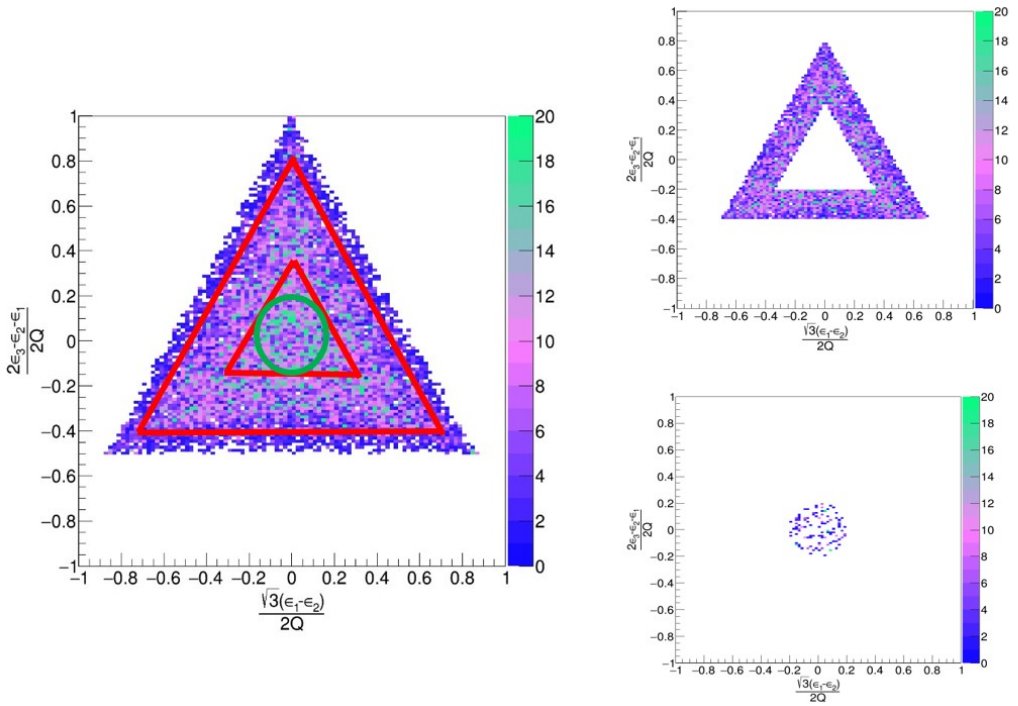

Figure 8.20: The figure on the right shows the events corresponding to three or more traces in the Dalitz plot after applying the highest angle trace filter. The events between the red triangles are used to calculate the sequential decays. The green circle indicates the boundary of the uncorrelated events of the Dalitz plot. On the right, you can see the finer selection of possible Hoyle events, considering range, angle, broken tracks, etc. In the final step, a manual selection is made from these events.

In this figure (Fig. 8.21), one can see the complication of finding rare channels like the one sought in this thesis, which has only a 0.04 % chance of appearing in the face of sequential decay.

Comparing this excitation energy with the number of counts obtained with this method, the energy value at which the Hoyle state is produced is estimated (Figure 8.22).

Once the possible Hoyle events have been identified, a more detailed study is carried out, as the data has numerous effects that could lead to misidentification. We found eight good events of possible direct Hoyle and approximately 17,000 sequential decay events. Only those events are considered, which, when analysed, are likely to be direct decay events at 3 *alpha*'s by the Hoyle effect due to angular opening between traces. The excitation energy of the peak arising from this second fit is $E_x = 14.765 \pm 2.443 MeV$ with a sigma $\sigma = 1.19 \pm 0.349$.

Once the excitation energy of the Hoyle state has been obtained, and considering that the experimental results of the cross sections of both the ground state and the excited states agree with the theory, it is possible to give a reliable result for the branching ratio and compare it with previous results.

This experiment (E20020) aims to search for resonance in ^{16}O, located just above the four alpha separation energy of 14.4 MeV, and observe its decay into four alpha particles. As seen

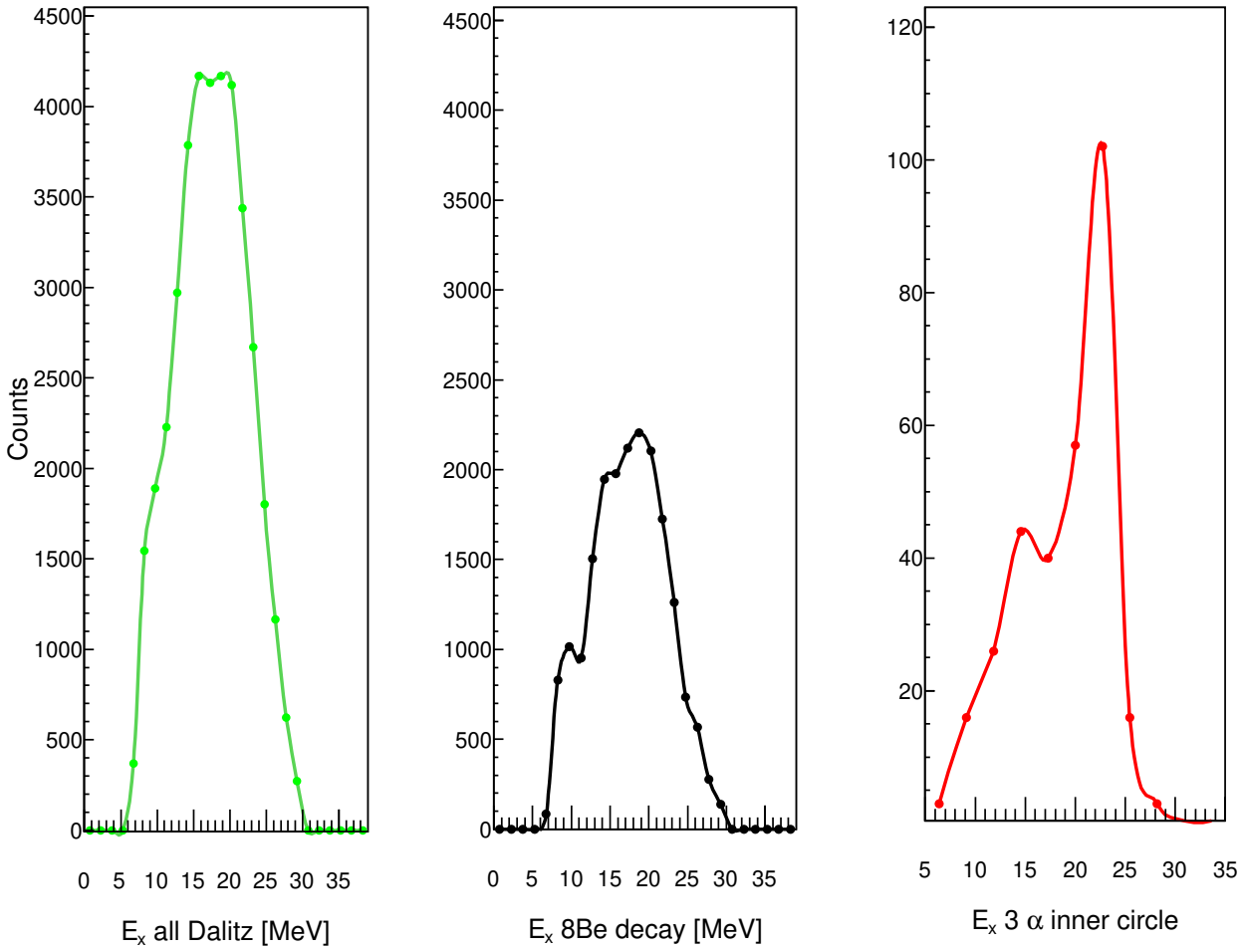

Figure 8.21: In this figure, you can see the different excitation energies for the Dalitz plot on the left (almost twice as high as those identified as Beryllium), in the middle those identified from correlated beryllium events and on the right the excitation energy of the direct Hoyle events after filtering and geometrical selection.

in the table 8.4, the result obtained for the Hoyle state is above 14.4 MeV after post-processing filtering. Specifically, a value of $14.765 \pm 2.443 MeV$ is obtained.

The difference between this experiment and those previously mentioned in the table is that a direct measurement is made of both the Hoyle processes, identifying after visual filtering which processes are of interest (Figure 8.23), and another direct measurement of the ^{12}C breakup processes in ^{8}Be plus α, with the same levels of demand when identifying events.

$$B.R._{Hoyle} = \frac{\Gamma_\alpha - \Gamma_{\alpha_0}}{\Gamma_\alpha} \tag{8.26}$$

For the Hoyle State B.R. calculation in the rest of the articles, the equation 8.26 is used. Here Γ_α indicates the global width, and Γ_{α_0} is the partial width of the α emission leading to

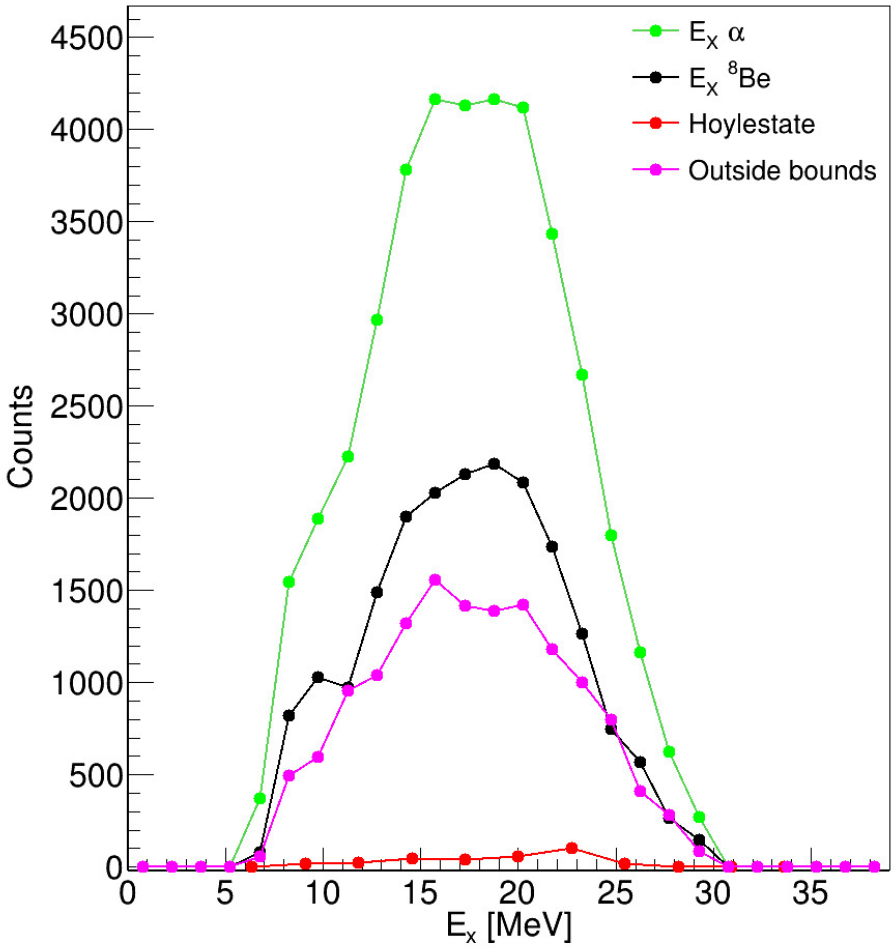

3

Figure 8.22: Histograms of the excitation energies selected as triple *alpha*. In green are represented the events that fall in the Dalitz plot; in black are the filtered events corresponding to the sequential decay; in red are selected as possible direct Hoyle; and finally, in pink, the events that belong to the Dalitz plot but do not correspond to any carbon decay.

the ^{8}Be ground state.

In the case of this experiment, the high resolution of the AT-TPC detector allows perfect resolution of events from the two reactions of interest. As shown in the figure, the two processes in which Carbon can decay are the Hoyle state with a 0.04 % probability and mainly through a reaction $\alpha +^{8} Be$ (99.96 %).

Identifying the two decay processes allows one to obtain the B.R. value of the Hoyle state directly from equation 8.27.

$$B.R._{Hoyle} = \frac{\Gamma_{\alpha} - \Gamma_{\alpha_0}}{\Gamma_{\alpha}} = \frac{NC_{Hoyle}}{NC_{^8Be} + NC_{Hoyle}} \cdot 100\ [\%] \tag{8.27}$$

WORK	$E_x(^{12}C \rightarrow 3\alpha[Hoyle])$ [MeV]	$\frac{\Gamma_\alpha - \Gamma_{\alpha_0}}{\Gamma_\alpha}$ [%]	C.L.[%]
Freer et al. [57]	7.65	< 4	99.5
Raduta et al. [58]	7.61	17.0 ± 5.0	...
kirsebom et al.[59]	7.65	< 0.5	95
Rana et al. [60]	7.654	0.91 ± 0.14	99.75
Morelli et al. [85]	7.65	1.1 ± 0.8	95
Itoh et al. [62]	7.65	< 0.2	95
D. Dell'Aquila et al. [3]	7.654	< 0.043	95
THIS WORK	7.603	$< 0.044^{+0.034}_{-0.026}$	95

Table 8.4: Results of previous experiments for the alpha decay energies for Carbon and their corresponding Branching Ratio with confidence level applied. The results of this work are shown in red. Considering the low statistics for direct Hoyle events, it is decided not to give a measure of the Branching Ratio error, which could be erroneous as it has so many losses for different experimental reasons.

Where $N.C._{^8Be} + N.C._{Hoyle}$ are the total carbon decays, and $N.C._{Hoyle}$ is the number of event counts identified as Hoyle.

The reason for making this calculation without considering the oxygen-to-carbon decay[1] events can be seen in the PID in figure 7.2. The loss of the heavy particles in the PID makes it challenging to identify events because the carbons come out at slight angles, making them difficult to determine for two reasons. At angles close to 0^o, there is an exclusion zone where the pads are disabled to not saturate the detection. On the other hand, the RANSAC identification method in Pattern Recognition suffers large deviations in energy for small angles, affecting the adjustment method's acceptance of the traces.

The result for the branching ratio errors seen in table 8.4 of $< 0.044^{+0.034}_{-0.026}$ corresponds only to the statistical error calculated for experiments with a low number of accounts as explained below[2].

To calculate the Branching Ratio errors, it has to be taken into account that the number of accounts identified as direct Hoyle is small, so the approximation $sqrtN_{counts}$ will not be valid in this case, and the asymmetric errors have to be calculated in another way.

The Poisson distribution is a statistical tool used to model the probability of observing a given number of events in a fixed interval or a fixed space, given that the events occur

[1] For this work, it has been taken into account that the initial reaction is $E_x(^{16}O + \alpha \rightarrow 3\alpha[Hoyle] + 2\alpha)$ [MeV], therefore, taking into account that the Q(α) of ^{16}O is 7.162 MeV and the energy found for the direct Hoyle effect is 14.765 $\pm$ 2.443 MeV in the experiment the resultant excitation energy of ^{12}C for the direct Hoyle effect is 7.603 MeV

[2] When calculating the systematic error that takes into account broken tracks, errors in the calculation of the Dalitz plot seen in the simulation section and the background of events that fulfil all the characteristics to be Hoyle events within the range of particles with angles less than 90^o, but that are not recognised as alphas in the PID, error is asymmetrically increased in the positive part a factor of 2 and the negative error by a factor of 1.62, leaving the total error at $< 0.044^{+0.068}_{-0.042}$.

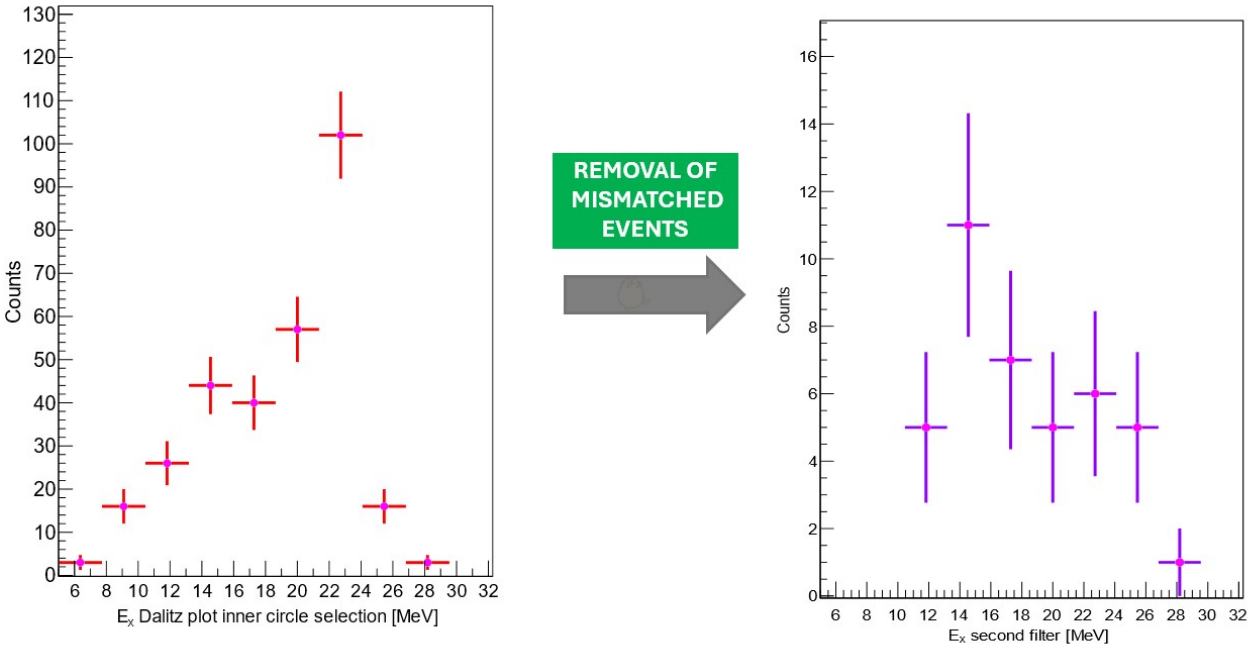

Figure 8.23: The figure on the left shows the excitation energy of the selected events within the inner circumference of the Dalitz plot. For the figure on the left, a hand selection is made within the events that fulfil the conservation rules applied to be considered direct Hoyle events, eliminating those that present doubts regarding the angle between identified traces, broken traces or range of the alpha particles, among other possibilities. The selection is rigorous; only a priori events are considered direct Hoyle events.

independently and with a constant average rate of occurrence. Given statistically independent events, the probability that n events will be observed if the average number of events is p, where p is defined as:

$$P(n|\mu) = \frac{e^{-\mu}\mu^n}{n!} \tag{8.28}$$

Karl Heinz's prescription for calculating asymmetric errors is used for the error in the number of counts and, thus, in the branching ratio of small statistics [86]. The following equations implicitly give confidence limits for n_m observed counts:

$$\sum_{n=n_m}^{\infty} p(n|\mu_{low}) = 1 - \sum_{n_m-1}^{n=0} \frac{\mu_l^n}{n!} e^{\mu_{low}} = \frac{\epsilon}{2} \tag{8.29}$$

$$\sum_{n=0}^{n_m} p(n|\mu_{up}) = \sum_{n_m}^{n=0} \frac{\mu_{up}^n}{n!} e^{\mu_{up}} = \frac{\epsilon}{2} \tag{8.30}$$

Where μ_{up} and μ_{low} are the values of the upper and lower errors respectively.

The following relationships give a good approximation of the confidence limits for $n_m > 2$

$$\mu_{up} \approx n_m + z(1 + \sqrt{n_m}) \tag{8.31}$$

$$\mu_{low} \approx n_m - z(\sqrt{n_m}) \tag{8.32}$$

Where z is related by the following integral over the density of a normal distribution to the confidence level (1-*epsilon*):

$$\frac{\epsilon}{2} = \int_{\infty}^{z} e^{-\frac{x^2}{2}}\, dx \tag{8.33}$$

The z-value is equal to the number of standard deviations that a data point is from the mean in a standard normal distribution. For a given confidence level, the z-value represents the critical value that cuts off a certain proportion of the tail of the distribution. Common confidence levels and their associated z-values are 68 % C.L. → z=1; 90 % C.L. → z=1.645; 95 % C.L. → z=1.96 or 99 % C.L. → z=2.576. In the experiment of the present thesis, a confidence level of 95 % is selected to compare with previous results working with these confidence levels.

For the calculation of the efficiency, which will also be taken into account when calculating the asymmetric errors, with an appropriate error treatment, the difference in the cross-section of the experimental and theoretical results is taken into account, as is the reconstruction efficiency after adjustment calculated with the simulations of section 8.3.2.

When only a few events have been observed, this is a convenient prescription for estimating errors in variables described by Poisson statistics, such as cross sections. Even in the case of one observed event, it gives a reasonable estimate of the upper bound.

This approximation for the upper bound is much more accurate than the commonly used symmetric error for small numbers. For large numbers of counts, the approximation $\sqrt{n_m}$ is again valid for the upper bound. So, this approach will continue to be used for sequential decays, as was done throughout the thesis for all measurements well above an acceptable number of counts.

Taking all this into account, the best option to obtain an adequate result of the B.R. of the Hoyle state is the filtering applied in this chapter and verification by direct observation, eliminating from the statistics the events identified by mistake as Hoyle (usually, they are events of ^8Be misidentified by trace breakage). The B.R. value of the Hoyle decay obtained in this work is $0.044^{+0.034}_{-0.026}$ %, which is very close to previous works such as that of D. Dell'Aquila et al. [3].

For the systematic error, a background calculation (Figure 8.24) is made and it is observed that in the area of interest for Hoyle state an error of 35% is made.

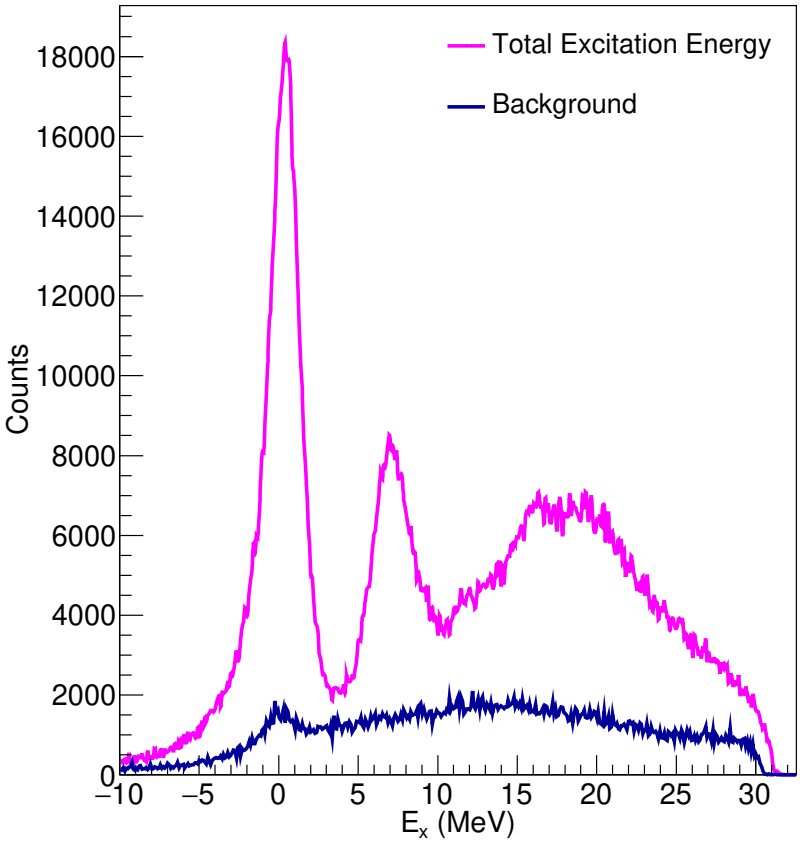

3

Figure 8.24: Figure of the total excitation energy and the calculated background for the events that do not fulfil the characteristics of being a reaction event. In the background calculation, all the particles that fulfilled all the requirements to be considered valid events but were not within the limits established in the P.ID have been taken into account.

On the other hand, having carried out the simulation, it can be seen that there is a loss of approximately 25% of tracks correctly identified by the Dalitz plot method in our method. All this is taken into account when calculating the error, leaving a final result for the Branching Ratio of $0.044^{+0.068}_{-0.042}$.

Chapter 9

Outlook

The chapter on the outlook will be divided into two main ideas. The first will discuss improvements to the experiment that may be useful for similar experiments in the future, and the second will discuss proposed modifications or upgrades to the ATTPC detector itself.

Throughout the experiment's analysis, we encountered a recurring problem due to disabled pads in the fourth quadrant region. A malfunctioning pad is a common problem in any detector of this type for various technical reasons.

In this type of magnetic field experiment, it is imperative to avoid this kind of problem as much as possible because, as it was seen in chapter 6.3.2 with the detections of curves in 3D clouds since the reconstruction of broken traces plays a crucial role the distance between them, and having a part of a quadrant disabled incorporates random noise that affects both the identification, junction, calculation of distance travelled or calculation of reaction vertex, which critically affects the statistics since at the time of the adjustment the well-reconstructed traces are taken into account as alphas in the PID.

The problem in question can come from the malfunctioning or disconnection of an AsAd card; each card obtains information from a group of pads. Several possible solutions after testing with radiative sources and identifying the problem would be a first step to check the connections; another more costly in economic and technical terms would be the replacement of the AsAd or, finally, a reconfiguration of the connections between the various AsAd and the pad-plane to spread the disabled pads evenly over the entire surface, a laborious technical and software work. This would facilitate the identification of traces as the identification parameters could be fixed with fewer problems of broken trace identification, and there would be better identification of the multiplicity of each event.

The need to incorporate the AT-TPC Multi-Channel Analyzer (MCA) camera to calculate the number of counts of the incident ^{16}O particles in the beam became evident when analysing the cross-section of the different energy states, as we were forced to incorporate a factor in the cross-section formula to compensate for the number of incident particles. To improve the quality of the final data, it is always advisable to incorporate such a counter before the measurement with the active target.

In terms of incident energy, it was seen from the SRIM-calculated range data (Table 7.1) that the beam formed from pure 16O at the pressures or densities we worked with in the

experiment could reach two metres at the energy of 10 MeV/n. This gives a wide margin of manoeuvre for the energy. Lowering the beam energy to 100 MeV total (6.25 MeV/n) would contain the whole beam in the chamber and increase the number of collision possibilities before the pad plane. Increasing the pressure would affect the ^{16}O range and make it decay entirely inside the chamber, improving the data obtained for the cross-sections. The decrease in beam energy would also affect the particles' curvature as it affects the kinetic energy of the outgoing particles. This effect can improve the identification with the RANSAC algorithm since the higher the curvature, the better the 2D identification of the Bρ.

The PID shows difficulty identifying heavy particles. This is due to multiple reasons. The gain in the central area of the pad plane is different to protect the detectors and not saturate them. This means that the number of ^{12}C and ^{16}O identified is much smaller than the experimental number. It is practically impossible to differentiate between them at these angles under these experimental conditions.

A possible solution to differentiate them is the presence of quenching, such as CO_2, to increase the number of electrons in the target in this type of structure experiment to increase the detection of deposited charge, possibly improving the energy deposition of every kind of trace. Still, it would not be the best option considering the difficulty of discretising very close particles, such as the ^{8}Be decay in two α coming from the same vertex.

Another solution that takes advantage of the AT-TPC capabilities is to remove altogether the pads affected by the beamline by placing a secondary solid-state detector (such as a CsI, for example) to detect and differentiate the heavy particles in the experiment and thus have a complete view of all the particles involved in each reaction.

Chapter 10

Conclusions

As discussed above, the abundance of heavy elements in the Universe is determined by the production of carbon and oxygen in the stars. To understand the abundance of these elements, it is essential to study specific cases, such as the one presented in this thesis. These cases give us a global vision of the formation and structure of these elements.

The study of the ^{16}O reaction on alpha has been used to further the understanding of the nuclear structure, with particular emphasis on the decomposition of oxygen into helium nuclei. In a second step, the different forms of carbon disintegration in helium clusters, as described by Fred Hoyle in direct or sequential form, are studied to obtain a suitable result for the B.R. of direct disintegration in 3 uncorrelated alphas, which explains the formation of heavy elements in stellar nuclei.

The experiment (E20020) aims to search for resonance in ^{16}O with at TPC just above the energy of the 4α particles splitting at 14.4 MeV. The experiment is designed to observe this resonance decaying into four α particles. This resonance would correspond to the Hoyle state, an excited state of ^{12}C close to the α-particle separation energy. This state was first proposed by Fred Hoyle in 1954 to explain the production of ^{12}C in stars. It is the first experiment to study this mechanism with an active target. It allows for the complete reconstruction and visualisation of the traces of the reactions of interest.

The AT-TPC was filled with 700 Torr of pure 4He gas and used as a reaction target and detector medium. The beam energy is 160 MeV (10 MeV/n) of pure ^{16}O, collimated to enter through the approximately 2 cm radius window at the chamber's entrance.

The experiment was performed in the Facility for Rare Isotope Beams (FRIB) at Michigan State University using the Active Target Time Projection Chamber (AT-TPC). This chamber was placed at the centre of the SOLARIS solenoid with a magnetic field of 3 Tesla, sufficient to contain the particles from the reactions inside the chamber for analysis.

The $B\rho$ measurement from AT-TPC was used to measure the energy of the light ejectile. This measurement resulted from the development of detailed algorithms to improve the reconstruction.

In the first step of the analysis, a pattern recognition analysis based on Random Sample Consensus Reconstruction Algorithms (RANSAC) is applied, an iterative method to estimate

initial parameters from a set of raw data containing outliers coming from the data obtained by digitising the data obtained with the pad plane. The direct variables obtained are X, Y and the drift time, which gives access to the z coordinate of each curve point. Once these direct variables have been obtained, the indirect variable scattering angle (*theta*) and energy can be obtained from the calculated radius of curvature.

With this information, the experimental data are adjusted by adapting the GenFit program to the needs of the ATTPCROOTv2 detector program (dimensional calculation, covariance matrices, etc.) to obtain the reaction vertex, which gives access to the particle identification (PID) in inverse kinematics. Finally, only the α particles are selected in the PID to study the events of interest to calculate the final observables, cross-sections and Hoyle state branching ratio.

To calculate the cross-sections, a study of the efficiency variation to different excitation energies is carried out to correctly adjust to the theoretical data provided by the members of the Instituto Nacional de Ciência e Tecnologia—Física Nuclear e Aplicações (INCT-FNA).

We determine the angular distributions for the ground state. For this state, the agreement with theory is good and in line with theoretical predictions. For the excited states, the resolution in terms of excitation energy was not good enough with the ATTPC detector. Therefore, a multi-decomposition analysis (MDA) was performed for the energy intervals of the first four excited states since they are at an energy distance of about one MeV, which makes each interfere with the XS results of the others.

An interval of 300 KeV is imposed around the theoretical data for the states studied in this work to calculate the XS of the excited states and the MDA. Given the closeness of the L=0, L=3 and L=2, L=1 states (less than 200 KeV between them as shown in Figure 8.8), the resolution of the detector and the low statistics for this experiment, the best option is to perform a multiple decomposition analysis studies for a range in excitation energy covering all four excited states.

To fit the data correctly, a larger excitation energy range, from 5.5 to 7.5 MeV, and an angular range from 20° to 50° are selected, in which the MDA fitting method converges and gives an acceptable solution for the composition of the four states under study. As can be seen, the fit under these conditions is notably better, making the energy loss adjustments for the final calculation more reliable.

To determine the branching ratio, we determine the number of direct decays compared to the ^{8}Be decay. Although the statistics are limited, we obtain an upper limit value of < 0.044 with an error of $^{+0.034}_{-0.026}$, with a confidence level of 95%.

The result agrees with D'Aquilla et al.'s last measurement of the maximum value of 0.044 for the B.R. of the direct Hoyle state. It is compatible with the results of previous experiments presented in this thesis.

Chapter 11

Resumo

11.1 Introducion

A abundancia de elementos pesados no Universo vén determinada pola produción de carbono nas estrelas, fundamental para a vida na Terra. O carbono e o osíxeno non se orixinaron no Big Bang, senón que se formaron posteriormente nos núcleos das estrelas. Non cabe dúbida de que as reaccións de fusión nuclear nas estrelas son responsables de cada gramo de carbono e osíxeno que se atopa en todos os seres vivos. Nas fases iniciais, as grandes estrelas de curta vida utilizan as reservas de hidróxeno, helio e litio para sintetizar elementos máis pesados como o carbono e o osíxeno. A continuación, estes elementos esenciais -carbono e osíxeno- dispérsanse polo espazo cando estas estrelas masivas achéganse ao final da súa vida e explotan de forma espectacular. Esta dispersión despexa o camiño para que se formen novas estrelas e planetas a partir do rico material cósmico, creando as condicións necesarias para que xurda a vida. O estudo do momento preciso e dos intrincados procesos que subxacen a estes acontecementos revela unha nova perspectiva da evolución da vida en todo o universo.

A investigación proposta validará un sistema de detección baseado en tecnoloxía de branco activo para mellorar a medición do proceso triplo alfa, crucial para a evolución estelar. O ^{12}C estable (6 protóns e 12 neutróns) prodúcese exclusivamente mediante o que se coñece como o suceso triplo alfa, no que dúas partículas alfa (2 protóns e 4 neutróns) combínanse para producir berilio-8 (4 protóns e 8 neutróns) e capturan unha terceira partícula alfa, producindo 12C nun estado de resonancia transitorio que decae electromagnéticamente ao ^{12}C no estado fundamental [2]. Este proceso ocorre só unha porcentaxe moi pequena das veces (0,04%), e aínda que é fundamental para a orixe da vida, é extremadamente ineficiente.

Esta estraña resonancia recibe o seu nome de Sir Fred Hoyle, quen predixo a súa existencia na década dos 50 a unha enerxía dada de 7,654 MeV e cun espín e paridade determinados de 0^+ [5]. Pouco despois de ser predito teoricamente, este estado fíxose observable experimentalmente [6].

A fusión de tres partículas alfa é practicamente a única forma posible de sintetizar carbono estable no Universo e quizais un dos procesos máis importantes que ocorren na Natureza. Recentemente, os resultados publicados en Nature [7] suxiren que este proceso inflúe moito máis do esperado na produción de elementos pesados (Gd-Sn) en supernovas ricas en protóns.

Aínda que as propiedades do estado Hoyle son cruciais para a nucleosíntesis do carbono nas estrelas, o noso coñecemento delas é aínda mínimo. Necesítanse medicións máis precisas para reducir as incertezas dos modelos de evolución estelar. Determinar con precisión a velocidade de reacción do proceso triplo α é actualmente un reto importante na astrofísica nuclear.

Para o experimento utilizouse un feixe de ^{16}O de 10 MeV/n procedente do acelerador lineal (linac) ReA6 do NSCL. O AT-TPC colocouse no centro do imán SOLARIS, que posteriormente se axustou a un campo de 3 Tesla. Este experimento (E20020) buscará ^{16}O xusto por encima de 14,4 MeV estudando a súa desintegración en catro partículas alfa. Esta resonancia está asociada ao estado Hoyle. Trátase dun estado excitado de ^{12}C próximo á enerxía de separación de partículas alfa, o limiar para a emisión de partículas alfa (^{4}Hei) desde o núcleo.

Realizado na "Facility for Rare Isotope Beams" (FRIB) da Universidade Estatal de Michigan, o experimento utilizou a Cámara de proxección de tempo en albos activos (ATTPC), situada no centro do imán SOLARIS e sometida a un campo magnético de 3 Tesla (T). O experimento E20020 utiliza un feixe de ^{16}O dirixido a un branco activo de ^{4}He procedente da instalación reaceleradora do NSCL, concretamente o acelerador lineal (linac) ReA6 de 10 MeV/n. Pretendese obter datos sobre a cinemática das reaccións producidas, tanto elásticas como inelásticas, obtendo valores axustados das seccións eficaces dentro dos valores teóricos para diferentes enerxías de excitación. Tamén se quere obter novos valores para medir a razón de ramificación do estado Hoyle, calculada neste experimento por primeira vez directamente coa cámara ATTPC.

11.2 O detector ATTPC

AT-TPC consiste nun detector cilíndrico de 1 m de lonxitude e 29,5 cm de radio nas bases. A parte interior do detector está chea dun gas que actúa como branco de dispersión para a reacción e como medio de seguimento para as partículas cargadas (Figura 11.1). Un cilindro de fibra de vidro recuberto de Epoxi de 1 m de lonxitude e 56 cm de diámetro constitúe a estrutura do AT-TPC. As extremo do volume está selado cun cátodo de aceiro inoxidable. No centro deste cátodo hai unha xanela de lámina delgada a través da cal o fai entra no sistema de detección. O extremo está pechado por unha brida de aluminio, que soporta o plano sensor que actúa como ánodo. Este volume interior énchese co gas que serve de branco.

A idea principal deste detector é utilizar o gas como branco activo; a parte interior do cilindro é un volume de apantallamento concéntrico contido por un recipiente cilíndrico de aluminio. O volume de blindaxe illa o alto potencial eléctrico do cátodo da contorna, evitando posibles faíscas no cátodo. Está situado no centro dun imán solenoidal de gran calibre para curvar as partículas cargadas. En función da enerxía, a Z do nucleido e a intensidade do campo magnético, a traxectoria da partícula se curva máis ou menos para determinar as súas enerxías. Na primeira aproximación da análise en liña, esta propiedade axuda a distinguir as partículas lixeiras, como o 4Hei, dos protóns. Unha das principais motivacións deste campo magnético lonxitudinal paralelo ao campo eléctrico é encapsular as partículas moi lixeiras, obrigándoas a describir unha traxectoria helicoidal e poder medir o seu alcance total. Outra vantaxe é a

adición do radio de curvatura de cada traxectoria, que permite obter a enerxía total de cada partícula implicada na reacción.

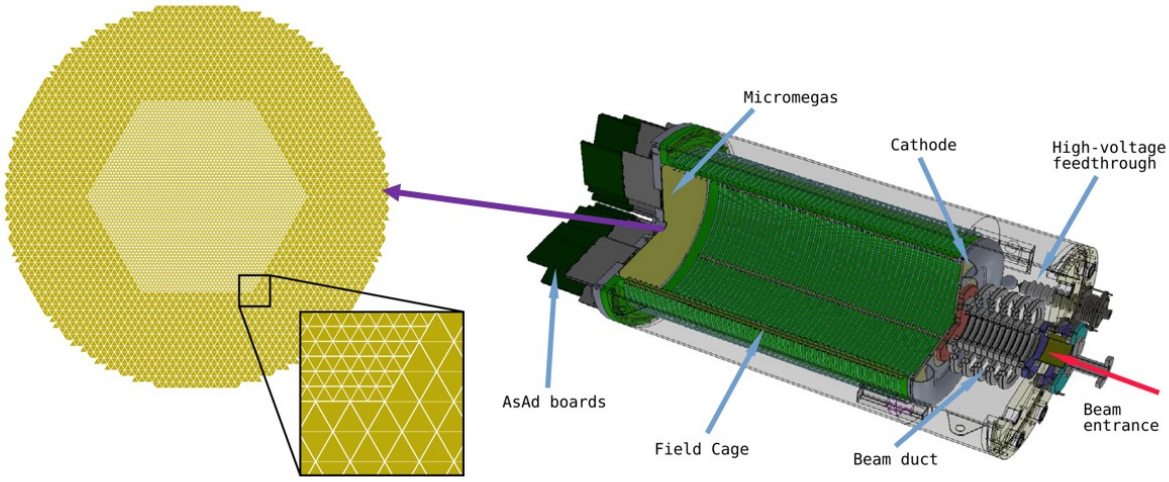

Figure 11.1: Na dereita vista esquemática dos principais elementos do detector ATTPC sobre o que se realiza o experimento proposto nesta tese. Figura extraída de [64] e na esquerda representación do plano de pads. Na figura pódese ver como os detectores centrais son máis pequenos que os exteriores. Este sistema está configurado para mellorar a resolución nas zonas próximas ao feixe e obter unha mellor medición do vértice de reacción.

Ten incorporado un dispositivo Micromegas que consiste nunha micromalla instalada no plano do sensor, que está situado entre o albo activo e o plano de pads ou detectores, separados por piares illantes a 122 μm por encima das almofadas. Para producir unha rexión de alto campo eléctrico por enriba dos "pads" aplícase unha voltaxe da orde de 100 a 1000 V. Cando os electróns de ionización dunha reacción derivan cara esta rexión separada a través dos orificios da malla, multiplícanse mediante un proceso de avalancha e producen un sinal detectable no pad máis próximo a dita avalancha. A distancia entre o plano de pads e a malla é relativamente pequena en comparación co tamaño dun pad, polo que o sinal inducido por un electrón de ionización determinado adoita limitarse a un só detector. A forma triangular dos pads elixiuse para maximizar a resolución espacial do detector. A distribución destes na área circular é de 6144 pads pequenos dispostos nun hexágono cunha altura individual de 0,5 cm rodeado por unha rexión exterior de 4096 pads grandes cunha altura de 1,0 cm, como se mostra en Figura 5.4. A idea principal é ter un número razoable de detectores en función da parte a estudo, se estamos fóra da rexión límite non é necesario ter unha resolución tan fina. Os 10240 pads do plano do sensor permiten unha reconstrución tridimensional realista do evento para reaccións arbitrarias.

11.3 Obtención e tratamento de datos: ATTPCROOTv2

No desempaquetado dos datos e a reconstrución ou dixitalización das trazas simuladas requiren un proceso de varios pasos no que interveñen moitas clases e algoritmos.

ATTPCROOTv2 é unha serie de algoritmos, clases, rutinas..., na súa maior parte, escritos en linguaxe C++, baseados en FairSoft e FairRoot, que constrúen un marco robusto para a simulación e análise de detectores de brancos activos, en particular, o AT-TPC (Active Target Estafe Projection Chamber), así como os detectores Prototype AT-TPC. A distribución FairSoft proporciona os paquetes de software necesarios para compilar e executar o marco FairRoot e os paquetes de experimentos baseados en FairRoot. FairSoft é unha distribución de código fonte con versións recorrentes para macOS e Linux. FairRoot e FairSoft non son desenvolvidos directamente polo grupo AT-TPC, senón que son utilizados por ATTPCROOTv2 para ser compilados e executados. Outros programas secundarios que utiliza ATTPCROOTv2 son, por exemplo, Eigen, FLANN, ou para o desempaquetado e visualización de datos en bruto a librería HDF5.

O marco permite desempaquetar os datos brutos dos experimentos, realizar unha análise completa e comparar os resultados con simulacións realistas baseadas no paquete Virtual Monte Carlo proporcionado por Geant4, que está totalmente integrado no programa principal. No caso das simulacións, o usuario pode crear unha reacción evento por evento nunha contorna de detector realista baseado na mesma idea de Geant4.

Tras desempaquetar os datos brutos ou crear os datos simulados, a análise da forma do pulso pode procesar a lectura dos planos de cada pad. Os puntos de recollida extraídos do padplane de cada evento poden analizarse mediante algoritmos de recoñecemento de patróns. A continuación, pódense rastrexar as traxectorias das partículas no detector, extraendo información sobre os ángulos ou a lonxitude da pista, entre outros detalles.

Os datos en bruto obtidos polo sistema DAQ comprimíronse e gardaron en formato hdf5. Os observables directos cos que traballamos son a carga depositada no plano do pad e a posición XY das trazas de cada pad que reconstrúen os eventos 2D. Para realizar unha reconstrución tridimensional das reaccións, é necesario basearse na velocidade de deriva creada polo campo eléctrico sobre os electróns libres no medio. Unha vez que os núcleos cargados positivamente atravesan o medio, sepáranse e arrastran aos electróns libres dos gases inseridos nel como fontes de electróns pouco ligados. Estes electróns son arrastrados polo intenso campo eléctrico cara ao cátodo, onde son amplificados e detectados polo plano de almofádaa, tanto en posición como en carga. No caso do experimento desta tese, a cámara está chea de helio puro, o que diminúe o número de electróns libres dispoñibles e evita reaccións non desexadas. A marca que cada traza deixa no plano XY dá acceso a outra variable directa: o ángulo phi debido á curvatura da partícula inducida polo campo magnético paralelo ao campo magnético.

11.4 Análise de datos

Nos experimentos con albos activos, especialmente os relacionados con ATTPC que incorporan un campo magnético, é necesario ter en conta a claridade á hora de obter observables directos.

No experimento que nos atañe (e20020), dispoñemos de dous observables: a enerxía da partícula en forma de carga depositada no volume de gas e as posicións XY das partículas detectadas polo plano de pads. Xunto co tempo de deriva, dannos unha reconstrución tridimensional que proporciona acceso aos ángulos de reacción.

Con esta información sobre os observables directos, e considerando que o campo magnético curva a traxectoria das partículas cargadas, podemos acceder aos observables indirectos, como o radio de curvatura das partículas saíntes da reacción ou a lonxitude da traza. Algoritmos de reconstrución como o Random SAmple Consensus (RANSAC) ou o filtro de Kalman serán os utilizados para determinalos. Con toda esta información, temos acceso á cinemática completa da reacción.

Para determinar estes observables utilízase a cinemática inversa nuclear que é un método utilizado en física nuclear para estudar as propiedades dos núcleos atómicos medindo as partículas que se dispersan desde eles. É unha potente ferramenta para estudar a estrutura interna dos núcleos atómicos e determinar as súas propiedades, como o tamaño, a forma das seccións eficaces diferenciais e as enerxías de excitación.

11.4.1 Algoritmos de reconstrución de trazas

A reconstrución de trazas realízase en tres etapas diferenciadas entre si a nivel software, pero cada unha delas é esencial e condiciona o ressultado final.

Nunha primeira etapa actúase sobre os datos en bruto obtidos dos ADC tentando limpar o sinal temporal que nos proporciona cada detector individual dos 10240 pads do pad plane. Para iso actúase sobre o ruído de fondo ou liña basee de ruído realizando unha combolución ao espazo de frecuencias para utilizar unha función coñecida (función cadrado) para a limpeza coa transformada de Fourier inversa das frecuencias altas responsables da maioría de ruídos como os electrónicos. Isto realízase para limpar o sinal e poder extraer en todos os pads por igual a liña de base sen afectar o número de sinais individuais detectados nin á súa intensidade.

Unha vez que se ten discretizados os sinais individuais pásase a unha segunda etapa que sería o "pattern recognition analysis". Realízase mediante un algoritmo de detección de nubes en 3D. O algoritmo TriplClust utilizado para a detección de nubes en 3D [68] agrupa os puntos en clústers que representan curvas ou ruído, onde os clústers que representan curvas poden solaparse nos vértices. Consta do seguintes catro pasos:

1. Suavizado mediante promediado de posición de puntos veciños.
2. Atopar tripletes de puntos que sexan aproximadamente colineales.
3. Agrupación xerárquica de tripletes de puntos.
4. Poda mediante a eliminación de grupos pequenos e (opcionalmente) a división de grupos con grandes espazos entre eles.

Os parámetros e seleccións tidos en conta para este experimento son os seguintes: suavizado de radio, puntos colineais, limiar do ángulo para ser considerado triplete de puntos, aberturas angulares entre puntos pertencentes ao mesmo triplete, número mínimo de tripletes por clúster, un factor de escala de distancia entre clústers da mesma traza e por último un limiar para a agrupación de clústers en trazas. Unha vez identificadas as trazas para obter os valores do radio de curvatura e dos ángulos de dispersión utilízase un algoritmo de consenso por mostras aleatorias (RANSAC), publicado por primeira vez por Fischler e Bolles en 1981 [69], é tamén un paso crucial para identificar as trazas que pertencen a unha mesma partícula e separalas do ruído.

Considérase que o algoritmo converxe cando alcanza un número mínimo de puntos para ser considerado unha traza, e o erro é inferior a un limiar aceptable. A idea xeral é seleccionar un subconjunto aleatorio de datos dentro da mostra de datos onde se atope nosa traza curva formada por puntos chamados "inliers" rodeados de ruído chamados "outliers". Este subconjunto analizarase para ver se se axusta ao modelo proposto dentro dunha incerteza predeterminada, e cada punto considérase dentro dos inliers ou un outlier. Este proceso repítese iterativamente ata que se alcanza unha tolerancia mínima imposta previamente para supoñer que se atopou unha traza. O evento descártase como baleiro se non se alcanza esta tolerancia (Fig. 6.6).

Un dos puntos máis críticos na reconstrución de trazas é o cálculo da matriz de covarianza, tanto na análise de recoñecemento de patróns como na súa posterior implementación no paso de axuste con GenFit, xa que se realiza unha reconstrución do vértice de reacción mediante chi2, que será indispensable na reconstrución da física por cinemática inversa.

Para o cálculo da matriz de covarianza faise un estudo da resolución espacial lonxitudinal e transversal en función da distancia de deriva chegando á conclusión da posiblidad de diagonalización da matriz de covarianza, o cal simplifica moito os cálculos computacionales. Modifícase o código basee de ATTPCROOTv2 en cuestión a cálculo de matrices de covarianza para unha boa comunicación entre os datos obtidos co PRA de ATTPCROOTv2 e o programa Genfit á hora de axustar o vértice de reacción que se calcula coa axuda do filtro de Kalman.

O filtro de Kalman impleméntase en GENFIT, un conxunto de ferramentas extensible e de código aberto para o axuste de trazas que combina algoritmos apropiados, representacións de trazas e xeometrías de impacto nun só programa. que combina algoritmos apropiados, representacións de trazas e xeometrías de impacto nun marco modular. É adecuado para varios experimentos, xa que funciona independentemente da topoloxía específica do evento, a configuración do detector ou a disposición do campo magnético. No paso de actualización, estas estimacións actualízanse utilizando unha media ponderada entre a predición e a medición a través da minimización χ^2, dando máis peso ás estimacións de maior certeza.

11.4.2 Reconstrución do vértice a partir da enerxía e cálculo de eficiencia

A dificultade engadida de incorporar un campo magnético paralelo á dirección do fai é que as trazas cargadas se curvan en traxectorias helicoidales con parametrizacións complicadas. No

lado positivo, ATTPC e SOLARIS proporcionan ao experimento novas variables para reconstruír a cinemática, como o radio de curvatura.

Para obter o radio de curvatura utilízanse diferentes métodos iterativos. En primeiro lugar, utilízase RANSAC para simular unha circunferencia cuxo radio de curvatura será o da nosa partícula cargada. En segundo lugar, utilízase un algoritmo baseado no filtro de Kalman para afinala.

A rixidez é unha medida do momento da partícula. Refírese ao feito de que unha partícula con maior momento é máis resistente a ser desviada por un campo magnético. Defínese como R = B ρ = pc/q, onde B é o campo magnético, ρ é o radio da partícula debido a ese campo, p é o momento da partícula, c é a velocidade da luz e q é a súa

Unha vez realizadas as correccións ao vértice de reacción realízase unha identificación de partículas (PID) tendo en conta a carga depositada e o radio de curvatura de cada unha das trazas seleccionando os helios para traballar con eles en cinemática inversa. Con esta selección calcúlanse as enerxías a partir do radio de curvatura e con elas traballarase para a selección de seccións eficaces do estado fundamental e dos excitados traballados nesta tese e a procura dos estados Hoyle.

Para o caso da eficiencia xeométrica do detector que se utiliza no cálculo das seccións eficaces diferenciais realízanse varias simulacións a distintas enerxías (unha diferente para cada enerxía de excitación) e calcúlanse as diferentes eficiencias para cada ángulo en centro de masas das partículas α dividindo o número de eventos Monte-Carlo que ocorren en cada ángulo desde 15º a 165º (cubrindo o máximo posible de apertura angular deste tipo de eventos) entre o número de contas por ángulo unha vez que se realizan exactamente os mesmos axustes que para os datos reais. Isto proporcciona unha curva de eficiencia que será aplicada en cada XS.

11.5 Resultados

O cálculo da sección eficaz diferencial baséase na ecuación 11.1.

$$\frac{d\sigma}{d\Omega} = \frac{N^{mesure}}{N_{beam} N_{target} \mathcal{E} \Delta\Omega} \tag{11.1}$$

Onde N^{mesure} é o número de partículas obtidas para un rango angular dado no centro de masa, N_{beam} é o número de partículas do fai que golpean o branco, N_{target} é o número de centros do branco por cm^2, $\Delta\Omega$ é o ángulo sólido mantido polo disco θ_{CM}, e ϵ é a eficiencia xeométrica.

$$\frac{d\sigma}{d\Omega} = \mathcal{F} \frac{N^{mesure}}{2\pi \Delta\theta_{CM} sin(\theta_{CM}) \mathcal{E}} \tag{11.2}$$

A partir desta fórmula que se pode reescribir como 11.2 calcúlanse a distintas sección eficaz do estado fundamental (Figura 11.2) e as dos estados excitados que aparecen na Anexo E

tendo un resultado sobre o axuste os resultados teóricos proporcionados por Jesús Lubián Ríos y Jonas Leonardo Ferreira, miembros del Instituto Nacional de Ciencia y Tecnología - Física Nuclear y Aplicaciones (INCT-FNA), con sede en el Instituto de Física de la Universidad Federal Fluminense:

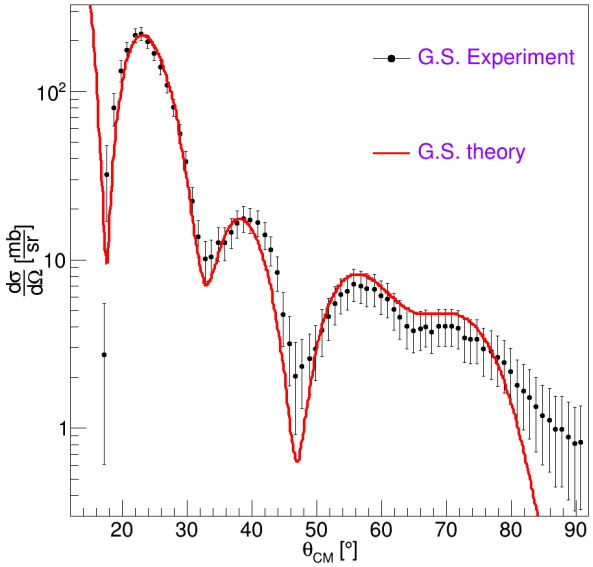

Figure 11.2: Sección transversal diferencial para o estado fundamental calculada sobre o corte de enerxía excitada entre -2 MeV e 2 MeV. Os erros calcúlanse escalando o erro do número de recontos como $\sqrt{N}$, sendo N o número de recontos para cada grao no centro de masas (CM).

E_x [MeV]	J^P	Factor	χ^2/ndf	$\theta_{CM}low[\circ]$	$\theta_{CM}high[\circ]$
0	0^+	0.295 10^{-3}	0.872	20	80
6.049	0^+	x 1.912	1.074	20	70
6.129	3^-	x 1.886	0.955	20	65
6.917	2^+	x 1.5067	2.121	20	50
7.117	1^-	x 2.499	2.114	20	50
9.845	2^+	x 0.406	0.765	20	60

Table 11.1: Resultados experimentais das seccións eficaces calculadas segundo a fórmula 11.2 entre os ángulos no centro de masa indicados na táboa. Estes valores calcúlanse a 300 KeV ao redor do estado excitado teórico para todos os estados excitados. No caso do GS son ± 2 MeV ao redor de 0 MeV.

Como se observa nos resultados experimentais do χ^2 para os estados excitados entre 6 e 7 MeV aproximadamente existe unha mestura de estados que se trata na tese cun método de análise de multidescomposición (MDA) para discretizar canto afecta cada estado nos estados próximos obtendo uns resultados expostos na gráfica 8.10 da tese que confirman os bos axustes anteriores xa que en cada caso os estados con máis peso coinciden coas predicións teóricas.

11.5.1 Relación de ramificación do Estado Hoyle

Para atopar os sucesos correspondentes ó efecto Hoyle, as reaccións $^{16}Ou^{*} + alpha \rightarrow {}^{12}C + \alpha$; $^{16}Ou^{*} + \alpha \rightarrow {}^{12}C^{*} + \alpha \rightarrow {}^{8}Be + 2\alpha$ e $^{16}Ou^{*} + \alpha \rightarrow {}^{12}C^{*} + \alpha \rightarrow \rightarrow 3\alpha + \alpha$ estúdanse separándoas en diferentes multiplicidades. Estas reaccións estúdanse precisamente para atopar un valor indirecto da relción de ramificación (B.R.) nas dúas primeiras ecuacións seguindo os pasos do artigo [3] e para obter un valor directo do estado de Hoyle directo a partir da desintegración do carbono excitado con enerxía suficiente para volver a desintegrarse α. Resultados experimentais recentes dan un límite superior na desintegración directa do estado Hoyle en 3 α comparado coa desintegración secuencial en $^{8}Be + \alpha$ de menos de **0,043**% (95% C.L.).

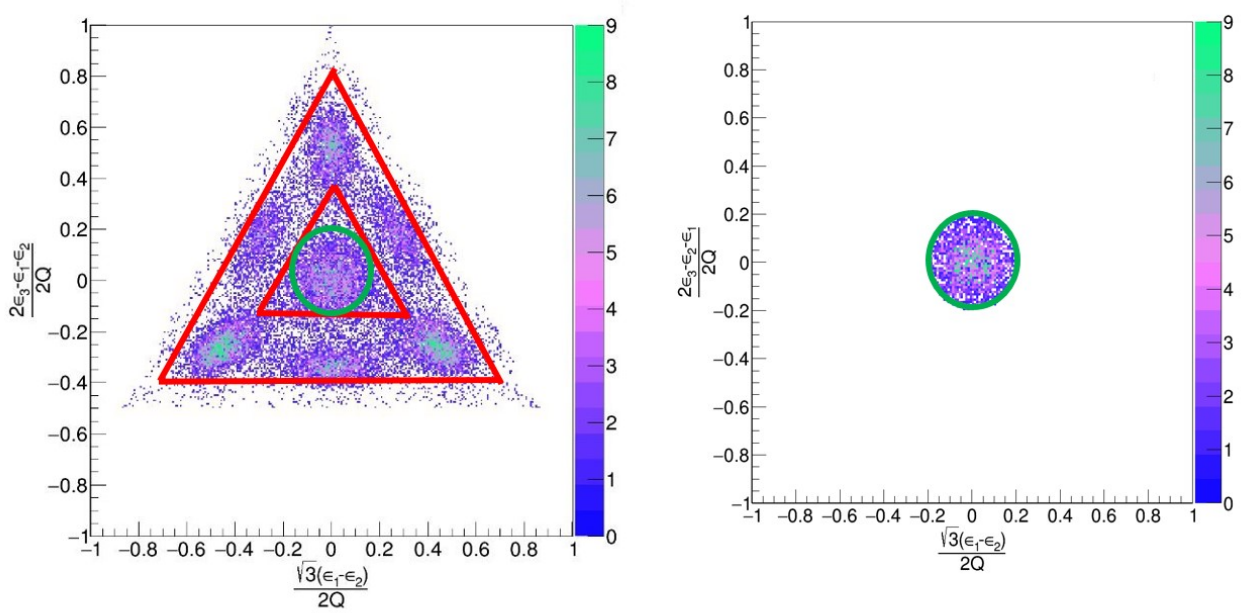

Figure 11.3: Representación gráfica de Dalitz para os 20000 eventos simulados. A figura da esquerda representa todos os datos extraídos tras aplicar o mesmo axuste que aos datos experimentais. A figura da dereita representa a selección circular dos sucesos non correlacionados que se realizarán no experimento.

Nun segundo paso de filtrado, utilizarase o diagrama de Dalitz. Un diagrama de Dalitz é unha representación gráfica da distribución de masas invariantes ao cadrado nunha desintegración a tres corpos. En física de partículas, utilízase a miúdo para analizar a distribución dunha partícula que decae en tres partículas fillas. O diagrama de Dalitz pode construírse a partir das masas invariantes ao cadrado das partículas fillas.

O diagrama de Dalitz, chamado así polo seu inventor Richard Dalitz (1925-2006), aplicouse por primeira vez ao "crebacabezas $\tau - \kappa$". Este crebacabezas involucraba partículas estrañas que decaían a 2 ou 3 piones, agora entendidos como diferentes modos de decaimiento de kaones [83].

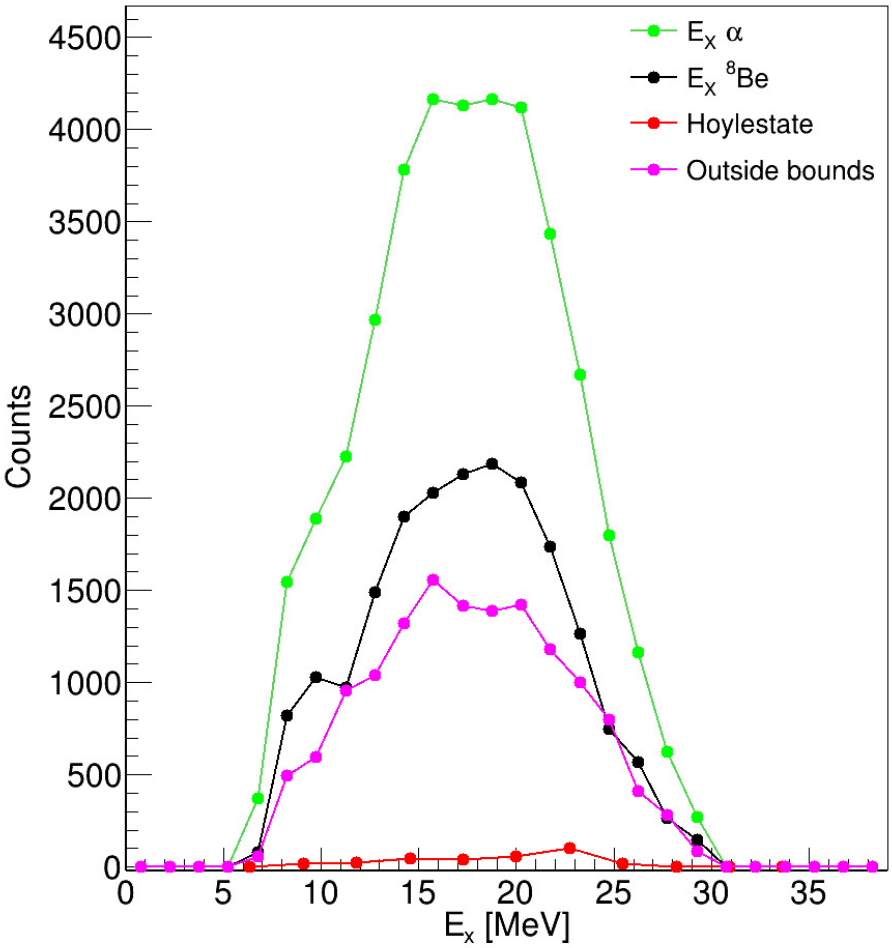

Figure 11.4: Histogramas das enerxías de excitación seleccionadas como triple *alpha*. En verde representanse os sucesos que caen no diagrama de Dalitz; en negro os sucesos filtrados correspondientes ó decaemento secuencial; en vermello os seleccionados como posibles directos de Hoyle; e por último, en rosa os sucesos que pertenecen o diagrama de Dalitz pero no corresponden a ningún decaemento do carbono.

Para verificar os datos obtidos no diagrama de Dalitz, realízanse dúas simulacións de 10000 eventos cada unha, unha para o decaimiento do carbono a través dun decaimiento previo a través de ^{8}Be, que decae en 2 α cunha anchura aproximada de 0,1 MeV, e outra para o decaimiento de ^{12}C en tres α (Figura 11.3).

Este tipo de simulación pretende probar a capacidade do método utilizado para resolver sucesos como os tratados nesta tese. Trátase de probar a selección de trazas realizada por recoñecemento de patróns e a posterior utilización destas variables no axuste realizado con Genfit. En todos os casos utilízanse as mesmas restricións para os datos reais. A simulación utiliza o conxunto de ferramentas Geant4 implementado en ATTPCROOTv2 e adáptao ao experimento analizado nesta tese. Dos resultados destas simulacións infirese a capacidade de separación dos dous tipos de decaementos por un lado os decaementos debidos a Hoyle secuencial dispersanse o redor do triángulo exterior da figura de Dalitz e os directos concentranse no centro da mesma.

TRABALLO	$E_x(^{12}C \rightarrow 3\alpha[Hoyle])$ [MeV]	$\frac{\Gamma_\alpha - \Gamma_{\alpha_0}}{\Gamma_\alpha}$ [%]	C.L.[%]
Freer et al. [57]	7.65	< 4	99.5
Raduta et al. [58]	7.61	17.0 ± 5.0	...
kirsebom et al.[59]	7.65	< 0.5	95
Rana et al. [60]	7.654	0.91 ± 0.14	99.75
Morelli et al. [85]	7.65	1.1 ± 0.8	95
Itoh et al. [62]	7.65	< 0.2	95
D. Dell'Aquila et al. [3]	7.654	< 0.043	95
	$E_x(^{16}O + \alpha \rightarrow ... \rightarrow$ $\rightarrow ... \rightarrow 3\alpha[Hoyle] + 2\alpha)$ [MeV]		
ESTE TRABALLO	14.765 ± 2.443	$< 0.044^{+0.034}_{-0.026}$	95

Table 11.2: Resultados de experimentos anteriores para as enerxías de desintegración alfa do Carbono e o seu correspondente Branching Cociente con nivel de confianza aplicado. Os resultados deste traballo móstranse en vermello.

Por último, pero non menos importante, realizase un estudo visual de todos os eventos seleccionados dentro do rango de eventos susceptibles de ser considerados Hoyle para refugar os eventos que se "coaron" ao tentar poñer unhas condicións o menos restritivas posibles. Na Figura 11.4 podemos observar a pouca estatística que se obtén para os eventos Hoyle directos frente os eventos de Hoyle secuencial, esto era de esperar xa que o ratio da reacción é de aproximadamente 0.044. Obtéñense os resultados para a relación de ramificación e enerxía de excitación da Táboa 11.2.

Para determinar a razón de ramificación, determinamos o número de desintegracións directas en comparación coa desintegración pasando por ^8Be secuencial. Aínda que as estatísticas son limitadas, obtemos un valor límite superior de < 0.044 cun erro de $^{+0.034}_{-0.026}$, cun nivel de confianza do 95%.

O resultado concorda coa última medición de D'Aquilla et al. do valor máximo de 0,044 para o B.R. do estado directo de Hoyle. É compatible cos resultados de experimentos anteriores que non se mediron de forma tan directa coma este.

Bibliography

[1] Y. Ayyad et al. "Next-generation experiments with the Active Target Time Projection Chamber (AT-TPC)". In: *Nuclear Instruments and Methods in Physics Research Section A: Accelerators, Spectrometers, Detectors and Associated Equipment* 954 (2020). Symposium on Radiation Measurements and Applications XVII, p. 161341. ISSN: 0168-9002. DOI: https://doi.org/10.1016/j.nima.2018.10.019. URL: https://www.sciencedirect.com/science/article/pii/S0168900218313342.

[2] M. Freer and H.O.U. Fynbo. "The Hoyle state in 12C". In: *Progress in Particle and Nuclear Physics* 78 (2014), pp. 1–23. ISSN: 0146-6410. DOI: https://doi.org/10.1016/j.ppnp.2014.06.001. URL: https://www.sciencedirect.com/science/article/pii/S0146641014000453.

[3] D. Dell'Aquila et al. "High-Precision Probe of the Fully Sequential Decay Width of the Hoyle State in ^{12}C". In: *Phys. Rev. Lett.* 119 (13 Sept. 2017), p. 132501. DOI: 10.1103/PhysRevLett.119.132501. URL: https://link.aps.org/doi/10.1103/PhysRevLett.119.132501.

[4] Katarzyna Schmidt et al. "Clustering in alpha conjugate nuclei". In: *EPJ Web of Conferences* 88 (Jan. 2015), p. 00024. DOI: 10.1051/epjconf/20158800024.

[5] E. E. Salpeter. "Nuclear Reactions in the Stars. I. Proton-Proton Chain". In: *Phys. Rev.* 88 (3 Nov. 1952), pp. 547–553. DOI: 10.1103/PhysRev.88.547. URL: https://link.aps.org/doi/10.1103/PhysRev.88.547.

[6] D. N. F. Dunbar et al. "The 7.68-Mev State in C^{12}". In: *Phys. Rev.* 92 (3 Nov. 1953), pp. 649–650. DOI: 10.1103/PhysRev.92.649. URL: https://link.aps.org/doi/10.1103/PhysRev.92.649.

[7] S. et al. Jin. "Enhanced triple-́ reaction reduces proton-rich nucleosynthesis in supernovae." In: *Nature* 588 (7836 Dec. 2020), pp. 57–60. DOI: 10.1038/s41586-020-2948-7. URL: https://doi.org/10.1038/s41586-020-2948-7.

[8] E. Simpsons. *Colorfur Nuclear Chart*. 2017. URL: https://people.physics.anu.edu.au/~ecs103/chart/ (visited on 06/02/2023).

[9] Sareh P. et al. Nouhi B. Darabi N. "The fusion-fission optimization (FuFiO) algorithm". In: *Springer Nature* 1 (July 2022), p. 00048. DOI: doi.org/10.1038/s41598-022-16498-4.

[10] E. Margaret Burbidge et al. "Synthesis of the Elements in Stars". In: *Rev. Mod. Phys.* 29 (4 Oct. 1957), pp. 547–650. DOI: 10.1103/RevModPhys.29.547. URL: https://link.aps.org/doi/10.1103/RevModPhys.29.547.

[11] A. G. W. Cameron. "On the origin of the heavy elements". In: *Astronomical Journal* 62 (2 Feb. 1957), pp. 9–10. DOI: 10.1086/107435. URL: https://ui.adsabs.harvard.edu/abs/1957AJ.....62....9C/abstract.

[12] Kazuyuki Ogata, Masataka Kan, and Masayasu Kamimura. "Quantum Three-Body Calculation of the Nonresonant Triple^{-} Reaction Rate at Low Temperatures". In: *Progress of Theoretical Physics* 122.4 (Oct. 2009), pp. 1055–1064. ISSN: 0033-068X. DOI: 10.1143/PTP.122.1055. eprint: https://academic.oup.com/ptp/article-pdf/122/4/1055/9681212/122-4-1055.pdf. URL: https://doi.org/10.1143/PTP.122.1055.

[13] Falk Herwig, Sam M. Austin, and John C. Lattanzio. "Nuclear reaction rate uncertainties and astrophysical modeling: Carbon yields from low-mass giants". In: *Phys. Rev. C* 73 (2 Feb. 2006), p. 025802. DOI: 10.1103/PhysRevC.73.025802. URL: https://link.aps.org/doi/10.1103/PhysRevC.73.025802.

[14] N. B. Nguyen, F. M. Nunes, and I. J. Thompson. "Investigation of the triple-α reaction in a full three-body approach". In: *Phys. Rev. C* 87 (5 May 2013), p. 054615. DOI: 10.1103/PhysRevC.87.054615. URL: https://link.aps.org/doi/10.1103/PhysRevC.87.054615.

[15] C. Angulo et al. "A compilation of charged-particle induced thermonuclear reaction rates". In: *Nuclear Physics A* 656.1 (1999), pp. 3–183. ISSN: 0375-9474. DOI: https://doi.org/10.1016/S0375-9474(99)00030-5. URL: https://www.sciencedirect.com/science/article/pii/S0375947499000305.

[16] Jacob Lund Fisker et al. "The 15O($\boldsymbol{\alpha}$,$\boldsymbol{\gamma}$)19Ne Reaction Rate and the Stability of Thermonuclear Burning on Accreting Neutron Stars". In: *The Astrophysical Journal* 665.1 (Aug. 2007), p. 637. DOI: 10.1086/519517. URL: https://dx.doi.org/10.1086/519517.

[17] Jacob Lund Fisker, Hendrik Schatz, and Friedrich-Karl Thielemann. "Explosive Hydrogen Burning during Type I X-Ray Bursts". In: *The Astrophysical Journal Supplement Series* 174.1 (Jan. 2008), p. 261. DOI: 10.1086/521104. URL: https://dx.doi.org/10.1086/521104.

[18] Niels Bohr and John Archibald Wheeler. "The Mechanism of Nuclear Fission". In: *Phys. Rev.* 56 (5 Sept. 1939), pp. 426–450. DOI: 10.1103/PhysRev.56.426. URL: https://link.aps.org/doi/10.1103/PhysRev.56.426.

[19] Maria Goeppert Mayer. "On Closed Shells in Nuclei. II". In: *Phys. Rev.* 75 (12 June 1949), pp. 1969–1970. DOI: 10.1103/PhysRev.75.1969. URL: https://link.aps.org/doi/10.1103/PhysRev.75.1969.

[20] J S C Mckee. "Nuclear Reactions and Nuclear Structure". In: *Physics Bulletin* 23.7 (July 1972), p. 410. DOI: 10.1088/0031-9112/23/7/020. URL: https://dx.doi.org/10.1088/0031-9112/23/7/020.

[21] Otto Haxel, J. Hans D. Jensen, and Hans E. Suess. "On the "Magic Numbers" in Nuclear Structure". In: *Phys. Rev.* 75 (11 June 1949), pp. 1766–1766. DOI: 10.1103/PhysRev.75.1766.2. URL: https://link.aps.org/doi/10.1103/PhysRev.75.1766.2.

[22] G. Gamow. "Mass Defect Curve and Nuclear Constitution". In: *Proceedings of the Royal Society of London Series A* 126.803 (Mar. 1930), pp. 632–644. DOI: 10.1098/rspa.1930.0032.

[23] D. R. Hartree. "The Constitution of Atomic Nuclei and Radioactivity. By G. Gamow. Pp. viii, 114. 10s. 6d. 1931. (Oxford; at the Clarendon Press)". In: *The Mathematical Gazette* 16.220 (1932), pp. 284–285. DOI: 10.2307/3605938.

[24] L. R. Hafstad and E. Teller. "The Alpha-Particle Model of the Nucleus". In: *Phys. Rev.* 54 (9 Nov. 1938), pp. 681–692. DOI: 10.1103/PhysRev.54.681. URL: https://link.aps.org/doi/10.1103/PhysRev.54.681.

[25] John Archibald Wheeler. "Molecular Viewpoints in Nuclear Structure". In: *Phys. Rev.* 52 (11 Dec. 1937), pp. 1083–1106. DOI: 10.1103/PhysRev.52.1083. URL: https://link.aps.org/doi/10.1103/PhysRev.52.1083.

[26] H. Margenau and E. Wigner. "Magnetic Moments of Odd Nuclei". In: *Phys. Rev.* 58 (2 July 1940), pp. 103–110. DOI: 10.1103/PhysRev.58.103. URL: https://link.aps.org/doi/10.1103/PhysRev.58.103.

[27] Kiyomi Ikeda, Noboru Takigawa, and Hisashi Horiuchi. "The Systematic Structure-Change into the Molecule-like Structures in the Self-Conjugate 4n Nuclei". In: *Progress of Theoretical Physics Supplement* E68 (July 1968), pp. 464–475. ISSN: 0375-9687. DOI: 10.1143/PTPS.E68.464. eprint: https://academic.oup.com/ptps/article-pdf/doi/10.1143/PTPS.E68.464/5216547/E68-464.pdf. URL: https://doi.org/10.1143/PTPS.E68.464.

[28] W. von Oertzen, Martin Freer, and Yoshiko Kanada-En'yo. "Nuclear clusters and nuclear molecules". In: *Physics Reports* 432.2 (2006), pp. 43–113. ISSN: 0370-1573. DOI: https://doi.org/10.1016/j.physrep.2006.07.001. URL: https://www.sciencedirect.com/science/article/pii/S0370157306002626.

[29] Martin Freer. "The clustered nucleus—cluster structures in stable and unstable nuclei". In: *Reports on Progress in Physics* 70.12 (Nov. 2007), p. 2149. DOI: 10.1088/0034-4885/70/12/R03. URL: https://dx.doi.org/10.1088/0034-4885/70/12/R03.

[30] H. Morinaga. "Interpretation of Some of the Excited States of 4*n* Self-Conjugate Nuclei". In: *Phys. Rev.* 101 (1 Jan. 1956), pp. 254–258. DOI: 10.1103/PhysRev.101.254. URL: https://link.aps.org/doi/10.1103/PhysRev.101.254.

[31] Kiyomi Ikeda, Hisashi Horiuchi, and Sakae Saito. "Chapter I. Introduction to Comprehensive Nuclear Structure Study Based on Cluster Correlations and Molecular Viewpoint". In: *Progress of Theoretical Physics Supplement* 68 (Jan. 1980), pp. 1–28. ISSN: 0375-9687. DOI: 10.1143/PTPS.68.1. eprint: https://academic.oup.com/ptps/article-pdf/doi/10.1143/PTPS.68.1/5433942/68-1.pdf. URL: https://doi.org/10.1143/PTPS.68.1.

[32] G.J. Gyapong et al. "Two-dimensional alpha cluster structures in 28Si". In: *Nuclear Physics A* 620.1 (1997), pp. 55–70. ISSN: 0375-9474. DOI: https://doi.org/10.1016/S0375-9474(97)00152-8. URL: https://www.sciencedirect.com/science/article/pii/S0375947497001528.

[33] Henry Margenau. "Interaction of Alpha-Particles". In: *Phys. Rev.* 59 (1 Jan. 1941), pp. 37–47. DOI: 10.1103/PhysRev.59.37. URL: https://link.aps.org/doi/10.1103/PhysRev.59.37.

[34] Martin Freer. "The clustered nucleus - cluster structures in stable and unstable nuclei". English. In: *Reports on Progress in Physics* 70.12 (Dec. 2007), pp. 2149–2210. ISSN: 0034-4885. DOI: 10.1088/0034-4885/70/12/R03.

[35] Martin Freer, Thomas Marsh, and James Souter. "Symmetries of the oblate deformed harmonic oscillator". In: *Journal of Physics G: Nuclear and Particle Physics* 49 (Mar. 2022). DOI: 10.1088/1361-6471/ac5a76.

[36] T Bengtsson et al. "Some Properties of Superdeformed Nuclei". In: *Physica Scripta* 24.1B (July 1981), p. 200. DOI: 10.1088/0031-8949/24/1B/016. URL: https://dx.doi.org/10.1088/0031-8949/24/1B/016.

[37] W.D.M. RAE. "CLUSTERING PHENOMENA AND SHELL EFFECTS IN NUCLEAR STRUCTURE AND REACTIONS". In: *International Journal of Modern Physics A* 03.06 (1988), pp. 1343–1372. DOI: 10.1142/S0217751X88000576. eprint: https://doi.org/10.1142/S0217751X88000576. URL: https://doi.org/10.1142/S0217751X88000576.

[38] W. Nazarewicz and J. Dobaczewski. "Dynamical symmetries, multiclustering, and octupole susceptibility in superdeformed and hyperdeformed nuclei". In: *Phys. Rev. Lett.* 68 (2 Jan. 1992), pp. 154–157. DOI: 10.1103/PhysRevLett.68.154. URL: https://link.aps.org/doi/10.1103/PhysRevLett.68.154.

[39] R. B. Wiringa et al. "Quantum Monte Carlo calculations of $A = 8$ nuclei". In: *Phys. Rev. C* 62 (1 June 2000), p. 014001. DOI: 10.1103/PhysRevC.62.014001. URL: https://link.aps.org/doi/10.1103/PhysRevC.62.014001.

[40] W. Bauhoff, H. Schultheis, and R. Schultheis. "Alpha cluster model and the spectrum of O-16". In: *Phys. Rev. C* 29 (1984), pp. 1046–1055. DOI: 10.1103/PhysRevC.29.1046.

[41] P J Haigh et al. "Alpha decay widths of excited states of 16O". In: *Journal of Physics G: Nuclear and Particle Physics* 37.3 (Jan. 2010), p. 035103. DOI: 10.1088/0954-3899/37/3/035103. URL: https://dx.doi.org/10.1088/0954-3899/37/3/035103.

[42] S. G. Nilsson. "Binding states of individual nucleons in strongly deformed nuclei". In: *Kong. Dan. Vid. Sel. Mat. Fys. Med.* 29N16 (1955), pp. 1–69.

[43] W. Bauhoff, H. Schultheis, and R. Schultheis. "Alpha cluster model and the spectrum of ^{16}O". In: *Phys. Rev. C* 29 (3 Mar. 1984), pp. 1046–1055. DOI: 10.1103/PhysRevC.29.1046. URL: https://link.aps.org/doi/10.1103/PhysRevC.29.1046.

[44] B. Buck, C. B. Dover, and J. P. Vary. "Simple potential model for cluster states in light nuclei". In: *Phys. Rev. C* 11 (5 May 1975), pp. 1803–1821. DOI: 10.1103/PhysRevC.11.1803. URL: https://link.aps.org/doi/10.1103/PhysRevC.11.1803.

[45] F. Brochard et al. "^{12}C(α,^{8} Be)^{8}Be reaction in the energy range $E_\alpha = 17 - 33$ MeV". In: *Phys. Rev. C* 13 (3 Mar. 1976), pp. 967–975. DOI: 10.1103/PhysRevC.13.967. URL: https://link.aps.org/doi/10.1103/PhysRevC.13.967.

[46] Fred Hoyle. "On Nuclear Reactions Occuring in Very Hot STARS. I. the Synthesis of Elements from Carbon to Nickel." In: *Astrophysical Journal Supplement, vol. 1, p. 121 (1954)* 1 (1954), p. 121.

[47] Evgeny Epelbaum et al. "Structure and Rotations of the Hoyle State". In: *Phys. Rev. Lett.* 109 (25 Dec. 2012), p. 252501. DOI: 10.1103/PhysRevLett.109.252501. URL: https://link.aps.org/doi/10.1103/PhysRevLett.109.252501.

[48] Robin Smith et al. "New Measurement of the Direct 3′ Decay from the C 12 Hoyle State". In: *Physical Review Letters* 119 (Sept. 2017). DOI: 10.1103/PhysRevLett.119.132502.

[49] H. Zheng et al. "Decay modes of the Hoyle state in C12". In: *Physics Letters B* 779 (2018), pp. 460–463. ISSN: 0370-2693. DOI: https://doi.org/10.1016/j.physletb.2018.02.040. URL: https://www.sciencedirect.com/science/article/pii/S0370269318301424.

[50] C. W. Cook et al. "B^{12}, C^{12}, and the Red Giants". In: *Phys. Rev.* 107 (2 July 1957), pp. 508–515. DOI: 10.1103/PhysRev.107.508. URL: https://link.aps.org/doi/10.1103/PhysRev.107.508.

[51] M. Kamimura. "Transition densities between the 01+, 21+, 41+, 02+, 22+, 11- and 31- states in 12C derived from the three-alpha resonating-group wave functions". In: *Nuclear Physics A* 351.3 (1981), pp. 456–480. ISSN: 0375-9474. DOI: https://doi.org/10.1016/0375-9474(81)90182-2. URL: https://www.sciencedirect.com/science/article/pii/0375947481901822.

[52] A. Tohsaki et al. "Alpha Cluster Condensation in ^{12}C and ^{16}O". In: *Phys. Rev. Lett.* 87 (19 Oct. 2001), p. 192501. DOI: 10.1103/PhysRevLett.87.192501. URL: https://link.aps.org/doi/10.1103/PhysRevLett.87.192501.

[53] Eiji Uegaki et al. "Structure of the Excited States in 12C. I†)". In: *Progress of Theoretical Physics* 57.4 (Apr. 1977), pp. 1262–1276. ISSN: 0033-068X. DOI: 10.1143/PTP.57.1262. eprint: https://academic.oup.com/ptp/article-pdf/57/4/1262/5447216/57-4-1262.pdf. URL: https://doi.org/10.1143/PTP.57.1262.

[54] Evgeny Epelbaum et al. "Ab Initio Calculation of the Hoyle State". In: *Phys. Rev. Lett.* 106 (19 May 2011), p. 192501. DOI: 10.1103/PhysRevLett.106.192501. URL: https://link.aps.org/doi/10.1103/PhysRevLett.106.192501.

[55] Takaharu Otsuka et al. "-Clustering in atomic nuclei from first principles with statistical learning and the Hoyle state character". In: *Nature Communications* 13 (Apr. 2022). DOI: 10.1038/s41467-022-29582-0.

[56] M. Takechi et al. "Evidence of halo structure in ^{37}Mg observed via reaction cross sections and intruder orbitals beyond the island of inversion". In: *Phys. Rev. C* 90 (6 Dec. 2014), p. 061305. DOI: 10.1103/PhysRevC.90.061305. URL: https://link.aps.org/doi/10.1103/PhysRevC.90.061305.

[57] M. Freer et al. "Limits for the 3α branching ratio of the decay of the 7.65 MeV, 0_2^+ state in ^{12}C". In: *Phys. Rev. C* 49 (4 Apr. 1994), R1751–R1754. DOI: 10.1103/PhysRevC.49.R1751. URL: https://link.aps.org/doi/10.1103/PhysRevC.49.R1751.

[58] Ad.R. Raduta et al. "Evidence for´-particle condensation in nuclei from the Hoyle state deexcitation". In: *Physics Letters B* 705.1 (2011), pp. 65–70. ISSN: 0370-2693. DOI: https://doi.org/10.1016/j.physletb.2011.10.008. URL: https://www.sciencedirect.com/science/article/pii/S0370269311012408.

[59] O. S. Kirsebom et al. "Improved Limit on Direct α Decay of the Hoyle State". In: *Phys. Rev. Lett.* 108 (20 May 2012), p. 202501. DOI: 10.1103/PhysRevLett.108.202501. URL: https://link.aps.org/doi/10.1103/PhysRevLett.108.202501.

[60] T. K. Rana et al. "Estimation of direct components of the decay of the Hoyle state". In: *Phys. Rev. C* 88 (2 Aug. 2013), p. 021601. DOI: 10.1103/PhysRevC.88.021601. URL: https://link.aps.org/doi/10.1103/PhysRevC.88.021601.

[61] D Dell'Aquila et al. "Investigation of the Hoyle state in12C with a new hodoscope detector". In: *Journal of Physics: Conference Series* 876.1 (July 2017), p. 012006. DOI: 10.1088/1742-6596/876/1/012006. URL: https://dx.doi.org/10.1088/1742-6596/876/1/012006.

[62] M. Itoh et al. "Further Improvement of the Upper Limit on the Direct 3α Decay from the Hoyle State in ^{12}C". In: *Phys. Rev. Lett.* 113 (10 Sept. 2014), p. 102501. DOI: 10.1103/PhysRevLett.113.102501. URL: https://link.aps.org/doi/10.1103/PhysRevLett.113.102501.

[63] Yassid Ayyad et al. "Overview of the data analysis and new micro-pattern gas detector development for the Active Target Time Projection Chamber (AT-TPC) project." In: *Journal of Physics: Conference Series* 876.1 (July 2017), p. 012003. DOI: 10.1088/1742-6596/876/1/012003. URL: https://dx.doi.org/10.1088/1742-6596/876/1/012003.

[64] J. Bradt et al. "Commissioning of the Active-Target Time Projection Chamber". In: *Nuclear Instruments and Methods in Physics Research Section A: Accelerators, Spectrometers, Detectors and Associated Equipment* 875 (2017), pp. 65–79. ISSN: 0168-9002. DOI: https://doi.org/10.1016/j.nima.2017.09.013. URL: https://www.sciencedirect.com/science/article/pii/S0168900217309683.

[65] "MICROMEGAS: a high-granularity position-sensitive gaseous detector for high particle-flux environments". In: *Nuclear Instruments and Methods in Physics Research Section A: Accelerators, Spectrometers, Detectors and Associated Equipment* 376.1 (1996), pp. 29–35. ISSN: 0168-9002. DOI: https://doi.org/10.1016/0168-9002(96)00175-1. URL: https://www.sciencedirect.com/science/article/pii/0168900296001751.

[66] I. Giomataris et al. "Micromegas in a bulk". In: *Nuclear Instruments and Methods in Physics Research Section A: Accelerators, Spectrometers, Detectors and Associated Equipment* 560.2 (2006), pp. 405–408. ISSN: 0168-9002. DOI: https://doi.org/10.1016/j.nima.2005.12.222. URL: https://www.sciencedirect.com/science/article/pii/S0168900205026501.

[67] E.C. Pollacco et al. "GET: A generic electronics system for TPCs and nuclear physics instrumentation". In: *Nuclear Instruments and Methods in Physics Research Section A: Accelerators, Spectrometers, Detectors and Associated Equipment* 887 (2018), pp. 81–93. ISSN: 0168-9002. DOI: https://doi.org/10.1016/j.nima.2018.01.020. URL: https://www.sciencedirect.com/science/article/pii/S0168900218300342.

[68] Christoph Dalitz, Jens Wilberg, and Lukas Aymans. "TriplClust: An Algorithm for Curve Detection in 3D Point Clouds". In: *Image Processing On Line* 9 (2019). https://doi.org/10.5201/ipol.2019.234, pp. 26–46.

[69] Martin A. Fischler and Robert C. Bolles. "Random Sample Consensus: A Paradigm for Model Fitting with Applications to Image Analysis and Automated Cartography". In: *Commun. ACM* 24.6 (June 1981), pp. 381–395. ISSN: 0001-0782. DOI: 10.1145/358669.358692. URL: https://doi.org/10.1145/358669.358692.

[70] José Lezama et al. "An Unsupervised Algorithm for Detecting Good Continuation in Dot Patterns". In: *Image Processing On Line* 7 (2017). https://doi.org/10.5201/ipol.2017.176, pp. 81–92.

[71] Don S. Lemons and Anthony Gythiel. "Paul Langevin's 1908 paper "On the Theory of Brownian Motion" ["Sur la théorie du mouvement brownien," C. R. Acad. Sci. (Paris) 146, 530–533 (1908)]". In: *American Journal of Physics* 65.11 (Nov. 1997), pp. 1079–1081. ISSN: 0002-9505. DOI: 10.1119/1.18725. eprint: https://pubs.aip.org/aapt/ajp/article-pdf/65/11/1079/12107627/1079_1_online.pdf. URL: https://doi.org/10.1119/1.18725.

[72] Blum et al. *Particle detection with drift chambers*. Heidelberg: Springer Berlin, 2008. DOI: 10.1007/978-3-540-76684-1.

[73] Noori Shirazi, Amir and Fleck, Ivor. "Bivariate normal distribution for finding inliers in Hough space for a Time Projection Chamber". In: *EPJ Web Conf.* 150 (2017), p. 00010. DOI: 10.1051/epjconf/201715000010. URL: https://doi.org/10.1051/epjconf/201715000010.

[74] Are Strandlie and Rudolf Frühwirth. "Track and vertex reconstruction: From classical to adaptive methods". In: *Rev. Mod. Phys.* 82 (2 May 2010), pp. 1419–1458. DOI: 10.1103/RevModPhys.82.1419. URL: https://link.aps.org/doi/10.1103/RevModPhys.82.1419.

[75] Wolfgang Waltenberger. "RAVE—A Detector-Independent Toolkit to Reconstruct Vertices". In: *Nuclear Science, IEEE Transactions on* 58 (May 2011), pp. 434–444. DOI: 10.1109/TNS.2011.2119492.

[76] F. James. "MINUIT Function Minimization and Error Analysis: Reference Manual Version 94.1". In: (1994).

[77] James F. Ziegler, M.D. Ziegler, and J.P. Biersack. "SRIM – The stopping and range of ions in matter (2010)". In: *Nuclear Instruments and Methods in Physics Research Section B: Beam Interactions with Materials and Atoms* 268.11 (2010). 19th International Conference on Ion Beam Analysis, pp. 1818–1823. ISSN: 0168-583X. DOI: https://doi.org/10.1016/j.nimb.2010.02.091. URL: https://www.sciencedirect.com/science/article/pii/S0168583X10001862.

[78] F. Michel et al. "Optical model description of alpha+ O-16 elastic scattering and alpha-cluster structure in Ne-20". In: *Phys. Rev. C* 28 (1983), pp. 1904–1917. DOI: 10.1103/PhysRevC.28.1904.

[79] Jonas Ferreira et al. "Analysis of the alpha-transfer reaction in the 12C + 16O system using the semi-microscopic algebraic cluster model". In: *The European Physical Journal A* 55 (June 2019). DOI: 10.1140/epja/i2019-12773-7.

[80] Ian J. Thompson. "Coupled reaction channels calculations in nuclear physics". In: *Computer Physics Reports* 7.4 (1988), pp. 167–212. ISSN: 0167-7977. DOI: https://doi.org/10.1016/0167-7977(88)90005-6. URL: https://www.sciencedirect.com/science/article/pii/0167797788900056.

[81] S. Adachi et al. "Systematic analysis of inelastic α scattering off self-conjugate $A = 4n$ nuclei". In: *Phys. Rev. C* 97 (1 Jan. 2018), p. 014601. DOI: 10.1103/PhysRevC.97.014601. URL: https://link.aps.org/doi/10.1103/PhysRevC.97.014601.

[82] C. D. Pruitt, J. E. Escher, and R. Rahman. "Uncertainty-quantified phenomenological optical potentials for single-nucleon scattering". In: *Phys. Rev. C* 107 (1 Jan. 2023), p. 014602. DOI: 10.1103/PhysRevC.107.014602. URL: https://link.aps.org/doi/10.1103/PhysRevC.107.014602.

[83] R.H. Dalitz. "CXII. On the analysis of´-meson data and the nature of the´-meson". In: *The London, Edinburgh, and Dublin Philosophical Magazine and Journal of Science* 44.357 (1953), pp. 1068–1080. DOI: 10.1080/14786441008520365. eprint: https://doi.org/10.1080/14786441008520365. URL: https://doi.org/10.1080/14786441008520365.

[84] Jack Bishop et al. "An improved upper limit on the direct 3 decay of the Hoyle state". In: *AIP Conference Proceedings* 2038 (Nov. 2018), p. 020035. DOI: 10.1063/1.5078854.

[85] L Morelli et al. "The 12C* Hoyle state in the inelastic 12C + 12C reaction and in 24Mg* decay". In: *Journal of Physics G: Nuclear and Particle Physics* 43.4 (Feb. 2016), p. 045110. DOI: 10.1088/0954-3899/43/4/045110. URL: https://dx.doi.org/10.1088/0954-3899/43/4/045110.

[86] K H et al Schmidt. "Some remarks on the error analysis in the case of poor statistics". In: *AC* 361:1 (Mar. 1984), p. 00024. DOI: 10.1007/BF01415656.

[87] J. Hüfner, C. Mahaux, and H.A. Weidenmüller. "DWBA in the shell-model approach to nuclear reactions". In: *Nuclear Physics A* 105.2 (1967), pp. 489–521. ISSN: 0375-9474. DOI: https://doi.org/10.1016/0375-9474(67)90533-7. URL: https://www.sciencedirect.com/science/article/pii/0375947467905337.

[88] G.R. Satchler. "Isospin and macroscopic models for the excitation of giant resonances and other collective states". In: *Nuclear Physics A* 472.2 (1987), pp. 215–236. ISSN: 0375-9474. DOI: https://doi.org/10.1016/0375-9474(87)90208-9. URL: https://www.sciencedirect.com/science/article/pii/0375947487902089.

[89] Ian J. Thompson and Filomena M. Nunes. *Nuclear Reactions for Astrophysics: Principles, Calculation and Applications of Low-Energy Reactions*. Cambridge University Press, 2009. DOI: 10.1017/CBO9781139152150.

[90] D.R. Tilley, H.R. Weller, and C.M. Cheves. "Energy levels of light nuclei A = 16–17". In: *Nuclear Physics A* 564.1 (1993), pp. 1–183. ISSN: 0375-9474. DOI: https://doi.org/10.1016/0375-9474(93)90073-7. URL: https://www.sciencedirect.com/science/article/pii/0375947493900737.

Appendix A

Mandelstam variables

Mandelstam variables are Lorentz invariant, meaning they have the same value in all inertial reference frames. They are instrumental in analysing high-energy collisions and are widely used in theoretical calculations and experimental analyses in particle physics. The Mandelstam variables s, t, and u are then defined as follows:

P1 and P2 are the incoming four-momentum particles, and P3 and P4 are the outgoing, as seen in the following figure.

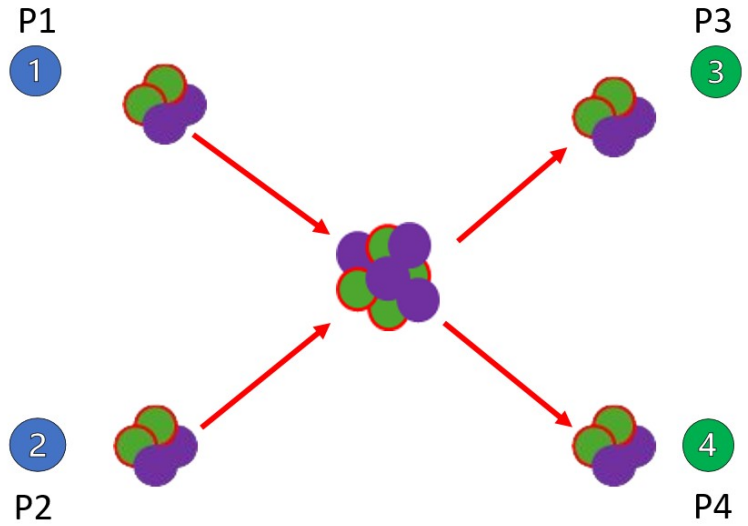

Figure A.1: In this diagram, two particles of momentum p1 and p2 enter the system. They interact in some way, and then two particles of different momentum (p3 and p4) leave the system.

- s (centre-of-mass energy squared) is the square of the total energy in the centre-of-mass frame.

$$s = (p_1 + p_2)^2 \tag{A.1}$$

- t (momentum transfer squared), where p3 is the four-momentum of particle three produced in the scattering process. t measures the momentum transfer between the initial and final states.

$$t = (p_1 - p_3)^2 \tag{A.2}$$

- u (another momentum transfer squared), where p4 is the four-momentum of particle four produced in the scattering process.

$$u = (p_1 - p_4)^2 \tag{A.3}$$

- The total energy-momentum conservation relation can be written in terms of these variables as

$$s + t + u = \sum m_i^2 \tag{A.4}$$

Rewriting the Mandelstam variables as a function of the energies of the projectile, the scattering particle and the excitation energy, and taking into account that in this definition, m1, m2, m3 and m4 are the masses of the projectile, target, ejectile and recoil respectively, we have that:

$$s = m_1^2 + m_2^2 + 2 * m_2 * E_1 \leftarrow E_1 = K_{proj} + m_1 \tag{A.5}$$

$$u = m_2^2 + m_3^2 - 2 * m_2 * E_3 \leftarrow E_3 = K_{eje} + m_3 \tag{A.6}$$

$$t = m_2^2 + m_4(ex) - 2 * m_2 * (E_1 + m_2 - E_3) \leftarrow m_4(ex) = E_x + m_4 \tag{A.7}$$

Appendix B

Optical potential

The Distorted-Wave Born Approximation (DWBA) [87] is a theoretical framework used in nuclear physics to describe the scattering of particles, such as electrons or nuclei, from target nuclei. It is a more sophisticated approach than the simpler Born approximation and is particularly useful when the interaction between the incident particle and the target nucleus is complex.

The DWBA treats the incident particle as a wave. Its wave function is modified or "distorted" by the nuclear potential of the target nucleus. This distortion considers that the wave function of the incident particle is limited as it interacts with the nucleus. The DWBA aims to calculate the differential cross-section for scattering, which describes how particles are scattered in different directions. It is particularly valuable for studying nuclear reactions, such as neutron or proton scattering from nuclei. It provides a more accurate description of the scattering process than the simple Born approximation. It includes the effects of the nuclear structure and considers the angular momentum and energy transfer during the scattering event.

The central equation in DWBA is the transition amplitude [88], which can be written as

$$T_{fi} = \langle \psi_f^{(-)} | V | \psi_i^{(+)} \rangle \tag{B.1}$$

Where T_{fi} is the transition amplitude, which represents the probability amplitude for a particle to transition from an initial state $\psi_i^{(+)}$ to a final state $\psi_f^{(-)}$ due to interaction with the potential V.

The wave functions $\psi_i^{(+)}$ and $\psi_f^{(-)}$ are solutions of the Schrödinger equation for the incoming and outgoing waves, respectively. They are typically represented as distorted waves to account for the interaction with the nuclear potential:

$$\psi_i^{(+)} = e^{i\mathbf{k}\cdot\mathbf{r}} + f(\theta, \phi)\frac{e^{ikr}}{r} \tag{B.2}$$

$$\psi_f^{(-)} = \frac{e^{ikr}}{r} \tag{B.3}$$

Where $\mathbf{k}$ is the wave vector of the incident particle, $\mathbf{r}$ is the position vector, $f(\theta, \phi)$ is the scattering amplitude, which depends on the scattering angles θ and ϕ and k is the wave number,

given by $k = \frac{\sqrt{2\mu E}}{\hbar}$, where μ is the reduced mass of the system, E is the energy of the incident particle and $\hbar$ is the reduced Planck constant.

The potential V represents the interaction between the incident particle and the target nucleus. In DWBA, this potential is often described by optical models, where V can be expressed as

$$V = U(r) + iW(r) \tag{B.4}$$

Where $U(r)$ is the real part of the optical potential, representing the nuclear potential and $W(r)$ is the imaginary part of the optical potential, representing absorption or inelastic scattering effects.

The scattering amplitude $f(\theta, \phi)$ in DWBA can be calculated by solving the appropriate equations involving the optical potential and the distorted wave functions. The final differential cross-section for the scattering process is then related to the square of the magnitude of the scattering amplitude:

$$\frac{d\sigma}{d\omega} = |f(\theta, \phi)|^2 \tag{B.5}$$

This formula describes how particles are scattered in different directions as a function of the scattering angles θ and ϕ. The DWBA is a robust theoretical framework for describing complex nuclear and atomic scattering processes. Still, its actual implementation can involve considerable mathematical and computational work due to the detailed calculations involved.

The optical potential is the basis for reproducing the theoretical results of the cross-sections in this thesis. The potential in the above equations, U(r), is called the optical potential in the optical model. An average potential characterises the projectile's interaction with all the nucleons in the target during an elastic diffusion. It is described as the sum of a real and imaginary potential.

The potential energy function, U (r), depends on the composition and energy of the nuclei involved in the reaction. Two methods can determine it: one consists of deriving it from elastic diffusion data, while the other involves a microscopic evaluation in the context of a convolution (folding) model.

The optical model is a widespread framework for describing nuclear potential. In this model, nuclear potential is characterized as a complex entity consisting of a material component responsible for scattering and an immaterial part responsible for absorption of the incoming flux. The absorbing portion considers inelastic interactions within the system.

The term 'optical' is used because it draws an analogy with light scattering in a partially opaque medium, where the imaginary segment of a complex refractive index can quantify the amount of light absorbed by the medium [20]. An optical model is typically formulated using the Woods-Saxon potential (Eq: 4.8).

The central potential describing the target used is given by equation B.6. R is the radius, a is the diffusivity parameter and V and W are the depth of the potential in the real and imaginary parts. V_C corresponds to the Coulomb potential, a homogeneously charged sphere.

$$U(r) = V_C - \frac{V(r) - iW(r)}{1 + exp(\frac{r-R}{a})} \tag{B.6}$$

The nuclear potential includes only the influence of the strong nuclear force, which operates at short distances. However, charged particles, such as protons, also encounter a long-range Coulomb force resulting from the nuclear charge. An additional concept is added to the total potential. This term is attributed to the nuclear charge force [89].

$$V_{\mathrm{C}}(r) = Z_{\mathrm{proj.}} Z_e \times \begin{cases} \frac{3}{2}\left(1 - \frac{r^2}{R_{\mathrm{C}}^2}\right) & \text{for } r \leq R_{\mathrm{C}} \\ \frac{1}{R_{\mathrm{C}}} & \text{for } r \geq R_{\mathrm{C}} \end{cases} \tag{B.7}$$

This potential depends on several factors, including the projectile's charge Z_{proj}, the nucleus Z_e and the Coulomb radius R_{Coul}. It's worth noting that the Coulomb radius R_C is often proportional to $A^{1/3}$ for nuclei with mass number A.

Appendix C

RANSAC pseudo-code

Pseudocode used in trace recognition by the RANSAC method. This pseudocode shows the computational information flow for trace distinction by circular RANSAC.

```
INPUT::

    n_data -> Pads enabled each event

    n_min == 3 -> minimum number required to fit the model

    iter_max == 200 -> maximum number of iterations

    threshold == 15 -> Distance to be an inlier (mm)

    d_min == 30 -> Required number of points to form a pattern

OUTPUT::

    RANSAC_fit - model parameters which best fit the data
    (or nil if no good model is found)

    iterations = 0

    best_err = number large
```

LOOP FOR BEST MODEL:

```
for ( iter = 0; iter <= itermax; iter++):
{
    a_inliers = n_min randomly selected values
    a_model = model parameters fitted to a_inliers
    also_inliers = empty set

    for (n_data != a_inliers)
    {
        if point fits a_model with an error smaller
        than threshold add a point to also_inliers
    }

        if the nr of elements in also_inliers is > d_min
        {
        % We may have found a good model, so test
        how good it is:

        better_model = model parameters fitted to
        all points in a_inliers and also_inliers

        this_err = a measure of how well the model
        fits these points

        if this_err < best_err
                {
                    RANSAC_fit = better_model
                    best_err = this_err
                }
        }

}   return RANSAC_fit
```

Appendix D

^{16}O and ^{12}C levels scheme

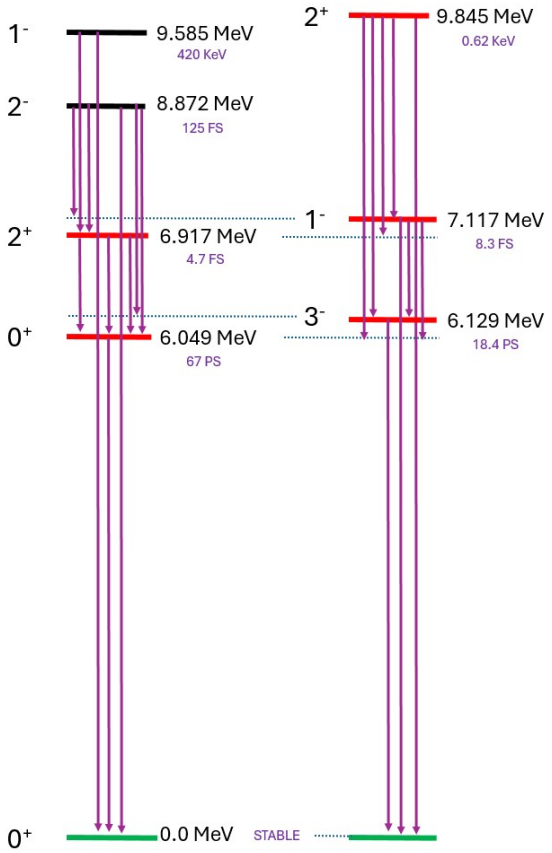

Figure D.1: Scheme of energy levels and J^p for the ^{16}O. The figure highlights the levels for which their cross-section is studied in red in this thesis.

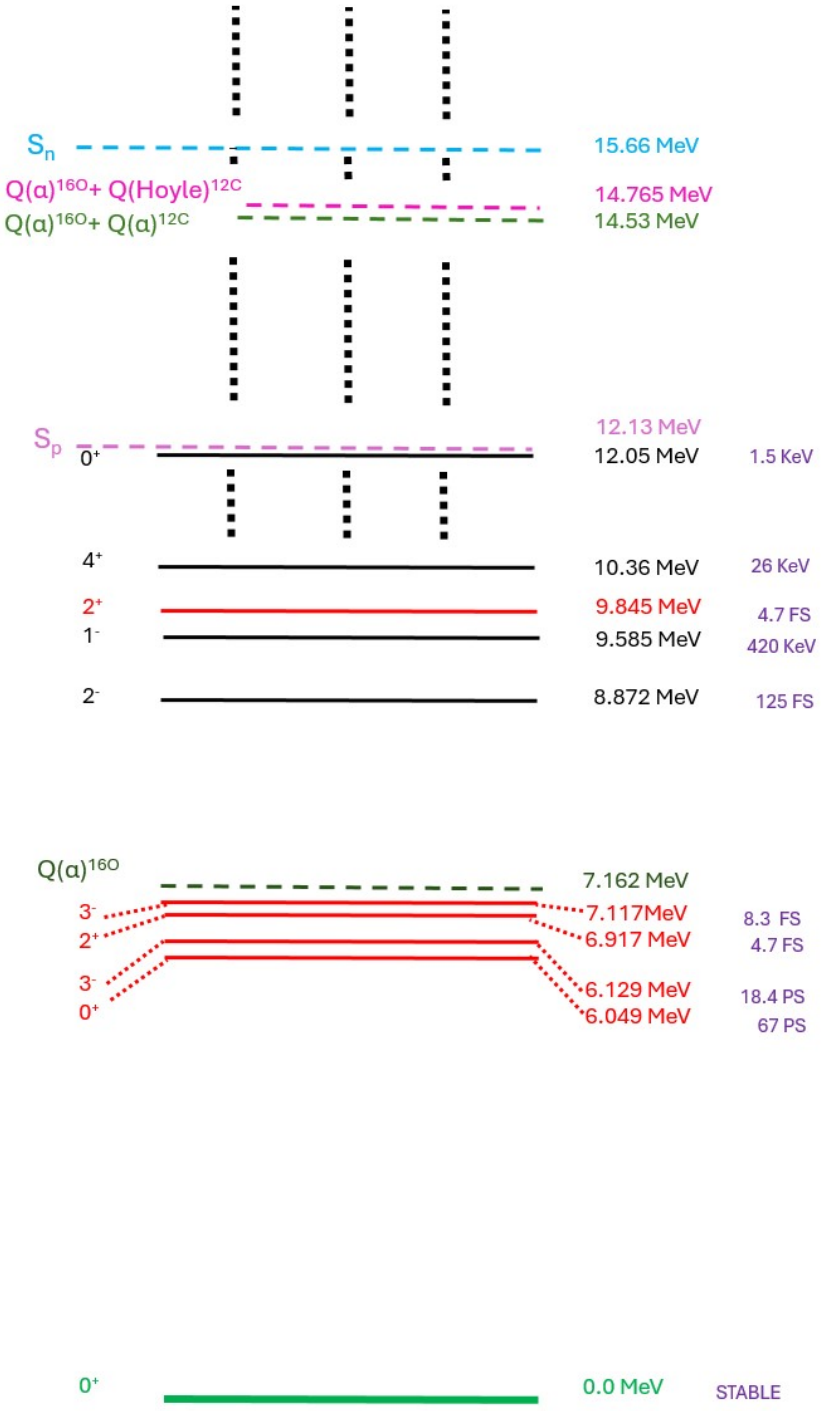

Figure D.2: Diagram of energy levels and J^p for the ^{16}O. Figure adapted from [90]. The figure shows in blue the neutron separation energy for the nucleus of ^{16}O, in purple that of the protons, in dark green the $Q(\alpha)$ and in pink the energy for the decay of ^{16}O into carbon and the subsequent decay in 3α of the Hoyle state corresponding to 14.765 MeV.

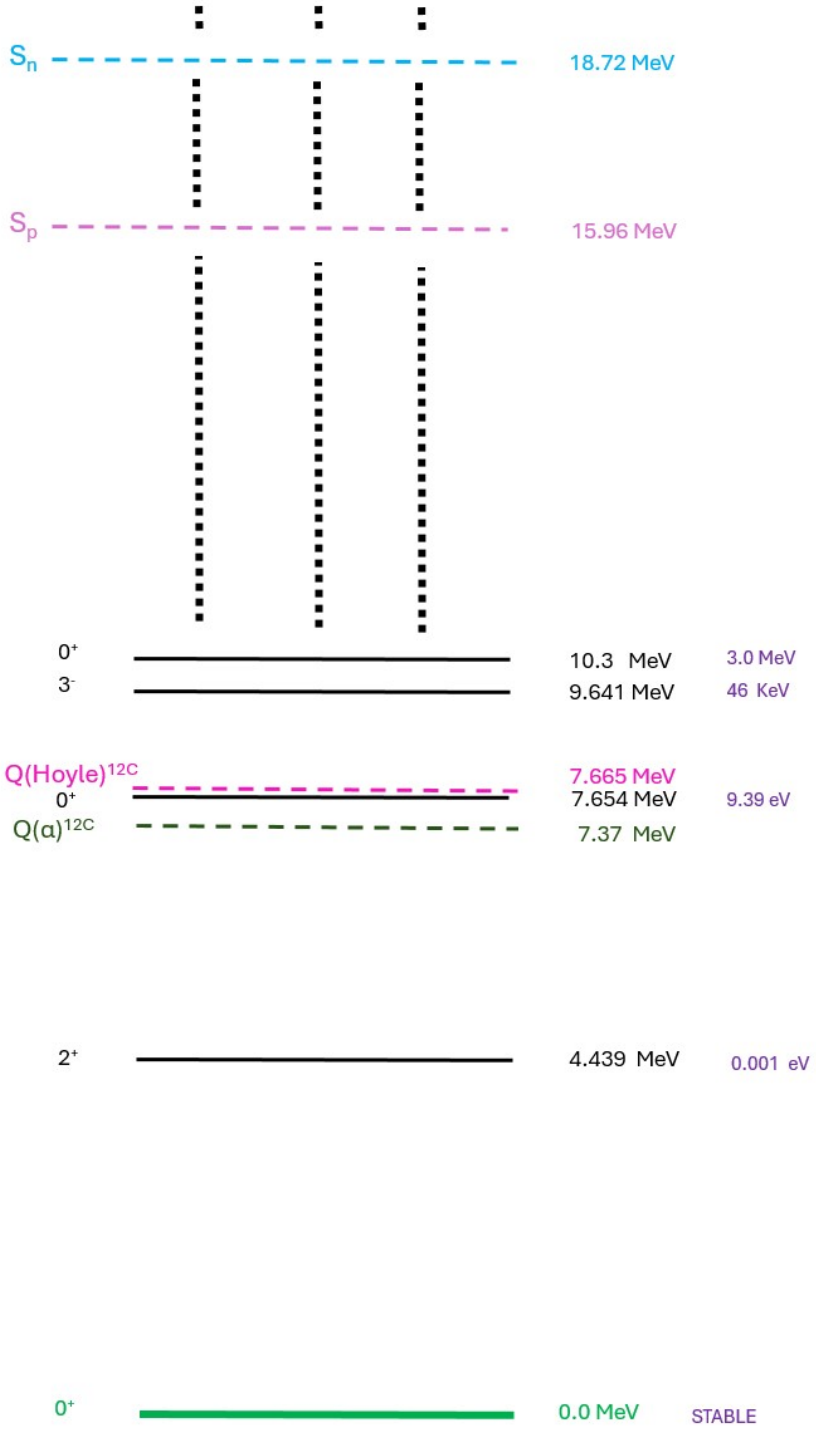

Figure D.3: Diagram of energy levels and J^p for ^{12}C. The figure shows in blue the neutron separation energy for the nucleus of ^{12}C, in purple that of the protons, in dark green the minimum $Q(\alpha)$ for ^{12}C to detach from a α particle corresponding to 7.37 MeV and near of that level the experimental Hoyle state for the carbon in pink.

Appendix E

Cross-sections excited states

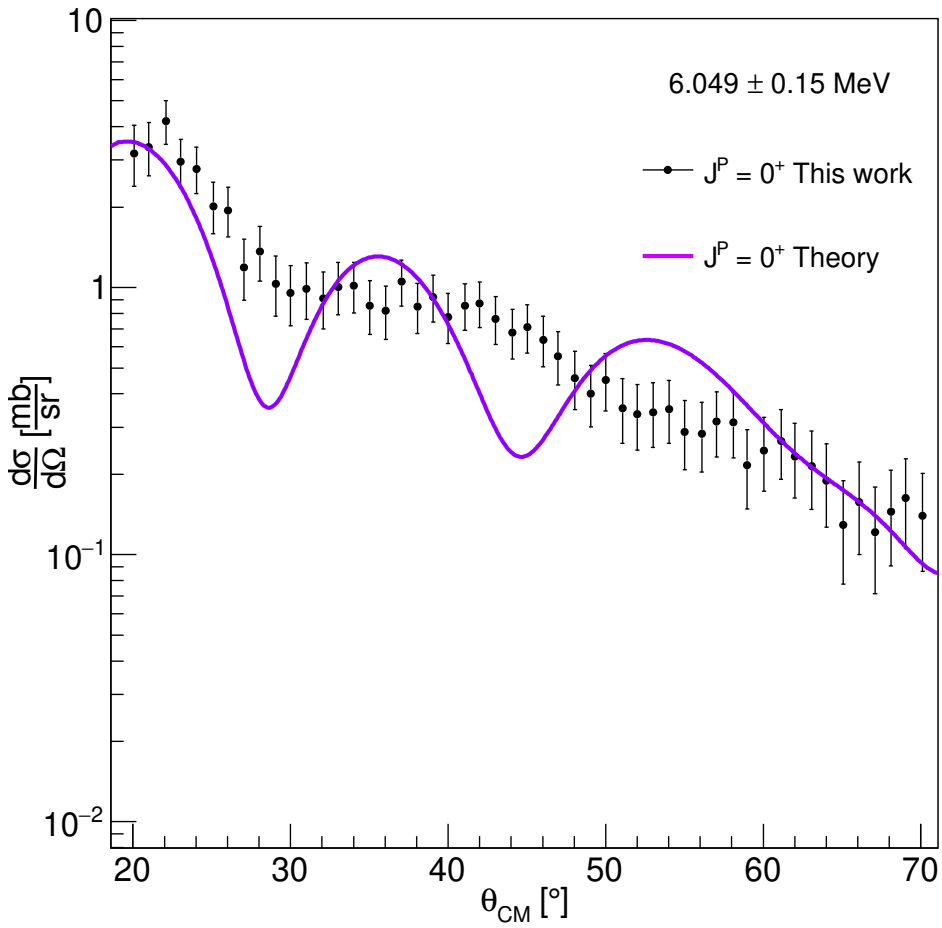

Figure E.1: Differential cross section for the first excited state corresponding to the theoretical excitation energy 6.049 MeV of oxygen $L = 0^+$. The calculation is performed for an excitation energy cutoff of 300 KeV around this value. The purple line corresponds to the theoretical XS value.

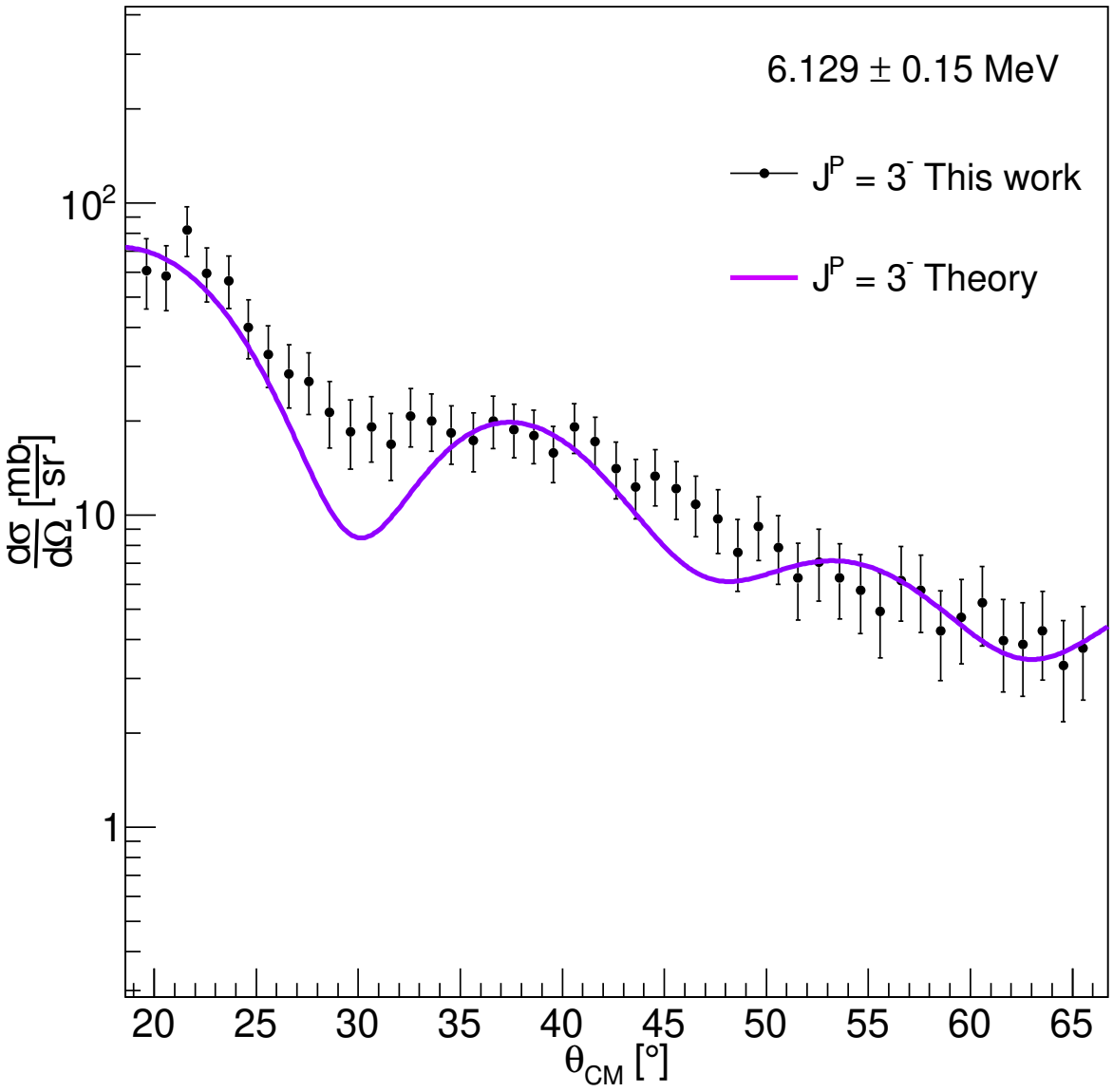

Figure E.2: Differential cross section for the second excited state corresponding to the theoretical excitation energy 6.129 MeV of oxygen $L = 3^-$. The calculation is performed for an excitation energy cutoff of 300 KeV around this value. The purple line corresponds to the theoretical XS value.

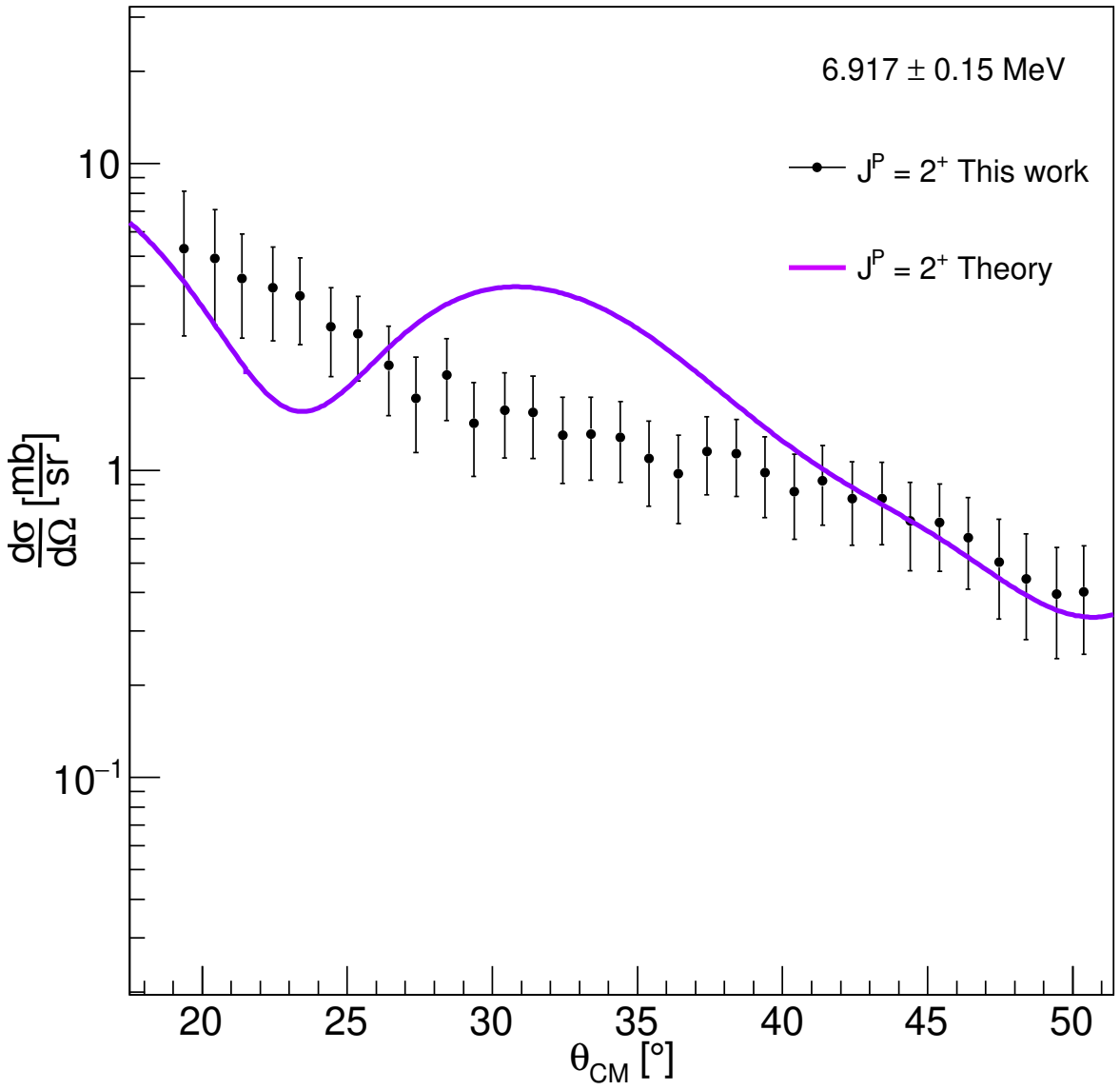

Figure E.3: Differential cross section for the third excited state corresponding to the theoretical excitation energy 6.917 MeV of oxygen $L = 2^+$. The calculation is performed for an excitation energy cutoff of 300 KeV around this value. The purple line corresponds to the theoretical XS value.

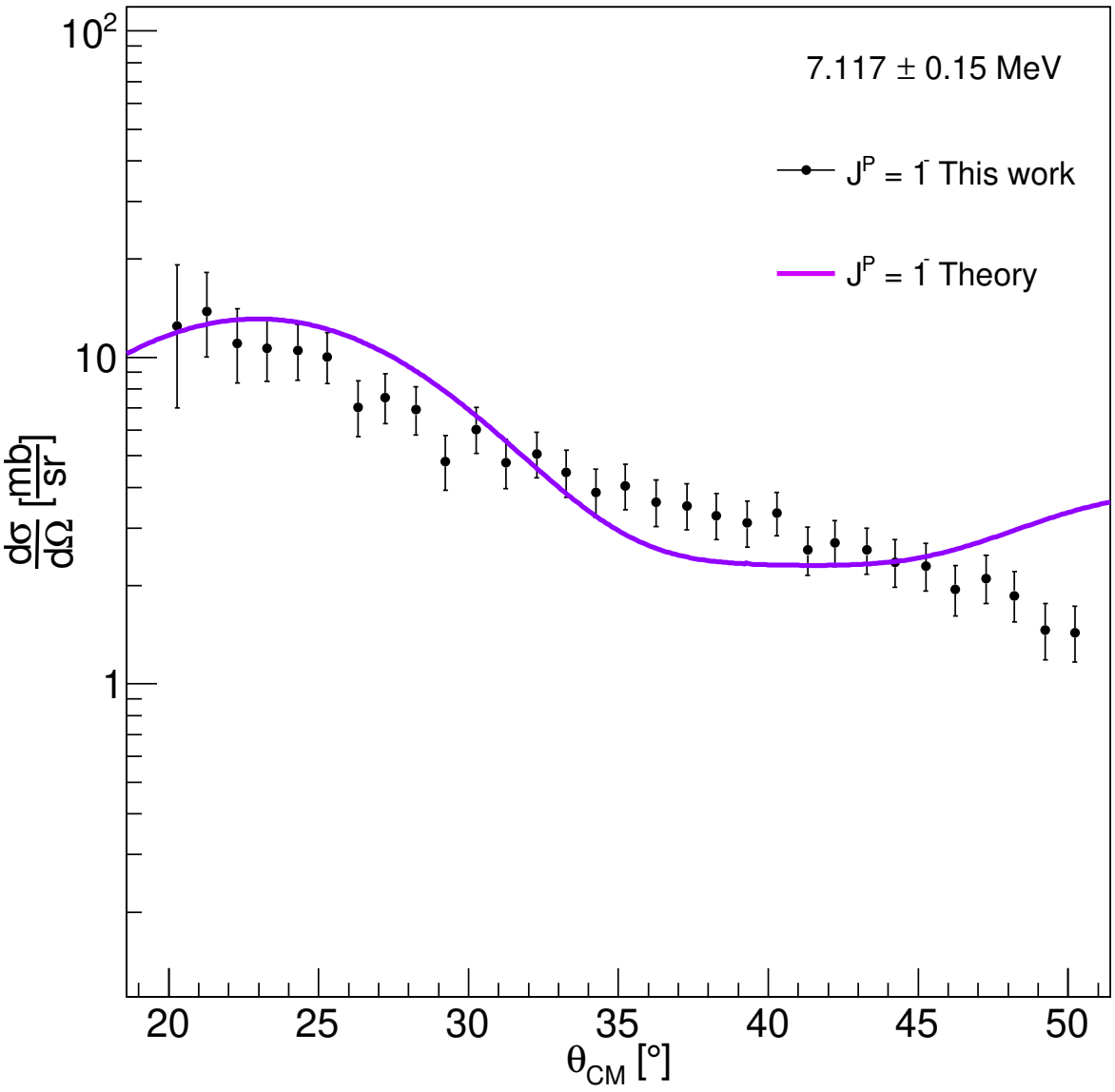

Figure E.4: Differential cross section for the fourth excited state corresponding to the theoretical excitation energy 7.117 MeV of oxygen $L = 1^-$. The calculation is performed for an excitation energy cutoff of 300 KeV around this value. The purple line corresponds to the theoretical XS value.

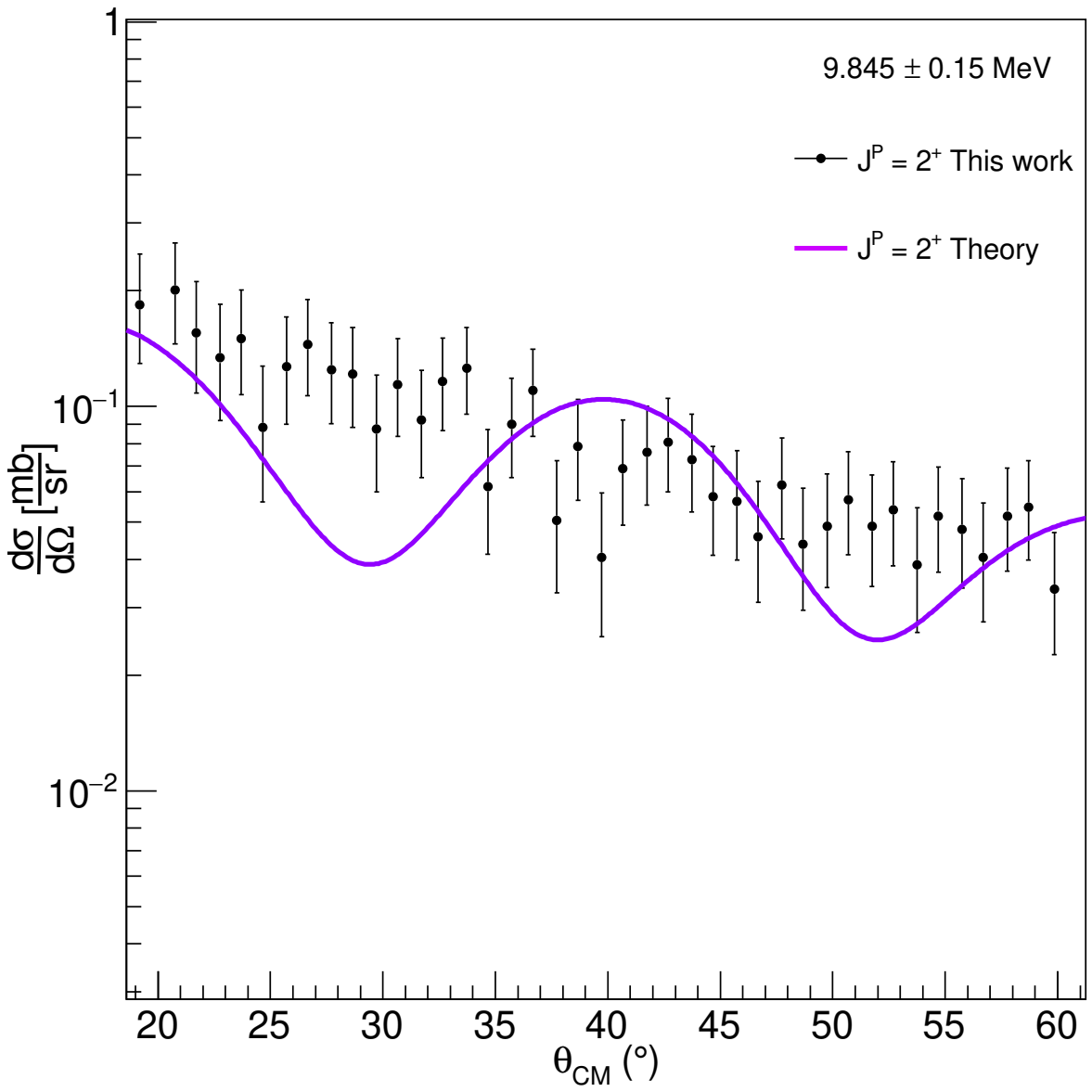

Figure E.5: Differential cross section for the excited state corresponding to the theoretical excitation energy 9.845 MeV of oxygen $L = 2^+$. The calculation is performed for an excitation energy cutoff of 300 KeV around this value. The purple line corresponds to the theoretical XS value.

Appendix F

Trace collection

The following appendix summarises the representation after pattern recognition of a collection of traces that can be resolved as ATTPC in the ^{16}O experiment in alpha at 10 MeV/n. All traces studied in the present thesis are from forward, elastic or inelastic events.

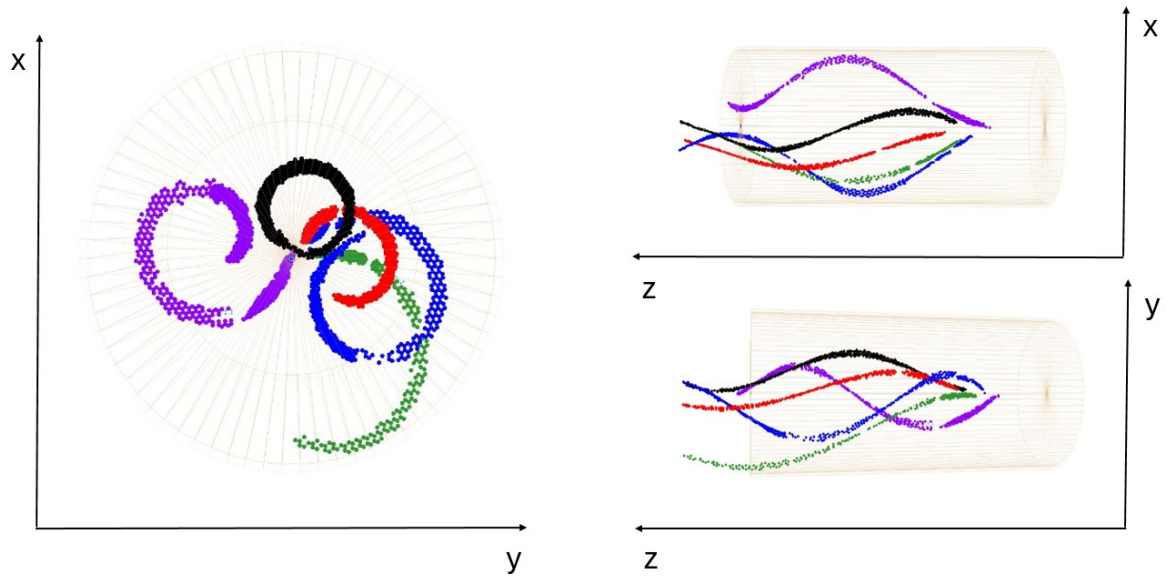

Figure F.1: Hoyle state direct with excitation energy $E_x = 14.914 MeV$. In this event, one can observe the difficulty in some events of recovering the entire scattering trace. This is solved by taking for all the traces the 60 % or 40 % from the beginning of the trace for the PID since these effects are avoided and, on the other hand, most of the energy loss occurs in that area of the trace, avoiding energy deposition tails that do not provide relevant information to the PID.

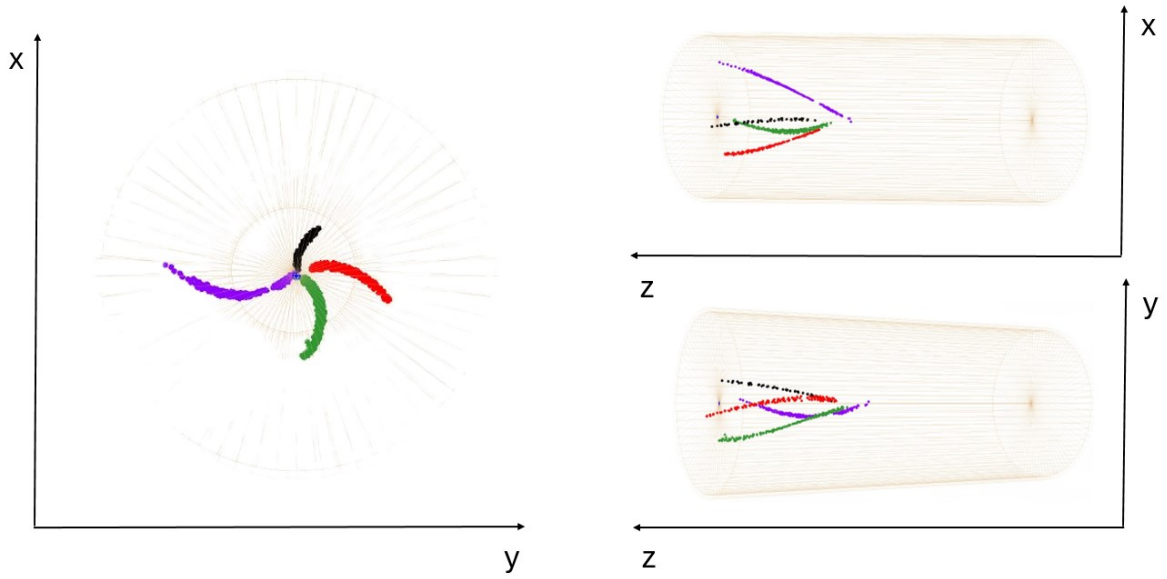

Figure F.2: Hoyle state direct with excitation energy $E_x = 14.97MeV$. In this event, as in the previous one, it can be seen that the vertex of the three traces is slightly shifted concerning the scattering particle. This is because, in the PRA, the vertex is calculated for each trace and depends on multiple factors for reconstruction. The vertex that accounts for the event's energy is that of the scattering particle, so even though these distortions exist in the three-dimensional representation, the energy is perfectly calculated for the PID.In this event it has not been possible to reconstruct the scattering trace because it is very close to 90 degrees and the tracking is very small.

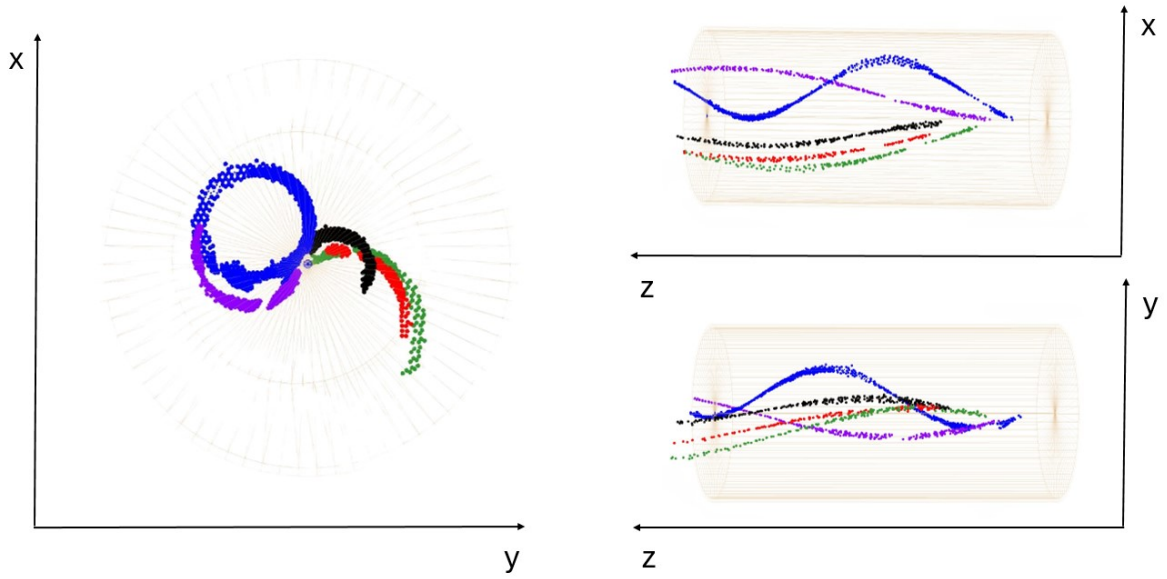

Figure F.3: Three-dimensional reconstruction of the direct Hoyle state in which the three uncorrelated alpha particles and the complete scattering alpha can be seen in black, red and green. This event corresponds to a scattering alpha energy of 14.43 MeV, the excitation energy calculated after fitting.

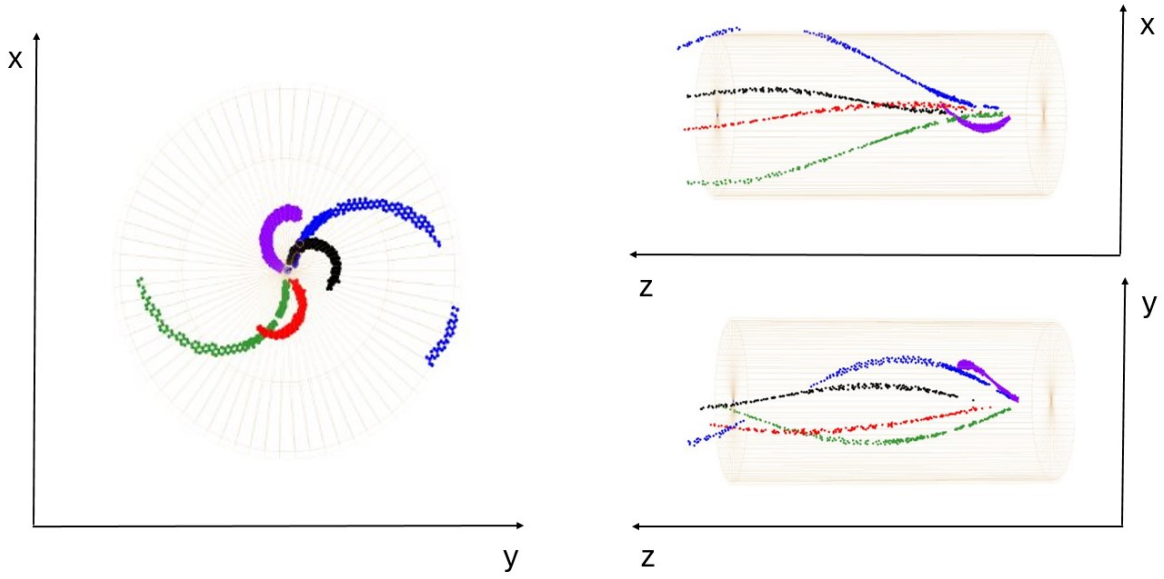

Figure F.4: Importance of the three-dimensional reconstruction in the PRA as a priori this event could be recognised as a direct Hoyle by erroneously counting the purple trace as one of the triads of alphas, from the XY point of view. In this case, the analysis of the event shows that it corresponds to direct Hoyle with an energy of 15.03 MeV.

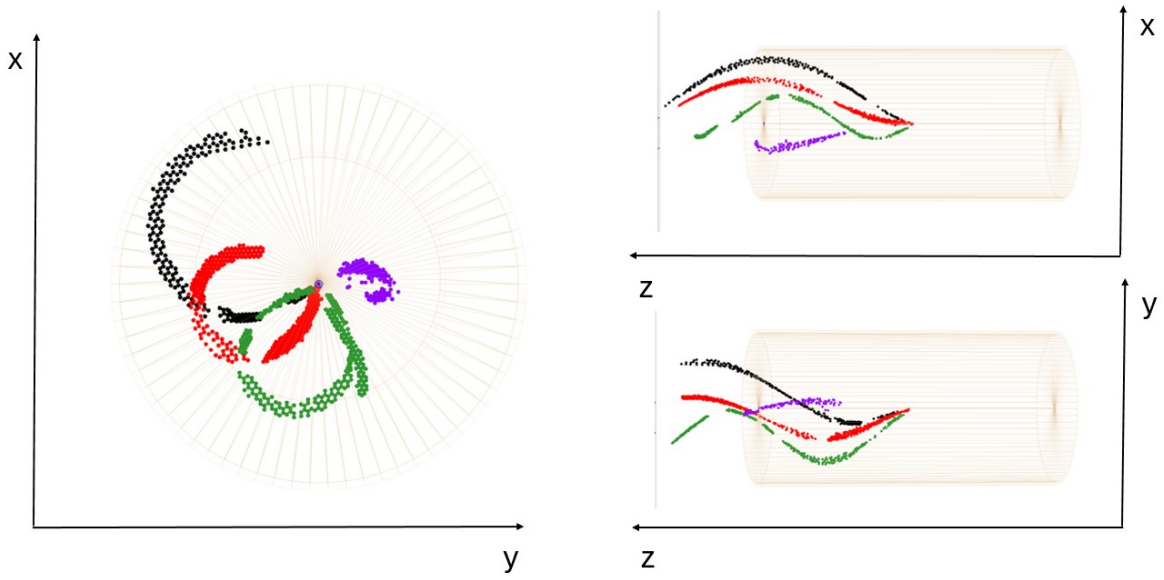

Figure F.5: Direct Hoyle example taken as a possible event in which the dependence of the outgoing alphas on the applied magnetic field can be seen to depend on the angulation. The event fulfils the criteria of the Dalitz plot and lies within the excitation energy range $E_x = 14.47 MeV$.

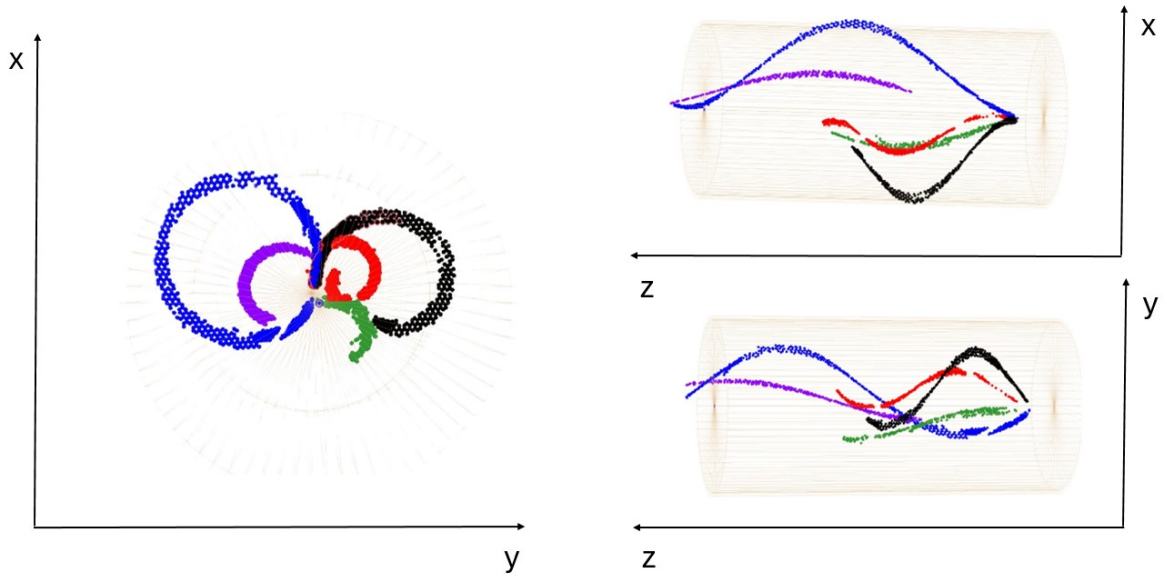

Figure F.6: Direct example of Hoyle taken as a possible event in which it is difficult to filter by trace length since the magnetic field acts depending on the exit angle of each trace, and can curve some traces much more than others, making it more likely to break in the identification of some of them. The event fulfils the criteria of the Dalitz diagram and lies within the excitation energy interval $Ex = 14.39MeV$.

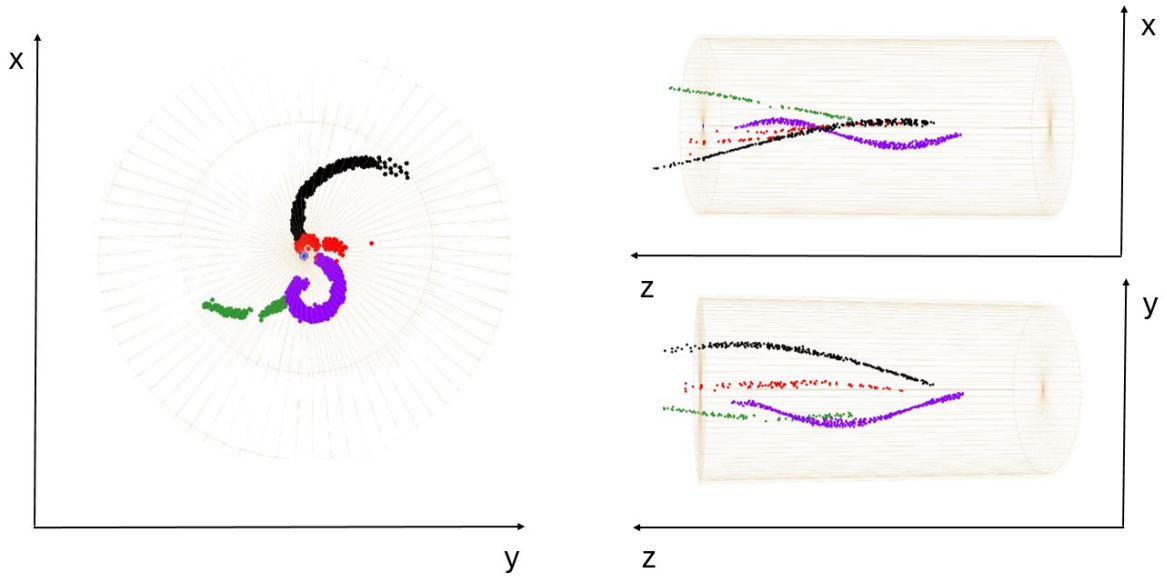

Figure F.7: In this reconstruction of the direct Hoyle effect, apart from losing the scattering alpha, it can be seen that the red trace belonging to the direct decay of ^{12}C cannot be completely reconstructed due to its small angulation. This highlights the difficulty of reconstructing Hoyle effects by trace length since carbon and oxygen will mostly come out at small angles. The event fulfils the criteria of the Dalitz plot and lies within the excitation energy range $E_x = 14.67MeV$.

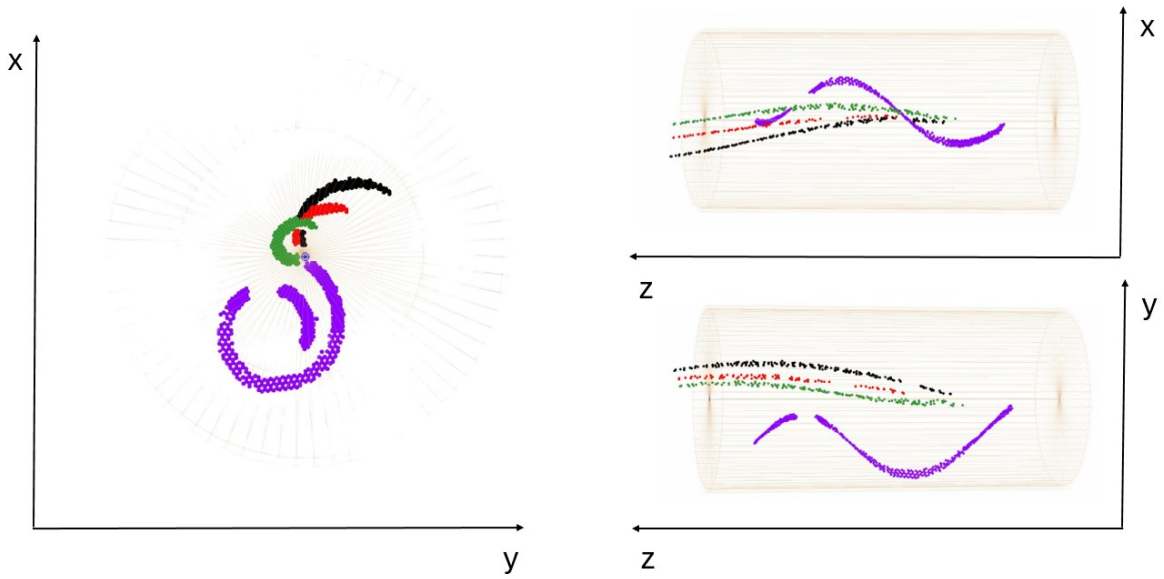

Figure F.8: Direct Hoyle effect where a perfect reconstruction of the three uncorrelated traces can be observed, and the reconstruction power of the fitting algorithm can be seen, where three very close traces are perfectly differentiated.The event fulfils the criteria of the Dalitz plot and lies within the excitation energy range $E_x = 14.83 MeV$.

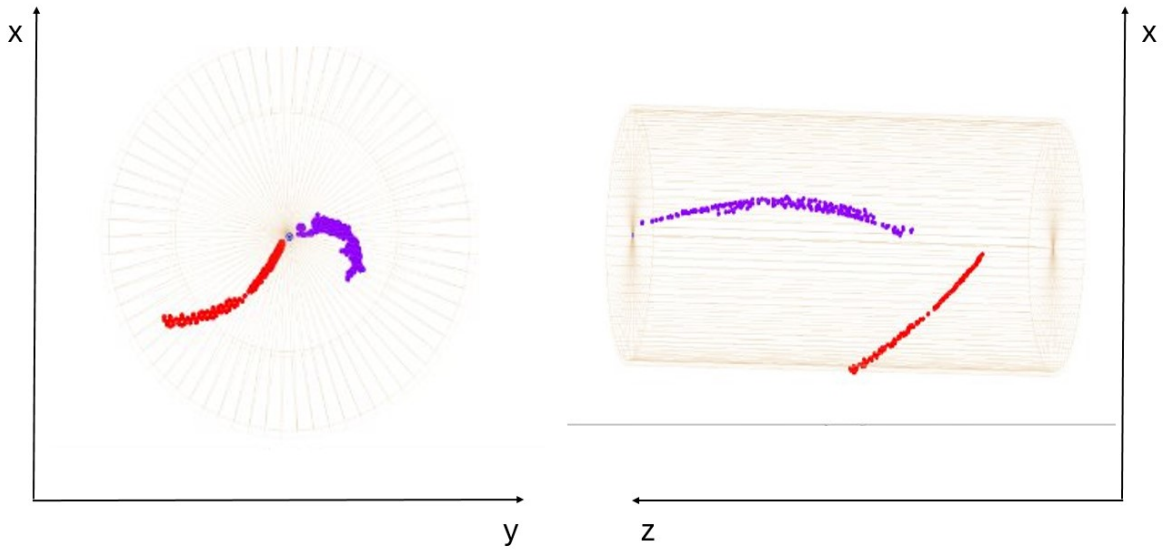

Figure F.9: The figure represents an elastic event of ^{16}O in a α particle. The purple trace represents the heavy particle, and the red one represents the scattering particle.

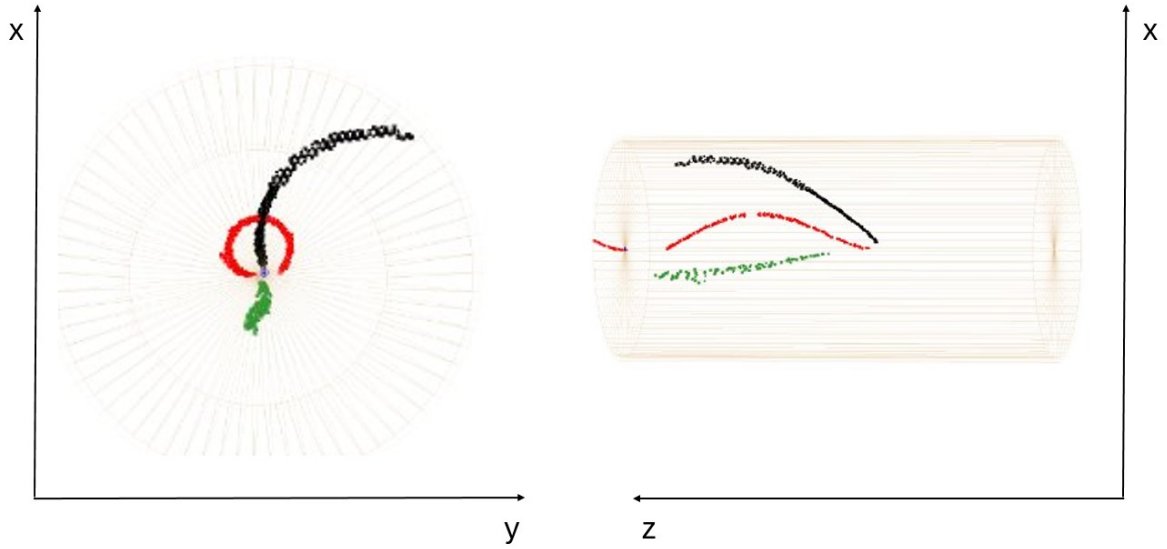

Figure F.10: The figure depicts an inelastic event in which oxygen collides with α particle to give rise to a ^{12}C (green), ^{4}He (red) and an α scattering particle (black).

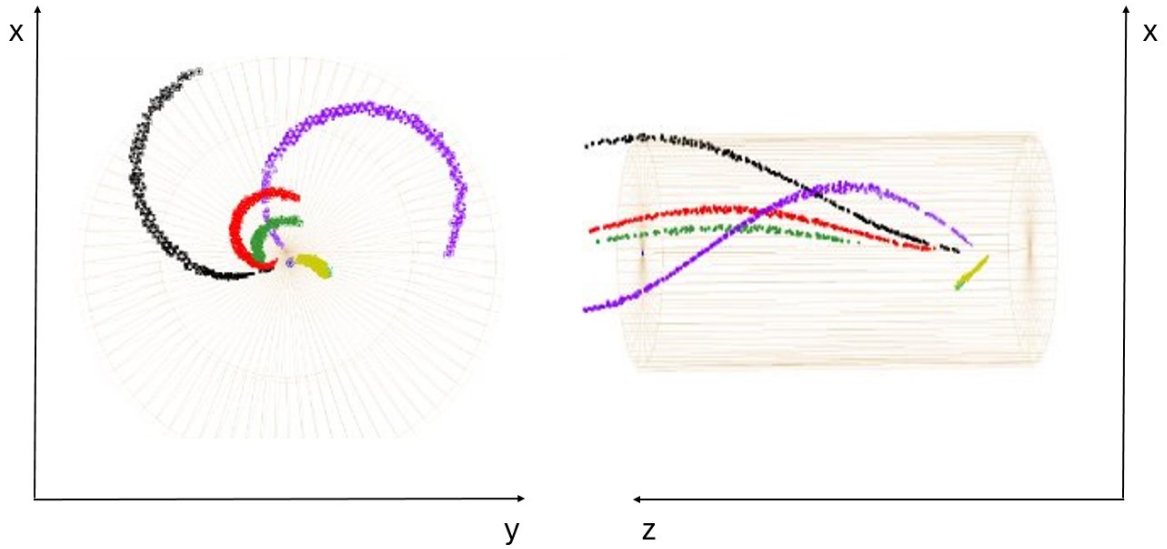

Figure F.11: This depicted event is the next step in disintegrating the previous event. In it, you can see how the carbon from the inelastic collision of the event described in figure F.10 disintegrates into an ^{4}He particle (black) and ^{8}Be, which almost instantaneously disintegrates into 2 α's (red and green). Such events are called sequential Hoyle events.

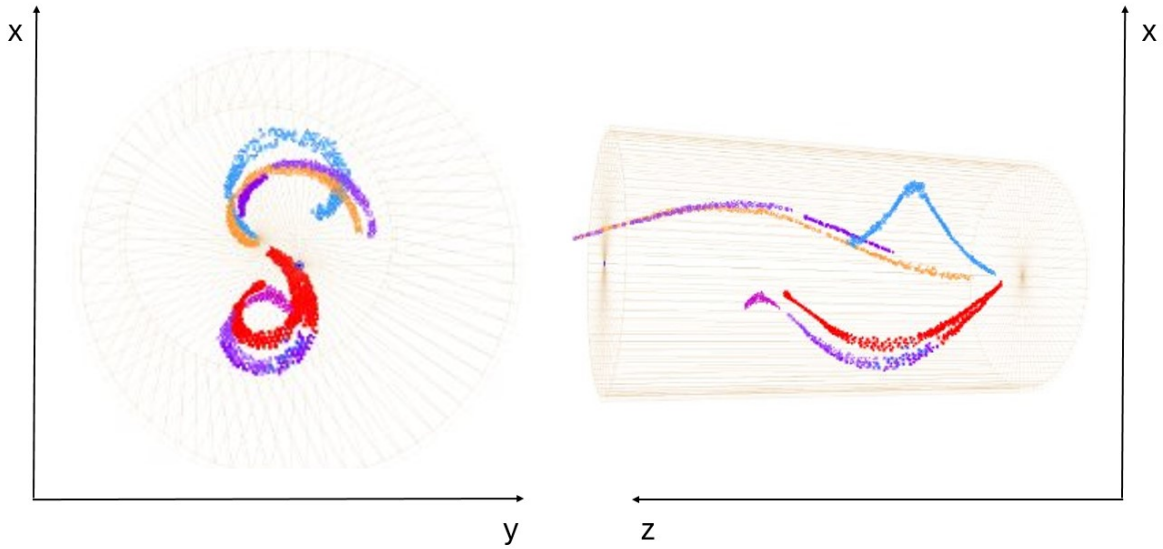

Figure F.12: Another type of event found in the decay of oxygen into 2 ^{8}Be's, which immediately decay into two pairs of correlated α particles, as shown in the figure.

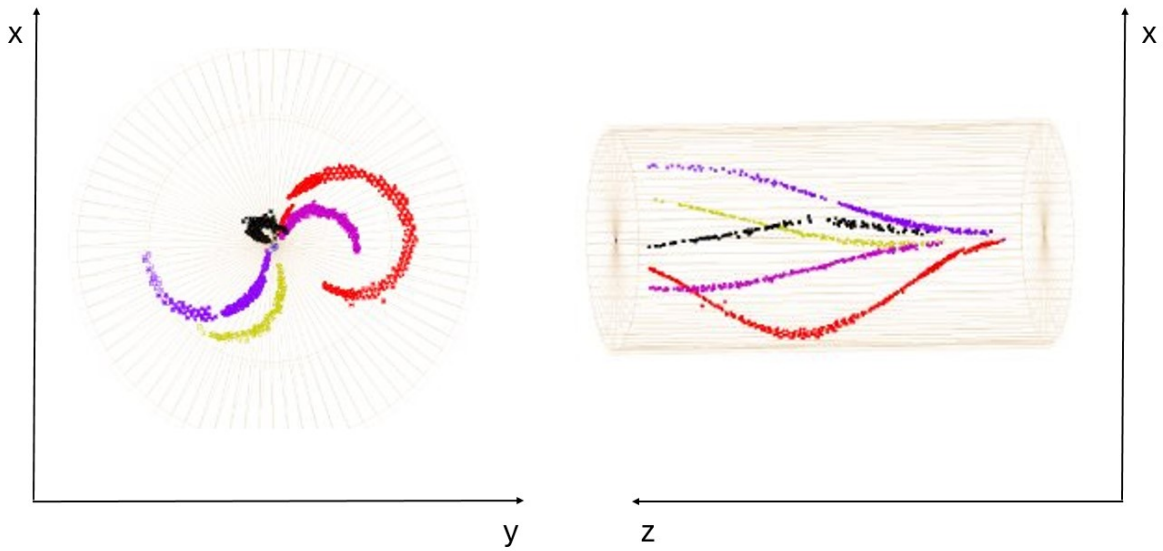

Figure F.13: The figure shows an ^{16}O disintegrating in direct decay to 4 α particles. In red, you can see the scattering alpha particle.

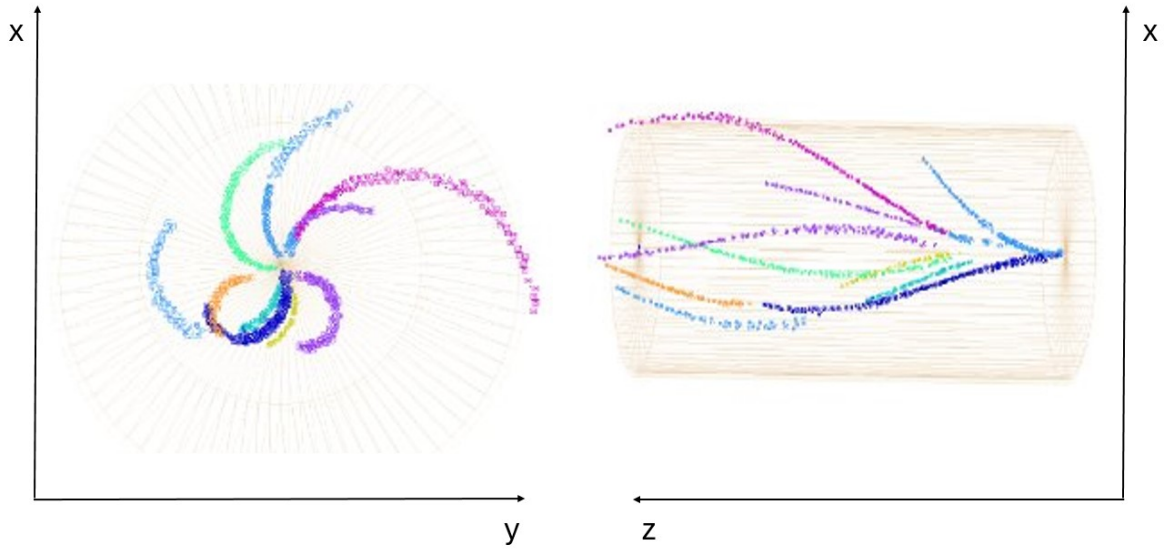

Figure F.14: Another typical event that can be found in this type of experiment is the so-called window event. In these, the heavy particle reacts with the materials forming the window before entering the chamber, giving rise to multiple traces from different reactions. These events also contribute to noise generation.

This experiment (E20020) aims to search for resonances in ^{16}O just above the energy of the four α-particles splitting 14.4 MeV. The experiment was designed to observe this resonance decaying into four α particles. The resonance studied in this thesis would correspond to the Hoyle state, an excited state of ^{12}C close to the α-particle separation energy. Fred Hoyle proposed this state in 1954 to explain the production of ^{12}C in stars. The Active Target Time Projection Chamber (AT-TPC) was filled with 700 Torr of pure ^{4}He gas and used as a reaction target and detector medium.

The experiment was conducted in the Facility for Rare Isotope Beams (FRIB) at Michigan State University with the AT-TPC detector at the centre of the 3 Tesla SOLARIS solenoid.